

# Electrokinetics in Low Salinity Waterflooding

## Experimental and Modeling Study for Sandstones

R.M. de Velde Harsenhorst

Technische Universiteit Delft



# ELECTROKINETICS IN LOW SALINITY WATERFLOODING

## EXPERIMENTAL AND MODELING STUDY FOR SANDSTONES

by

**R.M. de Velde Harsenhorst**

in partial fulfillment of the requirements for the degree of

**Master of Science**  
in Applied Earth Sciences

at Delft University of Technology,  
to be defended publicly on Monday September 29, 2014 at 15:30 PM.

TA report number: AES/PE/14-25

Professor:	Prof. ir. C. P. J. W. van Kruijsdijk,	Shell/ TU Delft
Supervisors:	Dr. H. Mahani,	Shell
	Dr. V. Joekar Niasar,	Shell
Thesis committee:	Dr. H. Hajibeygi,	TU Delft
	Prof. dr. ir. T. J. Heimovaara,	TU Delft

Copyright ©2014 Section for Petroleum Engineering

*All rights reserved. No parts of this publication may be reproduced, stored in a retrieval system, or transmitted, in any form or by any means, electronic, mechanical, photocopying, recording, or otherwise, without the prior permission of the section of Petroleum Engineering.*

An electronic version of this thesis is available at <http://repository.tudelft.nl/>.



# PHYSICAL CONSTANTS

<b>Constant</b>	<b>Symbol</b>	<b>SI</b>
Avogadro's constant	$N_A, N_O$	$6.022 * 10^{23} \text{ mol}^{-1}$
Boltzmann's constant	$k_B = R/N_A$	$1.381 * 10^{-23} \text{ J K}^{-1}$
Molar gas constant	$R = N_A k$	$8.314 \text{ J K}^{-1} \text{ mol}^{-1}$
Electronic charge	$-e$	$1.602 * 10^{-19} \text{ C}$
Faraday constant	$F = N_A e$	$9.649 * 10^4 \text{ C mol}^{-1}$
Permittivity of free space	$\epsilon_0$	$8.854 * 10^{-12} \text{ C}^2 \text{ J}^{-1} \text{ m}^{-1}$
Standard atmospheric pressure	$p_0$	$1.01325 * 10^5 \text{ Pa}$
Zero of Celsius scale	$T_0$	$273.15 \text{ K}$



# DERIVED SI UNITS

In order to understand the origin of derived SI (Système International) units, it is good to consider the basic units. These are the kilogram ( $kg$ ) for mass, the meter ( $m$ ) for length, the second ( $s$ ) for time, the kelvin ( $K$ ) for temperature, the ampere ( $A$ ) for electrical quantities, and the mole ( $mol$ ) for quantity of mass. From these basic units the following units can be derived [Israelachvili, 2011]:

Quantity	SI Unit	Symbol	Definition of Unit
Energy	Joule	$J$	$Nm = CV = kg\ m^2\ s^{-2}$
Force	Newton	$N$	$J\ m^{-1} = kg\ ms^{-2}$
Power	Watt	$W$	$J\ s^{-1} = kg\ m^2\ s^{-3}$
Pressure	Pascal	$P$	$N\ m^{-2}$
Electric charge	Coulomb	$C$	$A\ s$
Electric potential	Volt	$V$	$J\ A^{-1}\ s^{-1} = J\ C^{-1}$
Electric field	Volt/meter		$V\ m^{-1}$
Frequency	Hertz	$Hz$	$s^{-1}$



# PREFACE

First of all, I'd like to thank prof. ir. Van Kruijsdijk for giving me the opportunity to do my thesis within Shell and for the enormous amount of ideas, guidance and direction he has given me to come to this end result. Secondly, I'd like to thank my two supervisors, dr. Mahani and dr. Joekar Niasar, for their willingness to help me out with all my questions, and their time and devotion to think about ways to improve both the experimental and modeling work. Also, they were always ready to have a critical view on my work and redirect me, in spite of, sometimes, hesitations on my side.

I would also like to thank the other committee members, namely dr. Hajibeygi and prof. dr. ir. Heimovaara for showing their sincere interest in my work and for the willingness to take place in my thesis committee.

Furthermore, I would like to thank all the people in the Rock Fluid (RF) and Recovery Optimization (RO) departments that have helped me out either with experiments, modeling or general ideas and testing: Niels Brussee, Ab Coorn, Sebastiaan Pieterse, Frank van der Heyden, Bart Suijkerbuijk, Carl van Rijn, Hilbert van der Linde, Fons Marcelis, Leandra David, Willem-Bart Bartels, Steffen Berg, Ryan Armstrong, Ali Fadili and Koenraad Elewaut. Also my fellow students, Pauline and Vincent, for the 'countless' coffee breaks. And a special thanks to the boss, Diederik Boersma, for good stories and optimism.

For the helping hands in the laboratory in Delft, I'd like to thank Karel Heller, Marc Friebel, Michiel Slob, Jan Etienne, Ellen Meijvogel, Dick Delforferie, Jolanda van Haagen, Karl-Heinz Wolf, Alex Kirichek (for support in the lonely ground floor lab) and former Delft post-doc Christiaan Schoemaker. The warm tunes provided by Radio 538, Radio Decibel and Sublime FM kept me going as well. Also, I'd like to thank all my other study mates in Delft for the amazing lunch times and in-depth or superficial and shallow conversations about anything.

This project has kept me incredibly busy the last ten months, and although it has been a roller coaster from time to time, I must admit that I am happy with the end result and the amount of experience I have gained. I've grown into the project and it taught me ever more so not to give up and to keep pushing for the desired end results. I have witnessed the art of learning by doing and this provided a steep learning curve. I've come to learn more about my strengths and weaknesses and I've grown more self esteem. I especially enjoyed working together with all the people in the RF and RO departments in Rijswijk and the people in Delft. It is nice to have so much knowledge close at hand in all these individuals.

I am now very eager to graduate and I am curious to see where I will be in one year from now. Time will tell! To wrap things up I'd like to thank my roommates (Christof, Hein, Kees and Roeland), my parents and family, all my good friends and my girlfriend, Charlotte, for their support when a moody and despairing (or happy and cheerful) Robert stormed into their surroundings. And last but not least, as is appropriate in a thank you letter, I would like to opt for world peace. My time in Delft has been a pleasure. Thanks to everyone!

*R.M. de Velde Harsenhorst  
Delft, September 2014*



## ABSTRACT

Low salinity waterflooding (LSF) is a promising improved oil recovery (IOR) technique. The enhanced composition of injected water in LSF can change the wettability of the formation from oil-wet/ mixed-wet towards a more water-wet state. This leads to improved relative oil permeability ( $k_{ro}$ ). The zeta ( $\zeta$ ) potential, which is the electric potential at the shear plane, generally a couple of nanometers away from the rock/clay surface, can give an indication on rock wettability.

Streaming potential measurements and electrophoretic (zetalyzer) measurements give information on the zeta potential. Electrophoretic measurements can only be performed with crushed rock – brine or crushed rock – oil combinations. Streaming potential measurements are performed with sandstone cores. This allows for measurements with a full crude oil-brine-rock (COBR) system, which takes into account the proper ratio between rock/clay surface and bulk rock. In this thesis, we assess whether streaming potential measurements can give more information on rock wettability and wettability alteration for LSF.

Therefore, we first compare the obtained experimental single-phase streaming potential data with bundle-of-tubes (BOT) models that use the zeta potential from electrophoretic measurements and the pore geometry from micro CT data as an input. Secondly, single-phase streaming potential measurements are compared with two-phase streaming potential measurements. These two-phase measurements are then compared to specifically designed water-wet and oil-wet BOT models. The two-phase measurements are performed at residual oil saturation ( $S_{or}$ ). The last objective is to see the qualitative streaming potential response of an aged COBR system, consisting of Dagang brine, Berea 700 sandstone and crude oil H.

This thesis describes the streaming potential capabilities for single- and two-phase measurements that have been established at Delft University of Technology. Also, the results as obtained from streaming potential measurements and electrophoretic measurements are described in detail.

Furthermore, a model (single- and two-phase (water-wet and oil-wet)) has been developed that contains both the overlapping of double layers and Stern layer conduction. The models use input from micro CT data (pore throat radius) and zetalyzer measurements. This has not been done in literature before.

A comparison of modeling data to experimental data shows that the models that include the overlapping of double layers and Stern layer conduction represent the laboratory data best. The Stern layer conduction can be used as a fitting parameter. The two-phase water-wet models show similar trends compared to the lab data. The three effects that have the largest influence on the coupling coefficient are Stern layer conduction, the overlapping of double layers and the effective flow (velocity) through the pores.

At a higher salinity ( $10^{-3} - 1 M$ ), which coincides with the LSF region of interest (1500 – 5000 ppm), the coupling coefficients are geometry independent, not influenced by Stern layer conduction and more difficult to obtain, due to a high bulk conductivity of the liquid. It is hard to distinguish between measurements in this region; they all lie on the same line.

Charge inversion in presence of Dagang brine in Berea 700 at 70 °C, indicates a flipped sign of the zeta potential. This might indicate that the positively charged system would like to bind negative oil components to it. This might influence the wettability of the rock.

In final conclusion, streaming potential measurements should become standard practice in core flooding experiments. As this thesis shows, SP measurements give insight on surface processes occurring inside the core plug and therefore are a valuable addition to pressure drop measurements. This thesis provides valuable insights for continued research on IOR and EOR (enhanced oil recovery) topics. However, the continuation of streaming potential research for LSF should be assessed.



# CONTENTS

<b>Physical Constants</b>	<b>iii</b>
<b>Derived SI Units</b>	<b>v</b>
<b>Preface</b>	<b>vii</b>
<b>Abstract</b>	<b>ix</b>
<b>Contents</b>	<b>xi</b>
<b>List of Figures</b>	<b>xiii</b>
<b>List of Tables</b>	<b>xvii</b>
<b>Abbreviations</b>	<b>xix</b>
<b>Symbols</b>	<b>xxi</b>
<b>1 Introduction</b>	<b>1</b>
1.1 Discovery of the Low Salinity Effect . . . . .	1
1.2 Relevance of Low Salinity Waterflooding . . . . .	2
1.3 Thesis Objective . . . . .	3
1.4 Approach and Deliveries . . . . .	3
<b>2 Literature Review</b>	<b>5</b>
2.1 Basic Concepts . . . . .	5
2.1.1 Clays in Sandstones . . . . .	5
2.1.2 Properties of Reservoir Fluids . . . . .	6
2.1.3 Zeta Potential . . . . .	9
2.1.4 Basics of Electrokinetic Effects . . . . .	10
2.1.5 Wettability and Imbibition Tests . . . . .	12
2.2 Prerequisites of LSF . . . . .	16
2.3 Theories behind Low Salinity Waterflooding . . . . .	16
2.4 Electrokinetics . . . . .	18
2.4.1 The Charging of a Surface . . . . .	18
2.4.2 Electric Double Layer . . . . .	19
2.4.3 Charge Inversion. . . . .	20
2.4.4 Debye Length . . . . .	20
2.5 Basic Electrokinetic Equations . . . . .	21
2.5.1 Helmholtz Model . . . . .	23
2.5.2 Gouy-Chapman Model. . . . .	23
2.5.3 Stern Model . . . . .	24
2.5.4 Onsager Relations: Coupled Electrokinetic Phenomena . . . . .	25
2.5.5 Single-Phase Streaming Potential . . . . .	26
2.5.6 Two-Phase Streaming Potential . . . . .	36
2.5.7 Electrophoresis . . . . .	37
<b>3 Materials and Methods</b>	<b>39</b>
3.1 Rocks and Fluids . . . . .	39
3.1.1 Selection of Cores (Rocks) . . . . .	39
3.1.2 Core Characterization . . . . .	39
3.1.3 Selection of Fluids . . . . .	41
3.1.4 Experimental Conditions . . . . .	44

3.2	Experimental Setup (Streaming Potential)	45
3.2.1	Process and Instrumentation Diagram	45
3.2.2	Setup Components	45
3.2.3	Experimental Protocol and Sequence	50
3.3	Experimental Setup (Electrophoresis: Zetasizer)	50
3.3.1	Experimental Protocol and Sequence	50
3.4	Recap Materials and Methods	50
<b>4</b>	<b>Modeling</b>	<b>51</b>
4.1	Pore-Scale Modeling	51
4.2	Modeling Scope of This Thesis	51
4.3	Pore Network Extraction	52
4.4	Capillary Tube Model	52
4.4.1	Stern layer conduction	54
4.4.2	Modeling Geometries	54
4.4.3	Flow Chart Modeling	58
4.5	Bundle of Tubes Model	59
4.6	Pore Network Model	59
4.7	Recap Modeling	62
<b>5</b>	<b>Results and Discussion</b>	<b>63</b>
5.1	Experiments	63
5.1.1	Streaming Potential	63
5.1.2	Electrophoresis: Zetasizer	72
5.2	Modeling	74
5.2.1	Network Extraction	75
5.2.2	Gouy-Chapman Model	76
5.2.3	Single-Phase	77
5.2.4	Two Phase	83
5.3	Comparison of Experiments and Model	84
5.4	Further Discussion	89
5.5	Recap Results and Discussion	91
<b>6</b>	<b>Summary and Conclusions</b>	<b>93</b>
<b>7</b>	<b>Recommendations</b>	<b>95</b>
<b>A</b>	<b>Electrophoresis</b>	<b>97</b>
<b>B</b>	<b>Experimental Protocol and Sequence</b>	<b>101</b>
B.1	Streaming Potential	101
B.2	Zetasizer	104
<b>C</b>	<b>Pore Network Extraction</b>	<b>107</b>
<b>D</b>	<b>Experimental Data</b>	<b>111</b>
D.1	Streaming Potential	111
D.2	Zetasizer	112
	<b>Bibliography</b>	<b>115</b>

# LIST OF FIGURES

1.1	Oil droplet under high salinity brine and under low salinity brine. A change in contact angle can be observed over time [Mahani et al., 2014] . . . . .	2
1.2	Schematic sketch of the ROS in a porous sandstone rock after low salinity waterflooding [Mahani et al., 2014] . . . . .	2
2.1	Tetrahedral - Octahedral clay structure 1:1 [Hughes et al., 2012] . . . . .	6
2.2	Clay minerals: (a) kaolinite, (b) illite and (c) montmorillonite [Craig, 2004] . . . . .	6
2.3	Several ways of oil and clay to interact, without direct adsorption on the clay [Lager et al., 2006]	7
2.4	Compatibility criteria for different types of clay. The blue lines indicate the safe border, that is maintained throughout the experiments [Scheuerman and Bergersen, 1990] . . . . .	9
2.5	Electric double layer according to the Stern model. The inner and outer Helmholtz planes are indicated as IH and OH, respectively. The slipping plane (shear plane) is denoted by S and its potential is characterized by the $\zeta$ -potential [Schoemaker et al., 2012] . . . . .	10
2.6	Electrophoresis: The motion of the particles can be followed by observing the movement of the boundary between the cloudy suspension and the clear supernatant [Hunter, 1981] . . . . .	11
2.7	Top: Wettability in a porous medium, the oil is displayed in green, the water in blue and the rock in brown; Bottom: Wettability in a capillary, where the oil phase is white and the water grey. The charged surface is displayed in grey with a striped pattern (left: water wet surface; right: oil-wet surface) [Abdallah et al., 2007] . . . . .	12
2.8	Contact angle asperity [Abdallah et al., 2007] . . . . .	15
2.9	Production profiles of several Berea core plugs during imbibition with formation water and with low salinity brine. Brine changes to LS Brine E and LS brine E refresh are indicated by arrows [Suijkerbuijk et al., 2012] . . . . .	15
2.10	Divalent metal analysis of $Ca^{2+}$ and $Mg^{2+}$ during a low salinity waterflood in a reservoir condition field core flood. Solid red and blue lines are the high salinity in situ levels of $Ca^{2+}$ and $Mg^{2+}$ and the dashed red and blue lines are the low salinity injected concentration, respectively [Lager et al., 2006] . . . . .	17
2.11	Schematic depiction of the development of three different water zones during low salinity waterflooding. The evolution of the solution normality of the brine and the fraction of divalent cations on the clays as the LS slug moves through the reservoir are shown. This process creates a 'Salinity front' and a 'Retardation front' [Suijkerbuijk et al., 2013] . . . . .	18
2.12	Acquisition of surface charge by ionization of a) acidic groups and b) basic groups [Masliyah and Bhattacharjee, 2006] . . . . .	19
2.13	Potential variation with distance for a charged surface: a) potential reversal due to adsorption of surface active or multivalent counterions, b) adsorption of surface active co-ions [Masliyah and Bhattacharjee, 2006] . . . . .	20
2.14	Two models of the electric double layer: a) Helmholtz model, b) Gouy-Chapman model [Masliyah and Bhattacharjee, 2006] . . . . .	23
2.15	Effect of a dielectric between the plates of a parallel plate capacitor. The electrometer measures the potential difference. For a), with a given charge, the potential difference is $\psi_0$ . For b), with the same charge but with a dielectric between the plates, the potential difference $V$ is smaller than $\psi_0$ . . . . .	26
2.16	Illustration of the streaming potential phenomenon in a capillary tube or slit ( <i>modified from larryisgood (<a href="http://en.wikipedia.org/wiki/Double_layer_(interfacial))">http://en.wikipedia.org/wiki/Double_layer_(interfacial))</a>) . . . . .</i>	27
2.17	Geometry of the capillary used for the derivation of the streaming current [Modified from larryisgood ( <a href="http://en.wikipedia.org/wiki/Double_layer_(interfacial))">http://en.wikipedia.org/wiki/Double_layer_(interfacial))</a> ] . . . . .	28
2.18	Surface area and perimeter of a cylinder . . . . .	34
2.19	Effect of surface conductance illustrated [Stein et al., 2004] . . . . .	35
2.20	Coupling coefficients from literature compared to the empirical model [Glover et al., 2012] . . . . .	36

3.1	Three different core materials: Bentheimer, Berea 700 and Berea 18	40
3.2	Pore size distribution of Berea 700 deduced from capillary pressure curves as obtained by MICP (Mercury Injection Capillary Pressure)	41
3.3	Sandstone grains with abundant secondary quartz overgrowths (q). Clays (c) (mainly kaolinite and illite (i)) occur as pore-filling aggregates and in-part grain coating associated with secondary quartz. Pore space indicated as (p) [Marcelis, 2012a].	42
3.4	Electric conductivities of water under different conditions [Masliyah and Bhattacharjee, 2006]	43
3.5	Process Instrumentation Diagram (PID) of the streaming potential experimental setup (SPP = Set Point Pressure, BPR = Back Pressure Regulator)	46
3.6	Berea 700 and 18 Core Holder	47
3.7	Berea 700 Core Holder	47
3.8	Bentheimer Core Holder	47
3.9	QF20 Core Holder	47
3.10	Cross-section of the core holder displayed in Figure 3.7	48
3.11	Cross-section of the electrode fitting method	48
3.12	Effect of filtering on the signal as observed from the oscilloscope. Above: without filtering; below: with filtering	49
3.13	Zetasizer Nano Z (left) with MPT-2 autotitrator (right)	50
4.1	Example of a pore-network model. Pore bodies are symbolized as red spheres and pores throats as white lines. Pore bodies and pore throats all have different radii	52
4.2	Different geometries used to describe pore throats in a pore-network model [Joekar-Niasar, 2010]	52
4.3	Oversight of all the modeling activities in this thesis	53
4.4	Different geometries used in modeling. Top row: single phase cylindrical and triangular model. Middle row: triangular two-phase real case models for an WW and OW system. Bottom row: triangular two-phase model situation for an WW and OW system	55
4.5	Real and model situation for a mixed-wet triangle	58
4.6	Flow chart for the modeling. Inputs for the capillary tube model, bundle-of-tubes model and pore-network model are shown	58
4.7	Schematic of the bundle-of-tubes model (BOT)	59
4.8	Schematic of the pore-network model with 6 pores (PNM)	60
5.1	Coupling coefficients plotted against molarity for QF20, Bentheimer and Berea 700	64
5.2	Coupling coefficients plotted against fluid conductivity for QF20, Bentheimer and Berea 700	64
5.3	Coupling coefficient against fluid molarity: concept of geometry dependence	65
5.4	Debye length plotted against fluid molarity of an <i>NaCl</i> solution	66
5.5	Fines released from the Berea 700 sample after a switch from HS to LS (large step salinity change)	66
5.6	Flow rate plotted against pressure of a measurement on Berea 700	67
5.7	Flow rate plotted against pressure of a measurement on Berea 700	67
5.8	Coupling coefficients plotted against molarity for Bentheimer sandstone (single phase and two phase at 20 °C)	68
5.9	Coupling coefficients plotted against fluid conductivity for Bentheimer sandstone (single phase and two phase at 20 °C)	68
5.10	Coupling coefficients plotted against molarity for Berea sandstone (single phase at 20 and 70 °C, two phase at 70 °C)	69
5.11	Coupling coefficients plotted against fluid conductivity for Berea sandstone (single phase at 20 and 70 °C, two phase at 70 °C)	70
5.12	Coupling coefficients plotted against fluid conductivity for two phase experiments in Berea 700: Unaged and Aged	71
5.13	Zeta potential plotted against pH for several molarities for Berea 700 at 20 °C	72
5.14	Zeta potential plotted against pH for several molarities for Bentheimer at 20 °C	72
5.15	Zeta potential plotted against pH for several molarities for Berea 18 at 20 °C	73
5.16	Zeta potential plotted for several molarities for Berea 700, Bentheimer, Berea 18 and crude oil H (pH equal to pH in streaming potential experiments)	74
5.17	Zeta potential plotted against molarity for Berea 700 (pH equal to pH in streaming potential experiments). A trendline is fitted and used as modeling input	74

5.18 Zeta potential plotted against molarity for Bentheimer (pH equal to pH in streaming potential experiments). A trendline is fitted and used as modeling input . . . . .	74
5.19 Zeta potential plotted against molarity for Berea 18 (pH equal to pH in streaming potential experiments). A trendline is fitted and used as modeling input . . . . .	74
5.20 Zeta potential plotted against molarity for crude oil H. A trendline is fitted and used as modeling input . . . . .	74
5.21 Pore throat size and pore body size distribution for Berea 700 sandstone . . . . .	75
5.22 Pore throat size and pore body size distribution for Bentheimer sandstone . . . . .	76
5.23 Pore throat size and pore body size distribution for Berea 18 sandstone . . . . .	76
5.24 Potential variation with distance for a charged surface of $\psi = 25 \text{ mV}$ : a) and b) $10^{-4} \text{ mol/l}$ 1:1 electrolyte solution, c) and d) $10^{-4} \text{ mol/l}$ 2:2 electrolyte solution. $\Psi_s$ symbolizes the surface potential . . . . .	77
5.25 Coupling coefficient plotted against capillary radius and fluid molarity (only NaCl) for a cylindrical capillary for Berea 700 at 20 °C . . . . .	78
5.26 Effect of surface conductance in a single circular capillary of $r = 1E-7$ for different fluid molarities (only NaCl) for a Berea 700 sandstone at 20 °C . . . . .	78
5.27 Trends in the single phase model for Berea 700 sandstone with a capillary channel of $r = 1E-7$ (amount of divalents, temperature, geometry) . . . . .	79
5.28 Trends in the single phase model for a cylindrical capillary channel of $r = 1E-7$ without divalents at 20 °C for different lithologies) . . . . .	80
5.29 Coupling coefficient curves for Bentheimer and Berea 700 sandstone for their assigned average pore throat radius ( $r_{throat,average}$ ) and a cylindrical geometry) . . . . .	80
5.30 Trends in the single phase model for a cylindrical capillary channel of $r = 1E-7$ for Berea 700 with divalents at 20 °C for for a case with Stern layer conduction and one without Stern layer conduction . . . . .	81
5.31 Bundle-of-tubes models for single-phase streaming potential in Bentheimer and Berea 700. Input are the pore throat radii from micro CT data. Bentheimer is only considered at 20 ° and without divalents (as in the experiments) and Berea 700 is considered at both temperatures and with divalents. Three curves include Stern layer conduction with a value of $\Sigma_S^{Stern} = 1E-8$ to sketch the influence of the Stern layer conduction . . . . .	82
5.32 Bundle-of-tubes models for single-phase streaming potential in Bentheimer and Berea 700. Input are the pore throat radii from micro CT data. Bentheimer is only considered at 20 ° and without divalents (as in the experiments) and Berea 700 is considered at both temperatures and with divalents. Three curves have an adjusted pore size distribution as input; all the pore throat sizes are multiplied by a factor of $10^{-2}$ . . . . .	82
5.33 Water-wet bundle-of-tubes models for two-phase streaming potential in Berea 700. Three curves have original pore throat radii as input and different capillary pressures (in $Pa$ ) determine the different saturations. The other three curves have an adjusted pore size distribution as input, and therefore need a higher capillary pressure (in $Pa$ ) for the same saturations; all the pore throat sizes are multiplied by a factor of $10^{-2}$ . . . . .	84
5.34 Water-wet bundle-of-tubes models for two-phase streaming potential in Berea 700. The four curves have original pore throat radii as input and include Stern layer conduction of $\Sigma_S^{Stern} = 1E-8$ and different capillary pressures determine the different saturations . . . . .	85
5.35 Oil-wet bundle-of-tubes models for two-phase streaming potential in Berea 700. The four curves have original pore throat radii as input and different capillary pressures determine the different saturations . . . . .	85
5.36 A comparison for Bentheimer 20°C single-phase lab data with models: a capillary tube model, a bundle-of-tubes model, a BOT model with Stern layer conduction (5E-9 S) and a BOT model with an adjusted pore size distribution (multiplied with $10^{-2}$ ) . . . . .	86
5.37 A comparison for Bentheimer 20 °C two-phase lab data with models: a bundle-of-tubes model, a BOT model with Stern layer conduction (5E-9 S) and a BOT model with an adjusted pore size distribution (multiplied with $10^{-2}$ ). $S_o = 0.22$ in all cases . . . . .	86
5.38 A comparison for Bentheimer 20 °C two-phase (with added divalents) lab data with models: a bundle-of-tubes model, a BOT model with Stern layer conduction (5E-9 S) and a BOT model with an adjusted pore size distribution (multiplied with $10^{-2}$ ). $S_o = 0.22$ in all cases . . . . .	87
5.39 All Bentheimer lab data compared to the best-fit models . . . . .	87

5.40	A comparison for Berea 700 20 °C single-phase lab data with models: a capillary tube model, a bundle-of-tubes model, a BOT model with Stern layer conduction (2E-8 S) and a BOT model with an adjusted pore size distribution (multiplied with $0.25 * 10^{-2}$ ) . . . . .	88
5.41	A comparison for Berea 700 70 °C single-phase lab data with models: a capillary tube model, a bundle-of-tubes model, a BOT model with Stern layer conduction (5E-8 S) and a BOT model with an adjusted pore size distribution (multiplied with $0.2 * 10^{-2}$ ) . . . . .	88
5.42	A comparison for Berea 700 70 °C two-phase unaged lab data with models: a bundle-of-tubes model, a BOT model with Stern layer conduction (5E-8 S) and a BOT model with an adjusted pore size distribution (multiplied with $0.25 * 10^{-2}$ ). $S_o = 0.24$ in all cases . . . . .	89
5.43	A comparison for Berea 700 70 °C two-phase aged lab data with models: a bundle-of-tubes model, a BOT model with Stern layer conduction (5E-8 S) and a BOT model with an adjusted pore size distribution (multiplied with $0.2 * 10^{-2}$ ). $S_o = 0.20$ in all cases . . . . .	89
5.44	All Berea 700 lab data compared to the best-fit models . . . . .	90
B.1	Viscosity of PAO40/Decane mixtures plotted against the volume percentage of PAO40 . . . . .	103
B.2	Example of a streaming potential response on the oscilloscope for Bentheimer SST . . . . .	103
B.3	Comparison of manual titration to autotitration for Berea 18 with a $3.33 * 10^{-4} \text{ mol/l}$ (with 10 % of divalents) brine. The blue dots represent the measurements from autotitration, the green dots the manual measurements and the red dots are the average value of the manual measurements per pH . . . . .	105
C.1	Filtered micro-CT data in AVIZO . . . . .	108
C.2	Filtered and cropped micro-CT data in AVIZO . . . . .	108
C.3	Filtered and cropped micro-CT data in AVIZO . . . . .	108
C.4	Binary image of the filtered and cropped micro-CT data in AVIZO . . . . .	108
C.5	Flow chart of the steps taken in AVIZO in order to obtain correct input for the pore-network extraction code . . . . .	108
C.6	Pore throat radius and pore body radius distribution for a Berea 18 SST . . . . .	109

# LIST OF TABLES

2.1	Oversight of wetting tendency with different interfacial charges [Dubey and Doe, 1993] . . . . .	13
3.1	Semi-quantitative results of the whole rock and clay fraction ( $< 2\mu m$ ) XRD analysis on Berea 700 and Bentheimer sandstone samples [Marcelis, 2006] . . . . .	41
3.2	Fluid and rock combination oversight for single-phase and two-phase experiments. SP stands for combinations that are performed in streaming potential (SP) experiments, ZS stands for combinations that are performed in the zetasizer (ZS) experiments . . . . .	43
3.3	Fluid composition of the <i>NaCl</i> brines without added divalents. This table shows the example for an ionic strength of 1M . . . . .	44
3.4	Fluid composition of the <i>NaCl</i> brines with 10 % added divalents. This table shows the example for an ionic strength of 1M . . . . .	44
3.5	Fluid composition of Dagang brine in mg/l, mol/l and g/l . . . . .	44
3.6	Density, viscosity and conductivity of oils at 20 and 70 °C and 1 atm . . . . .	44
3.7	Other properties crude oil H (The interfacial tension is from initial $\rightarrow$ equilibrium) . . . . .	45
5.1	Sizes of the input images for the pore network extraction (number of voxels in each direction), the porosity and average pore throat and body radii . . . . .	75
6.1	Reflection on goals set at the start of this thesis . . . . .	94
D.1	Single-phase data QF20 at 20 °C, no divalents are added to the <i>NaCl</i> brines . . . . .	111
D.2	Single-phase data Bentheimer at 20 °C, no divalents are added to the <i>NaCl</i> brines . . . . .	111
D.3	Two-phase data Bentheimer at 20 °C, no divalents are added to the <i>NaCl</i> brines . . . . .	111
D.4	Two-phase data Bentheimer at 20 °C, 10 % divalents ( <i>CaCl</i> <sub>2</sub> ) are added to the <i>NaCl</i> brines . . . . .	112
D.5	Single-phase data Berea 700 at 20 °C, 10 % divalents ( <i>CaCl</i> <sub>2</sub> ) are added to the <i>NaCl</i> brines. The value in bold is the coupling coefficient measured with Dagang brine (reverse sign) . . . . .	112
D.6	Single-phase data Berea 700 at 70 °C, 10 % divalents ( <i>CaCl</i> <sub>2</sub> ) are added to the <i>NaCl</i> brines . . . . .	112
D.7	QC of single-phase data Berea 700 at 70 °C, 10 % divalents ( <i>CaCl</i> <sub>2</sub> ) are added to the <i>NaCl</i> brines. Brine at 0.4 M is Dagang brine . . . . .	112
D.8	Two-phase unaged data Berea 700 at 70 °C, 10 % divalents ( <i>CaCl</i> <sub>2</sub> ) are added to the <i>NaCl</i> brines. The top value in bold is the coupling coefficient measured with 0.4 M synthetic brine, the bottom one with Dagang brine (reverse sign) . . . . .	113
D.9	Two-phase aged data Berea 700 at 70 °C, 10 % divalents ( <i>CaCl</i> <sub>2</sub> ) are added to the <i>NaCl</i> brines. The value in bold is the coupling coefficient measured with Dagang brine (reverse sign) . . . . .	113
D.10	Zeta potential data for rock-brine combinations. The top matrix indicates the measurement pH, the middle matrix the measured zeta potential in mV and the bottom matrix indicates the standard deviation of the measurements in mV . . . . .	113
D.11	Zeta potential data for oil-brine combinations. Ratio of 1:10 oil:brine. Top vector indicates the zeta potential in mV, bottom vector the standard deviation in mV . . . . .	114



# ABBREVIATIONS

<b>Abbreviation</b>	<b>Meaning</b>
<b>BOT</b>	<b>B</b> undle- <b>o</b> f-Tubes
<b>BPR</b>	<b>B</b> ack Pressure <b>R</b> egulator
<b>CEC</b>	<b>C</b> ation Exchange <b>C</b> apacity
<b>COBR</b>	<b>C</b> rude <b>O</b> il - <b>B</b> rine - <b>R</b> ock
<b>DLE</b>	<b>D</b> ouble <b>L</b> ayer <b>E</b> xpansion
<b>DLVO</b>	<b>D</b> erjaguin, <b>L</b> andau, <b>V</b> erwey and <b>O</b> verbeek
<b>EDL</b>	<b>E</b> lectric <b>D</b> ouble <b>L</b> ayer
<b>FM</b>	<b>F</b> ormation
<b>GDP</b>	<b>G</b> ross <b>D</b> omestic <b>P</b> roduct
<b>HS</b>	<b>H</b> igh <b>S</b> alinity
<b>IFT</b>	<b>I</b> nterfacial <b>T</b> ension
<b>IH</b>	<b>I</b> nnner <b>H</b> elmholtz
<b>IOC</b>	<b>I</b> nternational <b>O</b> il <b>C</b> ompanies
<b>IOR</b>	<b>I</b> mproved <b>O</b> il <b>R</b> ecovery
<b>LHS</b>	<b>L</b> eft <b>H</b> and <b>S</b> ide
<b>LS</b>	<b>L</b> ow <b>S</b> alinity
<b>LSF</b>	<b>L</b> ow <b>S</b> alinity <b>W</b> aterflooding
<b>mEq</b>	<b>M</b> illiequivalent
<b>MICP</b>	<b>M</b> ercury <b>I</b> njection <b>C</b> apillary <b>P</b> ressure
<b>micro(<math>\mu</math>)-CT</b>	<b>M</b> icro- <b>C</b> omputed <b>T</b> omography
<b>MIE</b>	<b>M</b> ulti-component <b>I</b> on <b>E</b> xchange
<b>MOV</b>	<b>M</b> ovable <b>O</b> il <b>V</b> olume
<b>MSc</b>	<b>M</b> aster of <b>S</b> cience
<b>MW</b>	<b>M</b> ixed <b>W</b> et
<b>OH</b>	<b>O</b> uter <b>H</b> elmholtz
<b>OW</b>	<b>O</b> il <b>W</b> et
<b>PALS</b>	<b>P</b> hase <b>A</b> nalysis <b>L</b> ight <b>S</b> cattering
<b>PAO</b>	<b>P</b> oly <b>A</b> lpha <b>O</b> lefin
<b>PEEK</b>	<b>P</b> olyether <b>E</b> ther <b>K</b> etone
<b>pH</b>	<b>p</b> ower of <b>H</b> ydrogen
<b>PID</b>	<b>P</b> rocess and <b>I</b> nstrumentation <b>D</b> iagram
<b>PNM</b>	<b>P</b> ore- <b>n</b> etwork <b>M</b> odel
<b>ppm</b>	<b>p</b> arts <b>p</b> er <b>m</b> illion
<b>PVC</b>	<b>P</b> oly <b>V</b> inyl <b>C</b> hloride
<b>PZC</b>	<b>P</b> oint of <b>Z</b> ero <b>C</b> harge
<b>REV</b>	<b>R</b> epresentative <b>E</b> lementary <b>V</b> olume
<b>RHS</b>	<b>R</b> ight <b>H</b> and <b>S</b> ide
<b>ROS</b>	<b>R</b> emaining <b>O</b> il <b>S</b> aturation
<b>SARA</b>	<b>S</b> aturates, <b>A</b> romatics, <b>R</b> esins and <b>A</b> sphaltenes
<b>SEM</b>	<b>S</b> canning <b>E</b> lectron <b>M</b> icroscope
<b>SI</b>	<b>S</b> ystème <b>I</b> nternational
<b>SP</b>	<b>S</b> treaming <b>P</b> otential
<b>SPP</b>	<b>S</b> et <b>P</b> oint <b>P</b> ressure
<b>SST</b>	<b>S</b> andstone
<b>STOIP</b>	<b>S</b> tock <b>T</b> ank <b>O</b> il <b>I</b> nitially <b>I</b> n <b>P</b> lace
<b>TAN</b>	<b>T</b> otal <b>A</b> cid <b>N</b> umber
<b>TBN</b>	<b>T</b> otal <b>B</b> ase <b>N</b> umber
<b>TDS</b>	<b>T</b> otal <b>D</b> issolved <b>S</b> olids

---

<b>VdW</b>	<b>Van der Waals</b>
<b>WW</b>	<b>Water Wet</b>
<b>XRD</b>	<b>X-ray Diffraction</b>

---

# SYMBOLS

Symbol	Meaning	SI
$a$	Side length equilateral triangle	$m$
$A$	Hamaker constant	$J$
$A$	Area	$m^2$
$A_1$	Calculation term	-
$A_c$	Cross-sectional area capillary	$m^2$
$b$	Corner fill triangle side length (OW, WW situation)	$m$
$C$	Concentration	$mol\ m^{-3}$
$C$	Capacitance	$CV^{-1}$
$c_i$	Molar concentration of ion i	$mol\ m^{-3}$
$C_r$	Relative coupling coefficient	-
$C_s$	Coupling coefficient	$VPa^{-1}$
$d$	Mean grain diameter	$m$
$d$	Distance	$m$
$D$	Diffusion coefficient	$m^2\ s^{-1}$
$E = \nabla\psi$	Electric field	$V\ m^{-1}$
$E_s$	Streaming Potential	$V$
$EM$	Electrophoretic mobility (U/E)	$m^2\ (Vs)^{-1}$
$f$	Calculation term	-
$F$	Formation factor	-
$F_{cc}$	Calculation term	-
$F_E$	Electric force	$N$
$F_H$	Hydrodynamic drag force	$N$
$h$	Film thickness	$m$
$I$	Ionic strength	$mol\ m^{-3}$
$I_0$	0th order modified Bessel function of the 1st kind	-
$I_1$	1st order modified Bessel function of the 1st kind	-
$J$	Current	$A$
$J_c$	Conduction current	$A$
$J_s$	Streaming current	$A$
$k$	Cell (porous medium) constant of the sample	-
$k$	Permeability	$m^2$
$k_{rn}$	Relative permeability of phase n	$m^2$
$l$	Length of a capillary	$m$
$L_{11}$	Darcy term	$m^3(Pa\ s)^{-1}$
$L_{12}$	Coupled Streaming current term	$m^3\ (Vs)^{-1} = ms^2\ A\ kg^{-1}$
$L_{21}$	Coupled Streaming current term	$A\ Pa^{-1} = ms^2\ A\ kg^{-1}$
$L_{22}$	Conduction current term in the coupled matrix	$A\ V^{-1}$
$m$	Cementation factor	-
$M$	Molar mass	$g\ mol^{-1}$
$n$	Saturation exponent	-
$n_i$	Ionic number concentration	$m^{-3}$
$n_\infty$	Ionic number concentration in the bulk fluid	$m^{-3}$
$p$	Perimeter	$m$
$P$	Pressure	$Pa$
$P_c$	Capillary pressure	$Pa$
$Q$	Charge	$C$
$Q$	Flow rate	$m^3\ s^{-1}$
$r$	Particle radius / capillary radius	$m$

$r_c$	Radius of curvature	$m$
$r_{c,entry}$	Entry radius of curvature	$m$
$r_{inscribed}$	Inscribed radius of a triangle	$m$
$R_0$	Resistivity of porous sample at HS	$mS^{-1}$
$R_\theta$	Resistivity of porous sample at LS	$mS^{-1}$
$S$	Wetted perimeter	$m$
$S_o$	Oil saturation	-
$S_{or}$	Residual oil saturation	-
$S_w$	Water saturation	-
$S_{wc}$	Connate water saturation (also $S_{wirr}$ )	-
$S_{wi}$	Initial water saturation	-
$S_{wr}$	Residual water saturation	-
$t$	Hexagonal side length	$m$
$T_C$	Temperature	$^{\circ}C$
$T_K$	Temperature	$^{\circ}K$
$U$	Electrophoretic particle velocity	$m s^{-1}$
$u_x$	Fluid velocity tangential to plate	$m s^{-1}$
$v$	Liquid velocity	$m s^{-1}$
$V$	Potential	$V$
$W$	Wettability index	-
$x, y, z$	Position along the x-, y- or z- axis	$m$
$z$	Pore coordination number	-
$z_i$	Valency of ion i	-
$\alpha$	Geometrical correction factor	-
$\alpha$	Tortuosity	-
$\beta$	Corner half angle	$rad$
$\beta$	Calculation term	-
$\epsilon$	Electrical permittivity	$C^2 J^{-1} m^{-1}$
$\epsilon_r$	Dielectric constant of the electrolyte	-
$\zeta$	Zeta potential	$V$
$\zeta_o$	Zeta potential of oil in water	$V$
$\zeta_r$	Zeta potential of rock in water	$V$
$\eta$	Viscosity	$Pa s$
$\theta$	Contact angle	$rad$
$\theta_R$	Receding contact angle	$rad$
$\kappa$	Inverse Debye length	$m^{-1}$
$\lambda_0$	Bulk fluid conductivity	$S m^{-1}$
$\lambda_D$	Debye length	$m$
$\lambda_s$	Surface conduction caused by the EDL	$S$
$\lambda_T$	Total conductivity	$S m^{-1}$
$\lambda_{T,\theta}$	Total conductivity at LS	$S m^{-1}$
$\Pi$	Disjoining pressure	$Pa$
$\rho$	Charge density (also $\rho_f$ )	$C m^{-3}$
$\rho$	Density	$kg m^{-3}$
$\sigma$	Fluid-fluid interfacial tension	$Nm^{-1}$
$\phi$	Porosity	-
$\psi$	Potential	$V$
$\psi_d$	Stern plane potential	$V$
$\psi_s$	Surface potential	$V$
$\Omega$	Self defined variable	$\epsilon\zeta\eta^{-1}$

---

# 1

## INTRODUCTION

This chapter briefly discusses the discovery of the Low Salinity Effect, the relevance of the Low Salinity Waterflooding technique and the relation to future global energy need. After this the goal and hypothesis of this MSc thesis will be discussed.

### 1.1. DISCOVERY OF THE LOW SALINITY EFFECT

Already in the 1960's [Bernard \[1967\]](#) has shown that the ionic strength of a fluid flowing in a porous medium influences the measured permeability of that same fluid. In the 1990's [Tang and Morrow \[1999\]](#) found out that in laboratory core waterfloods an increase in crude oil recovery occurred as the salinity of the displacing water decreased. This was for clastic cores containing some crude oil and clays. This triggered the interest of international oil companies (IOC) in the concept of Low Salinity Waterflooding, such as Shell, BP, Statoil and ExxonMobil. Up until then, the composition of the injected water in oilfields was not of much concern, apart from scaling and reservoir souring issues [[Hughes et al., 2012](#)]. Generally, the operator picked a source of water that was closest, easiest and cheapest available. This is still the dominant approach to waterflooding though and most operators inject seawater in their offshore oilfields. When water cut becomes too high or already in an earlier stage, the designing of the injected water composition could be a solution to this.

Low Salinity Waterflooding (LSF) is a promising method in Improved Oil Recovery (IOR). So far, some field trials have shown the successful application of LSF; for BP in the Endicott (North Slope) oilfield in Alaska [[Seccombe et al., 2010](#); [Mcguire et al., 2005](#)]. For Shell the successful application has been shown in the Omar oilfield [[Vledder et al., 2010](#); [Mahani et al., 2011](#)], where the effect was seen accidentally, after switching to Low Salinity injection water. A successful log-inject-log test was later performed in the Isba oilfield [[Mahani et al., 2011](#)]. In contrast to this there have also been unsuccessful cases, such as the Snorre oilfield operated by Statoil [[Skrettingland et al., 2011](#)]. In this field no incremental oil recovery was obtained by injecting Low Salinity water. This was due to the initial wettability (tendency for oil or water of the rock) of the reservoir.

The LSF process is basically an enhanced waterflooding process, in which the injected brine has a specifically designed composition with a lower salinity or lower TDS (Total Dissolved Solids) than the original formation water or the previously injected seawater. The injected brine with a controlled composition generally has a lower threshold of around 1500 ppm and an upper threshold of between 5000 – 7000 ppm. It is important that the ionic strength of the injected water is lower than the original formation water [[Mahani, 2013](#)].

Key advantages of the Low Salinity Waterflooding process are [[Mahani, 2013](#); [Suijkerbuijk et al., 2013](#)]:

1. Quite similar to regular waterflooding, easy to implement
2. Low CO<sub>2</sub> footprint
3. Low-cost IOR method
4. Less scaling
5. Less reservoir souring
6. Better water injectivity

As the term IOR already implicates, the main objective of LSF is to increase the oil production and decrease the remaining oil saturation ( $ROS$ ). Application of LSF in sandstones is believed to lead to a wettability modification towards a more water-wet state, which is observed in experiments at the core, droplet scale (Figure 1.1) and atomic scale [Suijkerbuijk et al., 2013], leading to a larger movable oil volume (MOV). It is shown that crude oil and clay-bearing sandstone are required for the effect to occur; the effect is not seen in water-wet, clay-free porous media with mineral oils [Sorbie and Collins, 2010]. The LSF procedure reduces  $ROS$  (Figure 1.2 shows the reduction of  $ROS$  in a sandstone) and it can improve sweep efficiency by means of an increase of relative oil permeability ( $k_{ro}$ ). Probably this is combined with a reduction of the residual oil saturation ( $S_{or}$ ), but as the rock becomes more water-wet,  $S_{or}$  might also increase. In the lab Tang and Morrow [1999] showed an incremental oil recovery in the range of 5 – 10 percent Stock Tank Oil Initially in Place (STOIIP). In a real field this number could be both larger and smaller, depending on for example oil composition, rock composition, temperature and pressure in a reservoir. An analytical assessment of changes in oil saturation showed an incremental oil recovery of 10 – 15 percent STOIIP for the Omar field [Vledder et al., 2010]. In the Isba field an incremental oil recovery of 15 percent was estimated [Mahani et al., 2011].

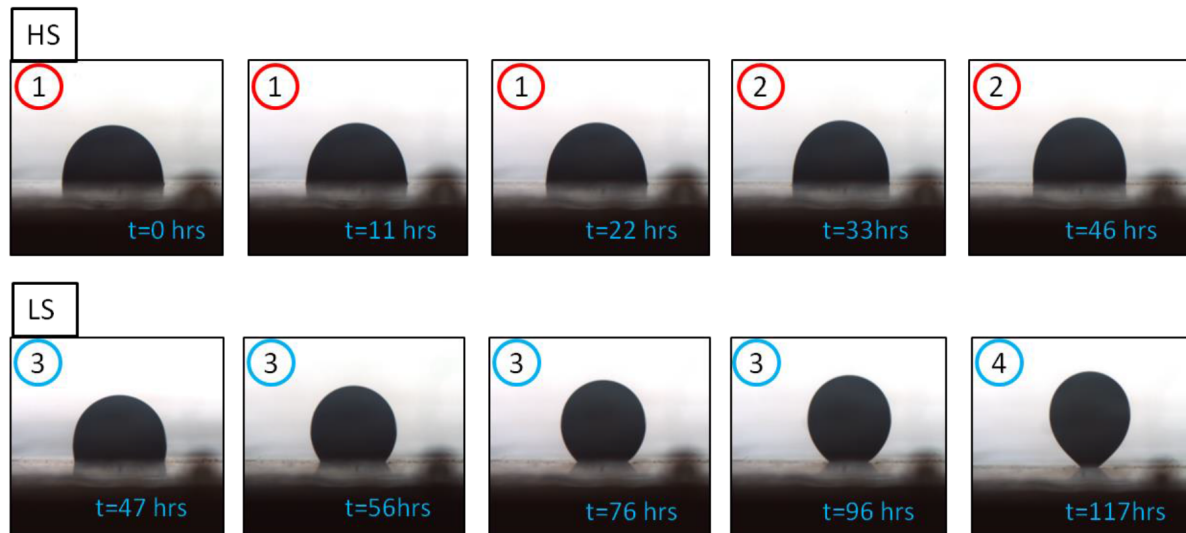


Figure 1.1: Oil droplet under high salinity brine and under low salinity brine. A change in contact angle can be observed over time [Mahani et al., 2014]

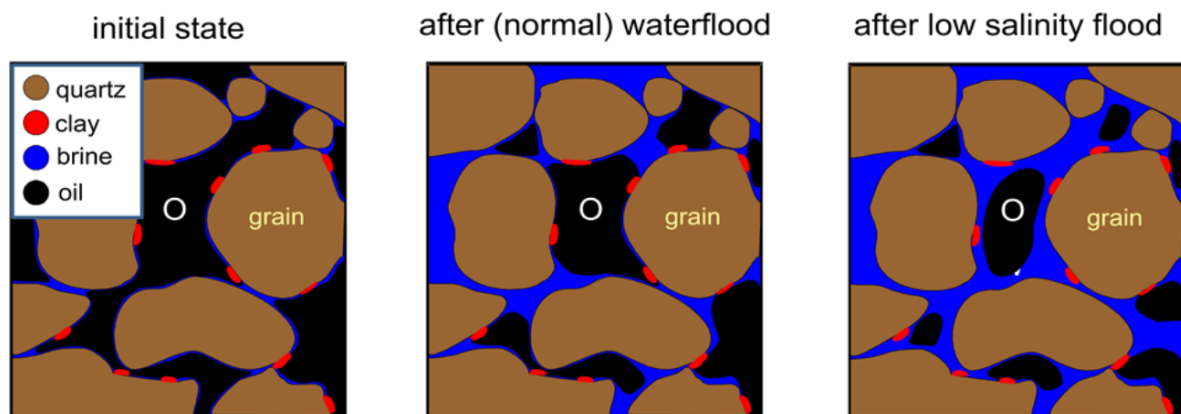


Figure 1.2: Schematic sketch of the  $ROS$  in a porous sandstone rock after low salinity waterflooding [Mahani et al., 2014]

## 1.2. RELEVANCE OF LOW SALINITY WATERFLOODING

By 2035 the world's population will have grown by 1.7 billion to 8.9 billion persons. GDP in this period will double and the energy use of this growing population will increase with a staggering 41 percent compared

to today's energy consumption. According to the BP statistical review 85 percent of this energy will come from fossil fuels. Although there may be regional differences in this percentage of fossil energy use, based on political decisions and the ability to afford renewable energy sources, worldwide, oil, gas and coal will each account for 27 percent of total energy generation [Ruhl, 2014]. To be able to achieve this enormous increase in energy consumption the world will need all energies in the energy mix. Getting the extra drop out of new and mature oilfields is a subchallenge of this bigger picture. Improved Oil Recovery (IOR) methods, such as Low Salinity Waterflooding, can play a big part in meeting this huge global energy demand.

### 1.3. THESIS OBJECTIVE

The zeta ( $\zeta$ ) potential, which is the electric potential at the shear plane (see Figure 2.5), generally a couple of nanometers away from the rock/clay surface, can give an indication on rock wettability. A common method to determine the zeta ( $\zeta$ ) potential is an electrophoretic method with a zetasizer experimental device. The advantages of this method are that it is fast and easy to perform and one can control pH. A disadvantage is that crushed rock is used, so bulk material and surface material influence zeta potential. Also, it is not possible to increase temperature to reservoir conditions, such as 70 °C. Another method to determine zeta potential, is by means of streaming potential measurements. These measurements are more difficult to perform, but they do take into account the pore morphology, the fluid flow (influenced by permeability) and the right ratio of rock to fluids and only surface rock, not the bulk.

In this MSc thesis the focus will be on the relation between streaming potential (measurements) and the zeta ( $\zeta$ ) potential. The main objective is to compare single-phase streaming potential measurements at different salinities with the models of the streaming potential, where electrophoretic measurements (zetasizer) are an important input (the zeta ( $\zeta$ ) potential) to the model. The modeling will consist of capillary tube, bundle-of-tubes (BOT) and pore-network modeling (PNM). The second objective is to compare two-phase streaming potential measurements to single-phase data and to models, where geometry is simple, and able to represent a water-wet and an oil-wet case. Here also, capillary tube, BOT and PNM modeling will be used. The third objective is to see the qualitative two-phase response of streaming potential when flooding an aged core (crude oil and formation brine) with HS and then LS brine. The idea is that the streaming potential response will show wettability alteration happening inside the core plug, when salinity is lowered.

### 1.4. APPROACH AND DELIVERIES

This thesis will assess this problem in an integrated way, where streaming potential measurements, electrophoretic measurements, core characterization and pore-scale modeling form the parts of this assessment.

The streaming potential measurements will be performed on 'Berea 700' outcrop sandstone, which has shown the 'low salinity effect' (an increase in oil recovery as seen in previous studies [Suijkerbuijk et al., 2012]) in spontaneous imbibition experiments. The experimental set-up will be developed and the 'Berea 700' will be flooded with brine of different salinities to compare the measurements with the available literature. The sandstone core will be aged with crude oil and formation brine. The core will then be flooded with high salinity first and then low salinity water to investigate the streaming potential response. As a control, we also use Bentheimer and Berea Block 18 sandstones, because of their wide availability and their respectively dissimilar (Bentheimer has a very low clay content) and similar properties compared to Berea 700.

To characterize the sandstone core several analysis techniques will be deployed. The core mineralogy is determined by X-ray Diffraction analysis. The pore morphology is analyzed using micro CT data and electrophoretic (zetasizer) measurements will be done to get the zeta potential.

In order to assess the relation between the zeta potential and the streaming potential, equations from literature will be used. Furthermore, pore-scale modeling techniques will be applied to include electrical surface forces in a bundle-of-tubes and a pore-network model. Input for this will be formed by the core characterization through micro CT. The results from the BOT model and the pore-network modeling can be compared to the streaming potential measurements.

To summarize, this thesis will consist of the following:

1. Streaming potential and electrophoretic measurements and analysis
2. Core characterization
3. Pore-scale modeling

This work differs from previous work in multiple ways:

1. The comparison of single-phase streaming potential measurements to models (BOT and PNM) with electrophoretic measurements as zeta potential input
2. The comparison of single-phase streaming potential measurements to two-phase streaming potential measurements
3. The comparison of two phase streaming potential measurements with water-wet and oil-wet models (BOT)
4. The use of streaming potential measurements to assess the qualitative response in two-phase core flooding and the relation to wettability change

These are the thesis deliveries:

1. Literature review
2. Experimental set-up and results
3. Data-analysis and comparison to previous work
4. Capillary Tube, Bundle-of-Tubes and Pore-network modeling
5. Report and presentation
6. Preparation and submission of a paper

# 2

## LITERATURE REVIEW

In this chapter the relevant literature for this MSc thesis work will be reviewed. The scope will be the electrokinetic phenomena related to Low Salinity Waterflooding and streaming potential/ electrophoresis theory and measurements as well as the basic concepts. First, the basic concepts will be discussed, then the concepts behind LSF. After this, a section on electrokinetics follows and then a section on the mathematical descriptions.

### 2.1. BASIC CONCEPTS

In the Basic Concepts section, all components of the Crude Oil - Brine - Rock (COBR) are shortly explained and introduced. Also, the concepts of wettability, zeta potential and formation damage are introduced.

#### 2.1.1. CLAYS IN SANDSTONES

The composition of sandstones is important to describe, as this composition greatly influences the electrokinetic effects, which will be described later on in this thesis. It influences the surface charge, the zeta potential, ion exchange, formation damage and many more things. The rocks that are used in this research are Berea and Bentheimer sandstones, and a fused silica (QF20). Most sandstones (SST) contain a certain amount of clay. Berea and Bentheimer sandstones are clay bearing sandstones. The main component of sandstones is quartz ( $SiO_2$ ). Berea sandstones contain more clays (between 6 – 8 %) than Bentheimer sandstone, which have a higher quartz content (over 98 %). Small fractions of kaolinite clay can be found in Bentheimer sandstone. The clays that can be found in Berea sandstones are kaolinite, illite/ mica, chlorite, orthoclase and albite. This will be described in more detail in Subsection 3.1.2.

Clay particles are mainly a result of weathering. The composition and structure of these clays depends on the source of the clays. Most clays are derived from primary silicates, so most clays come from weathered micas, amphiboles, pyroxenes and olivines [Meunier, 2005].

Clays are formed by layers of alumino-silicates stacked on top of each other. Clays are built from layers (sheets) of  $SiO_4$  tetrahedrons and octahedrons like  $Al_2(OH)_6)_n$  or  $((Fe/Mg)_3(OH)_6)_n$ . They can be subdivided in two groups, based on the number of sheets required to form one layer [Hughes et al., 2012]:

1:1 Clay mineral consists of one octahedral sheet and one tetrahedral sheet

2:1 Clay mineral consists of one octahedral sheet between two tetrahedral sheets

Figure 2.1 shows two 1:1 clay layers, consisting of an octahedral and a tetrahedral sheet and it shows some bonding methods between two such layers. Two clay layers can bind together by means of direct adhesion and bonding through interlayer cations. 1:1 clay layers bind by adhesion. The dipole in the OH molecule in  $AlOH^-$  creates a positive charge on the H atom, which can then bind with  $SiO_2^-$  groups of other layers.

The structure of the clays is important for the behaviour of clays. A 1:1 clay (e.g. kaolinite) does not have an interlayer, so the interlayer cannot swell. The bonding between kaolinite sheets is so strong that water and cations cannot get in between and they are thus not able to increase interlayer distance. For a 2:1 clay, this is different. The structures in a 2:1 clay repel each other, so the only way to bind is by interlayer ions and water. When the repulsion of layers grows, the interlayer distance grows as well, causing the clay to swell. This

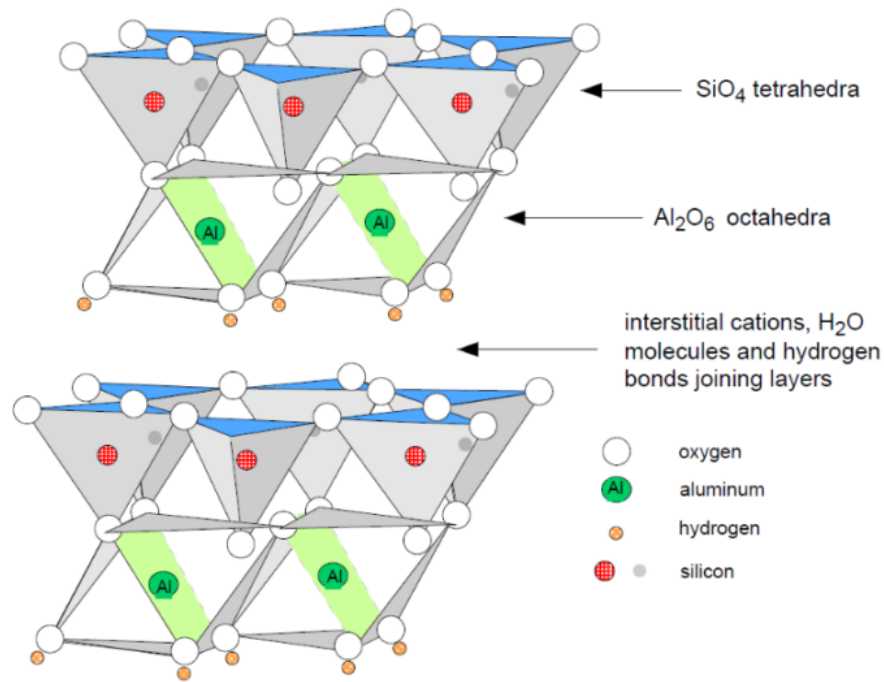


Figure 2.1: Tetrahedral - Octahedral clay structure 1:1 [Hughes et al., 2012]

behaviour is not preferred in reservoirs as the swelled clay may reduce permeability by clogging pore throats [Meunier, 2005]. Later on in Subsection 2.1.2.3 we will discuss the Scheuerman limits for formation damage, which are deduced from this reduced permeability due to clay swelling. Figure 2.2 shows the structure of kaolinite, illite and montmorillonite. From left to right the swelling ability of the clays increases.

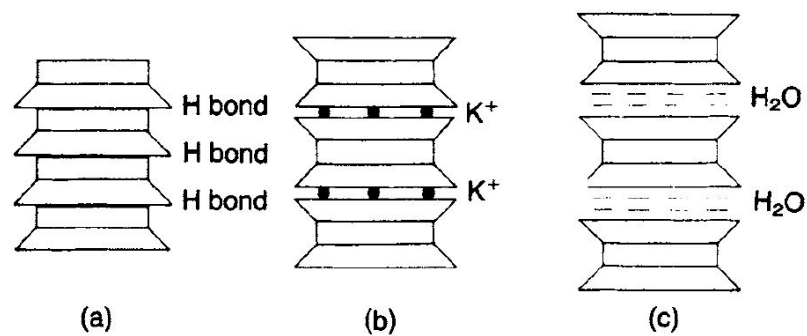


Figure 2.2: Clay minerals: (a) kaolinite, (b) illite and (c) montmorillonite [Craig, 2004]

There are three ways for a clay surface to obtain charge. This can be due to structural charge, pH induced charge and due to the adsorption or desorption of cations. The concept behind this will be further explained in Subsection 2.4.1. The point of zero charge (PZC) of pure silica (Si) lies around  $\text{pH} = 2$  and the PZC of Al lies around  $\text{pH} = 8$ . The difference in this PZC means that the surfaces of Si and Al are not equally protonated for a given pH. The capability of a clay to adsorb or desorb cations is called the cation exchange capacity (CEC) and is pH dependent.

### 2.1.2. PROPERTIES OF RESERVOIR FLUIDS

#### CRUDE OIL

The composition of a crude oil influences its ability to wet (from water-wet to oil-wet) a surface, in other words to come close to a sandstone surface and to interact with it. This is important when looking at a core,

aged with crude oil, because this affects the flow properties and the electrokinetic properties of the core, which will be measured in streaming potential experiments. Crude oil is a mixture of many hydrocarbon components and contains traces of oxygen, nitrogen, sulfur and halogen components. The hydrocarbons in crude oil can be subdivided in four groups: the saturates, aromatics, resins and asphaltenes (SARA classification). The saturates are apolar and saturated, such as alkanes and cyclo-alkanes. The aromatics are components that contain an aromatic group, such as benzene. They are very stable and therefore occur in large frequency. Resins constitute the most polar fraction of the oil components that dissolve in n-alkane, which lies at the basis of the SARA method. Naphthenic acids are commonly regarded as part of the resin fraction and are believed to be responsible for a large part of the behavior of crude oil at liquid interfaces [Speight, 1980].

Asphaltenes are of interest if one looks at the wettability alteration that can be caused by crude oils. The asphaltene fraction contains the largest percentage of heteroatoms (O, S, N) and organometallic constituents (Ni, V, Fe) in the crude oil. The asphaltenes precipitate easily, because of their chain length. Components in the oil that are capable of carrying charge are thought to cause the adhesion of oil to clays. In a reservoir setting, the free oil is dominated by saturated hydrocarbons (61.4-87.5%) with a low content of resins and asphaltenes (6.0-22.0%), while the adsorbed oil is dominated by resins and asphaltenes (84.8-98.5%) with a low content of saturated hydrocarbons (0.6-9.5%). Oil fractions that interact with the rock surface are expected to bind to it through either specific interactions or non-specific adsorption. For the former type of interactions to occur the relevant class of oil components should possess particular functional groups, such as alkyls, alcohols, ethers, aldehydes, ketons, carboxylic acids, esters, amines and amides. Amines can cause direct oil-clay adsorption and acids could cause oil to be bridged to the rock via cations. This means the presence of trace amounts of for example N, O, P and S may alter properties of the crude oil significantly [Speight, 1980].

Functional groups can be classified in terms of Total Acid Number (TAN) and Total Base Number (TBN). During the formation of oil, numerous functional groups are destroyed and generated. Two terms are used to quantify the amount of acid and base in a particular oil sample: TAN and TBN. These consist of Bronsted acids and bases. Bronsted acids are molecules that can donate a proton (leaving a negative anion) and Bronsted bases are able to accept a proton (leaving a positive cation). The TAN and TBN numbers give information about the ability of a mixture to release or accept protons, but the numbers do not say anything directly on the surface binding potential [Speight, 1980]. This means that even if TAN and TBN numbers of two crudes are exactly the same, the wettability modification caused by the crude oil mixture components might be completely different. Although this might differ, research in the past has shown that in general the wettability of sandstone is more oil-wet (less water-wet) with a higher crude oil TBN, a higher resins/asphaltenes concentration and at lower pH [Suijkerbuijk et al., 2012].

To summarize, crude oil may vary in terms of polar component content, aromatic content, density, viscosity, asphaltenes and many more. Together with the other elements in the COBR system, this contributes to the wettability of the rock. Figure 2.3 shows several ways of oil and clay to interact, without direct adsorption on the clay. Physical bonding and direct adsorption are not shown in this Figure.

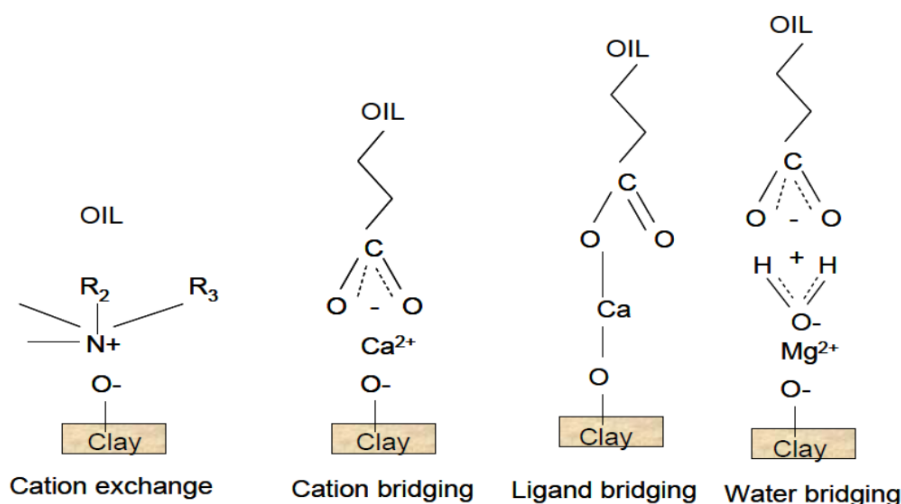


Figure 2.3: Several ways of oil and clay to interact, without direct adsorption on the clay [Lager et al., 2006]

### FORMATION BRINES

The last component of the COBR system, is the brine present in the formation or in the core plug. The ionic composition (salinity) of this brine can determine whether the rock prefers oil or water on its surface and the salinity also determines the conductivity of the electrolyte. The ions in the electrolyte can bridge oil components to the rock surface. Also, the brine can influence ion exchange processes. These factors make the brine the third essential component of the COBR system.

Formation water can greatly differ in salinity and can be as high as 200000 to 300000 ppm or mg/l of dissolved solids. To put this large salinity in perspective, fresh water contains less than 1 ppm of dissolved solids, drinking water salinity ranges from 0 to 1000 ppm (soft to very hard water) and seawater ranges between 30000 to 40000 ppm [Mahani, 2013]. Common cations in formation water are  $Na^+$ ,  $Ca^{2+}$ ,  $Mg^{2+}$  and sometimes  $K^+$ ,  $Ba^{2+}$ ,  $Li^+$ ,  $Fe^{2+}$  and  $Sr^{2+}$ . Common anions in formation water are  $Cl^-$ ,  $SO_4^{2-}$ ,  $HCO_3^-$  and sometimes  $CO_3^{2-}$ ,  $NO_3^-$ ,  $Br^-$ ,  $I^-$  and  $BO_3^-$ . The salinity range of Low Salinity (LS) is from 1500 – 7000 ppm. For an effect of LSF, it is vital that the injected brine salinity is lower than the salinity of the formation water.

A measure of the salinity of a brine is its ionic strength, which can be calculated as follows:

$$I = \frac{1}{2} \sum_{i=1}^n c_i z_i^2 \quad (2.1)$$

where  $I$  is the ionic strength ( $mol/m^3$ ),  $c_i$  is the molar concentration of ion  $i$  ( $mol/m^3$ ),  $z_i$  is the valency of that ion. Multivalent ions contribute stronger to the ionic strength than monovalent ions [Israelachvili, 2011]. The ionic strength is usually used to express the salinity of a certain brine, as it takes into account that ions of higher valency contribute more to the fluid salinity and conductivity.

Another way to express the salt content in a brine is in milliequivalents per liter (mEq/l). A certain amount of divalent ions provides the same amount of milliequivalents as twice the same amount of univalent ions would. As an example, 1 mmol/l of  $Na^+$  is equal to 1 mEq/l; 1 mmol of  $Ca^{2+}$  is equal to 2 mEq/l or mEq [Scheuerman and Bergersen, 1989].

### FORMATION DAMAGE: SCHEUERMAN LIMITS

If water of lower salinity is injected into the formation, this disturbs the equilibrium present in the COBR system. If salinity falls below a certain limit, clays may start to deflocculate, thus plug pores and reduce the permeability of the formation. This limit depends on the type of clays and minerals present in the formation rock, as well as whether the rock is aged with crude oil.

Scheuerman and Bergersen [1990] describe injection-water/formation-clay compatibility criteria in their paper. These criteria were developed to determine whether injected water has sufficient total cations and/or divalent cations in order to prevent clay in the formation to deflocculate and disperse, causing permeability impairment. The main clay components in Berea sandstone are kaolinite and illite. For these two clays Figure 2.4 illustrates the salinity limits. On the y-axis the total cation concentration (meq/l) and on the x-axis the amount of divalent cations as percentage of the total cations. The limits for illite clays are higher than for kaolinite, due to the composition of this clay. Because Berea sandstone contains both kaolinite and illite clays, this higher limit of illite should be maintained.

If a brine contains more than 10 % divalent cations as percentage of the total cations, according to Figure 2.4, in a Berea sandstone no formation damage should occur. The NaCl flocculation salinity that Scheuerman and Bergersen [1990] describe for one Berea SST they tested lies at 68 meq/l. One should also take into account that a fast switch from HS to LS can lead to 'cation stripping'. This means the salinity in the formation or core plug becomes lower than the salinity of the injected water, as the formation retains divalents from the injected water.

Several predecessors of Scheuerman and Bergersen [1990] already found in the 60's and 70's [Mungan, 1967; Clementz, 1977] that rock has an increasing sensitivity to fresh water if no crude oil components are present in the system. In other words, the presence of oil can shield clays from swelling and this prevents formation damage. The main point, which can be concluded from this earlier research is that the criteria formulated by Scheuerman and Bergersen [1990] might be too conservative for COBR systems. The damage potential of a brine to an oil-bearing or previously oil-bearing (a waterflooded zone for example) zone of the reservoir is lower. For outcrop rock, without any modification, the Scheuerman limits are a good guideline.

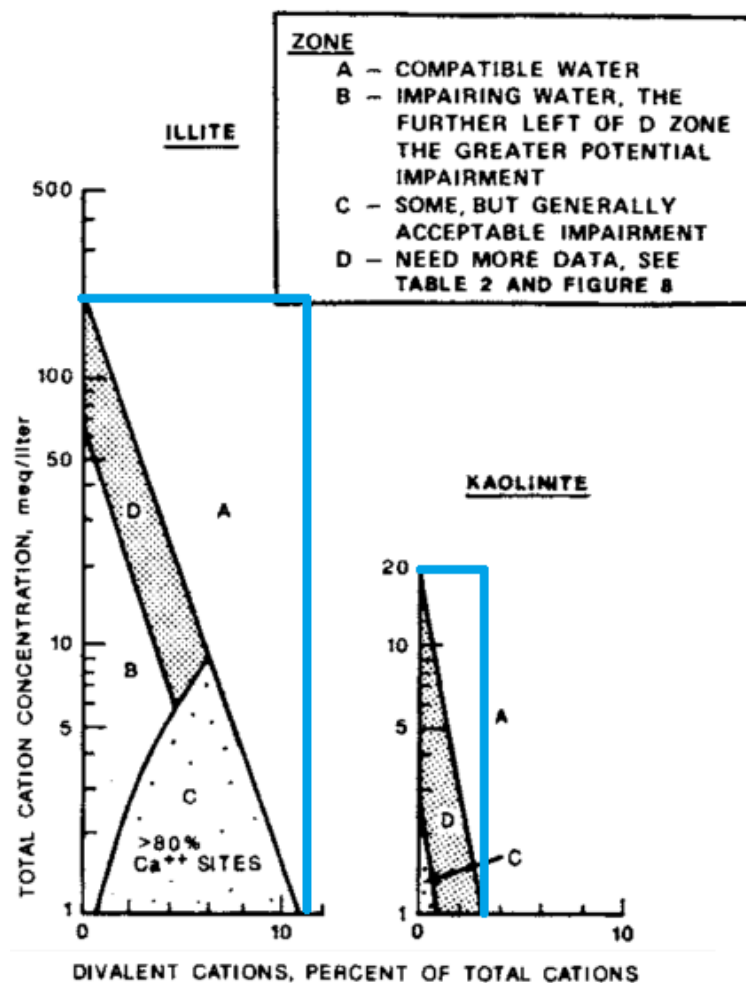


Figure 2.4: Compatibility criteria for different types of clay. The blue lines indicate the safe border, that is maintained throughout the experiments [Scheuerman and Bergersen, 1990]

### 2.1.3. ZETA POTENTIAL

Now that we have introduced the elements of the COBR system, it is time to understand the concept of the zeta ( $\zeta$ ) potential. The zeta potential of the rock/clay surface influences its interaction with crude oil and brine in the system. The zeta ( $\zeta$ ) potential is the electric potential at the shear plane, which is shown in Figure 2.5. On one side of this plane, we assume to there is no flow, whereas on the other side of this plane, everything is able to flow. Because of this assumption, the zeta potential, in other words the electric potential at the shear plane, influences all electrokinetic phenomena. In most electrokinetic phenomena a fluid moves with respect to a solid surface. To characterize the electric phenomena, one has to have an idea on the relation between the velocity of the fluid (parabolic in a channel for example) and the electric field in the channel. The surface charge will cause part of the electric field, but there may also be an external field, either caused by a deliberately generated field, like in the processes of electrophoresis and electro-osmosis, or an electric field that is caused by the motion of charged particles or ions, like in sedimentation potential and streaming potential measurements. These basics of the electrokinetic effects will be further explained in Subsection 2.1.4. Figure 2.5 illustrates the concept of the shear plane, zeta potential and the development of the potential when one moves further away from the charged surface. This Figure is based on the Stern model, which is further explained in Subsection 2.5.3. On the left, in brown, one can see the negatively charged surface of the rock/clay. The negative surface charge is compensated in an electric double layer (EDL), first the Stern layer and then the diffuse layer. Together, the surface and the fluid obey the law of electroneutrality. The potential at the shear plane, is the zeta ( $\zeta$ ) potential. Random thermal motion plays a large role in the distribution of counterions (in this case positively charged ions) in the diffuse layer. In the diffuse layer thermal motion 'battles' the electrostatic attractive forces.

### TEMPERATURE AND pH DEPENDENCE OF THE ZETA ( $\zeta$ ) POTENTIAL

The zeta ( $\zeta$ ) potential is influenced by both temperature and pH. As will be described further in this thesis in Subsection 2.4.1 and Subsection 2.5.3, the charge of a surface can be influenced by the pH. A surface containing deprotonated silanol (representing silica bearing sandstone) is negatively charged. When pH is lowered, the surface charge will become less negative. For carbonates, this is the other way around. If the plot of zeta potential against pH crosses the y-axis, this is called the point of zero charge (PZC) or iso-electric point. At this pH, the surface is neutrally charged, or in other words the zeta potential is zero. As will be discussed in the description of the Gouy-Chapman and Stern model in Subsection 2.5.2 random thermal motion plays a large role in the distribution of counterions in the diffuse layer. Recall that in the diffuse layer thermal motion 'battles' the electrostatic attractive forces. So, at a higher temperature, one can expect the zeta ( $\zeta$ ) potential to be higher as the distance to counter the surface charge will increase, in other words the Debye length (Equation 2.5) will become larger.

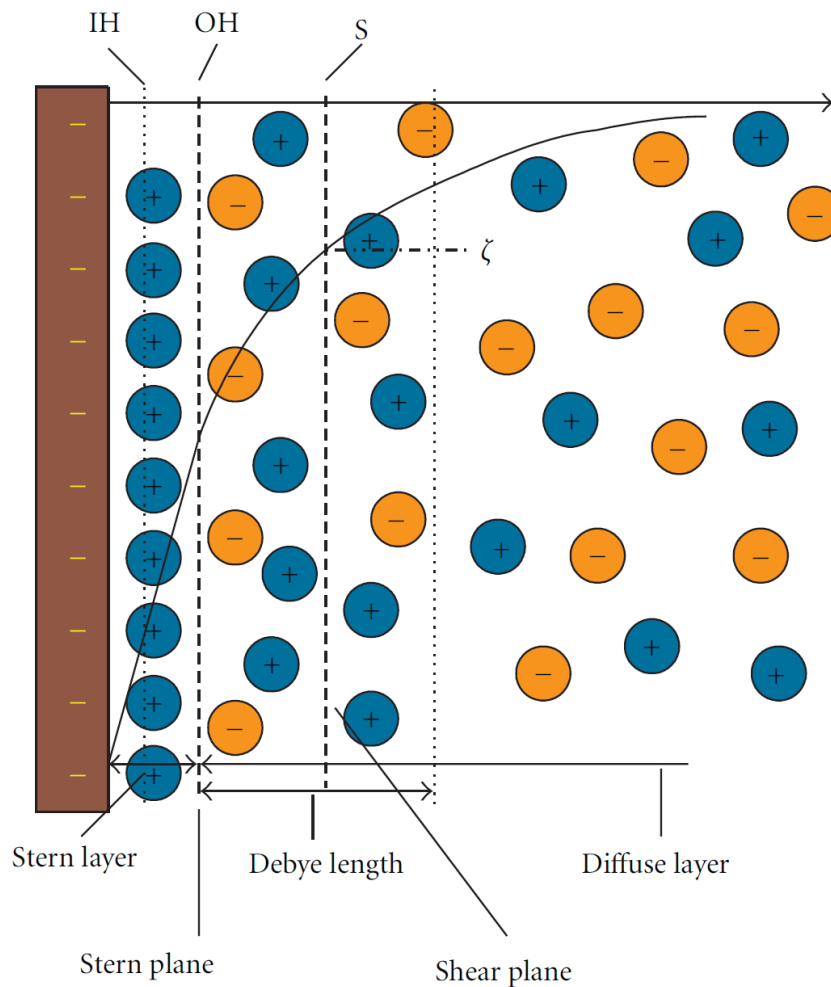


Figure 2.5: Electric double layer according to the Stern model. The inner and outer Helmholtz planes are indicated as IH and OH, respectively. The slipping plane (shear plane) is denoted by S and its potential is characterized by the  $\zeta$ -potential [Schoemaker et al., 2012]

#### 2.1.4. BASICS OF ELECTROKINETIC EFFECTS

When one of the two phases in a system moves tangentially past the second one (solid and liquid or gas and liquid) there are a number of phenomena that can be observed, which can be grouped as 'electrokinetic effects'. There are four distinct effect, which depends on how the motion is created. The four phenomena are:

1. Electrophoresis

2. Electro-osmosis
3. Streaming Potential
4. Sedimentation Potential

### ELECTROPHORESIS

If solid or liquid particles are suspended in a liquid or a gas, the particles can be induced to move by the application of an electric field across the system. This process is called electrophoresis, which is also the basis of the zetasizer technique used and explained later on. One can get information on the net charge of a particle, or their surface potential with respect to the bulk of the suspending phase, by the measurement of the velocity of the particles (electrophoretic mobility) under a known electric field [Hunter, 1981].

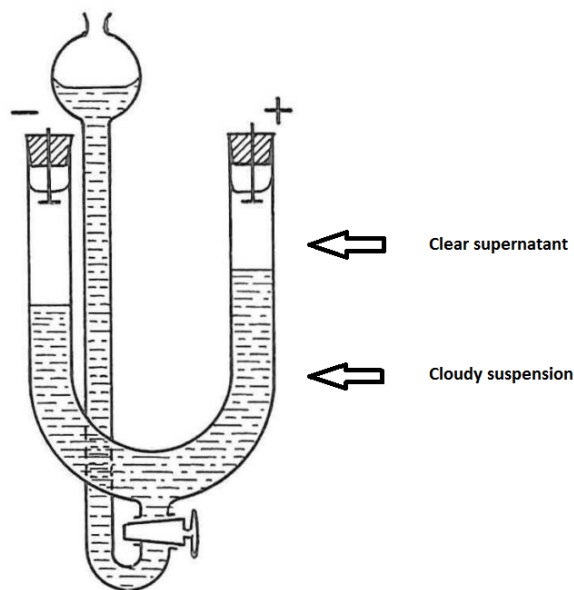


Figure 2.6: Electrophoresis: The motion of the particles can be followed by observing the movement of the boundary between the cloudy suspension and the clear supernatant [Hunter, 1981]

### ELECTRO-OSMOSIS

When the solid phase remains stationary and a liquid moves in response to an applied electric field, this process is called electro-osmosis. The solid phase is in the form of a capillary or a porous plug filled with the liquid. The electric field acts upon the charged ions in the liquid and as they move they drag the liquid with them. Information about the net surface charge or the electrical potential in the neighborhood of the wall can be found by the measurement of the velocity of the liquid, or the volume of liquid transported per unit current flow [Hunter, 1981].

### STREAMING POTENTIAL

The streaming potential is in a way the reverse process of electro-osmosis. Instead of applying an electric field to cause the liquid to move through the capillary or porous medium, a pressure gradient can be applied over the system forcing the fluid through the medium and hereby causing an electrical potential. The excess charge near the wall in the fluid caused by the presence of the EDL is carried downstream and the accumulation of charge there, causes a build-up of an electric field, which drives an electrical current back (by ionic conduction through the liquid) against the direction of the liquid flow. When a steady state is accomplished, the measured potential across the medium is called the streaming potential. This streaming potential is related to the driving pressure and the potential near the wall [Hunter, 1981].

### SEDIMENTATION POTENTIAL

When charged colloidal particles rise or settle in a liquid, either by gravity or a centrifugal field, these particles generate a potential difference, which is named the sedimentation potential. As the particle moves, it continuously leaves its atmosphere behind and new surroundings are established by a flow of charge into one side

and out of the other. Negative particles set up a field, which is negative in the direction of their motion and the steady-state is established by a back-flow of positive ions [Hunter, 1981].

### 2.1.5. WETTABILITY AND IMBIBITION TESTS

The interaction between the elements in the COBR system leads to a tendency of either the water or the oil phase to reside on the rock/clay surface. This tendency is the wettability of the rock surface. Wettability is important, as it influences the response of two-phase streaming potential measurements in a core plug, because the coverage of the surface influences the potential at the shear plane, the zeta potential ( $\zeta$ ). One way to define the degree of wetness of the rock is by measuring the amount of surface covered by either water or oil. This can give a wettability index of  $W=0$  if the surface is fully water covered and  $W=1$  if it is fully oil covered. Another method to define wettability is to look at the contact angle between the oil, brine and rock. Wettability in this method is roughly defined as (which can also be seen in Figure 2.7):

$\theta > 90^\circ$ : Oil-wet

$\theta < 90^\circ$ : Water-wet

where the contact angle ( $\theta$ ) is taken through the water-phase.

A more subtle definition also exists, where an 'intermediate-wet' region around a contact angle of  $90^\circ$  is added to the classification. The concept of intermediate-wet is not to be confused with a 'mixed-wet' situation, where the smaller pores are fully filled with water (water-wet) and the larger pores have been filled with oil and have become oil-wet. In such a system, wettability differs according to pore size. This is due to capillary entry pressure that the non-wetting phase needs to overcome to enter a certain pore with a certain pore throat radius.

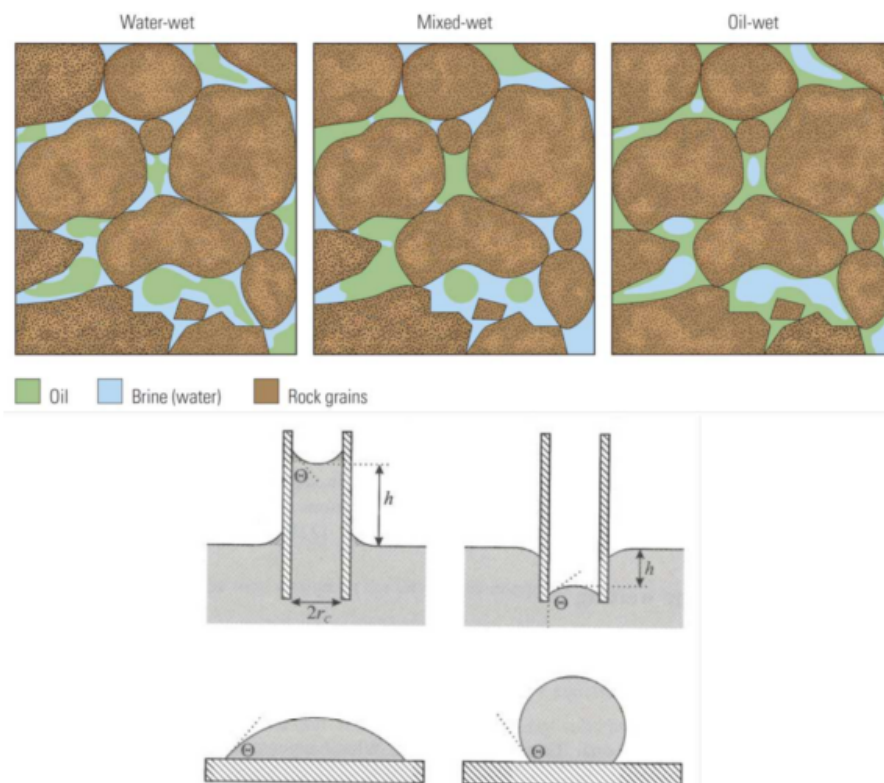


Figure 2.7: Top: Wettability in a porous medium, the oil is displayed in green, the water in blue and the rock in brown; Bottom: Wettability in a capillary, where the oil phase is white and the water grey. The charged surface is displayed in grey with a striped pattern (left: water wet surface; right: oil-wet surface) [Abdallah et al., 2007]

Let's discuss the theory and ideas behind wettability now. The concept of the electrical double layer becomes a lot more complicated, when we look at two-phase conditions. It is good to see where wettability and the zeta potential meet, which will be crucial to the expected outcome of the two-phase streaming potential

experiments later on in this research. The wettability condition of an oil reservoir influences such basic properties as capillary pressure, relative permeability and resistivity index. It requires a definition of wettability. As mentioned above, wettability can be defined as a number, which represents the amount of rock covered by oil or water. In this case  $W=1$  would mean a completely water wet (thick water film on the rock) situation and  $W=0$  would mean a completely oil wet (very thin water film on the rock) situation. This idea is essential to keep in the back of your mind: even in an oil-wet case, there is still a very thin water film on the rock. This is caused by the geological history, as explained in the next paragraph.

The mineral surfaces of an oil reservoir will be water wet, if a relatively thick, stable water film remains between the oil and water surface. This stability of the water film is determined by the disjoining pressure. Disjoining pressure (force per unit area) arises from an attractive interaction between two surfaces. The most variable component in the determination of the disjoining pressure is the electrostatic force between the oil-brine and mineral-brine interfaces. A strong electrostatic repulsion between oil and rock/clay can overcome the attractive Van der Waals forces between oil and rock/clay and therefore cause a completely water wet situation, where the contact angle is zero. This electrostatic component can be quantified via measurements of the zeta ( $\zeta$ ) potential [Dubey and Doe, 1993]. This quantification can be done by measuring oil-brine and brine-rock interface zeta potentials, which can be obtained in electrophoretic measurements or in streaming potential measurements, which is a result of both the influence of the brine-rock and brine-oil interactions, either with thick (water wet) or thin (oil wet) brine films in between the two.

If we go back to the basics of oil migration into a reservoir, we know that a reservoir starts off being fully water filled, because during sand and clay deposition in a basin, the sedimentation basin is filled with water. This would mean that the reservoir is used to water and will be water-wet. The rock is progressively buried. When a source rock below the reservoir rock comes inside of the oil generating window, it starts generating oil and this oil wants to migrate up by a density difference, until it finds a reservoir rock capped by a cap rock. The water is partially displaced from the reservoir rock and a water film remains in between the mineral surface and the oil. What happens to this water film will determine the final wettability of the rock. As noted before this water layer is bounded by a oil-brine and mineral-brine interface.

As Hirasaki [1991] has reviewed in his thermodynamical study on thin films and wettability, a thick enough water film will yield a water wet situation. On the other hand, a sufficiently thinned film, will cause the oil-brine and mineral-brine interfaces to approach each other, which can cause an interaction between the two surfaces. This interaction can give rise to a force, that may act to either stabilize or destabilize this thin film. The force discussed here is called the disjoining pressure. Depending on this force, the situation will become oil wet or not. Some pores might also remain fully filled with water, as their size is too small to have oil migration into them. This will prohibit the pores from becoming oil-wet and leads to a mixed-wet situation.

Contributing to the disjoining pressure are the electrostatic force, the van der Waals force and structural and hydration forces. The net disjoining pressure is a combination of the three. As the electrostatic contribution is the most variable, it is reasonable to believe that a variation in this force can cause a variation in wettability. Table 2.1 shows the oversight of wetting tendencies herein.

Mineral-Brine	Oil-Brine	Wetting Tendency
Positive	Negative	Nonwater wet
Positive	Positive	Water wet
Negative	Negative	Water wet
Negative	Positive	Nonwater wet

Table 2.1: Oversight of wetting tendency with different interfacial charges [Dubey and Doe, 1993]

When there is no very strong specific adsorption of counterions, the zeta potential can give a correct representation of the surface charge and it can be used to represent the electrostatic potential at film thicknesses of interest to calculate wetting transitions. The zeta ( $\zeta$ ) potential of sandstone/clay surfaces, and oils, is positive at low pH and negative at high pH. Somewhere in between, the zeta potential is zero. This point is called the isoelectric point or point of zero charge (PZC). For example, the isoelectric point of silica is around pH 2 and it is likely to be negatively charged above that. For carbonate rocks, this is different, they may be positively charged under many reservoir conditions. Oils that do not contain surface active compounds almost always have isoelectric points below pH 4 and do not ever show more than a small positive charge. Therefore, they are unlikely to wet silica, although they might wet a carbonate. Also, a clay like kaolinite displays very negative zeta potentials around pH 6. Crude oils do contain surface active acids and bases. Acids will start to ionize around pH 3 to produce negative charge at the interface. This is expected to move the isoelectric

point down. Petroleum bases generate positive charge up to around pH 8, which will consequently move the isoelectric point up [Dubey and Doe, 1993]. Generally one can say that crude oils are positively charged at low pH and negatively charged at higher pH. This trend can be seen in all oils and the isoelectric point lies between pH 2 and pH 6 [Nasralla et al., 2011].

The wetting state can be calculated from the balance between electrostatic forces and van der Waals forces. The simplified derivation of this equation has been done by Hirasaki [1991]. The situation is considered where the thin water film is trapped between the oil and the mineral. Structural and hydration forces are ignored, which is acceptable when only looking at 'thick' films.

The van der Waals contribution is:

$$\Pi_a = -\frac{A}{6\pi h^3} \quad (2.2)$$

where A is the Hamaker constant for the film (zeptoJoule) and h is the film thickness (m). The electrostatic contribution for thick films ( $\kappa h \gg 1$ ) is defined as follows:

$$\Pi_e = 2\epsilon\kappa^2\psi_1\psi_2 \exp(-\kappa h) \quad (2.3)$$

where  $\epsilon$  is the electric permittivity (F/m),  $\psi$  the potential (V) and  $\kappa$  is the inverse Debye length ( $m^{-1}$ ). This leads to a total net disjoining pressure as the sum of these both components:

$$\Pi_{tot} = \Pi_e + \Pi_a \quad (2.4)$$

Mahani et al. [2014] have done further research on wettability change when switching from higher salinity brines to lower salinity brines. This research on the kinetics of the detachment of oil droplets from a clay surface shows that exposure to a low salinity brine causes the interfacial angle (contact angle) to change and eventually can lead to the detachment of droplets from the surface, which can be seen as the reestablishment of a stable thick water film in between the oil phase and the mineral. Figure 1.1 shows the start of the detachment of an oil particle from the clay patches on top of a silica surface.

So, wettability can be defined as the preference of a solid to stay in contact with one fluid over the other. Contact angles or surface coverage of the rock can be used to quantify the wettability of a rock. To summarize, wettability of a rock depends on the following factors [Abdallah et al., 2007]:

1. History of fluid contact
2. Composition of the fluids
3. The state of the system (P and T)
4. The composition and distribution of the surface (rock and clay)

The Figures 2.7 and 2.8 give some more insight in wettability. Figure 2.7 shows that the distribution of oil and water inside a pore space depends on the wettability and it also shows capillary rise or fall based on the wetting tendency of a capillary. Figure 2.8 shows that the apparent contact angle may be different from the true contact angle due to the roughness of a surface.

The first two methods to define wettability were the measuring of contact angle and looking at the total coverage of a surface. One other method is to perform imbibition tests, where specifically one might see a wettability alteration by an increase in oil production, when switching to water of a different (lower) salinity. In an imbibition test, a core is saturated with crude oil and formation brine (at residual saturation  $S_{wc}$ ) and aged at reservoir conditions, where after it is placed in a beaker with formation water. From then on the oil production will be measured at each step. The beaker with formation water is refreshed. After this, the core is placed in a beaker with low salinity water, and this could lead to an increase in oil production. If so, this may indicate wettability alteration inside the core plug from an oil-wet state to a more water-wet state. Suijkerbuijk et al. [2012] have done research into oil production by means of spontaneous imbibition tests on various oils, brines and sandstone cores. They designed their experiments in such a way that the impact of formation water, imbibing water and crude oil composition on wettability and on a wettability alteration by LSF could be determined. They conclude several things in their research: an increasing concentration of divalent cations in the formation brine make a COBR system more oil-wet; the types of cations in the formation brine determine the extent of wettability modification towards more oil-wet during aging and different crudes

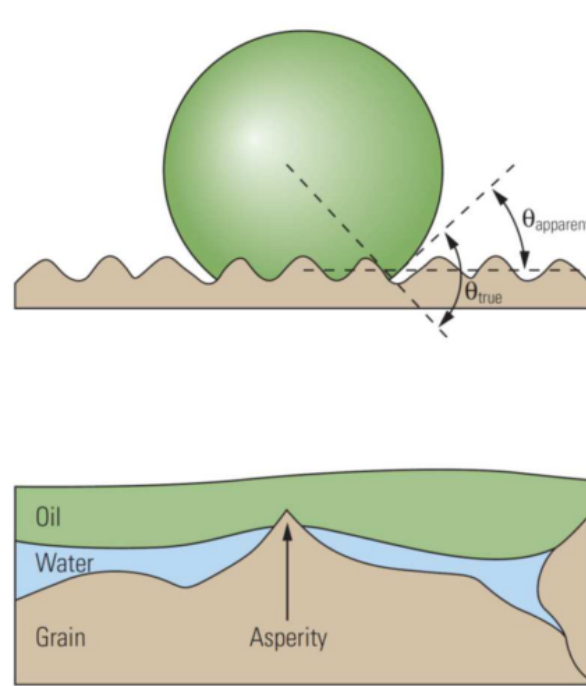


Figure 2.8: Contact angle asperity [Abdallah et al., 2007]

showed different results in combination with the same brine/rock systems. There is a spread in wettabilities after aging and the low salinity effect depends on the crude oil.

The core of our interest from this research, is the number Berea-91 core plug (which is actually a Berea 700 core sample), which was initialized with Dagang brine (at  $S_{wi}$ ) and crude oil H. This combination showed a large increase of oil production in the imbibition test, when the switch was made from Dagang brine (HS) to LS brine. After a while the low salinity brines were refreshed. Results of oil production with low salinity brine can be seen in Figure 2.9.

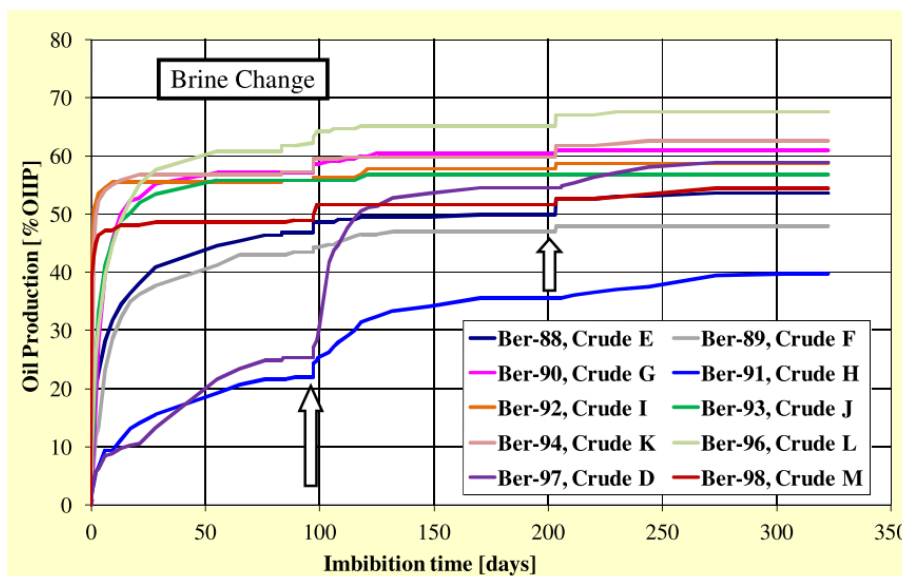


Figure 2.9: Production profiles of several Berea core plugs during imbibition with formation water and with low salinity brine. Brine changes to LS Brine E and LS brine E refresh are indicated by arrows [Suijkerbuijk et al., 2012]

The results show that two core plugs have a very good reaction to the LS brine injection, namely sample 97 (Ber-97) with crude D and sample 91 (Ber-91) with crude oil H. These samples show a larger wettability

change, which may indicate that the crude oils used can deliver a more oil-wet situation after aging. In the experiments later on, Berea 700 outcrop rock, Dagang brine, several LS brines (also LS Brine E) and crude oil H will be used.

## 2.2. PREREQUISITES OF LSF

Before going into further detail, it is convenient to summarize all the prerequisites known from literature that contribute to the low salinity effect. These prerequisites touch upon all parts of the COBR system. In the oil industry, there is an increasing consensus on the main subsurface screening criteria:

1. Crude Oil: The presence of polar components in the hydrocarbon phase is essential. The LS effect does not show effect with refined oil. The system should also be properly aged, as unaged samples may not show the effect [Tang and Morrow, 1999]. A change from an oil-wet  $\rightarrow$  a more water-wet state is essential. Aging causes a more oil-wet state.
2. Brine: Formation brine should be of (relatively) high salinity and contain a sufficient amount of divalent/ multivalent ions. The injected brine should be of low salinity, with the threshold ranging between 3000 and 5000 mg/liter [Hughes et al., 2010]. It should also contain a certain amount of divalents to prevent formation (FM) damage.
3. Rock: The presence of clay in the sandstone is important. The reservoir rock should contain active clay minerals, such as kaolinite and illite. Also the reservoir should be non water-wet [Hughes et al., 2010].

## 2.3. THEORIES BEHIND LOW SALINITY WATERFLOODING

As the mechanism behind the low salinity effect is not yet fully known, there exist several theories that try to explain the low salinity effect. The main theories are:

1. MIE: Multi-component ion exchange [Lager et al., 2006]
2. DLE: (Diffuse) double-layer expansion [Ligthelm et al., 2009]
3. pH increase [Austad et al., 2010]
4. Fines mobilization and formation damage [Tang and Morrow, 1999]
5. Alkali/ surfactant flooding (IFT) effect [Mcguire et al., 2005]

1. *MIE*: Lager et al. [2006] argue that MIE is the dominant mechanism in LSF. During the injection of low salinity brine, MIE takes place and this removes organic polar compounds and organo-metallic complexes from the rock surface. These are replaced by uncomplexed cations. Theoretically, the desorption of polar compounds from the clay surface should lead to a more water-wet surface. This would mean an increase in oil recovery. The process of MIE can create a zone where the concentration of  $Mg^{2+}$  and  $Ca^{2+}$  is lower than both the injected and the connate brines. This is called the 'self freshening zone', as is shown in Figure 2.10. The process of MIE explains why LSF does not work when a core is acidized and fired as the cation exchange capacity of the clay minerals is destroyed. It also explains why low salinity water injection has no effect on mineral oil as no polar compounds are present to strongly interact with the clay minerals.

2. *DLE*: Ligthelm et al. [2009] argue that the lowering of the ionic strength of an injected solution by lowering the salinity and especially the amount of divalents in the injected brines, reduces the screening potential of the cations. This allows for the electrical double layers around the clay and oil particles to expand and increase the absolute level of the zeta potential. The repulsion between oil and clay particles hereby increases. They argue that when electrostatic repulsion is larger than binding forces via multivalent cation bridges, oil particles can desorb from the clay surface. As one can define the degree of wetness of the rock by the amount of surface covered by either water or oil ( $W=0$  for all water,  $W=1$  for all oil), the rock becomes more water-wet when oil particles desorb from the surface. Ligthelm et al. [2009] say that this mechanism would especially occur at the interface between banked-up highly saline formation water and the invading low salinity flood.

3. *pH increase*: Austad et al. [2010] argue the following theory, based on pH increase. At reservoir conditions, the pH of formation water is about 5 due to dissolved acidic gases like  $CO_2$  and  $H_2S$ . At this low pH, the clay minerals, which act as cation exchange material, are adsorbed by acidic and protonated basic components from the crude oil. The clay minerals are also adsorbed by cations, especially divalent cations from

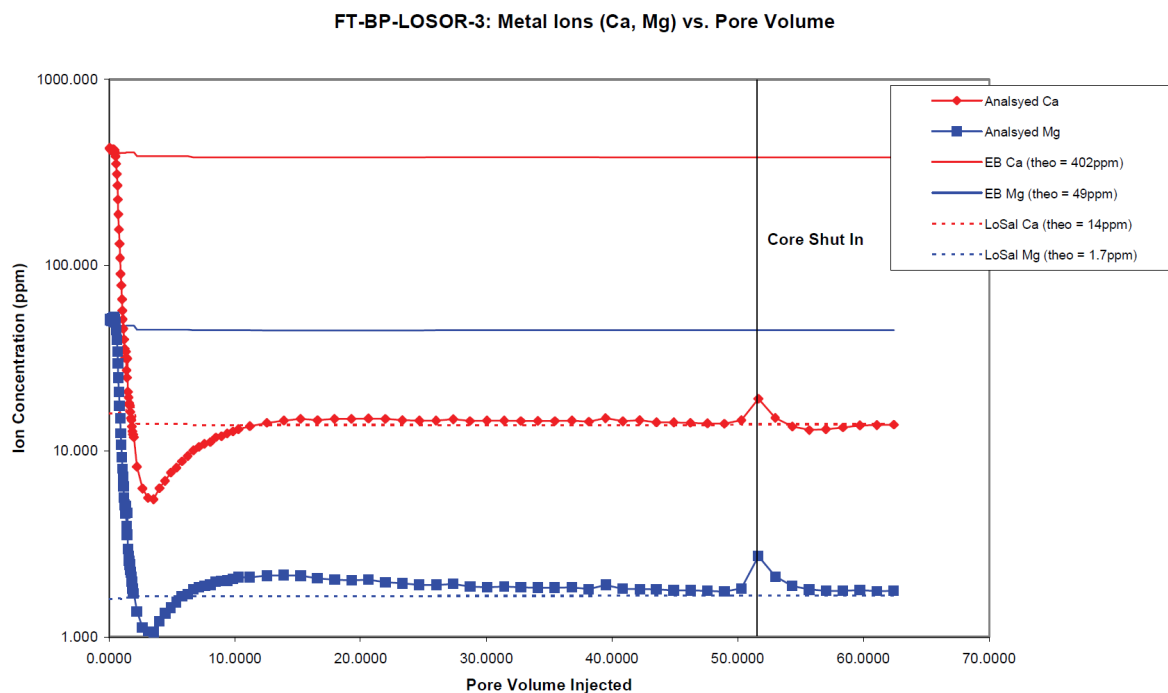


Figure 2.10: Divalent metal analysis of  $Ca^{2+}$  and  $Mg^{2+}$  during a low salinity waterflood in a reservoir condition field core flood. Solid red and blue lines are the high salinity in situ levels of  $Ca^{2+}$  and  $Mg^{2+}$  and the dashed red and blue lines are the low salinity injected concentration, respectively [Lager et al., 2006]

the formation water, like for example  $Ca^{2+}$ . Injection of a low salinity (LS) fluid will promote desorption of  $Ca^{2+}$ . This in turn will create a local increase in pH close to the brine-clay interface, because the  $Ca^{2+}$  ions are substituted by the  $H^+$  ions from the water. A fast reaction between  $OH^-$  and the adsorbed acidic and protonated basic material will cause desorption of organic material (components of the crude oil) from the clay. This means the rock becomes more water-wet, as the oil coverage has been lowered. Also at this point increased oil recovery is observed. [Lager et al., 2006] argue though that pH induced IFT reduction or emulsification and fines migration are not ubiquitous during LSF, so it cannot be the unique cause.

4. *Fines mobilization and formation damage:* Tang and Morrow [1999] argue that due to the expansion of the electric double layer (and maybe also ion exchange) clay particles and other mixed-wet fines are removed from the rock surface at low salinity conditions leaving a water-wet spot. The migrating fines might block narrow pore throats and cause microscopic diversion of the injected water. This causes the waterflood to sweep places that were otherwise untouched.

5. *Alkali / surfactant flooding (IFT) effect:* Mcguire et al. [2005] argue that the pH during low salinity flood rises high enough to saponify certain components of the oil (generation of surfactants). In this manner the interfacial tension between water and oil is lowered, in a similar way to alkaline flooding. This changes the wettability. Detachment of clay particles may also be involved.

Sorbie and Collins [2010] extend the work of Lager et al. [2006] and Ligthelm et al. [2009] and argue that when low salinity water contacts regions of increasing kaolinite content, which is always oil-wet in a formation, the reduced salinity allows the electrical double layers to expand. This in turn allows the bound multivalent ions to be accessible for a multicomponent ion exchange process. The complexed cations are replaced by uncomplexed cations. This releases the bound material and leads to a change of the clay surface from oil-wet to water-wet, increasing oil recovery, as oil fractional flow increases. This zone of even further reduced salinity (lower than injected water salinity) is named the 'self-freshening' zone. Figure 2.10 shows this distinct 'self-freshening' zone.

Suijkerbuijk et al. [2013] combine both the theory of Lager et al. [2006], Ligthelm et al. [2009] and Sorbie and Collins [2010]. They illustrate their theory schematically in Figure 2.11. They argue that the incremental oil during LSF is produced at, or just after breakthrough of the injected LS slug, which is around the 'salinity front'. Very little divalents exist behind the 'salinity front' as they are retarded by the formation. Cation exchange and therefore MIE occur at the 'retardation front'. There a new equilibrium exists in the crude oil -

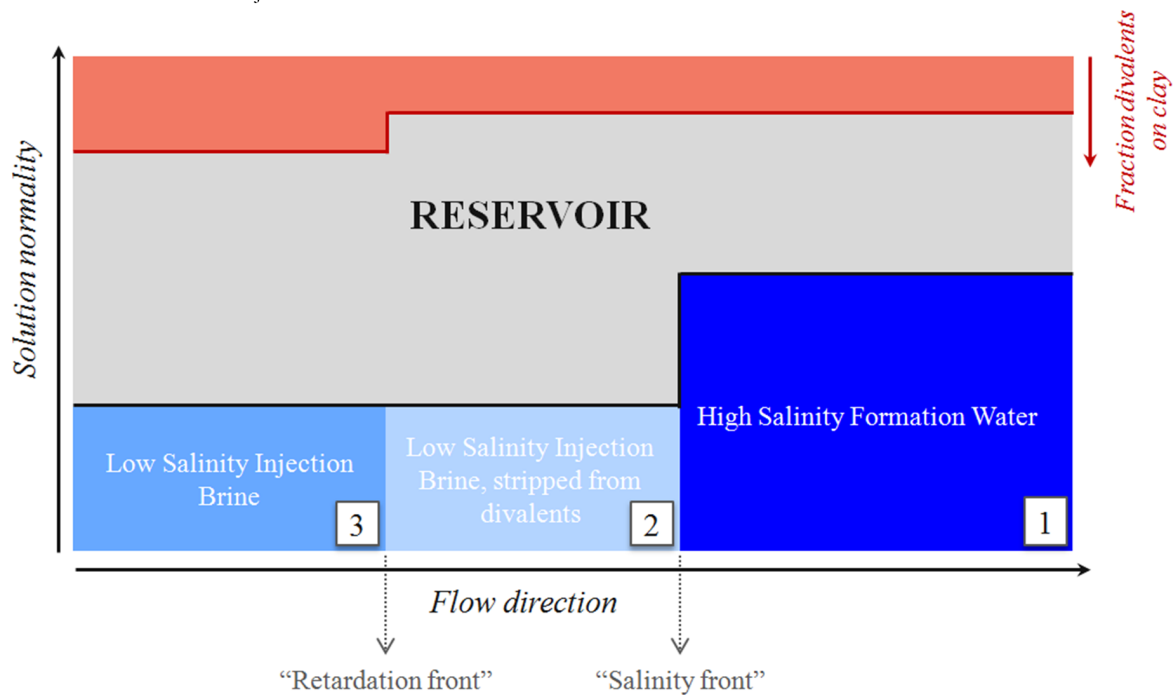


Figure 2.11: Schematic depiction of the development of three different water zones during low salinity waterflooding. The evolution of the solution normality of the brine and the fraction of divalent cations on the clays as the LS slug moves through the reservoir are shown. This process creates a 'Salinity front' and a 'Retardation front' [Suijkerbuijk et al., 2013]

brine - rock (COBR) system. This is the reason why the process of MIE cannot be the cause of the incremental oil recovery, which is occurring at the 'salinity front'. If MIE would be the dominant process, this would delay oil production and therefore most likely make the process of LSF uneconomical. Suijkerbuijk et al. [2013] argue that it is likely that the lowering of the ionic strength of the solution during LSF causes the incremental oil recovery. A decrease in the ionic strength leads to a more negatively charged rock surface zeta ( $\zeta$ ) potential and a more negatively charged oil surface. This causes the electrical double layer to expand based on the theory by Ligthelm et al. [2009].

## 2.4. ELECTROKINETICS

The section on electrokinetics will be about the electrical double layer, the zeta potential, electrokinetic phenomena (such as streaming current/potential) and equations or correlations that model the electrokinetic phenomena.

### 2.4.1. THE CHARGING OF A SURFACE

On the very small scale, there are two forces that are crucial. These are the always attractive short-range Van der Waals forces and the long-range electrostatic forces. If only Van der Waals forces would exist, one would expect all dissolved particles to coagulate immediately and precipitate out of solution. This does not happen though, because all particles suspended in water or any liquid of a high dielectric constant, are usually charged and repulsive electrostatic forces prevent the particles to coagulate [Israelachvili, 2011].

The charging of a surface in a liquid can originate in several ways:

1. The first possibility is the ionization or dissociation of surface groups. This can be the deprotonation of surface carboxylic groups ( $-COOH \leftrightarrow COO^- + H^+$ ) or for example the deprotonation of surface silanol groups ( $SiOH \leftrightarrow SiO^- + H^+$ ). So, when the surface contains such an acidic group, it leaves a negative surface behind [Israelachvili, 2011]. Conversely, a basic surface can cause a positive charge. The magnitude of the surface charge depends on the acidic or basic strengths of the surface groups and on the pH of the solution. By suppressing surface ionization, one can reach the point of zero charge (PZC), where the surface charge is zero. For a basic surface, this can be achieved by reducing the pH.

The two processes are illustrated in Figure 2.12 [Masliyah and Bhattacharjee, 2006]

- The adsorption or binding of atoms from solution onto a previously uncharged surface forms the second possibility.  $OH^-$  groups can be adsorbed to the water-hydrocarbon interface.  $Ca^{2+}$  can be bonded to zwitterionic groups of lipid bilayer surfaces, which would charge them positively or cationic  $Ca^{2+}$  could be adsorbed to anionic  $COO^-$  sites, which were previously vacated by  $Na^+$  and  $H^+$ . These type of surfaces are also called ion exchangeable surfaces. Ion exchange can take a remarkable long time though [Israelachvili, 2011]
- Differential dissolution of ions from surfaces of sparingly soluble crystals are also a cause of surface charges. This effect is caused by the preference of certain ions to dissolve compared to the other ion in the dissolved salt [Masliyah and Bhattacharjee, 2006]
- Isomorphic substitution. Clays can exchange an adsorbed intercalated or structural ion with one of lower valency, which produces a negatively charged surface.  $Al^{3+}$  may replace  $Si^{4+}$  in the surface of the clay. This would cause the surface to become negative. If one wants to reach the point of zero charge, it is possible to reduce the pH. This will cause the added  $H^+$  ions to be combined with the negative charges on the surface to form  $OH$  groups [Masliyah and Bhattacharjee, 2006]
- Charged crystal surfaces. Surfaces with different properties can be exposed, when a crystal is broken. When a platelet would break in a clay, for example a kaolinite clay, the exposed edges contain  $Al(OH)_3$  groups which take up  $H^+$  ions resulting in a positively charged edge. This positively charged edge can be next to the negatively charged bulk material, leading to special properties of the surface. There will not be a single PZC for this surface, each type of surface will have its own PZC. For kaolinite at low pH, the flat bulk surface is negatively charged and the edges are positively charged. The positive charges on the edges decreases at high pH [Masliyah and Bhattacharjee, 2006]

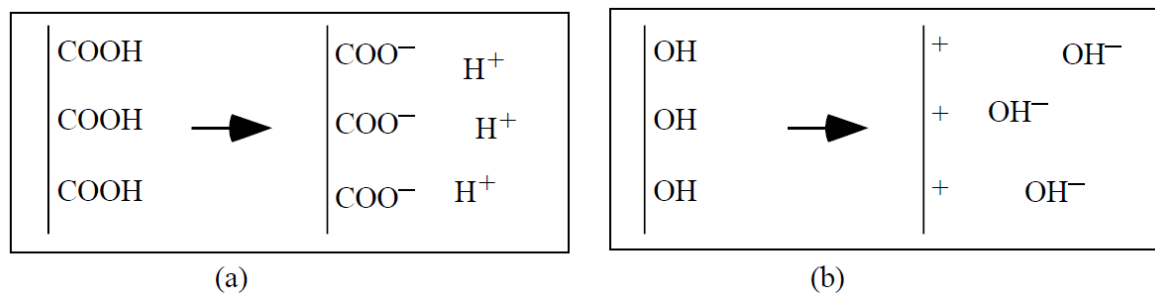


Figure 2.12: Acquisition of surface charge by ionization of a) acidic groups and b) basic groups [Masliyah and Bhattacharjee, 2006]

These surface charges (either positive or negative) cause a specific charge distribution to exist in the liquid phase near the surface. This redistribution of free ions in the solution caused by the presence of charged surfaces together with the surface ions is called the electric double layer.

### 2.4.2. ELECTRIC DOUBLE LAYER

A concept of the electric double layer was already presented in Subsection 2.1.3 on the zeta potential. The double layer is nothing more than a redistribution of ions in the electrolyte to compensate for the surface charge of the rock/ clay. Moving further away from the surface as shown in Figure 2.5, the law of electroneutrality holds. The law of electroneutrality enholds that the sum of all the charges will add up to zero. In a bulk solution there is no preferential orientation of the ions due to random Brownian motion. A surface submerged in an electrolyte, though, can develop a surface charge in ways defined above, and this means that the charge distribution in the nearby electrolyte will be influenced by the surface. The surface will attract ions of opposite charge (counterions) and ions of the same charge (coions) will be repulsed from the surface. This will result in a non-uniform ionic distribution normal to the solid surface. One would expect a high concentration of ions nearby the surface, and far away in the bulk surface electroneutrality will be reached ('far away' means for distances between 5–200 nm depending on the electrolyte concentration). Again, this redistribution will be named the diffuse electric double layer (EDL) [Masliyah and Bhattacharjee, 2006]. More detailed models of the EDL will be discussed in Subsections 2.5.1, 2.5.2 and 2.5.3.

### 2.4.3. CHARGE INVERSION

Adsorbed ions can have a large effect on the zeta potential compared to the surface potential. If the surface adsorbs multivalent or surface active counterions, this could cause reversal of charge to occur inside the Stern layer. The zeta potential would then still be a reasonable representation of the Stern plane potential, but it will be very far off regarding the surface potential, to the extent of different signs. Adsorption of surface active co-ions could also lead to a higher Stern plane potential compared to the surface potential. The process of charge reversal and the adsorption of co-ions are displayed in part a) and b) of Figure 2.13, respectively. Shaw [1980] even argues that the zeta potential does not give any direct information on the surface potential when any adsorbed ions are present [Masliyeh and Bhattacharjee, 2006].

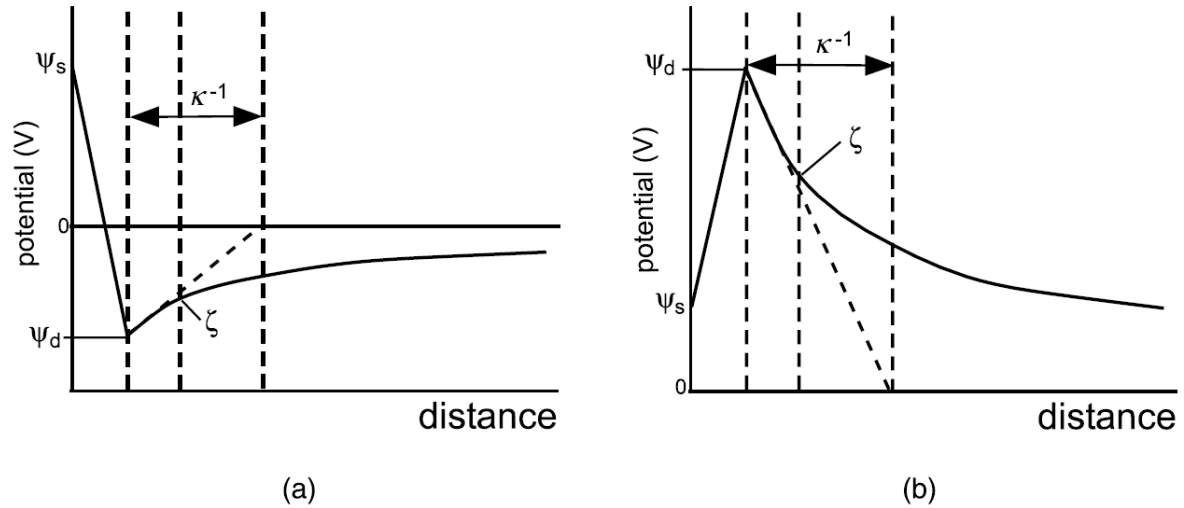


Figure 2.13: Potential variation with distance for a charged surface: a) potential reversal due to adsorption of surface active or multivalent counterions, b) adsorption of surface active co-ions [Masliyeh and Bhattacharjee, 2006]

### 2.4.4. DEBYE LENGTH

In Figure 2.5 in Subsection 2.1.3, one can also see the schematic representation of the Debye length. It runs from the Outer Helmholtz (OH) plane, or Stern plane, to a certain plane inside the diffuse layer. In a 1:1 electrolyte (both ions forming a molecule have a valency ( $z$ ) of 1, such as NaCl) solution at 298 K (25°C) the Debye length is given by:  $k^{-1} = \frac{0.304}{\sqrt{c_{NaCl}}}$ , which is the Debye length given in nm. The concentration of NaCl ( $c_{NaCl}$ ) is given in  $mol\ m^{-3}$ . An electric field that is being screened in an aqueous solution, decays roughly exponentially with distance according to  $e^{-kD}$ , in which  $k^{-1}$  is known as the Debye screening length. Typical values for the Debye screening length in an aqueous electrolyte solution are 10 nm for a  $10^{-3}$  M solution and around 1 nm in a 0.1 M solution [Israelachvili, 2011]. Important to realize is although the Debye length is usually referred to as the thickness of the electric double layer, the actual thickness of the double layer extends well beyond  $\kappa^{-1}$ . The Debye length represents a characteristic distance from the charged surface to a point where the electric potential decays to approximately 33 % of the surface potential. The general equation for the Debye length in an symmetric 1:1 electrolyte solution is given by [Glover, 2013]:

$$k^{-1} = \sqrt{\frac{\epsilon_r \epsilon_0 k_B T_K}{2 N_A e^2 I}} \quad (2.5)$$

where

$\kappa$  is the inverse Debye length ( $m^{-1}$ )

$I$  is the ionic strength of the electrolyte ( $mol\ m^{-3}$ )

$\epsilon_0$  is the permittivity of free space ( $8.854 * 10^{-12}\ C^2\ J^{-1}\ m^{-1}$ )

$\epsilon_r$  is the dielectric constant of the electrolyte (-)

$k_B$  is the Boltzmann constant ( $1.381 * 10^{-23} J K^{-1}$ )

$T_K$  is the absolute temperature ( $K$ )

$N_A$  is the Avogadro number ( $6.022 * 10^{23} mol^{-1}$ )

$e$  is the elementary charge ( $1.602 * 10^{-19} C$ )

It is important to realize that the dielectric constant of the electrolyte is temperature dependent. For water, one can use the following formula [Malmberg and Maryott, 1956]:

$$\epsilon_r = 87.740 - 0.40008 T_C + 9.398(10^{-4}) T_C^2 - 1.410(10^{-6}) T_C^3 \quad (2.6)$$

where  $T_C$  is the temperature in degrees Celsius.

## 2.5. BASIC ELECTROKINETIC EQUATIONS

As discussed in the section on the Zeta Potential, the zeta ( $\zeta$ ) potential is the electric potential at the shear plane. In most electrokinetic phenomena a fluid moves with respect to a solid surface. To characterize the electric phenomena, one has to have an idea on the relation between the velocity of the fluid (parabolic in a channel for example) and the electric field in the channel. The surface charge will cause part of the electric field, but there may also be an external field, either caused by a deliberately generated field, like in the processes of electrophoresis and electro-osmosis, or an electric field that is caused by the motion of charged particles or ions, like in sedimentation potential and streaming potential measurements. The relation between the potential and the charge density is given by the Poisson equation, which is given by:

$$\Delta\psi = -\frac{\rho_f}{\epsilon} \quad (2.7)$$

where

$\psi$  is the the potential ( $V$ )

$\rho_f$  is the charge density of the fluid ( $C/m^3$ )

$\epsilon$  is the electrical permittivity of the fluid ( $F/m$ )

The charges in a system can respond to three sorts of forces:

1. The electric potential ( $\psi$  in  $V$ )
2. The diffusion force (caused concentration differences) ( $mol m^{-2} s^{-1}$ )
3. Convection (bulk movement of charge caused by flow) ( $m^3 s^{-1}$ )

The liquid itself is subjected to forces caused by a velocity profile in the liquid, such as shear forces, and forces caused by the pressure gradient in the system and the electrical charges in the liquid. To represent experimental measurements, there are still a lot of simplifications necessary, despite of advanced computer technology. Liquids are assumed to be Newtonian (viscosity does not depend on shear rate) and flow is linear (pressure drop and flow rate scale linearly). Geometries are mainly simple, such as spheres, a cylinder or a large flat plates. Also, there is the concept of the surface of shear, which forms the no-slip boundary close to the solid. According to Hunter [1981] the surface of shear is actually a constant varying one, with indentations on a scale of the order of  $10^{-8}$  m. These fluctuations are on a very small time scale though. Another assumption apparent to the concept of the surface of shear is the fact that the bulk fluid retains its properties up until the shear surface (density, conductivity, viscosity etc.) and then suddenly changes properties, such as infinitely large viscosity inside the shear surface [Hunter, 1981].

In describing electrokinetic phenomena, one must start from the fundamental equations, which describe [Hunter, 1981]:

1. The electrostatic potential
2. The fluid flow
3. The ionic current flows generated by relative motion

The most important assumptions that lie at the basis of this treatment are that each phase is treated as a continuum and quantum effects are ignored. The electrostatic potential is assumed to be described by Poisson's equation ( $\Delta\psi = -\frac{\rho_f}{\epsilon}$ ) as described in Equation 2.7. The ion distribution is assumed to obey to the Boltzmann equation [Masliyah and Bhattacharjee, 2006]:

$$n_i = n^\infty \exp\left(\frac{-z_i e \psi}{k_B T_K}\right) \quad (2.8)$$

where

$n_i$  is the ionic number concentration ( $m^{-3}$ )

$n^\infty$  is the ionic number concentration in the bulk fluid ( $m^{-3}$ )

$z_i$  is the valency of an ion (-)

$e$  is the elementary charge (C)

$\psi$  is the potential (V)

$k_B$  is the Boltzmann constant ( $J K^{-1}$ )

$T_K$  is the temperature (K)

The equation for the charge density is as follows:

$$\rho_f = \sum_i n_i z_i e \quad (2.9)$$

where  $\rho_f$  is the charge density in ( $C m^{-3}$ ). When both the Poisson equation and Boltzmann equation are combined via the charge density, this leads to the Poisson-Boltzmann equation, which describes the potential distribution (for small  $\psi$  and a planar interface, this is given by  $\Delta\psi = \kappa^2\psi$ ), where  $\kappa$  is the Debye length as in Equation 2.5 [Masliyah and Bhattacharjee, 2006]. This approximation for small  $\psi$  is called the Debye-Hückel approximation. These equations will be more extensively described in the derivation for a cylindrical geometry further down in this chapter.

At the basis of the Poisson-Boltzmann equation lie the following assumptions [Hunter, 1981]:

1. Ions are point charges
2. The solvent is continuous and has a constant permittivity, which is not affected by the overall field strength or by the local field in the neighborhood of an ion
3. The only work done in bringing an ion from the bulk solution up to a certain point in the field, where the electric potential is  $\psi$ , is the electrical work term  $z_i e \psi$

The other work terms, such as the work done to make room for the ion by displacing some solvent, the change in energy caused by the local reorientation solvent around the ions and the effect of the atmosphere of other ions on the electrostatic potential experienced by a given ion, are neglected. The limitations of these assumptions are most prominent in the close neighborhood of the solid, approximately 1 nm. The outer part is well described by the Poisson-Boltzmann treatment. The part close to the solid can be closer described by a molecular condenser, such as described in Subsection 2.5.3 on the Stern model.

In the treatment of the fluid flow, there will also be several assumptions, either when we make use of the Navier-Stokes equation or Poiseuille flow in a cylindrical geometry. For example, the existence of a no flow boundary at the surface of shear and the fact that the Poisson-Boltzmann equation holds with fluid flowing past it (without turbulence) are assumptions in this part. More will follow in the part on streaming potentials and coupled phenomena.

### 2.5.1. HELMHOLTZ MODEL

The electric double layer was first defined by Helmholtz. His first idea was that the layer consisted of two parallel planes of opposite charge, behaving like a capacitor. Capacitors are indeed a good representation of electric models [Israelachvili, 2011]. The idea behind this can be seen in part a) of Figure 2.14. This model does not take into account thermal diffusivity and thus expects a linear decrease in electric potential in the bound layer.

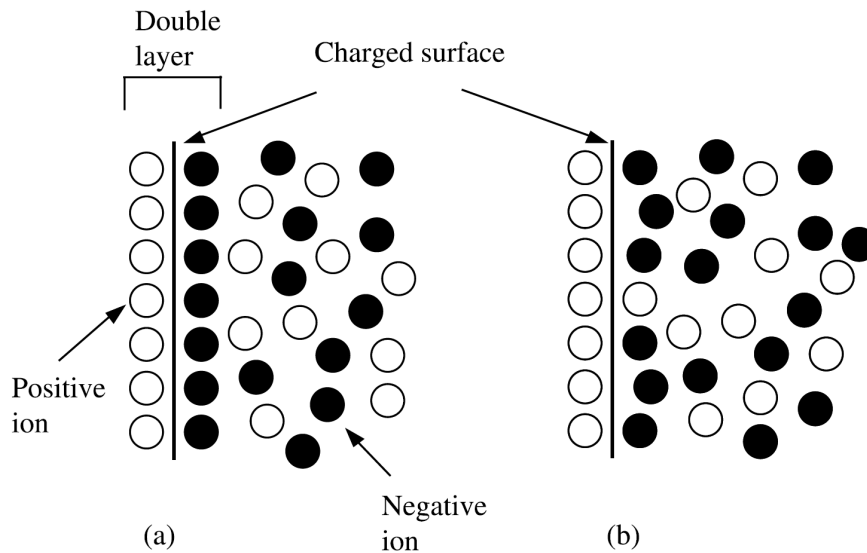


Figure 2.14: Two models of the electric double layer: a) Helmholtz model, b) Gouy-Chapman model [Masliyah and Bhattacharjee, 2006]

### 2.5.2. GOUY-CHAPMAN MODEL

The random thermal motion causes counterions to redistribute into a diffuse layer, and thus the model of the diffuse double layer was created. This can be seen in part b) of Figure 2.14. In this Gouy-Chapman diffuse double layer model, the charged surface, composed of one layer of charges, has a surface potential  $\psi_s$ . In the diffuse layer the ions are free to move and molecular diffusion mitigates non-uniformities in charge distribution, whereas static electric forces favor charge separation. The counterions are considered being point charges immersed in a continuous dielectric medium. This results in a diffuse layer in which the electric potential exponentially decreases if one moves away from the interface. Within this diffuse layer, there is no charge neutrality. In the bulk, electroneutrality is reached again, as further away from the solid surface the sum of charges will be zero and Brownian (random thermal motion) motion will create a homogeneous spatial distribution of the ions [Masliyah and Bhattacharjee, 2006]. This model was created by Louis Georges Gouy and David Chapman in the early 1900's [Hunter, 1981]. The Gouy-Chapman model is valid in a low range of surface potentials (around 0.025 V) and low electrolyte concentrations. The inner boundary of the Gouy-Chapman model is the so-called  $\zeta$ -potential at the no-slip boundary. This will be further explained in the coming sections. Limitations of the model are the negligence of the finite size of molecules, because it assumes that the ions are point charges. Another assumption that lies at the basis of the model is the non-ideality of the solution and the dielectric permittivity of the medium is taken to be constant all the way to the surface [Masliyah and Bhattacharjee, 2006].

The derivation of the Gouy-Chapman model in a 1D infinite plate is the simplest way of obtaining a potential and ionic distribution in order to get an idea how these two develop away from a surface.

From the Poisson equation (Equation 2.7) and the charge density equation (Equation 2.9) one can get the Poisson-Boltzmann equation:

$$\epsilon \frac{d^2 \psi}{dx^2} = - \sum_{i=1}^N z_i e n_{i\infty} \exp\left(-\frac{z_i e \psi}{k_B T}\right) \quad (2.10)$$

where N is the number of ions (N=2 for only NaCl). In the case of symmetric electrolytes ( $z : z$ ), such as NaCl, and planar electric double layers, one can obtain an analytical solution for  $\psi$  without further approxi-

mations. This solution is known as the Gouy-Chapman theory. For a symmetric electrolyte,  $z_+ = -z_- = z$ , so Equation 2.10 can be rewritten as:

$$\epsilon \frac{d^2\psi}{dx^2} = -zen_\infty \left[ \exp\left(-\frac{ze\psi}{k_B T}\right) - \exp\left(\frac{ze\psi}{k_B T}\right) \right] = 2zen_\infty \sinh\left(\frac{ze\psi}{k_B T}\right) \quad (2.11)$$

where the term  $n_\infty$  is given as:

$$n_\infty = IN_A \quad (2.12)$$

where  $I$  is the bulk fluid ionic strength ( $mol/m^3$ ). For two boundary conditions,  $\psi = \psi_s$  at  $x = 0$  and  $\psi = 0$  at  $x \rightarrow \infty$ , the above equation solves as:

$$\Psi = 2 \ln \left[ \frac{1 + \exp(-\kappa x) \tanh(\Psi_s/4)}{1 - \exp(-\kappa x) \tanh(\Psi_s/4)} \right] \quad (2.13)$$

where  $\Psi$  is the dimensionless potential defined as  $\Psi = \frac{ze\psi}{k_B T}$  and  $\Psi_s = \frac{ze\psi_s}{k_B T}$ . If the surface potential is low, so  $\Psi_s \ll 1$ , then Equation 2.13 can be approximated by [Masliyah and Bhattacharjee, 2006]:

$$\Psi = 2 \ln \left[ \frac{1 + 0.25\Psi_s \exp(-\kappa x)}{1 - 0.25\Psi_s \exp(-\kappa x)} \right] \quad (2.14)$$

When the surface potential is even lower, say  $\psi_s \ll 0.025V$ , the term in the exponential ( $ze\psi/k_B T$ ) would be smaller than one and the hyperbolic sine term of Equation 2.13 can be approximated to:

$$\sinh\left(\frac{ze\psi}{k_B T}\right) \approx \frac{ze\psi}{k_B T} \quad (2.15)$$

which in turn leads to the Debye-Hückel approximation of the Poisson-Boltzmann equation:

$$\epsilon \frac{d^2\psi}{dx^2} = \frac{2e^2 z^2 n_\infty}{\epsilon k_B T} \psi = \kappa^2 \psi \quad (2.16)$$

For the two boundary conditions,  $\psi = \psi_s$  at  $x = 0$  and  $\psi = 0$  at  $x \rightarrow \infty$ , the above equation solves as:

$$\boxed{\psi = \psi_s \exp(-\kappa x)} \quad (2.17)$$

or in the dimensionless form:

$$\boxed{\Psi = \Psi_s \exp(-\kappa x)} \quad (2.18)$$

### 2.5.3. STERN MODEL

A combination of these two models, the Helmholtz and the Gouy-Chapman model, leads to the model made by Stern in 1924. This model is suited for small values of  $\kappa x$  (close by the surface) and when surface potential  $\phi_s$  is large. This is the region where the Gouy-Chapman model runs into difficulties since in real systems, ions are of finite size and they cannot approach a surface at a distance smaller than their radius. The model by Stern is represented by Figure 2.5, as displayed in Subsection 2.1.3. In the model by Stern, the inner boundary of the electric double layer is given by one hydrated ion radius. This plane is called the Stern plane and forms the border of the Stern layer, which runs from the surface of the solid until the Stern plane. The center of the adsorbed ions are given by the Inner Helmholtz (IH) plane, the Outer Helmholtz (OH) plane passes directly through the electric centers of the non-specifically adsorbed ions closest to the surface and the OH plane corresponds with the Stern plane. The electric potential at the surface is noted as  $\psi_s$  and decays linearly to the electric potential at the Stern plane, which is noted as  $\psi_d$ . From there on the potential decays to zero in the bulk fluid. Ions between the surface and the shear plane are considered to be immobile, ions beyond this plane are considered to be mobile; it is the no-slip fluid flow boundary. At this plane electrostatic forces and molecular diffusion are on the same order of magnitude. This means that the ions are not stuck anymore, due to the electrostatic attraction, but are able to break loose from this attraction. The shear plane is located between one to two radii away from the surface, the potential at this surface is known as the  $\zeta$ -potential. This potential is not very different from the Stern plane potential. The introduced errors by taking the  $\zeta$ -potential as the Stern plane potential  $\psi_d$  are small, as can be intuitively seen in Figure 2.5. The  $\zeta$ -potential of a surface can be determined via electrophoretic (the physical phenomenon the 'zetasizer' machine records

based on Phase Analysis Light Scattering (PALS) techniques) and streaming potential measurements. The Gouy-Chapman model as in the section before deals with the diffuse electric layer, whose inner boundary is the shear plane, and therefore the  $\zeta$ -potential.

The Stern model also has its limitations: ions are modeled as point charges; the only significant interactions in the diffuse layer are Coulombic; dielectric permittivity for the solvent is assumed constant throughout the double layer; the molecular nature of the solvent is not taken into account and the viscosity of fluid is constant above slipping plane [Masliyah and Bhattacharjee, 2006].

The Stern layer itself can be treated as a parallel plate capacitor, where the potential decays linearly from the surface. The equation describing this is simple and relates in essence the charge on the surface and surface potential with the potential at the Stern plane. The ability of a dielectric material, such as silica, to accumulate charges at its outer surfaces is termed as its capacitance. The capacitance is related to the charge accumulated across the surface of the dielectric and the applied potential difference by the following relation [Masliyah and Bhattacharjee, 2006]:

$$\Delta\psi = \frac{Q}{C} \quad (2.19)$$

where  $\Delta\psi$  is the potential difference across a dielectric (V),  $Q$  is the total accumulated charge across the dielectric (C) and  $C$  is the capacitance ( $Q = C/\psi$ ).

Now, the situation of two parallel plates with potentials  $\psi_1$  and  $\psi_2$ , separated by a distance of  $d$ . If the intervening medium is vacuum, the electric field, the potential difference and charge on the plates will be related as follows:

$$E_0 = \frac{Q}{\epsilon_0 A} = \frac{\Delta\psi}{d} \quad (2.20)$$

where  $\epsilon_0$  is the electric permittivity of vacuum and  $A$  is the cross-section of the plate area. This means the charge density on the plate is  $Q/A = \rho$ . If we now consider a dielectric medium in between the two parallel plates, the medium will be polarized in presence of an electric field and, if the left plate is positively charged, the surface of the medium adjacent to the left plate will acquire a negative charge  $-Q_m$ . The surface of the medium adjacent to the right plate will acquire a positive charge  $+Q_m$ . The magnitude of the net charge will be  $Q - Q_m$  and the effective electric field between the plates will be:

$$E_m = \frac{(Q - Q_m)}{\epsilon_0 A} \quad (2.21)$$

If we rewrite  $E_m = \Delta\psi/d$ , then:

$$\Delta\psi = \frac{(Q - Q_m)}{\epsilon_0 \frac{A}{d}} = \frac{Q}{\epsilon_0 \frac{Q - Q_m}{Q} \frac{A}{d}} = \frac{Q}{\epsilon_0 \epsilon_r \frac{A}{d}} \quad (2.22)$$

where the relative permittivity is defined as:  $\epsilon_r = \frac{Q}{(Q - Q_m)}$ . Comparing Equation 2.19 to Equation 2.22, one can see that the capacitance  $C$  of the dielectric medium is defined by:  $C = \epsilon_0 \epsilon_r \frac{A}{d}$  [Masliyah and Bhattacharjee, 2006]. The dielectric constant is quite large for highly polarizable materials, such as water. The value of  $\epsilon_r$  for water is 78.54 at 25 °C. Figure 2.15 shows the two situations; a) for the parallel plate in vacuum and b) for the parallel plate with a dielectric medium.

#### 2.5.4. ONSAGER RELATIONS: COUPLED ELECTROKINETIC PHENOMENA

The flow of an electrolyte through a porous medium causes the development of an electrical potential difference. A potential difference over a porous medium causes a flow through that same medium. In electrokinetic processes, one is concerned with the coupled influence of these multiple forces, such as electrical, pressure and gravity forces, and how they influence the behavior of a multicomponent system [Masliyah and Bhattacharjee, 2006]. These two processes of electro-osmosis and streaming potential are related to each other by the principle of an Onsager reciprocity relation as described by Brunet and Ajdari [2004]. This description is in light of non-equilibrium thermodynamic theories. In nature, several physical phenomena exist that can be described via a linear relationship between the flux and the driving force. Examples are concentration for molecular diffusion, pressure for fluid flow, temperature for thermal conduction and an electric potential for electrical conduction. In its simplest form, such a relation can be written as [Masliyah and Bhattacharjee, 2006]:

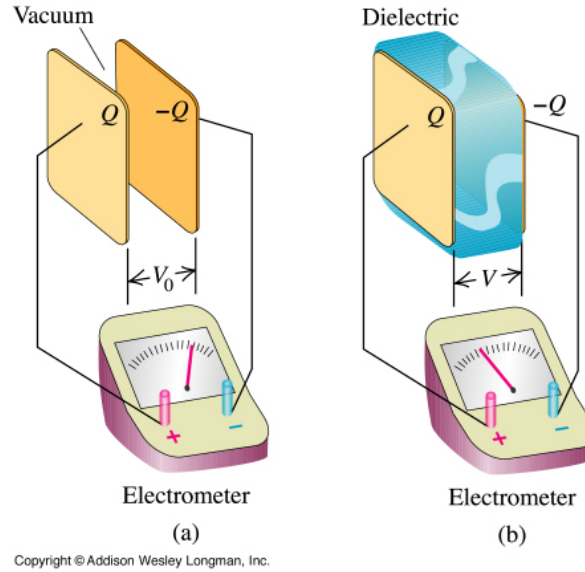


Figure 2.15: Effect of a dielectric between the plates of a parallel plate capacitor. The electrometer measures the potential difference. For a), with a given charge, the potential difference is  $\psi_0$ . For b), with the same charge but with a dielectric between the plates, the potential difference  $V$  is smaller than  $\psi_0$

$$\mathbf{J}_\alpha = L_{\alpha\alpha} \mathbf{X}_\alpha \quad (2.23)$$

where  $\mathbf{J}_\alpha$  is the flux,  $L_{\alpha\alpha}$  is the proportionality constant and  $\mathbf{X}_\alpha$  is the conjugated driving force. The existence of a driving force in these processes signifies a deviation from equilibrium. In order to describe electrokinetic processes, such a relation does not satisfy, as for example a pressure difference over a capillary not only causes fluid flow, but this fluid flow also causes the creation of an electric field, causing coupled electrical conduction. This electrical conduction is called non-conjugated electrical conduction, as it is not related directly to an electrical potential gradient. In order to describe these cross effects, one simply adds terms to Equation 2.23, leading to the following relation:

$$\mathbf{J}_\alpha = \sum_{\beta=1}^n L_{\alpha\beta} \mathbf{X}_\beta \quad (2.24)$$

where  $\alpha, \beta = 1, 2, \dots, n$ ,  $\mathbf{J}_\alpha$  stands for different fluxes,  $L_{\alpha\beta}$  are the different cross terms and proportionality constants and  $\mathbf{X}_\beta$  represents the different driving forces.

Coupled irreversible transport phenomena are governed by Onsager's law, which means that for a proper choice of the fluxes and driving forces, the matrix of phenomenological coefficients  $L_{\alpha\beta}$  is symmetric.

In the case of electrokinetic effects, the coupling of effects is called electro-hydrodynamic coupling and can be described by the following matrix equation:

$$\begin{pmatrix} Q \\ J \end{pmatrix} = \begin{pmatrix} L_{11} & L_{12} \\ L_{21} & L_{22} \end{pmatrix} \begin{pmatrix} \Delta P \\ \Delta \Psi \end{pmatrix} \quad (2.25)$$

where  $L_{12} = L_{21}$ ,  $J$  represents the current ( $A$ ) and  $Q$  represents the flow ( $m^3/s$ ). The current and flow are the two relevant fluxes; the electric potential gradient and pressure difference are the corresponding driving forces. The proportionality constants and cross terms can be derived under different assumptions. This will be displayed in the coming Subsections 2.5.5.1 and 2.5.5.3.

### 2.5.5. SINGLE-PHASE STREAMING POTENTIAL

This section will discuss several ways of deriving the equations for single phase streaming potentials. Furthermore, streaming potential in porous plugs and the definition of surface conduction are discussed. Figure 2.16 shows again the concept of streaming potential in a capillary.

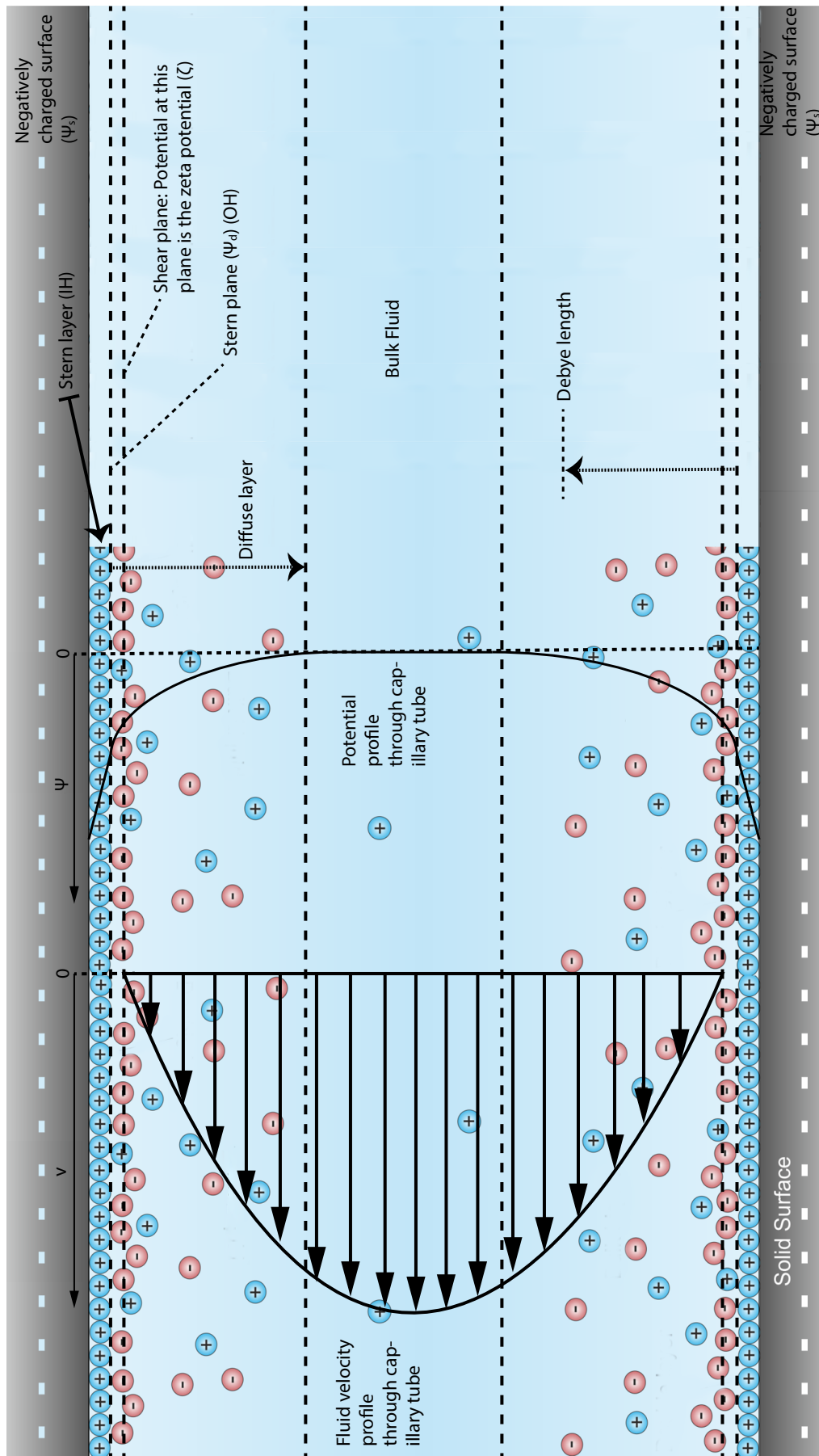


Figure 2.16: Illustration of the streaming potential phenomenon in a capillary tube or slit (modified from larryisgood ([http://en.wikipedia.org/wiki/Double\\_layer\\_\(interfacial\)\)](http://en.wikipedia.org/wiki/Double_layer_(interfacial))))

First, it is important to illustrate the concept of streaming potential inside a charged medium with Figure 2.16. The two grey blocks are the negatively charged surfaces, which could be a sandstone/ clay surface or a glass surface. The charge of this surface is compensated in two phases. First, a part of the charge is compensated by positively charged ions in the Stern layer. This plane lies between the surface of the material and the Stern plane, which is also the Outer Helmholtz (OH) plane. The Inner Helmholtz (IH) plane is located at the distance of one ionic radius from the surface. From the Stern plane onwards, the charge is compensated in the diffuse layer. When all charge is compensated, in other words the law of electroneutrality between the surface and the fluid holds, one enters the region of the bulk fluid, where there are as much positive as negative ions in solution. When the diffuse layers from both sides are larger and overlap each other, this is called an overlapping double layer. The tendency of overlapping double layers is higher when either the surface potential is higher, the radius of the capillary is smaller or when the ionic strength of the fluid is lower. The part important for charge transport downstream is the area between the shear plane (at this plane, the is a no-slip boundary assumption, the potential at this plane is the zeta ( $\zeta$ ) potential) and the end of the diffuse layer. In that region, there is both fluid flow and an excess of positive ions. The charge transport back upstream occurs through the whole tube. In most models we use later on in this thesis, the charge transport backwards is only in the region between the two shear planes. In other words, conduction through the Stern layer is neglected. When current downstream (streaming current  $J_s$ ) and conduction upstream (conduction current  $J_c$ ) are equal, there is a steady state with the assigned streaming potential value. Also, one can see from this picture, that a constant potential is assumed at the shear plane, the zeta potential, and that ion exchange processes are not included in this treatment.

#### DERIVATION OF CYLINDRICAL STREAMING POTENTIAL RELATION FOR THIN DOUBLE LAYERS (HELMHOLTZ-SMOLUCHOWSKI EQUATION)

Hunter [1981] describes a simplified derivation of a relation for the streaming potential. As described before, when a liquid is forced through a capillary, the charges in the mobile part of the double layer near the wall are carried towards one end. This causes a streaming current,  $J_s$  to develop. The accumulation of charge on one end, sets up an electric field. This electric field causes a conduction current,  $J_c$  in the other direction. At steady state, these two terms are equal to each other. What remains is an electrostatic potential difference over the capillary (or porous plug), which is called the streaming potential. The next step is to obtain a relation between the streaming potential and the zeta ( $\zeta$ ) potential. First, one starts by defining the fluid flow through a capillary with the geometry defined as in Figure 2.17 as given by linear velocity of the liquid by means of the Poiseulle equation:

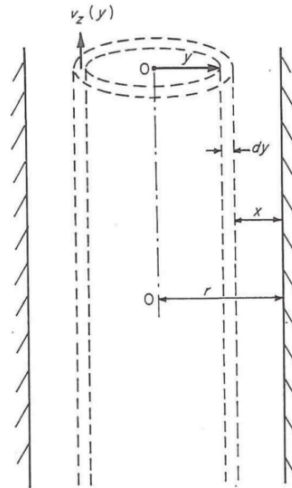


Figure 2.17: Geometry of the capillary used for the derivation of the streaming current [Modified from larryisgood ([http://en.wikipedia.org/wiki/Double\\_layer\\_\(interfacial\)](http://en.wikipedia.org/wiki/Double_layer_(interfacial)))]

$$v_z(y) = P \frac{(r^2 - y^2)}{4\eta l} \quad (2.26)$$

where  $r$  is the capillary radius,  $P$  is the pressure (Pa),  $\eta$  is the viscosity (Pa s),  $r$  is the radius of the capillary

cylinder (m),  $l$  is the length of the channel (m) and  $v_z$  is the linear velocity of the liquid (m/s). The pressure gradient is defined as  $\nabla P = P/l$ . The streaming current is defined as follows:

$$J_s = \int_0^r 2\pi y v_z(y) \rho(y) dy \quad (2.27)$$

where  $J_s$  is the streaming current (A) and  $\rho(y)$  is the charge density of the bulk liquid ( $C/m^3$ ).

An important assumption made now, is that the double layer is confined to a thin region near the capillary wall ( $\kappa a \gg 1$ ), so only values of  $y$  near  $y = r$  are important in determining the streaming current. One substitutes  $y = (r-x)$  and Equation 2.26 becomes:

$$v_z \approx \frac{Prx}{2\eta l} \quad (2.28)$$

So Equation 2.27 becomes:

$$J_s = - \int_r^0 2\pi(r-x) \frac{Prx}{2\eta l} \rho(x) dx \approx - \frac{\pi r^2 P}{\eta l} \int_r^0 x \rho(x) dx \quad (2.29)$$

In these approximations it is key that the square of already a small value, can be neglected as it turns into an even smaller number. Substituting for the charge density in Equation 2.29 gives:

$$J_s = \frac{\pi r^2 P}{\eta l} \int_r^0 x \epsilon \frac{d^2 \psi}{dx^2} dx = - \frac{\pi r^2 \epsilon P}{\eta l} \int_0^\zeta d\psi = - \frac{\epsilon \zeta}{\eta} \pi r^2 P \quad (2.30)$$

In this last step lies the assumption that  $\frac{d\psi}{dx} = 0$  at  $x = r$ . The streaming current generated by the flow of charge downstream generates an electric field and this generates a conduction current in the reverse direction:

$$J_c = \frac{\pi r^2 E_s \lambda_0}{l} + \frac{2\pi r E_s \lambda_s}{l} \quad (2.31)$$

where the first term on the RHS is the bulk conduction and the second term on the RHS is the surface conduction. When a steady-state is reached, the conduction current equals the streaming current,  $J_s + J_c = 0$ , which leads to the Helmholtz-Smoluchowski equation for streaming potential in a capillary:

$$C_s = \frac{E_s}{P} = \frac{E_z}{\nabla P} = \frac{\Delta V}{\Delta P} = \frac{\epsilon_0 \epsilon_r \zeta}{\eta(\lambda_0 + 2\lambda_s/r)} = \frac{\epsilon \zeta}{\eta(\lambda_0 + 2\lambda_s/r)} \quad (2.32)$$

where

$C_s$  is the coupling coefficient ( $V/Pa$ )

$E_s$  is the streaming potential ( $V$ )

$E_z$  is the electric field strength or streaming potential per unit length  $l$  ( $E_z = E_s/l$ ) ( $V/m$ )

$\Delta V$  is the potential difference over a certain length ( $V$ )

$P$  is the pressure ( $Pa$ )

$\nabla P$  is the pressure per unit length  $l$  or pressure gradient ( $Pa/m$ )

$\Delta P$  is the pressure difference over a certain length ( $Pa$ )

$\epsilon_0$  is the permittivity of free space ( $F/m$ )

$\epsilon_r$  is the relative permittivity of the dielectric ( $-$ )

$\zeta$  is the zeta potential ( $V$ )

$\eta$  is the viscosity of the fluid ( $Pa \cdot s$ )

$\lambda_0$  is the conductivity of the bulk solution ( $S/m$ )

$\lambda_s$  is the surface conductivity (S)

$r$  is the radius of the capillary ( $m$ )

This set of equations can of course be written in the matrix form as described in Equation 2.25. The terms  $L_{11}$ ,  $L_{12}$ ,  $L_{21}$  and  $L_{22}$  can be described as follows:

$$L_{11} = -\frac{\pi r^4}{8\eta l}$$

in the case of a capillary or in the case of a porous plug:

$$L_{11} = -\frac{kA}{\eta l}$$

and for both cases:

$$L_{12} = L_{21} = \frac{\epsilon\zeta}{\eta l}$$

$$L_{22} = -\left(\lambda_0 + \frac{2\lambda_s}{r}\right)\frac{1}{l}$$

where  $l$  is the length of a channel ( $m$ ),  $r$  is the radius of the channel ( $m$ ) and  $A$  is the area of the core plug ( $m^2$ ). This leads to the following matrix system:

$$\begin{pmatrix} Q \\ J \end{pmatrix} = \begin{pmatrix} -\frac{\pi r^4}{8\eta l} & \frac{\epsilon\zeta}{\eta l} \\ \frac{\epsilon\zeta}{\eta l} & -\left(\lambda_0 + \frac{2\lambda_s}{r}\right)\frac{1}{l} \end{pmatrix} \begin{pmatrix} \Delta P \\ \Delta \Psi \end{pmatrix} \quad (2.33)$$

#### BEHAVIOUR IN POROUS PLUGS

Equation 2.32 can also be applied to porous plugs if the surface conduction term is zero ( $\lambda_s = 0$ ). Flow must be linear and laminar for this to hold. Non-linearities are easily created in porous media; at a Reynolds number around 1, the non-linear terms of the Navier-Stokes equation can become significant [Hunter, 1981]. Briggs [1928] has come up with a procedure to correct for surface conduction in a porous plug. The actual resistance of the liquid in the plug is measured and compared to that expected of measurements at high salinity when surface conduction can be considered as negligible. If one defines the total conductivity as:

$$\lambda_T = \lambda_0 + \frac{2\lambda_s}{r} \quad (2.34)$$

When measuring the resistivity of the porous sample at high salinity ( $R_0$ ). Under high salinity conditions, one can say that  $\lambda_T = \lambda_0$  and the resistivity of the porous plug can be defined as  $R_0 = \frac{k}{\lambda_0}$ , or  $k = R_0\lambda_0$ , where  $k$  is a certain 'cell constant' of the sample. If the resistivity is remeasured at a lower electrolyte concentration, one obtains  $R_\theta = \frac{k}{\lambda_{T,\theta}}$ , which leads to:

$$\lambda_{T,\theta} = \frac{R_0\lambda_0}{R_\theta} \quad (2.35)$$

This means Equation 2.32 will become:

$$C_s = \frac{\Delta V}{\Delta P} = \frac{\epsilon\zeta}{\eta} \frac{R_0}{R_0\lambda_0} = \frac{\epsilon\zeta}{\eta\lambda_{T,\theta}} \quad (2.36)$$

where  $R_\theta$  is the total resistivity of the plug at low salinity ( $ohm\ m$ ),  $R_0$  is the resistivity of the plug at high salinity ( $ohm\ m$ ) and  $\lambda_0$  is the conductivity of the electrolyte solution at high salinity ( $S/m$ ). It is good to bear in mind that these relations are in close contact with Archie's law, which relates the in-situ electrical conductivity of a sedimentary rock to its porosity and brine saturation:

$$\lambda_T = \frac{1}{\alpha} \lambda_0 \phi^m S_w^n \quad (2.37)$$

where  $\alpha$  is the tortuosity,  $\phi$  is the porosity,  $m$  is the cementation factor (usually in the range 1.8–2.0 for sandstones),  $S_w$  is the water saturation and  $n$  is the saturation exponent (usually around 2) [Crain, 2014].

## DERIVATION OF CYLINDRICAL STREAMING POTENTIAL RELATION FOR THIN AND THICK DOUBLE LAYERS

Masliyah and Bhattacharjee [2006] demonstrate a derivation of the single-phase streaming potential for a capillary for both thick and thin double layers. This derivation starts with the same geometry as the simplified derivation by Hunter [1981], as in Figure 2.17. The derivation starts by analyzing the electro-osmosis in this geometry and then uses the Onsager principle of reciprocity to apply these equations for the streaming potential phenomenon.

For both thick and thin double layers, but only for low surface potentials (linearization of the Poisson-Boltzmann equation) one obtains the relation:

$$C_s = \frac{\Delta V}{\Delta P} = \left( \frac{E_x}{P_x} \right)_{J=0} = \frac{\Omega}{\lambda_0} \left( 1 - \frac{2A_1}{\kappa r} \right) f(\kappa r, \beta, F_{cc}) \quad (2.38)$$

where

$$\Omega = \frac{\epsilon \zeta}{\eta} \quad (2.39)$$

and  $\lambda_0$  is the fluid conductivity, which can also be expressed as:

$$\lambda_0 = \frac{2e^2 z^2 D n_\infty}{k_B T_K} \quad (2.40)$$

for a z:z electroneutral electrolyte solution, where the diffusion constant ( $D$ ) ( $m^2 s^{-1}$ ) is temperature dependent via the Stokes-Einstein relation (input temperature in Kelvin), which is given by [Flury and Gimmi, 2002]:

$$D(T_K) = \frac{T_K \eta(T_0)}{T_0 \eta(T_K)} D(T_0) \quad (2.41)$$

where  $T_0$  is the starting temperature at which  $D(T_0)$ . The values of  $D(T_0)$  at 298 °K are as follows:

$$D(T_0)_{NaCl} = 1.611 * 10^{-9} \quad (2.42)$$

$$D(T_0)_{CaCl_2} = 1.335 * 10^{-9} \quad (2.43)$$

Important to note is that the surface conduction term  $\lambda_s$  is not included in this derivation, as it is physically a wrong interpretation of the actual phenomenon. The term  $A_1$  can be defined as follows:

$$A_1 = \frac{I_1(\kappa r)}{I_0(\kappa r)} \quad (2.44)$$

where  $I_0$  is the zeroth-order modified Bessel function of the first kind and  $I_1$  is the first-order modified Bessel function of the first kind. Furthermore:

$$f(\kappa r, \beta, F_{cc}) = \frac{1}{F_{cc} - \beta(1 - 2A_1/(\kappa r) - A_1^2)} \quad (2.45)$$

$$\beta = \frac{\epsilon^2 \zeta^2 \kappa^2}{\eta \lambda_0} \quad (2.46)$$

$$F_{cc} = 1 + \left( \frac{ze\zeta}{k_B T} \right)^2 \frac{1}{I_0^2(\kappa r)} \int_0^1 I_0^2(\kappa r \cdot R) R dR \quad (2.47)$$

where

$$\int_0^1 I_0^2(\kappa r \cdot R) R dR = \frac{1}{2} (I_0^2(\kappa r) + I_1^2(\kappa r)) \quad (2.48)$$

This relation can further be simplified when only the leading term in  $ze\zeta/k_B T$  is retained (when it is smaller than 1, so at low zeta potentials), which gives:

$$\left(\frac{E_x}{P_x}\right)_{J=0} \approx \frac{\Omega}{\lambda_0} \left(1 - \frac{2A_1}{\kappa r}\right) \quad (2.49)$$

For thin double layers, so  $\kappa r \gg 1$ , the derivation leads to the Helmholtz-Smoluchowski equation without the inclusion of surface conduction:

$$\left(\frac{E_x}{P_x}\right)_{J=0} = \frac{\Omega}{\lambda_0} = \frac{\epsilon\zeta}{\eta\lambda_0} \quad (2.50)$$

The relation from Maslyah for streaming potential arises from the following equation for current:

$$\begin{aligned} J &= \Omega P_x A_c \left(1 - \frac{2A_1}{\kappa r}\right) + E_x A_c \Omega^2 \eta \kappa^2 \left(1 - \frac{2A_1}{\kappa r} - A_1^2\right) - E_x A_c \lambda_0 F_{cc} \\ &= -E_x A_c \lambda_0 F_{cc} \left[1 - \frac{\Omega^2 \eta \kappa^2}{\lambda_0 F_{cc}} \left(1 - \frac{2A_1}{\kappa r} - A_1^2\right)\right] + \Omega P_x A_c \left(1 - \frac{2A_1}{\kappa r}\right) \end{aligned} \quad (2.51)$$

and for flow:

$$Q = E_x \Omega A_c \left(1 - \frac{2A_1}{\kappa r}\right) - P_x \frac{\pi r^4}{8\eta} \quad (2.52)$$

which gives a matrix equation as follows:

$$\begin{pmatrix} Q \\ J \end{pmatrix} = \begin{pmatrix} -\frac{\pi r^4}{8\eta l} & \Omega A_c \left(1 - \frac{2A_1}{\kappa r}\right) \frac{1}{l} \\ \Omega A_c \left(1 - \frac{2A_1}{\kappa r}\right) \frac{1}{l} & -A_c \lambda_0 F_{cc} \left[1 - \frac{\Omega^2 \eta \kappa^2}{\lambda_0 F_{cc}} \left(1 - \frac{2A_1}{\kappa r} - A_1^2\right)\right] \frac{1}{l} \end{pmatrix} \begin{pmatrix} \Delta P \\ \Delta \Psi \end{pmatrix} \quad (2.53)$$

This can of course be named in terms of  $L_{11}$ ,  $L_{12}$ ,  $L_{21}$  and  $L_{22}$ :

$$L_{11} = -\frac{\pi r^4}{8\eta l}$$

or in the case of a porous plug:

$$L_{11} = -\frac{kA}{\eta l}$$

and for both cases:

$$\begin{aligned} L_{12} &= L_{21} = \Omega A_c \left(1 - \frac{2A_1}{\kappa r}\right) \frac{1}{l} \\ L_{22} &= -A_c \lambda_0 F_{cc} \left[1 - \frac{\Omega^2 \eta \kappa^2}{\lambda_0 F_{cc}} \left(1 - \frac{2A_1}{\kappa r} - A_1^2\right)\right] \frac{1}{l} \end{aligned}$$

#### DERIVATION OF TRIANGULAR STREAMING POTENTIAL RELATION FOR THIN AND THICK DOUBLE LAYERS

Mortensen et al. [2006] have done work on the derivation of transport coefficients ( $L_{11}$ ,  $L_{12}$ ,  $L_{21}$  and  $L_{22}$ ) for electrolyte in arbitrarily shaped nano and micro-fluidic channels. This work is useful if one wants to model streaming potential through a triangular shaped geometry, which can be used to make a simple approximation of a two-phase streaming potential system. In their work they assume laminar flow of incompressible electrolytes in long strait channels driven by pressure and electro-osmosis. They have used a Hilbert space eigenfunction expansion to address the general problem of an arbitrarily shaped cross-section and they obtain results for the hydraulic and electrical transport coefficients in linear-response theory. The relations satisfy the Onsager principles and thus are also applicable to streaming potential problems.

For thin double layers (when  $\kappa^{-1} = \lambda_D \ll \frac{A}{S}$ ) ( $S$  is the perimeter of the channel (m),  $A$  is the cross sectional area ( $m^2$ ), Mortensen et al. [2006] derive the following set of equations:

$$L_{11} = -\frac{A^2}{\alpha\eta l}$$

$$L_{12} = L_{21} = \Omega \frac{A}{l}$$

$$L_{22} = -\lambda_0 \frac{A}{l}$$

where  $\alpha$  is the dimensionless geometrical correction factor. This leads to the following matrix system:

$$\begin{pmatrix} Q \\ J \end{pmatrix} = \begin{pmatrix} -\frac{A^2}{\alpha \eta l} & \Omega \frac{A}{l} \\ \Omega \frac{A}{l} & -\lambda_0 \frac{A}{l} \end{pmatrix} \begin{pmatrix} \Delta P \\ \Delta \Psi \end{pmatrix} \quad (2.54)$$

For thick double layers (when  $\kappa^{-1} = \lambda_D \gg \frac{A}{3}$ ):

$$L_{11} = -\frac{A^2}{\alpha \eta l}$$

$$L_{12} = L_{21} = \Omega \frac{\sinh(\frac{ze\zeta}{k_B T_K})}{\frac{ze\zeta}{k_B T_K}} \frac{A^2 \kappa^2}{\alpha l}$$

$$L_{22} = -\left[ \cosh(\frac{ze\zeta}{k_B T_K}) + \frac{\epsilon \zeta^2}{\eta D} \frac{\sinh^2(\frac{ze\zeta}{k_B T_K})}{(\frac{ze\zeta}{k_B T_K})^2} \frac{A \kappa^2}{\alpha} \right] \frac{A \lambda_0}{l}$$

where  $D$  is the solute diffusion constant ( $m^2 s^{-1}$ ).

This leads to the following matrix system for thick double layers (overlapping):

$$\begin{pmatrix} Q \\ J \end{pmatrix} = \begin{pmatrix} -\frac{A^2}{\alpha \eta l} & \Omega \frac{\sinh(\frac{ze\zeta}{k_B T_K})}{\frac{ze\zeta}{k_B T_K}} \frac{A^2 \kappa^2}{\alpha l} \\ \Omega \frac{\sinh(\frac{ze\zeta}{k_B T_K})}{\frac{ze\zeta}{k_B T_K}} \frac{A^2 \kappa^2}{\alpha l} & -\left[ \cosh(\frac{ze\zeta}{k_B T_K}) + \frac{\epsilon \zeta^2}{\eta D} \frac{\sinh^2(\frac{ze\zeta}{k_B T_K})}{(\frac{ze\zeta}{k_B T_K})^2} \frac{A \kappa^2}{\alpha} \right] \frac{A \lambda_0}{l} \end{pmatrix} \begin{pmatrix} \Delta P \\ \Delta \Psi \end{pmatrix} \quad (2.55)$$

Again, it is important to realize that these results are valid for symmetric electrolytes, even beyond the Debye-Hückel approximation. In the Debye-Hückel limit ( $\frac{ze\zeta}{k_B T}$ ) they also hold for asymmetric electrolytes. In the Debye-Hückel limit the solutions by [Mortensen et al. \[2006\]](#) agree fully with the corresponding limits for a circular cross section, where explicit solutions exist in the Debye-Hückel limit in terms of Bessel functions.

[Mortensen et al. \[2006\]](#) have calculated all the dimensionless geometrical correction factors  $\alpha$  for the different geometries. Important in this work are a equilateral triangle (1:1:1) and hexagonal geometry.

$$\alpha_{triangle(1:1:1)} = 20\sqrt{3} \quad (2.56)$$

$$\alpha_{hexagon} = 26.08 \quad (2.57)$$

### SURFACE CONDUCTION

In the analysis of the derivation by [Masliyah and Bhattacharjee \[2006\]](#), the attention is on the flow region extending from the shear plane. The assumption here is that there is no flow or conduction in between the shear plane and the channel wall, the Stern layer. According to this analysis, the electric current is just due to the convection and conduction in the channel within a region bounded by the shear planes, where the no-slip boundary and the zeta potential was defined. Surface conductance does not consider conduction through the material that makes up the channel walls. The channel material is considered to be a perfect insulator, so the surface conductance has no relation to the channel material in terms of electrical conductivity.

The correction for the surface conduction arises historically from the Smoluchowski equation, that does not contain the effect of the electric double layer, but only the bulk conductivity of the electrolyte solution ( $\lambda_0$ ). Also, a striking feature of this same equation (Equation 2.50), is that it does not depend on the channel radius, given that the equation is an approximation and only valid in the range of large  $\kappa r \rightarrow \infty$ . The streaming potential equation as derived in [Masliyah and Bhattacharjee \[2006\]](#) shows a more general form, which implicitly contains the effect of the electric double layer and therefore the microchannel radius. This

is manifested in the term  $2A_1/\kappa r$ , which becomes 0 when  $\kappa r$  becomes large. This approach does not need an extra incorporation of surface conduction as long as it is used for low zeta potentials. This approach includes the overlapping of double layers, which in literature is often called 'surface conduction'; it is the conduction close to the shear plane, which differs from the bulk fluid conduction that is taken into account. Stern layer conduction is excluded in this treatment though.

For large values of  $\kappa r$ , the electric double layer is very thin, so only a small region near the capillary wall has a contribution to the streaming current, as the core of the capillary is essentially electroneutral. The expression of Smoluchowski for this streaming current is to be found in Equation 2.30. This is already an approximation. The conduction current is dominant in the core region of the medium and is given by the first term on the right-hand side of Equation 2.31. This function omits the  $F_{cc}$  term, which accounts for the conduction current in the electric double layer. The idea behind this approximation is that for large values of  $\kappa r$ , the double layer is very thin and its contribution to the migration current would be significantly small. If the conduction current and the streaming current are equaled ( $I_s = I_c$ ), one obtains the Smoluchowski equation as in Equation 2.50.

For small values of  $\kappa r$ , the electric double extends well into the capillary. This means that the co-ion and counter-ion concentrations differ at every radial position inside the capillary. This affects both the convective (streaming) and the conductive current through this same capillary. This is clear from the relation by Masliyah and Bhattacharjee [2006] in Appendix .

The term of 'surface conductance' was first introduced to find a way to incorporate the effect of a finite conductance that arises from the thin electric double layer in the Smoluchowski relationship. Conceptually, the contribution to the conductance arises from conduction through the bulk electrolyte and the surface conductance that accounts for the presence of the electrical double layer. This leads to the following expression for the conduction current:

$$I_c = E_z(\lambda_0 A_c + \lambda_s S) = \lambda_0 A_c E_z \left(1 + \frac{\lambda_s S}{\lambda_0 A_c}\right) \quad (2.58)$$

where  $S$  is the wetted perimeter of the microchannel and  $\lambda_s$  is the surface conductance term caused by the presence of the electrical double layer. In a cylindrical geometry,  $A_c = \pi r^2$  and  $S = 2\pi r$ , as illustrated in Figure 2.18. This gives the same result as Equation 2.32:

$$\frac{\Delta V}{\Delta P} = \frac{e\zeta}{\eta\lambda_0\left(1 + \frac{2\lambda_s}{\lambda_0 r}\right)} \quad (2.59)$$

where  $\lambda_s/r\lambda_0$  is defined as the Dukhin number,  $Du$ . When  $Du \ll 1$ , surface conductance is negligible and one reverts to Equation 2.50. There is no dependence on the channel radius in this case. For a cylindrical capillary the  $F_{cc}$  can be defined as:

$$F_{cc} = 1 + \frac{2\lambda_s}{r\lambda_0} \quad (2.60)$$

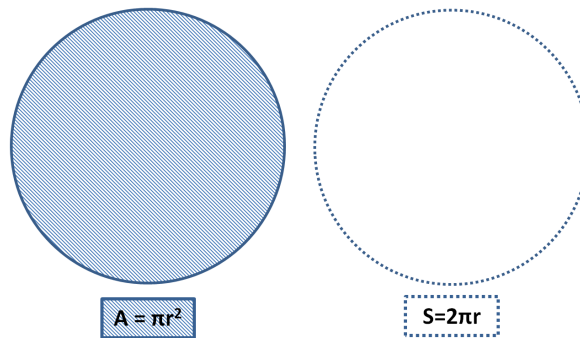


Figure 2.18: Surface area and perimeter of a cylinder

It is important to note that the surface conductance correction as applied in Equation 2.59 is only significant at small values of  $\kappa r$ ; in other words, at low salinity and/or small capillary radius. Comparing Equation 2.59 with Equation 2.49, one might think that the term  $1 - 2A_1/(\kappa r)$  might be the same correcting term for

surface conductance as the term in Equation 2.59, but this term arises from a detailed analysis of the streaming current. The equation by Smoluchowski does not include this term. Also, for small  $\kappa r$ , the dependence of the streaming current on  $\kappa r$  is way more prominent than the dependence of the conduction current on  $\kappa r$ . This leads to the very important conclusion that the attempt to incorporate a surface conductance term in the theory of the streaming potential without modifying the streaming current term from the Smoluchowski form is incorrect [Masliyah and Bhattacharjee, 2006].

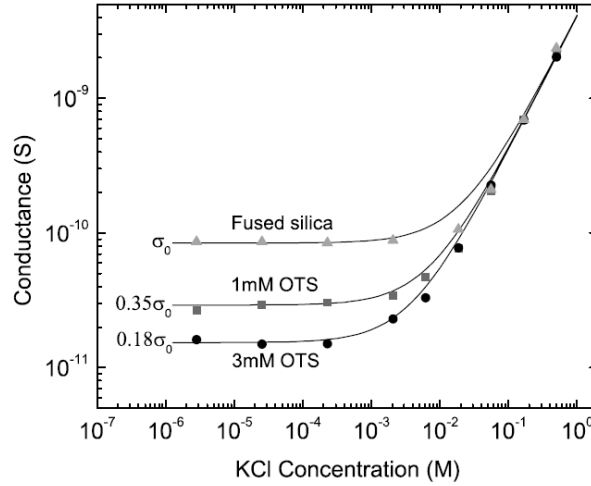


Figure 2.19: Effect of surface conductance illustrated [Stein et al., 2004]

Figure 2.19 by Stein et al. [2004] shows the effect of surface conductance as the bulk fluid molarity is plotted against the conductivity of the whole sample.

One should realize that the surface conductance mentioned up until now, was about conductance close to the shear plane, but not inside the Stern layer. Conductance inside the Stern layer is also called 'anomalous surface conduction' and is not included inside this analysis and the assumption is that it does not play a large enough role to influence calculations [Masliyah and Bhattacharjee, 2006].

#### OTHER WORKS ON SINGLE-PHASE STREAMING POTENTIAL

Apart from the textbook material by Masliyah and Bhattacharjee [2006] and Hunter [1981], a lot of other work has been done which is described in literature. To start with, Glover et al. [2012] have made a theoretical (empirical) model describing the zeta potential and coupling coefficients and they have compared their model to a lot of literature data. The model uses an adjusted version of the Helmholtz-Smoluchowski equation as in Equation 2.59, in which the radius of the capillary  $a$ , which they call a characteristic length scale for the porous medium, is defined as  $a = d/3(F - 1)$ , leading to:

$$C_s = \frac{\Delta V}{\Delta P} = \frac{d\epsilon\zeta}{\eta(d\lambda_0 + 6\lambda_s(F - 1))} \quad (2.61)$$

where  $d$  is the mean grain diameter (m) and  $F$  is the formation factor, defined as  $F = \frac{\alpha}{\phi^m}$ , where  $\phi$  is porosity (-),  $\alpha$  is tortuosity and  $m$  is the cementation exponent. Again, this approach is similar to the one described in Equation 2.37, where Archie's law is also used to describe the resistivity of the formation.

The model uses empirical relations as input for all the variables on the RHS of Equation 2.61. Glover et al. [2012] use relations by Revil and Glover [1998], Revil et al. [1999a], Revil et al. [1999b], Pride and Morgan [1991], Linde et al. [2007] and others as input into their model.

Figure 2.20 shows the fit of the empirical model for several pH values to the literature data as combined by Vinogradov et al. [2010]. This figure gives a good impression how a coupling coefficient curve plotted against molarity should look like for a single-phase situation. One can see that at high molarity, the coupling coefficients are small. This is because at high molarities, the conductivity of the fluid in the porous medium is high and this allows for a strong conduction current upstream, not enabling a higher steady state streaming potential value to build up. As molarity decreases, one can see that at first the coupling coefficient decreases linearly in the log-log plot. Then, around a molarity of  $10^{-3}$  mol/l, this linear trend fades and the points

scatter more. This is the region where the overlapping of double layers ('surface conduction') and the Stern conduction become more important. From here on, the coupling coefficient is geometry dependent, whereas at high salinity it is geometry independent, which you can also see in the equation presented earlier on.

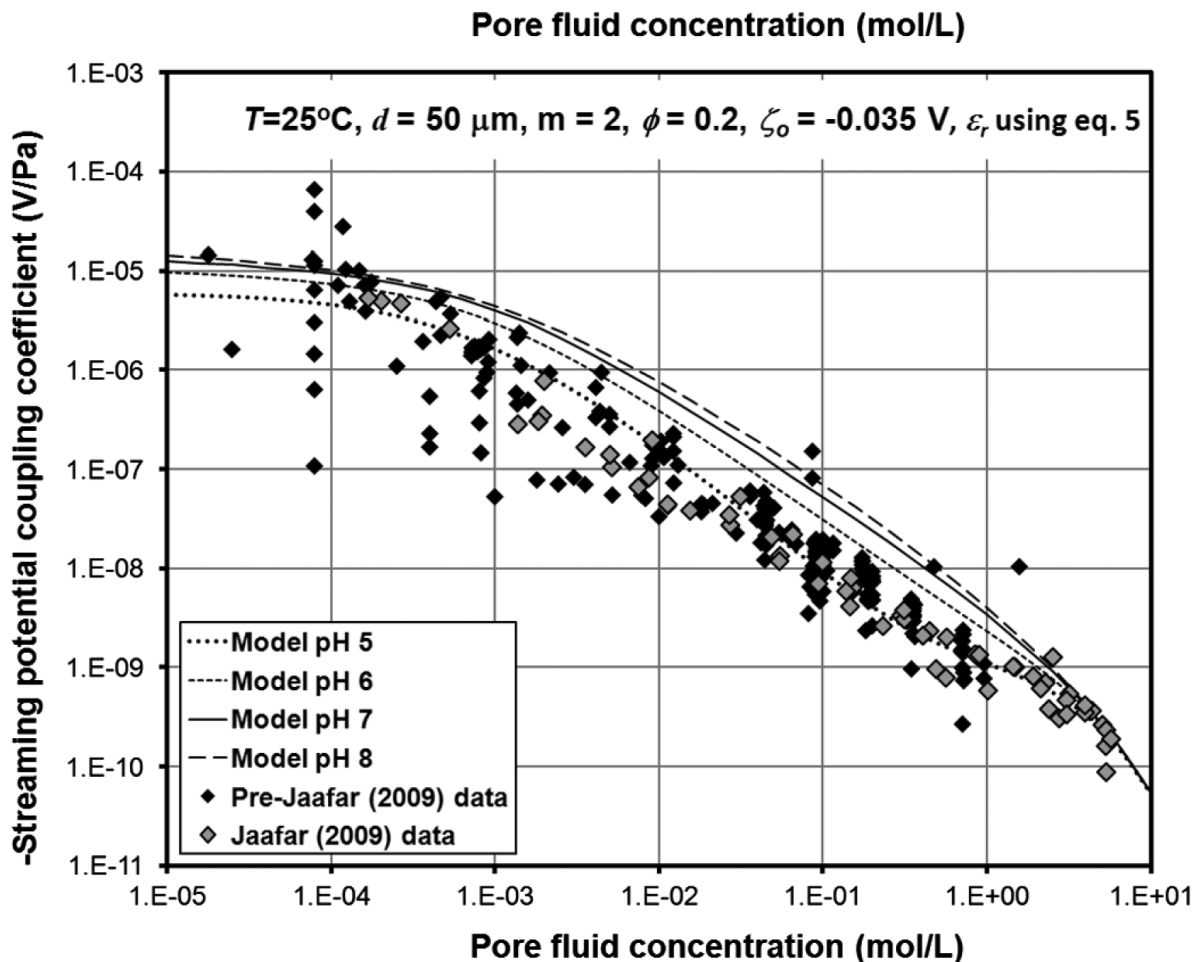


Figure 2.20: Coupling coefficients from literature compared to the empirical model [Glover et al., 2012]

### 2.5.6. TWO-PHASE STREAMING POTENTIAL

In a hydrocarbon reservoir, not only the fluid is moving with respect to the rock, but two immiscible fluids may also be moving with respect to each other and/or gas may be moving with respect to the fluid or fluids. Surface charge can also be present at the gas-liquid and liquid-liquid interfaces and these give rise to streaming potentials similar to the solid-liquid interface. In a medium that is mixed-wet, so where parts of the rock are covered by thick water films and other parts by thin water films overlain by crude oil, the streaming potential response is due to the different phases covering the rock. This streaming potential response is caused by the potential at the shear plane, also known as the zeta potential. We will now treat several different authors that have treated two-phase streaming potential measurements in their work.

Firstly, Sprunt et al. [1994] state that the electrokinetic potential arising from multiphase flow is the sum of the electrokinetic potentials at all the phase interfaces by the principle of superposition. If one of these potentials is significantly larger than the other, the largest potential will dominate the total electrokinetic potential. They note that the electrokinetic potential increases when two phases are flowing. The magnitude of an eventual two phase oil-brine signal depends on the composition of the oil and the brine.

Apart from that, Guichet [2003] have done experiments to understand two-phase streaming potentials. They have performed two phase streaming potential measurements by injecting various gases to reduce the water saturation in the sand column. The measured electrokinetic coupling coefficient in partial saturation conditions is either constant or decreases by a factor of around 3 with decreasing water saturation from 100

to 40 %. The electrical resistivity increases with a factor of around 5.

Jackson et al. [2012] have looked into the modeling of spontaneous potentials in hydrocarbon reservoirs during waterflooding. They suggest that measurements of SP could be used to detect and monitor water encroaching on a well while it is still several tens to hundreds of meters away from the producing well. They find that the SP signal can be large and that it peaks at the location of the moving water front, where there are steep gradients in saturation and salinity. The shape of the SP signal measured could also give an indication of the geometry of the encroaching waterfront.

In earlier research, Jackson [2008] have looked into the characterization of multiphase electrokinetic coupling when using a bundle of capillary tubes model. One phase is water and the other air or oil. It shows that the total electrokinetic coupling is the sum of the individual phase contributions. It also depends on capillary size distribution and wettability. They show that when water is the wetting phase and the second phase is nonpolar and does not contain an excess of charge, the relative coupling coefficient decreases with decreasing water saturation. This behavior has not been predicted previously, and occurs because oil occupies the large capillaries, and has a larger impact on the electrical conductivity than on the water relative permeability. However, when water is not the wetting phase, the coupling coefficient increases with decreasing water saturation. At irreducible water saturation this coupling coefficient falls to zero. However, the absolute value of the coupling coefficient in oil-wet media will depend upon the nature and distribution of electrical charge at water-oil interfaces, which is poorly understood. It is likely that the electrokinetic coupling in oil-wet media will be significantly smaller than in water-wet media, because the excess charge density in the water is lower.

The electrokinetic coupling coefficient can be described in terms of the water relative permeability and relative electrical conductivity, if water is the only phase that contains an excess of charge. In the model of Jackson [2008], predictions on multiphase electrokinetic coupling coefficients in porous media are dependent on rock type and wettability, which can be expressed in commonly measured petrophysical properties. Bear in mind that the model is based on a bundle of tubes and represents a simplified situation of the in-situ geometry. In real geologic porous media the relation between the petrophysical properties and the relative coupling coefficient is still poorly understood. Also, preliminary work shows that the multiphase coupling can be significantly enhanced, if the second phase is polar and contains an excess of charge. This is because polar hydrocarbon components support electrical double layers at solid-fluid and fluid-fluid interfaces and they might also cause wettability alteration. Pore-network modeling might be a solution to these problems.

In their model, Jackson [2008] use the concept of relative coupling coefficients. A relative coupling coefficient is a value by which the coupling coefficient at 100 % water saturation should be multiplied to obtain the coupling coefficient at at different water saturation:

$$C_r = \frac{C_s(S_w)}{C_s(S_w = 1)} \quad (2.62)$$

where  $C_r$  is the relative coupling coefficient (-),  $C_s(S_w)$  is the coupling coefficient (V/Pa) at a certain water saturation.

Lastly, Revil et al. [2007] model electrokinetic coupling in unsaturated porous media, where water is the wetting phase and the second phase consists of an electrical insulating viscous fluid. They use a volume averaging approach to derive current densities and velocities on the scale of a representative elementary volume. Some material properties entering the model are: water saturation, electrical formation factor and capillary pressure functions, relative permeabilities and conductivities that vary with saturation. Reference measurements confirm the model correctly.

When wettability in a system changes, one might expect the coupling coefficient curve of a rock to move from an oil-wet situation to a more water-wet situation, when moving from a higher salinity to a lower salinity, which may cause wettability alteration.

### 2.5.7. ELECTROPHORESIS

Appendix A will describe the equations and processes regarding electrophoresis.



# 3

## MATERIALS AND METHODS

In this chapter, the materials and methods used in this thesis are described. First, we discuss the fluid and rock selection reasoning, the boundary conditions of the experiments and the core characterization, then the experimental set-up of the streaming potential experiment. Thereafter, we discuss the electrophoretic experimental method and the protocols of both the streaming potential set-up and the electrophoretic (zetalyzer) experiments.

### 3.1. ROCKS AND FLUIDS

#### 3.1.1. SELECTION OF CORES (ROCKS)

The sandstones used in both the streaming potential and the electrophoretic experiments were selected based on both practical reasons and on ground to be able to compare the results of this work with previous work by [Suijkerbuijk et al. \[2012\]](#). Also geological reasons play a role, such as clay content and type of rock. Four different types of rock are used: QF20, Bentheimer, Berea 700 and Berea 18.

The QF20 fused silica rock and Bentheimer sandstone were used for the first measurements and were already available and coated in an epoxy core holder at the start of this thesis. This is why the first streaming potential experiments were done with this rock. The Bentheimer is also used in the electrophoretic experiments (zetalyzer) for comparison with the streaming potential measurements and the other sandstones. The QF20 is not analyzed in the zetalyzer experiments. Some information is available from the manufacturer Of the QF20 fused silica, but we did not perform a detailed analysis on the composition of the samples, as they are pure silica. The Bentheimer has been characterized with an XRD analysis and micro-CT scan.

The second sandstone that is used in the experiments, is the so-called 'Berea 700' sandstone. Berea 700 is a Berea sandstone, which is a clay bearing sandstone with a good permeability (around 700 mD). In previous work by [Suijkerbuijk et al. \[2012\]](#) the Berea 700 SST has shown to be able to change wettability after aging, as was clearly seen in the results of imbibition tests on aged Berea 700 with crude oil in this work (further explanation can be found in Subsection 2.1.5). Furthermore, porosity-permeability data, XRD analysis data and micro-CT data were available for characterization of the rock. This will be described in Subsection 3.1.2, together with the data on all the other samples.

The last sandstone selected is 'Berea Block 18' sandstone. It was chosen, because of its resemblance to the 'Berea 700' SST. Unlike the Berea 700 sandstone, which is very scarcely available, the Berea Block 18 is readily available. It also contains clays, although the low salinity effect/ wettability alteration has not showed to be as significant as in the Berea 700 sandstone. Berea Block 18 has a permeability around 100 mD and for this sandstone XRD data and porosity-permeability data were also available. A micro CT scan was performed especially for this research to be able to characterize the pore network structure in the Berea Block 18 as well.

Figure 3.1 shows the three different sandstones, Bentheimer on top, followed by Berea 700 and Berea Block 18. The slightly more greyish color of both Berea sandstones indicate that they contain more clays.

#### 3.1.2. CORE CHARACTERIZATION

In this subsection, the essential information on the materials used in the experiments is given.



Figure 3.1: Three different core materials: Bentheimer, Berea 700 and Berea 18

#### FUSED SILICA: QF 20

The first proof-of-concept experiments were performed on a fused silica QF20 core. This material is fabricated by Filtros Limited and is a glass bonded pure silica ( $SiO_2$ ). Porosity ranges from 35 – 45 %. The maximum pore diameter is around 80 microns. The sample has a diameter of 2 cm and a length of 15 cm.

#### BENTHEIMER SST

The Bentheimer Sandstone used in the experiments has a porosity of around 21 %. The liquid permeability of the sample ranges from 2 – 3 Darcy ( $2 - 3 * 10^{-12} m^2$ ). XRD-analysis shows that the Bentheimer Sandstone has a quartz content of 98.4 %, a kaolinite/chlorite content of 0.6 %, an orthoclase content of 0.8 % and traces of calcite and dolomite. The weight percentage of clay-sized material (based on diameter) is 0.24 weight %. Of the clay fraction, 93.6 % was determined to be kaolinite and 6.4 % illite [Marcelis, 2006]. Figure 3.1 shows these results, which were obtained by XRD analysis.

#### BEREA 700 SST

The Berea 700 Sandstone was chosen for its higher clay content and its ability to become more oil-wet when aged with crude oil H. Porosity of the Berea 700 SST ranges from 21.9 % to 22.4 %. The air permeability of the outcrop samples range from 579 to 801 mD ( $579 - 801 * 10^{-15} m^2$ ) and the Klinkenberg corrected liquid permeability ranges from 546 to 761 mD ( $546 - 761 * 10^{-15} m^2$ ). The Berea 700 contains 94.0 % quartz, 1.3 % of orthoclase, 1.6 % kaolinite/chlorite, 1.1 % of dolomite, 0.4 % of illite/mica and 0.2 % of siderite, calcite and albite. Traces of hematite were found. The clay-sized material forms a weight percentage of 0.16 weight %. Of the clay fraction, 40.4 % is kaolinite, 50.6 % illite and 9 % is chlorite [Marcelis, 2006]. Figure 3.1 shows the results of the XRD analysis.

There are also capillary pressure curves available from which a pore throat size distribution was constructed. This pore size distribution of the Berea 700 rock shows that the domination pore throat diameter lies around 25 microns. This can be seen in Figure 3.2.

Table 3.1: Semi-quantitative results of the whole rock and clay fraction ( $< 2\mu\text{m}$ ) XRD analysis on Berea 700 and Bentheimer sandstone samples [Marcelis, 2006]

Well	Sample number	Plug depth (m)	Sample Type	Whole Rock Composition (%BW)										TOTAL % (Whole Rock)	Clay Fraction (%BW)			TOTAL % (Clay Fraction)
				Quartz	Dolomite	Siderite	Illite/Mica	Kaolinite/Chlorite	Orthoclase	Albite	Calcite	Hematite	Clay-sized Material (weight %)		Illite	Kaolinite	Chlorite	
Berea Sandstone	1	outcrop	plug	94.9	1.1	0.2	0.4	1.6	1.3	0.2	0.2	tr	0.16	100.0	50.6	40.4	9.0	100.0
Bentheimer Sandstone	2	outcrop	plug	98.4	0.1	-	-	0.6	0.8	-	0.1	-	0.24	100.0	6.4	93.6	-	100.0

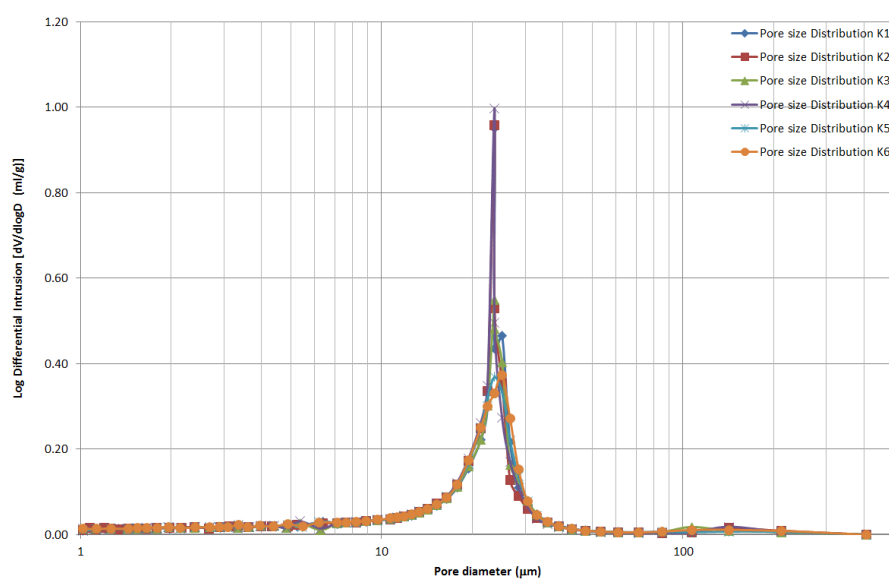


Figure 3.2: Pore size distribution of Berea 700 deduced from capillary pressure curves as obtained by MICP (Mercury Injection Capillary Pressure)

### BEREA 18 SST

The Berea 18 Sandstone has a porosity ranging from 20 – 21 %. The air permeability of the outcrop rock range from 109 to 164 mD ( $109 - 164 \cdot 10^{-15} \text{ m}^2$ ) and the Klinkenberg corrected liquid permeability ranges from 98 to 149 mD ( $98 - 149 \cdot 10^{-15} \text{ m}^2$ ). The Berea Block 18 sandstone contains 91 % quartz, 3 % kaolinite, 2 % potassium feldspars and 1 % of illite/mica, chlorite, plagioclase and ankerite. The clay-fraction semi-quantitative analysis showed that the clay fraction consists of 42 % kaolinite, 40 % illite, 13 % chlorite and 5 % illite-smectite [Marcelis, 2012b].

The Berea Sandstone has also been analysed with a scanning electron microscope (SEM). The images show that the sandstone grains are well-sorted. Pore-filling kaolinite is generated from unstable alkali-feldspar grains. The pores are well developed, but locally filled with kaolinite and illite and carbonate cements [Marcelis, 2012a]. An image of the SEM can be seen in Figure 3.3.

The pore structure of the Bentheimer, Berea 700 and Berea 18 sandstones were also analysed based on micro CT data. From this micro CT data a pore network was extracted with pore throats and bodies. This will be discussed in the chapter on the pore-network extraction.

### 3.1.3. SELECTION OF FLUIDS

The fluids (brine and oil) used in this thesis, have been selected to be able to compare results in this research with previous work by Glover et al. [2012] for single-phase streaming potential experiments, Suijkerbuijk et al.

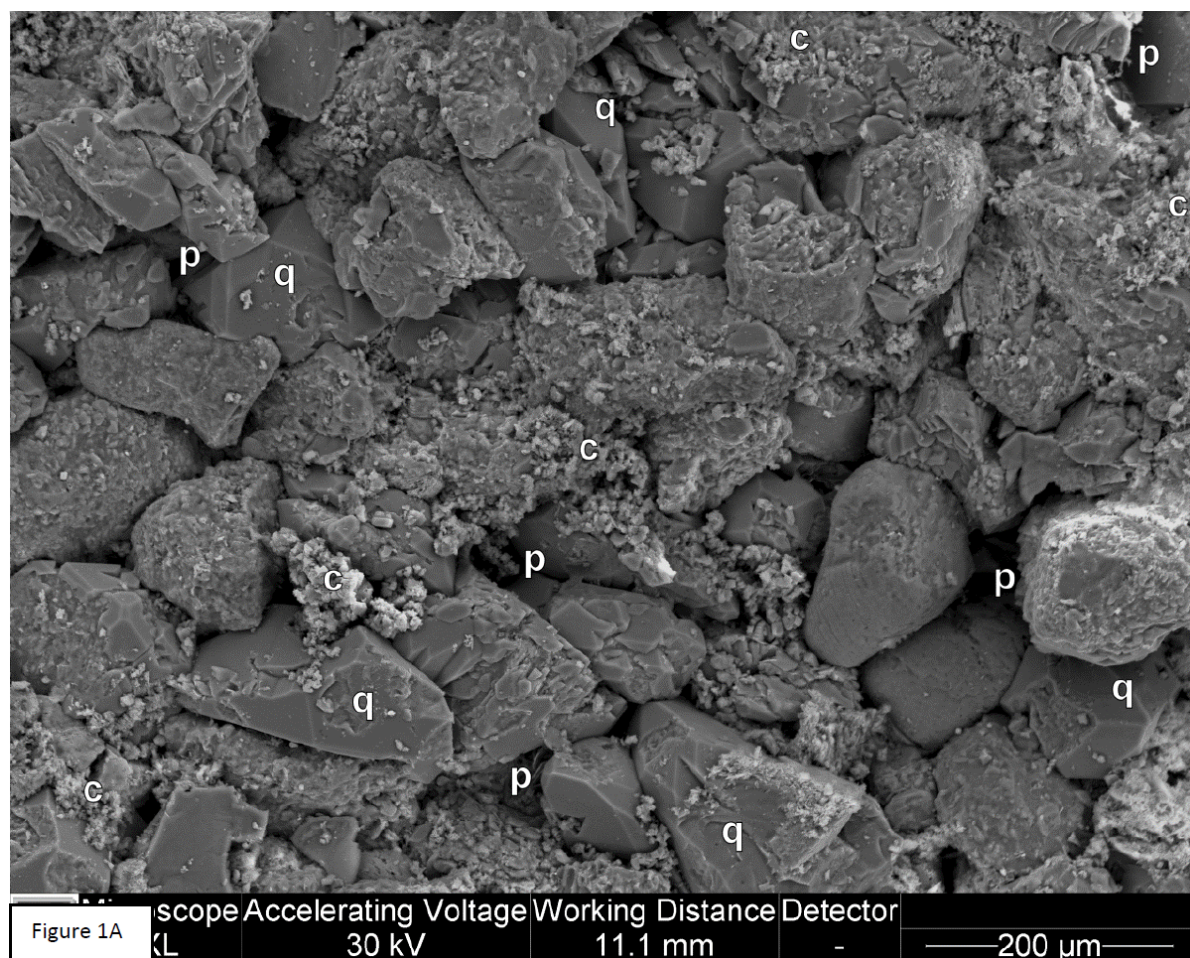


Figure 3.3: Sandstone grains with abundant secondary quartz overgrowths (q). Clays (c) (mainly kaolinite and illite (i)) occur as pore-filling aggregates and in-part grain coating associated with secondary quartz. Pore space indicated as (p) [Marcelis, 2012a].

[2012] for two-phase results, and Alotaibi et al. [2011] and Nasralla and Nasr-el din [2012] for electrophoretic measurements. Table 3.2 shows an oversight of all the fluid-rock combinations in the single-phase experiments (both zetasizer and streaming potential) and two-phase experiments (only streaming potential). On a side note, the zetasizer experiments are performed only with rock-brine combinations, so only single-phase and separate test are done with crude oil – brine combinations.

#### SELECTION OF BRINES

For the Bentheimer SST single-phase streaming potential measurements,  $10^{-5}$  –  $1M$   $NaCl$  brines are used. For two-phase streaming potential tests with Bentheimer SST, the core is saturated with Dagang brine at residual saturation and hexadecane. Then,  $10^{-5}$  –  $1M$   $NaCl$  brines,  $10^{-5}$  –  $1M$  ( $NaCl$  with 10%  $CaCl_2$ ) brines, (0.1) LS Brine E (with and without added divalents) and Dagang brine are used to flood the core. Figure 3.4 illustrates what a difference in salinity does to the conductivity of the fluid. The large range of brine salinity is chosen to be able to compare the coupling coefficients measured to the data by Glover et al. [2012].

For both the Berea sandstones at single-phase conditions, it is important to stay above the Scheuerman limits as described in Subsection 2.1.2.3. This resulted in adding 10% of divalent cations as a percentage of total cations to all  $NaCl$  brines, while the ionic strength was maintained. As can be seen in Table 3.2, the fluids selected for streaming potential experiments with the Berea 700 sandstone are  $10^{-5}$  –  $1M$  ( $NaCl$  with 10%  $CaCl_2$ ) brines, as well as (0.1) LS Brine E (with added divalents) and Dagang brine. The fluid compositions of the synthetic  $NaCl$  brines and the  $NaCl$  brines with added  $CaCl_2$  are given in Tables 3.3 and 3.4.

The zetasizer tests were performed with  $10^{-4}$  –  $0.4M$  ( $NaCl$  with 10%  $CaCl_2$ ) brines and Dagang brine for Bentheimer, Berea 700 and Berea 18. This range is broad enough to get an idea on the trend in zeta potential against salinity and it enables comparison with the work by Nasralla and Nasr-el din [2012] and Alotaibi et al.

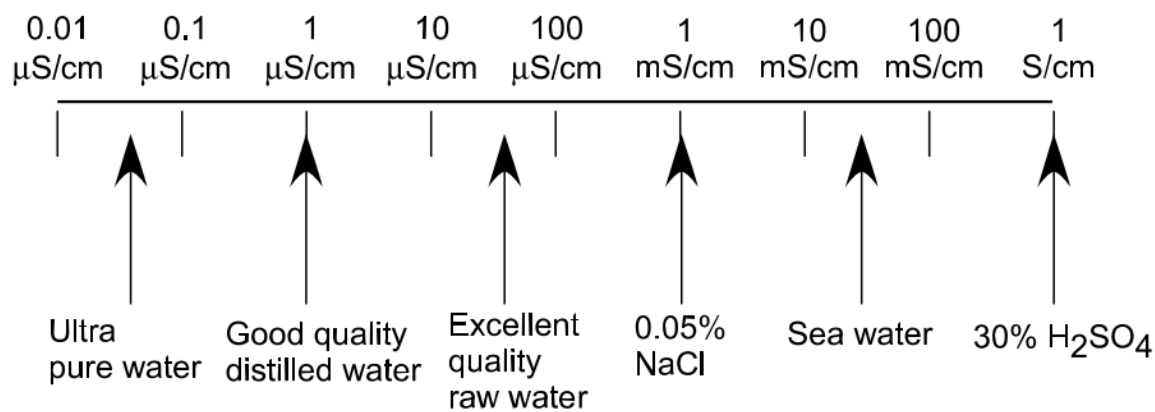


Figure 3.4: Electric conductivities of water under different conditions [Masliyah and Bhattacharjee, 2006]

[2011] possible.

Table 3.2: Fluid and rock combination oversight for single-phase and two-phase experiments. SP stands for combinations that are performed in streaming potential (SP) experiments, ZS stands for combinations that are performed in the zetazizer (ZS) experiments

Fluids	Rocks				
	Bentheimer Single-Phase	Bentheimer Two-Phase	Berea 700 Single-Phase	Berea 700 Two-Phase	Berea 18
$10^{-5}$ M NaCl	SP	SP	-	-	-
$10^{-4}$ M NaCl	SP	SP	-	-	-
$10^{-3}$ M NaCl	SP	SP	-	-	-
$10^{-2}$ M NaCl	SP	SP	-	-	-
$10^{-1}$ M NaCl	SP	SP	-	-	-
1 M NaCl	SP	SP	-	-	-
$10^{-5}$ M (NaCl with 10% CaCl <sub>2</sub> )	-	SP	SP	SP	-
$10^{-4}$ M (NaCl with 10% CaCl <sub>2</sub> )	ZS	SP	SP/ZS	SP	ZS
$3.33 \cdot 10^{-4}$ M (NaCl with 10% CaCl <sub>2</sub> )	-	-	SP	SP	-
$10^{-3}$ M (NaCl with 10% CaCl <sub>2</sub> )	ZS	SP	SP/ZS	SP	ZS
$10^{-2}$ M (NaCl with 10% CaCl <sub>2</sub> )	ZS	SP	SP/ZS	SP	ZS
$10^{-1}$ M (NaCl with 10% CaCl <sub>2</sub> )	ZS	SP	SP/ZS	SP	ZS
0.4 M (NaCl with 10% CaCl <sub>2</sub> )	ZS	-	SP/ZS	SP	ZS
1 M (NaCl with 10% CaCl <sub>2</sub> )	-	SP	SP	SP	-
LS E (0.026 M NaCl)	-	SP	-	-	-
0.1 LS E (0.0026 M NaCl)	-	SP	-	-	-
LS E (0.026 M) (with 10% CaCl <sub>2</sub> )	-	SP	SP	SP	-
0.1 LS E (0.0026 M) (with 10% CaCl <sub>2</sub> )	-	SP	SP	SP	-
Dagang (0.4M) (4.4 % divalents)	ZS	SP	SP/ZS	SP/ZS	ZS

Dagang brine was selected, because it was used in previous research by Suijkerbuijk et al. [2012], where the wettability alteration for a switch from HS to LS was studied. In those experiments, the cores were saturated with crude oil and Dagang brine. The fluid composition of Dagang brine is shown in Table 3.5.

#### SELECTION OF OILS

For two-phase streaming potential tests with Bentheimer SST, hexadecane was selected as oil, because of its non polar properties, its common use in the laboratory and stability (it has a rather high boiling temperature than decane) at the operating temperatures of the experiment (both room temperature and 70°C). The core was saturated with Dagang brine and hexadecane, whereafter it was flooded from HS to LS.

For the two-phase experiments with Berea 700 sandstone, crude oil H was selected. This crude oil was selected, because it showed great wettability alteration capacities in research performed by Suijkerbuijk et al. [2012]. Furthermore, the other oil showing good wettability alteration was not available anymore, so the

Table 3.3: Fluid composition of the  $NaCl$  brines without added divalents. This table shows the example for an ionic strength of 1M

<b>Desired brine</b>		
Ionic strength	M	1
Percentage divalents	%	0
$M_{CaCl_2}$	g/mol	110.99
$M_{NaCl}$	g/mol	58.44
$C_{CaCl_2}$	mol/l	<b>0</b>
$C_{NaCl}$	mol/l	<b>1</b>
$Weight_{CaCl_2}$	g/l	<b>0</b>
$Weight_{NaCl}$	g/l	<b>58.44</b>
$PPM_{CaCl_2}$	ppm	<b>0</b>
$PPM_{NaCl}$	ppm	<b>58440</b>

Table 3.4: Fluid composition of the  $NaCl$  brines with 10 % added divalents. This table shows the example for an ionic strength of 1M

<b>Desired brine</b>		
Ionic strength	M	1
Percentage divalents	%	0.1
$M_{CaCl_2}$	g/mol	110.99
$M_{NaCl}$	g/mol	58.44
$C_{CaCl_2}$	mol/l	<b>0.0476</b>
$C_{NaCl}$	mol/l	<b>0.857</b>
$Weight_{CaCl_2}$	g/l	<b>5.285</b>
$Weight_{NaCl}$	g/l	<b>50.091</b>
$PPM_{CaCl_2}$	ppm	<b>5285</b>
$PPM_{NaCl}$	ppm	<b>50091</b>

Table 3.5: Fluid composition of Dagang brine in mg/l, mol/l and g/l

$Na^+$	4267	mg/l	<b>0.186</b>	mol/l	$NaCl$	<b>10.85</b>	g/l
$K^+$	7237	mg/l	<b>0.185</b>	mol/l	$KCl$	<b>13.80</b>	g/l
$Mg^{2+}$	23	mg/l	<b>0.00095</b>	mol/l	$MgCl_2$	<b>0.091</b>	g/l
$Ca^{2+}$	301	mg/l	<b>0.0075</b>	mol/l	$CaCl_2$	<b>0.834</b>	g/l
$Cl^-$	13750	mg/l	<b>0.388</b>	mol/l			

choice was also based on practical limitations. The cores are saturated with Dagang brine, then crude oil H is flooded through the sample, until no water is further produced and the water is at residual water saturation. Then the core is aged for four weeks at 70 °C. After this aging period, the core is flooded with different brines starting at the highest ionic strength (Dagang) and moving to the lowest ionic strength ( $10^{-5}$  M  $NaCl$  (with 10%  $CaCl_2$ )). All brines have at least 10% added divalents as a percentage of total cations to prevent FM damage occurring. Table 3.6 and 3.7 give more information about the density, viscosity and conductivity of the oils injected and about TAN and TBN and other oil properties respectively.

Table 3.6: Density, viscosity and conductivity of oils at 20 and 70 °C and 1 atm

	<b>20 C</b>			<b>70 °C</b>		
	Density $kg/m^3$	Viscosity $Pa \cdot s$	Conductivity $\mu S/cm$	Density $kg/m^3$	Viscosity $Pa \cdot s$	Conductivity $\mu S/cm$
Crude oil H	855	-	0.1	792	1590	0.1
Hexadecane	773.6	3045	0	739.4	1000	0

### 3.1.4. EXPERIMENTAL CONDITIONS

The single-phase streaming potential experiments are performed at both 20 °C and 70 °C. The two-phase streaming potential measurements are performed only at 70 °C, as the crude oil (crude oil H) and formation

Table 3.7: Other properties crude oil H (The interfacial tension is from initial → equilibrium)

<b>Crude oil H</b>					
TAN	TBN	S	Saturate s	Aromatics	Resins
mg KOH / g oil	mg KOH / g oil	wt%	wt%	wt%	wt%
0.06	0.46	0.043	59.19	36.72	3.87
n-C7H16 Asphaltenes	P-value	IFT w FM			
wt%	–	mN/m			
0.21	1.5 – 2	27 → 13			

brine (Dagang brine) saturated sample is aged for four weeks at 70 °and atmospheric pressure (1 bar). This should bring the core in a more oil-wet state, representing the situation in a reservoir. The sample is saturated with Dagang brine at residual saturation after flowing through oil at high rates (10 – 15 ml/min), before the aging process starts.

To increase the oil saturation of the Berea 700 sample further, a mixture of PAO40 (Poly Alpha Olefin) and decane was injected at viscosities ranging from 50 cp to 1 cp at 70 °C. This increased the oil saturation in the sample from 50 % to 80%. The process of PAO40 injection is further described in the Subsection 3.2.3.

In- and outflow pressure in the streaming potential experiments are based on the strength of the signal. If the signal is weak the pressure difference over the core is increased. Flow rates range from 1 – 25 ml/min. For all fluid molarities, the test is done at several rates, where the signal is clear. The pressure difference over the cores ranges from 10 mbar to 6000 mbar.

The zetasizer experiments are performed at 20 °C and atmospheric conditions.

## 3.2. EXPERIMENTAL SETUP (STREAMING POTENTIAL)

This section describes the experimental setup constructed especially for the streaming potential experiments at Delft University of Technology in the Dietz laboratory.

### 3.2.1. PROCESS AND INSTRUMENTATION DIAGRAM

A schematic of the core flooding setup is shown in Figure 3.5. One can see in this Figure that the pump can be filled with brine or oil. Subsequently, these fluids can be pumped through the core holder, in which the sandstone core resides. Over this core, the pressure difference and the potential difference are measured. There is also the possibility to inject CO<sub>2</sub> into the core holder, in order to remove any air inside the core. The core holder is placed inside an oven to be able to reach temperatures of 70 °C. The potential signal is amplified (as it is a very small signal, at high salinity in the range of several mV) and sent to the oscilloscope for visual monitoring. In the outflow line from the core, there is a back pressure regulator, that is connected to compressed air. From the back pressure regulator, the liquids produced flow into an outflow vessel.

### 3.2.2. SETUP COMPONENTS

#### CORE AND CORE HOLDER

In this thesis, we used several types of core holders to perform the streaming potential experiments. These types of coreholders are displayed in Figure 3.6, 3.7, 3.8 and 3.9. In all these core holders, there are an in- and outflow opening, two openings for the electrodes and two openings to connect to the pressure differential meter. All core holders are made from material that are electrically insulating, in other words the materials conduct charge very poorly, in order prevent a shortcut of the streaming potential signal. The choice for these types of core holders was purely based on their practical availability, the time frame of fabrication and the fact that the materials are electrically insulating.

The core holder as displayed in Figure 3.6, is fabricated from polyether ether ketone (PEEK), which is a colorless organic thermoplastic polymer. It has a tensile strength of around 90 – 100 MPa and is able to withstand temperatures over 100 °C. The sandstone cores are drilled with a diameter of 1 inch (2.54 cm) and a length of 11 cm and these sandstone cores are casted into the PEEK holder with Huntsman Araldite 2000+ 2014-1 epoxy resin. It is then hardened at a temperature of 80 °C. The PEEK core holder has a length of 10 cm and the distance between the pressure connectors and the electrodes is 6 cm. All connectors have an outer diameter of 3/8 inch (0.9525 cm). On the top and at the the bottom of the core holder two end caps are fitted to make sure the core is sealed and no flow occurs outside the flow lines. This core was fabricated at Shell in

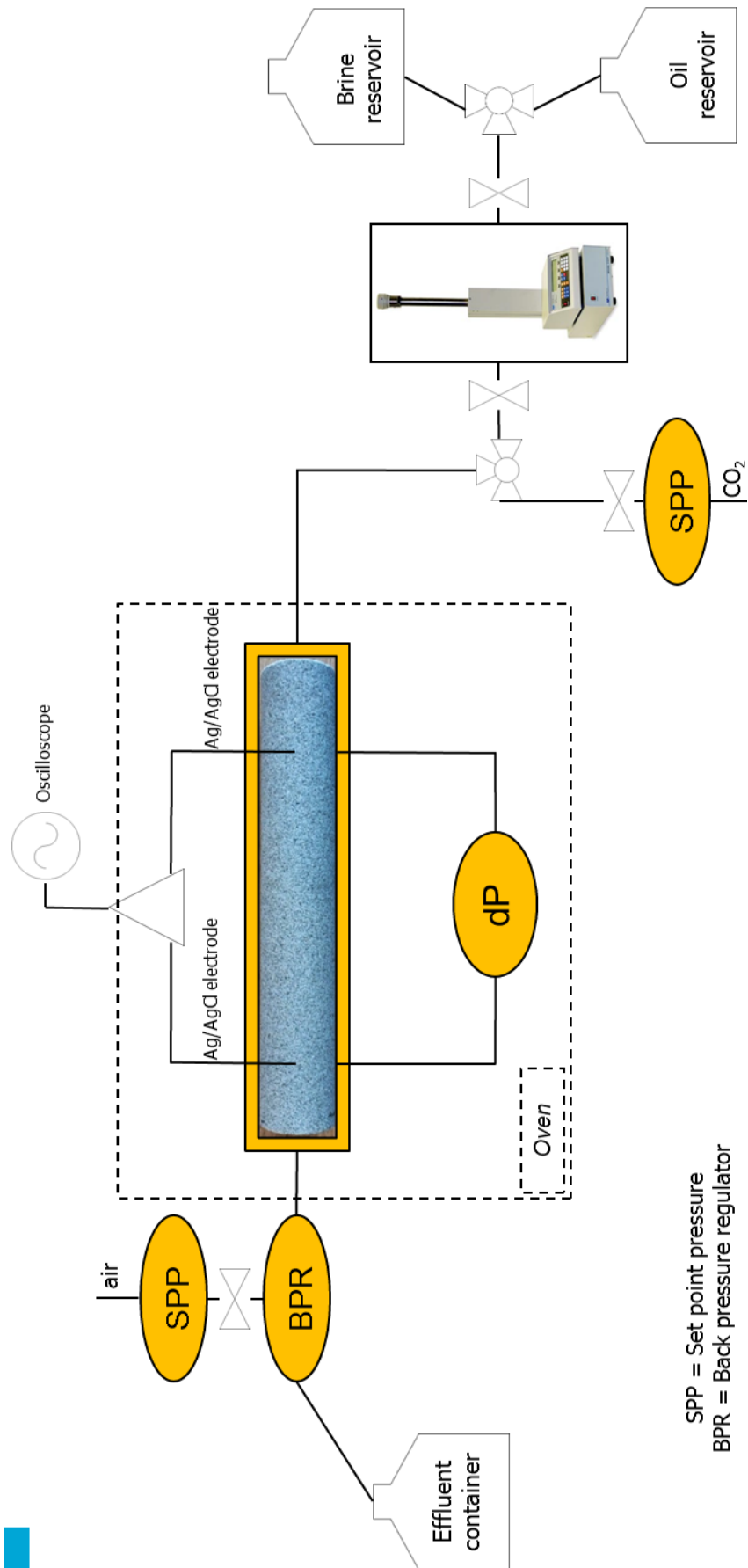


Figure 3.5: Process Instrumentation Diagram (PID) of the streaming potential experimental setup (SPP = Set Point Pressure, BPR = Back Pressure Regulator)

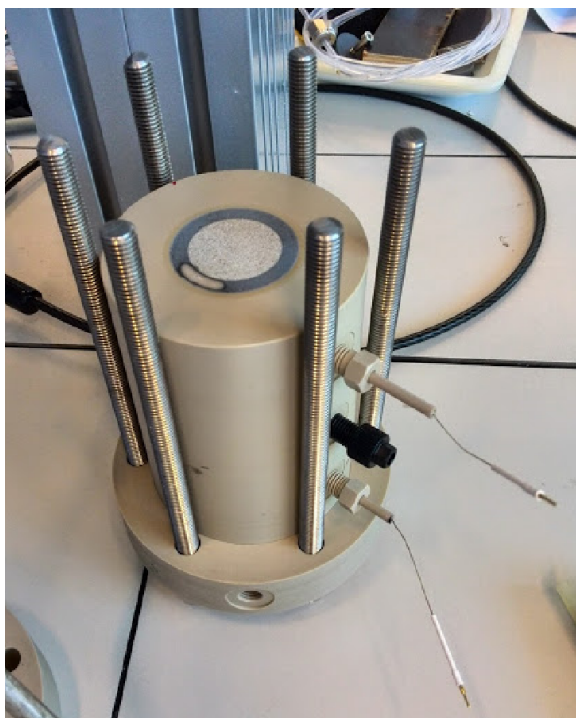


Figure 3.6: Berea 700 and 18 Core Holder



Figure 3.7: Berea 700 Core Holder

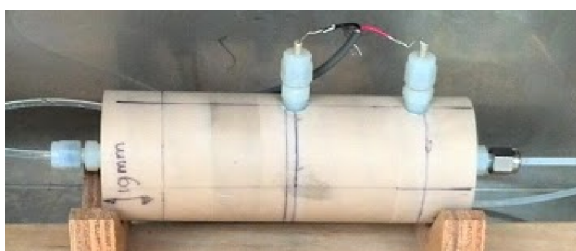


Figure 3.8: Bentheimer Core Holder

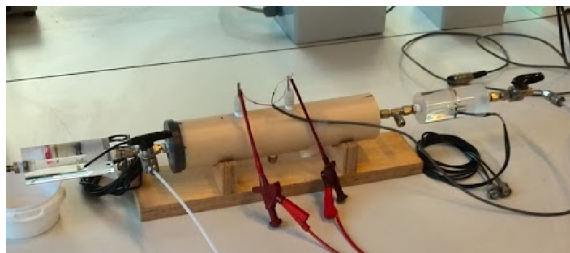


Figure 3.9: QF20 Core Holder

Rijswijk.

The core holder displayed in Figure 3.7, was fabricated in a different way. First, a foot is made to center the core on. A sleeve is placed over the sandstone core. Then, an outer PVC tube is placed over the foot and another piece of PVC was fitted on top of the core. The hollow space between the PVC tube and the core is filled with epoxy resin. A schematic cross-section of this core is displayed in Figure 3.7.

The core holder displayed in Figures 3.8 and 3.9 were fabricated in a similar fashion as the the core as displayed in Figure 3.10. These cores are all fabricated at Delft University. In the Bentheimer core holder the electrodes and pressure connectors were placed 5 cm from each other. Unlike in the PEEK core holder, here the pressure difference is measured over a different part of the core than the potential difference. In the QF20 core holder the electrodes are placed 6 cm apart. Here, the pressure drop is measured over a different piece of the core as well. The QF20 sample has a diameter of 2 cm and a length of 11 cm.

### ELECTRODES

The electrodes that are used in the experiments are sintered Silver/ Silver Chloride (Ag/AgCl) electrodes fabricated by *A-M Systems* (Catalog number: 541500). They have a diameter of 381 micron. The reference (standard) potential of the electrodes in demineralised water is around 220 mV at 25 °C. Ag/AgCl electrodes are preferred over platina and other materials as they are less sensitive to spurious potentials occurring and relatively affordable. The electrode is a silver (Ag) wire that is coated with a thin layer of silver chloride (AgCl). This is done by either physically dipping the wire in molten silver chloride, or chemically by electroplating the wire in concentrated hydrochloric acid. A porous plug on one end of the electrode allows contact be-

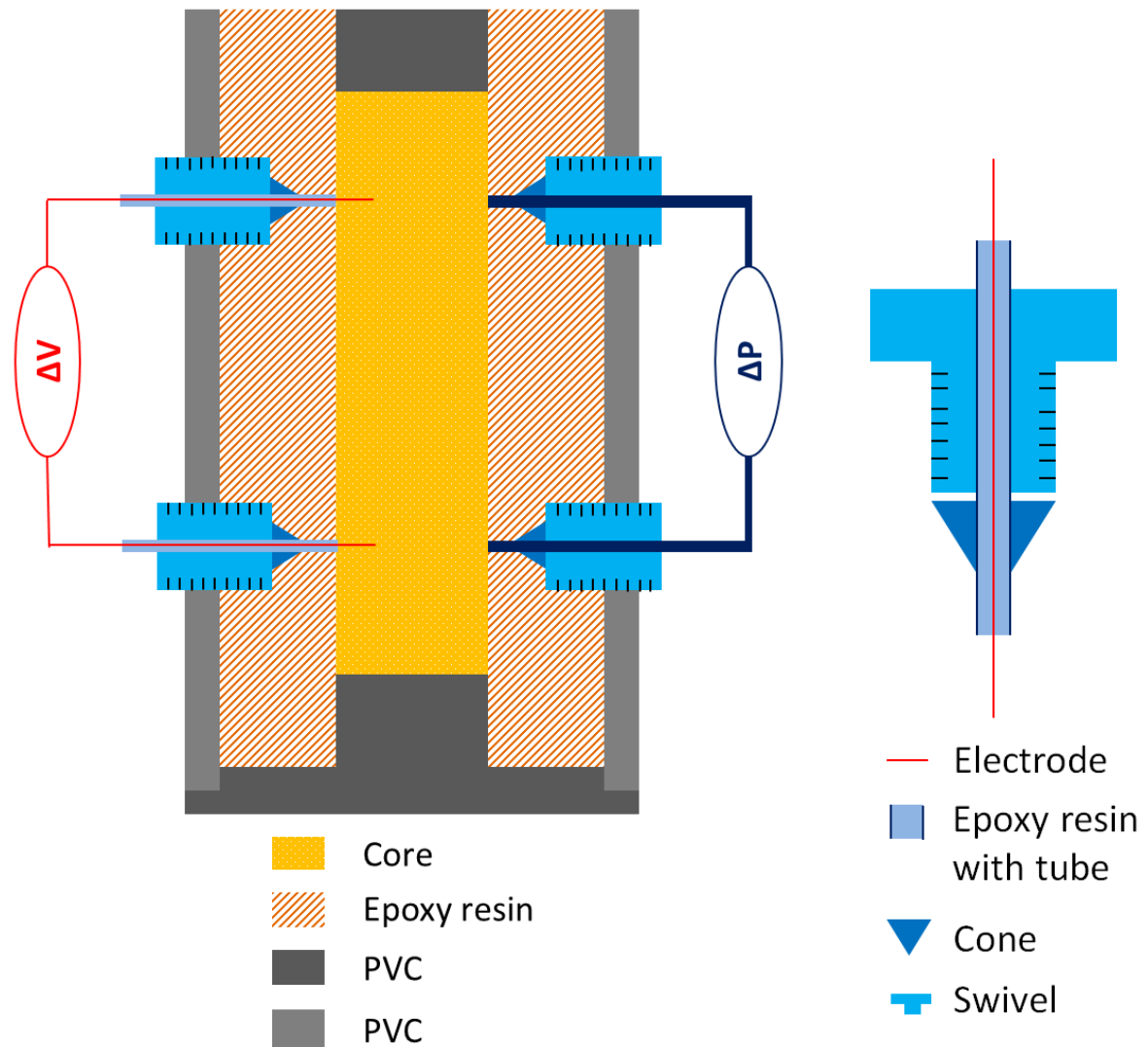


Figure 3.10: Cross-section of the core holder displayed in Figure 3.7

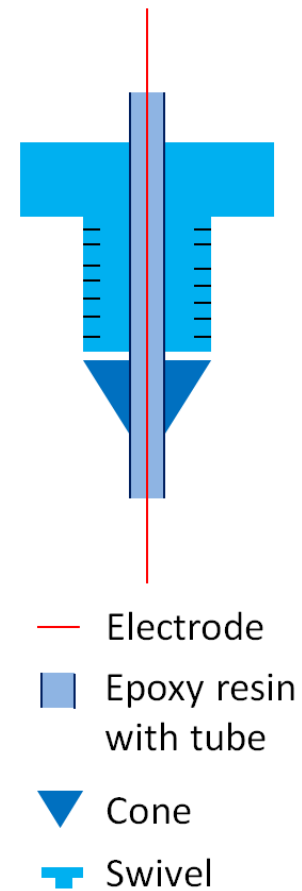


Figure 3.11: Cross-section of the electrode fitting method

tween the field environment with the silver chloride electrolyte. The lead wire to the measuring instruments is insulated.

In the core holder, at the place where the connectors for the electrodes are, holes are drilled into the core (sufficiently large to fit the electrodes/ roughly halfway into the core) and the electrodes are adapted to fit into the connectors. This process is illustrated in Figure 3.11.

The red wire is the electrode itself. This electrode is first casted with epoxy into a tube with the exact diameter that fits through the swivel (light blue). Then, a conical piece (dark blue) is fitted below that, so that the whole electrodes fits into the connectors in the core holder. Then the swivel is screwed tight, and the cone pushes against the conical surface of the core holder and against the tube holding the electrode. This prevents fluids from flowing out of the core holder. The two electrodes are connected to the amplifier by wires. The assumption is that the electrodes lie in an equipotential plane in the core holder.

#### PRESSURE DIFFERENTIAL METER

The pressure differential meters used in the streaming potential experiment are fabricated by *Endress+Hauser*. The meters range from -1000 to 1000 mbar and -3000 to 3000 mbar. Two flow lines from the the two connectors in the coreholders are attached to the pressure differential meter. These flow lines are filled with demineralised water with an as low as possible conductivity (around  $1 \mu\text{Siemens/cm}$ ). This is to prevent as much as possible conduction current in the upstream direction through the pressure differential meter. The

distance between the two connectors of the pressure differential meter is set equal to the distance between the electrodes. This distance differs per core holder.

#### PUMP AND PUMP HEATER

The pump used in the experiments is a *Teledyne ISCO* Syringe pump. The model is the 100 DM, which offers almost pulseless flow. It has a reservoir with 102.93 ml of volume. It can deliver pressures up to 10000 psi (69 MPa). One can choose for constant flow or constant pressure. The pump cylinder can take temperatures up to 200 °C. Around the pump cylinder, a heating element is placed, which has a water inflow and outflow port. The water is heated to the desired temperature by a *Lauda Master* heater. Water is circulated at high rates, such that the pump cylinder is always at the desired temperature and able to heat the fluids inside the pump quickly.

#### OVEN

The oven is fabricated by *Heraeus Instruments*. It has designated holes in it for flowlines going in and out of the oven. Furthermore, the temperature can be set to a specific temperature up until 150 °C.

#### OSCILLOSCOPE AND SIGNAL AMPLIFIER

The signal that is observed by the electrodes is amplified ten times by an amplifier. From this amplifier, the signal travels to the oscilloscope from which the signal is read visually. The oscilloscope is a *Yokogawa* DL9240L. It can be set to direct current (DC) input and both time and amplitudinal scales are adjustable. Also, the oscilloscope is able to filter out background noise. In the experiments the filter was set to filter out signals above 0.5 Hz. This leads to a far clearer signal as can be observed in Figure 3.12.

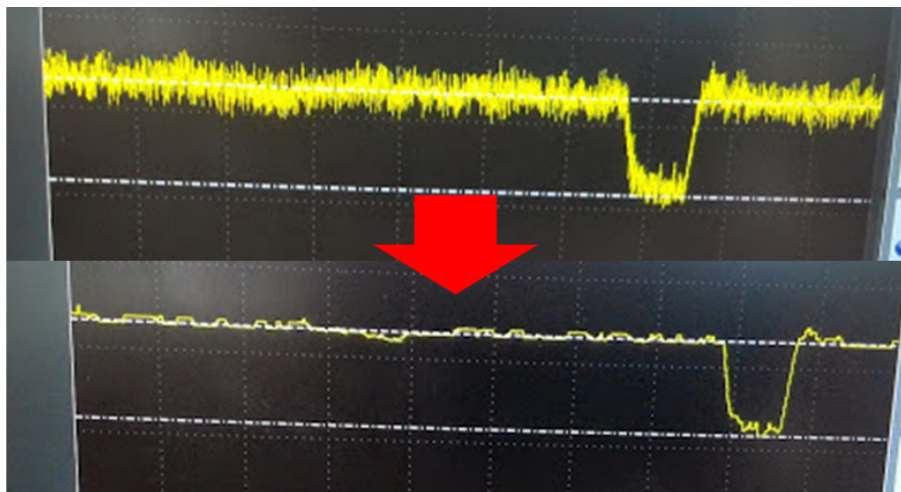


Figure 3.12: Effect of filtering on the signal as observed from the oscilloscope. Above: without filtering; below: with filtering

#### VALVES AND BACK PRESSURE REGULATOR

The valves that are used in the set up are all fabricated by *Swagelok*. Two-way and three-way valves are used to direct different flows in the right direction. The  $CO_2$  flowline and the air flowline to the back pressure regulator (BPR) are both regulated by a set point pressure (SPP) regulator. The BPR is located in the outflow line. The maximum back pressure that can be achieved in this setup is 5 bar.

#### CONDUCTIVITY AND pH METERS

To measure the conductivity of the fluids flowing in and out of the core, a hand held conductivity meter fabricated by *WTW* is used. The model is the *WTW* LF340. It measures conductivity in  $\mu\text{Siemens/cm}$  or  $\text{mSiemens/cm}$ . The principle behind the measurement is Ohm's law, where the surface of the electrodes and the distance of the electrode are input. The pH meter that is used to measure in- and outflow pH is the *WTW* 330i. The pH meter measures the potential difference between a glass electrode and an Ag/AgCl electrode. The glass electrode measures the amount of  $H^+$  ions in solution and the Ag/AgCl is the reference electrode.

### 3.2.3. EXPERIMENTAL PROTOCOL AND SEQUENCE

In Appendix B the experimental protocol and sequence for streaming potential measurements will be discussed.

### 3.3. EXPERIMENTAL SETUP (ELECTROPHORESIS: ZETASIZER)

For the electrophoresis zeta potential measurements, a commercial device by *Malvern* is used. The model is the Zetasizer Nano Z. It also has an MPT-2 autotitrator, which can automatically add acids and bases to measure the zeta potential curve against pH. The machine measures the electrophoretic mobility in aqueous and non-aqueous dispersions using Laser Doppler Micro-Electrophoresis. Figure 3.13 shows the device as placed in the Shell Laboratory in Rijswijk.

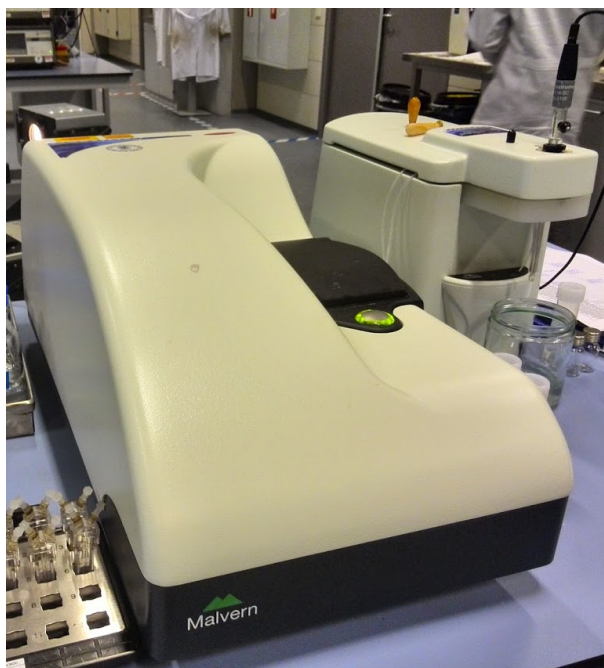


Figure 3.13: Zetasizer Nano Z (left) with MPT-2 autotitrator (right)

In Laser Doppler Micro-electrophoresis an electric field is applied to a solution of molecules or a dispersion of particles. The particles then move with a velocity, which is related to their zeta potential. The velocity is measured with a laser interferometric technique, which is called M3-PALS (Phase Analysis Light Scattering). Measuring this velocity, enables the calculation of the electrophoretic mobility, and from this, the zeta potential and the distribution of the zeta potential.

The device comes with software that displays the data quality and gives an expert advice on the measurement data. The solution to be measured is loaded into a disposable cell in the form of a cuvet. These cuvetts can be seen to the left of the Zetasizer Nano Z device in Figure 3.13.

#### 3.3.1. EXPERIMENTAL PROTOCOL AND SEQUENCE

In Appendix B the experimental protocol and sequence for zetasizer measurements will be discussed.

### 3.4. RECAP MATERIALS AND METHODS

In this section, a short recap will be given on the additions to previous work. First of all, a streaming potential setup has been established at Delft University. This setup can be used for follow-up experiments. The components of the setup and experimental protocols are described in detail. It is possible to do single-phase and two-phase experiments in the setup. Experiments with crude oil had not been done before. Detailed methods to obtain a low residual water saturation in the core for aging are also described. The fluid-rock combinations that are used in both the streaming potential and zetasizer experiments and the motivations behind these choices are described in detail. Protocols for the zetasizer experiments are also described; zetasizer experiments over a range of pH should not be performed automatically.

# 4

## MODELING

This chapter is about the modeling of electrokinetic phenomena in porous media. First, a small introduction on pore-scale modeling is given, whereafter the pore network extraction methods will be discussed. Then we move on to the different modeling methods used in this thesis. This ranges from a basic Gouy-Chapman model, representing the screening of charge on a flat surface, to streaming potential relations in several different geometries applied in capillary tube, bundle of tubes and pore-network models. Input of these models is based on micro-CT data, which was acquired for different types of sandstones. This micro-CT data is processed and a data on the pore-network are extracted. The goal of the modeling is to get a better understanding of the experimental observations, both for the single-phase and the two-phase measurements.

### 4.1. PORE-SCALE MODELING

To model phenomena in porous media, one can use models on the continuum scale (based on Darcy's law), models involving capillaries or bundles of capillaries and pore-network models. In capillary models and, even more so, in pore-network models the physics at the pore scale can be included. Pore-network models have been widely used to describe properties such as capillary pressures, interfacial tensions and mass transfer coefficients. The pore space of the rock is described by a network of connected pore bodies and pore throats, as can be seen in Figure 4.1. These pore bodies and pore throats get an assigned idealized model geometry (some examples of these geometries are displayed in Figure 4.2). Furthermore, rules are developed to determine the single- or multiphase flow fluid configurations and transport in the model elements. Several pores are combined in a network to find out what the micro-scale assigned configurations do to the meso-scale properties. A network of pore elements has an average coordination number,  $z$ , which is the average number of elements that meet at a node. For a sandstone this value lies between 3 –6. If the appropriate pore-scale physics are combined with a geologically representative description of the pore space, this gives a model that can enable the parametric understanding (sensitivity analysis) of average behavior, such as capillary pressures, relative permeabilities or electrokinetic effects. Pore-scale modeling can be used to better understand waterflood behavior of a field and the pore-scale results could be incorporated into the sensitivity analysis field-scale simulations [Blunt et al., 2002].

When looking at possibilities of modeling electrokinetic effects at the pore scale, one can make bundle-of-tubes and pore network models, which can model the incremental oil recovery by calculating the trapped oil and the changing wettability state of the model. A dynamic two-phase flow network model exists and this can be coupled with the transport of ions and geochemical processes [Joekar-Niasar et al., 2012]. In this thesis, we will take the first steps in this field. These first steps are the modeling of single-phase streaming potential in a capillary tube, a bundle-of-tubes and a pore-network model. Furthermore, we will look at a simple model to get a better understanding for the two-phase streaming potential responses.

### 4.2. MODELING SCOPE OF THIS THESIS

In this thesis, we model single-phase electrokinetic phenomena for several lithologies and several geometries (triangle and cylinder). This is done using capillary tube model, which is an input to the bundle-of-tubes and pore-network models. The relations used for the capillary tubes of different geometries are taken from literature. The single-phase modeling is done at 20 °C and 70 °C. We also model two-phase electrokinetic

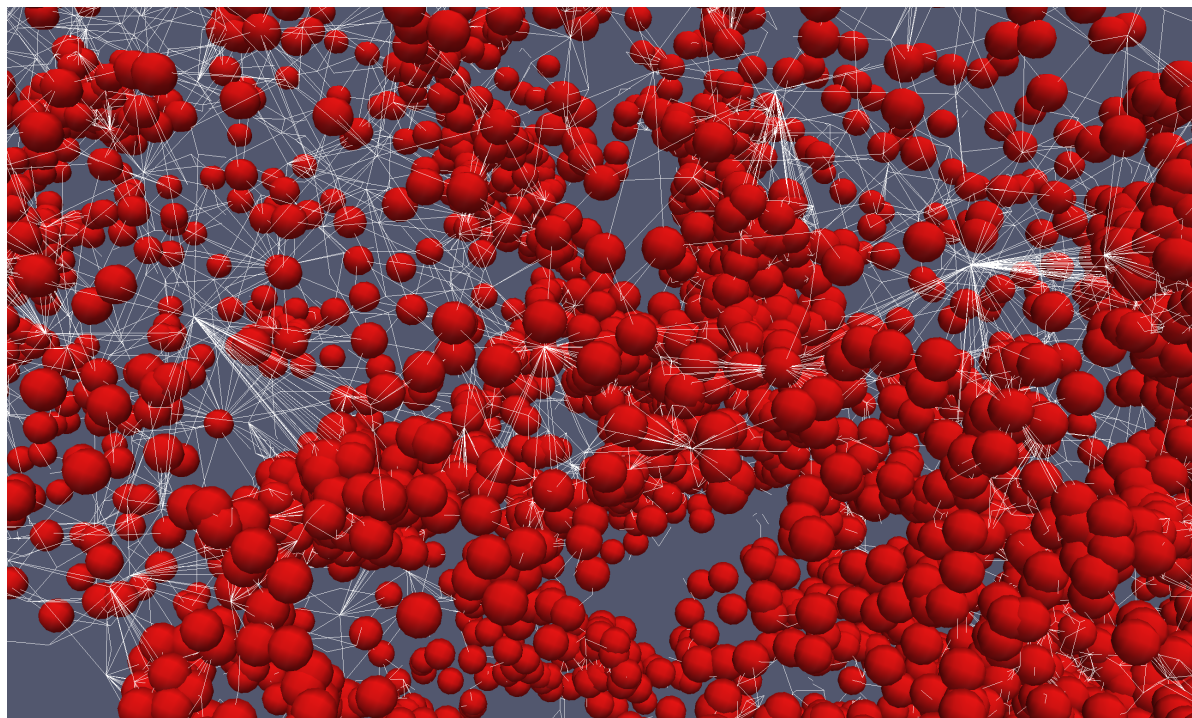


Figure 4.1: Example of a pore-network model. Pore bodies are symbolized as red spheres and pores throats as white lines. Pore bodies and pore throats all have different radii

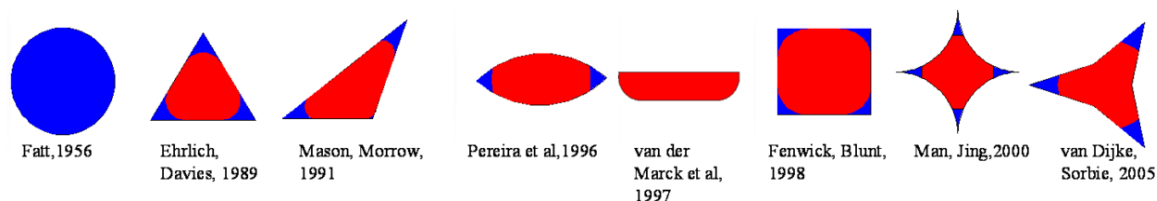


Figure 4.2: Different geometries used to describe pore throats in a pore-network model [Joekar-Niasar, 2010]

phenomena with a simplified model, in which different values for the water saturation change the size of the capillary tubes in the model. This is done for an oil-wet and a water-wet case. The two-phase modeling is done at 20 and 70 °C, depending at what temperature the experiments in the lab were done.

Figure 4.3 shows an oversight of all the modeling performed. Both Bundle-of-Tubes (BOT) and Pore-network Modeling (PNM) will be applied to all single-phase cases. For the two-phase modeling, we only use BOT models. Also, for Berea 700 in the two-phase case, both oil-wet and water-wet models are used, as the Berea 700 is known to be able to age. For the Bentheimer and two-phase, we only use a water-wet model, as it is not known to be able to age and we did not use crude oil in this sample, only hexadecane.

### 4.3. PORE NETWORK EXTRACTION

To generate input for all the different models, the raw data obtained out of the micro-CT scan is processed in AVIZO, whereafter a pore network extraction code extracts a network of pores and throats out of this data. This procedure is described in detail in Appendix C.

### 4.4. CAPILLARY TUBE MODEL

The first and simplest model is the capillary tube model. This models a porous medium as if it were one capillary tube with a certain radius. Over that tube a certain coupling coefficient is calculated, depending on the molarity of the fluid and the radius of the tube. This relation is independent of the length of the capillary, because the length is represented in the pressure drop over the capillary. This pressure drop is present in the

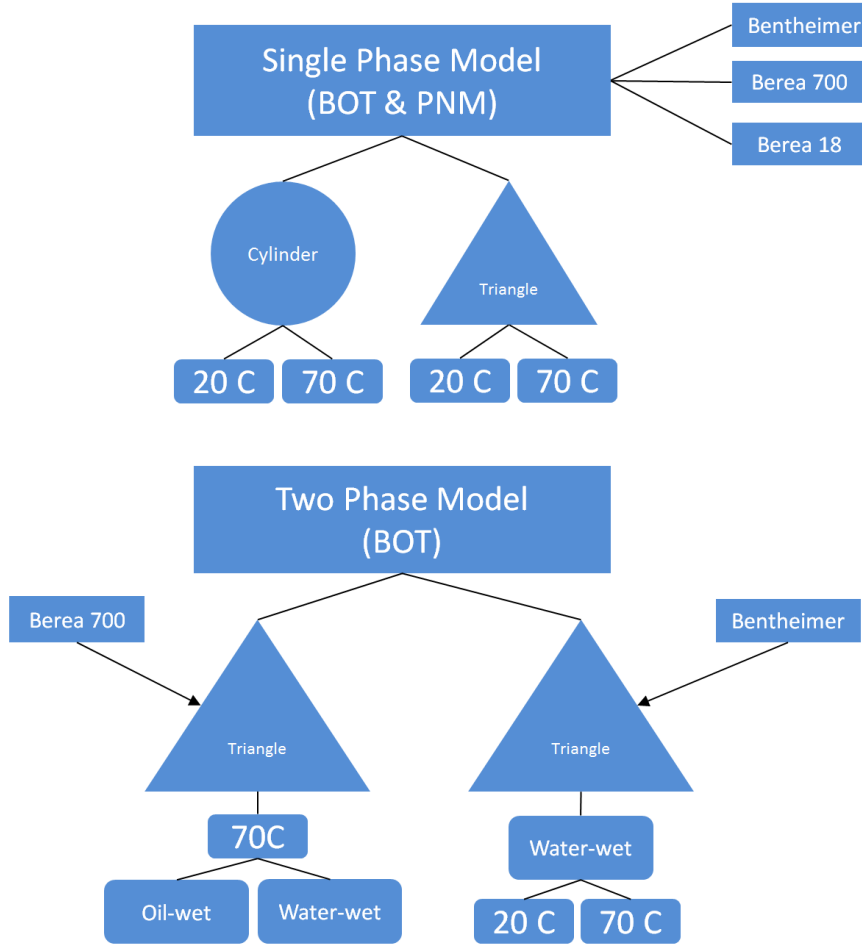


Figure 4.3: Oversight of all the modeling activities in this thesis

coupling coefficient (V/Pa).

The relation used for the calculation of the coupling coefficient of a cylindrical capillary tube is given in Subsection 2.5.5.3. It is good to bear in mind that the relation for the coupling coefficient comes forth by dividing the  $L_{21}$  term by  $L_{22}$ , as given in Equation 2.53.

This gives the relation for a cylindrical geometry as given in Equation 2.38:

$$C_s = -\frac{L_{21}}{L_{22}} = \frac{\Delta V}{\Delta P} = \frac{\Omega}{\lambda_0} \left(1 - \frac{2A_1}{\kappa r}\right) f(\kappa r, \beta, F_{cc}) \quad (4.1)$$

For a triangular geometry, one should use the relations as given in Equations 2.54 and 2.55. The former for thin double layers and the latter for thick double layers. Here too, the coupling coefficient comes forth by dividing the  $L_{21}$  term by  $L_{22}$  term, as is shown in Equation 4.2 for thin double layers and in Equation 4.3 for thick double layers.

$$C_s = -\frac{L_{21}}{L_{22}} = \frac{\Omega}{\lambda_0} \quad (4.2)$$

$$C_s = -\frac{L_{21}}{L_{22}} = \frac{\Omega \frac{\sinh(\frac{ze\zeta}{k_B T_K})}{\frac{ze\zeta}{k_B T_K}} \frac{A^2 \kappa^2}{\alpha l}}{\left[ \cosh\left(\frac{ze\zeta}{k_B T_K}\right) + \frac{e\zeta^2}{\eta D} \frac{\sinh^2\left(\frac{ze\zeta}{k_B T_K}\right)}{\left(\frac{ze\zeta}{k_B T_K}\right)^2} \frac{A\kappa^2}{\alpha} \right] \frac{A\lambda_0}{l}} \quad (4.3)$$

The capillary tube model lies at the basis of the bundle of tubes (BOT) and the pore-network model (PNM). It is the input for the elements of both these models. In the bundle of tubes it is the input for the separate tubes which are parallel to each other. In the PNM it is the relation applied to the throats that connect the pores in the model to each other.

#### 4.4.1. STERN LAYER CONDUCTION

Here, we describe a way to include Stern layer conduction in the equations for streaming potential. The Stern layer conduction ( $\Sigma_S^{Stern}$ ) contributes to the conduction of current upstream, and can therefore be added to the  $L_{22}$  term in the several matrix equations, namely Equations 2.53 and 2.55. In these equations, the overlapping of the double layers is included, but the Stern layer conduction is not. The term that can be added to the  $L_{22}$  term is as follows:

$$\boxed{\frac{2\Sigma_S^{Stern}}{rl}} \quad (4.4)$$

where  $\Sigma_S^{Stern}$  is the Stern layer conduction (Siemens),  $r$  is the capillary radius (m) and  $l$  is the channel length (m). The capillary radius and length are already input to the Equation 2.53 and 2.55. The Stern layer conduction term can be used as a fitting parameter to fit laboratory data to the model. The assumption here is that the difference between these two sets of data, is caused by the Stern layer conduction.

#### 4.4.2. MODELING GEOMETRIES

The three geometries that will be used in modeling are cylinders, triangles and hexagons. For single phase modeling, only cylinders and triangles are used. For two-phase modeling triangles and hexagons are used. The hexagonal shape is only used in two-phase oil-wet models, as in those models the water flows through a hexagonal shape in the simplified model. This can be seen in the bottom right figure of Figure 4.4, which also shows an oversight of the different cases. The top row shows the two single-phase geometries. One cylinder, where the radius is that from the pore network extraction and one triangle, where the inscribed radius is taken from the pore-network extraction to calculate the side length of the triangle. The middle row shows real scenario of a water-wet and an oil-wet case for two phases. Here the interfaces between the oil and water are curved.

In the two-phase model in this thesis, the corner films are represented by triangles, as shown in the bottom row, and the water or oil is assumed to be around residual saturation. This is analogous to the experiments, where oil is brought back to residual saturation, when streaming potential measurements are done. The streaming potential is measured through the water phase, this is done so as well in the models.

For a triangle, the side length  $a$  can be calculated from the inscribed radius (from pore-network extraction) as follows:

$$\boxed{a = r_{inscribed} \frac{6}{\sqrt{3}}} \quad (4.5)$$

where  $a$  is the equilateral triangle side length (m) and  $r$  is the inscribed radius (m). The perimeter (circumference) of the triangle can be calculated as follows:

$$\boxed{p = 3a} \quad (4.6)$$

where  $p$  is the perimeter (m). The area of the triangle can be calculated as follows:

$$\boxed{A = \frac{\sqrt{3}}{4} a^2} \quad (4.7)$$

where  $A$  is the area of the triangle ( $m^2$ ). For a cylinder, the perimeter can be calculated as follows:

$$p = 2\pi r_{inscribed} \quad (4.8)$$

The area of the cylinder can be calculated as follows:

$$A = \pi r_{inscribed}^2 \quad (4.9)$$

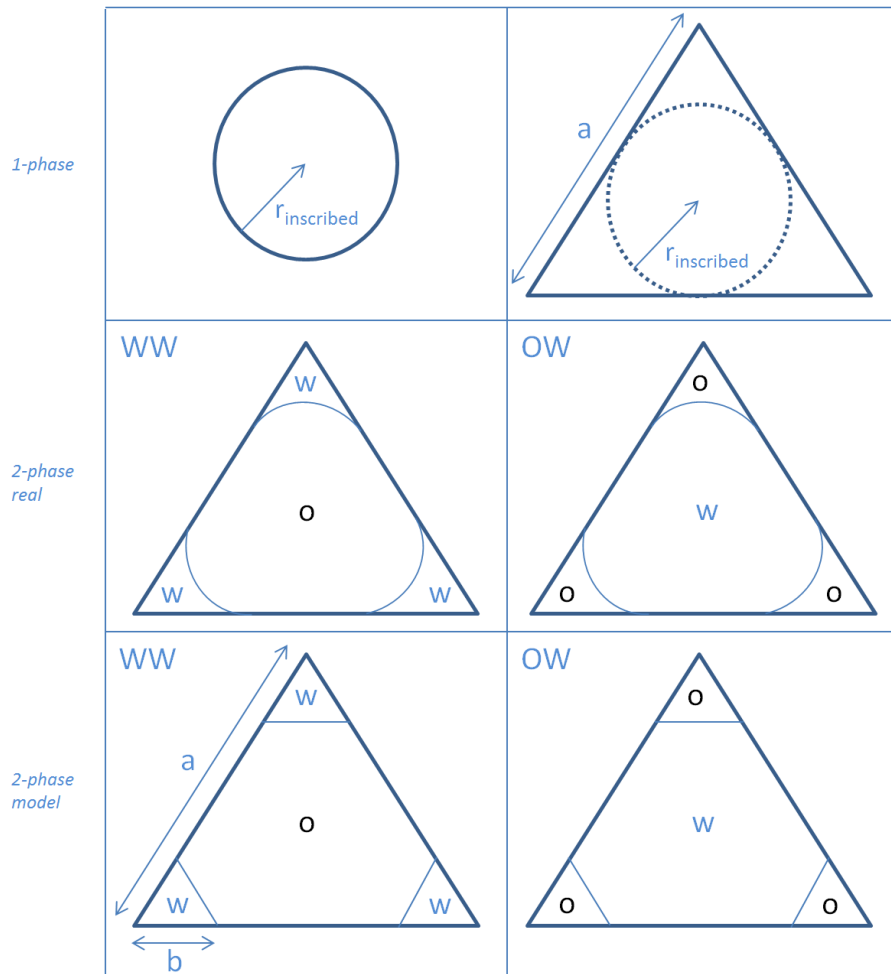


Figure 4.4: Different geometries used in modeling. Top row: single phase cylindrical and triangular model. Middle row: triangular two-phase real case models for an WW and OW system. Bottom row: triangular two-phase model situation for an WW and OW system

#### WATER-WET CONFIGURATION

The water-wet configuration is shown in the bottom left image of Figure 4.4. The side length  $a$  of this triangle is given by Equation 4.5. The area of this triangle is given by Equation 4.7 and the perimeter by Equation 4.6. It is now important to determine how large  $b$  is, and whether capillary pressure is high enough to penetrate a triangular element with a certain side length  $a$ .

The capillary pressure is the pressure difference between the pressure in the oil phase and the pressure in the water phase:

$$P_c = P_o - P_w \quad (4.10)$$

where  $P_c$  is the capillary pressure (Pa), the  $P_o$  is the pressure in the oil phase (Pa) and  $P_w$  is the pressure in the water phase (Pa). The geometry remains constant in the pore throat direction and this is when the capillary pressure can also be expressed with the Young-Laplace equation:

$$P_c = \frac{\sigma_{nw}}{r_c} \quad (4.11)$$

where  $\sigma_{nw}$  is the fluid-fluid interfacial tension (N/m) and  $r_c$  is the radius of curvature in the cross-sectional direction (m). If the capillary pressure and the interfacial tension are known, this equation can be used to determine the radius of curvature.

To determine whether a pore throat can be entered by oil (the non-wetting phase, we presume that all pores are filled with water at first), one needs to compare the radius of curvature ( $r_c$ ) with the entry radius

of curvature ( $r_{c,entry}$ ). If the entry radius of curvature is larger than the radius of curvature (this is when the entry capillary pressure is smaller than the capillary pressure), oil is able to enter the pore element:

$$r_{c,entry} > r_c \quad (4.12)$$

The entry radius of curvature can be calculated as follows [Hogenkamp, 2014]:

$$r_{c,entry} = a \left( \frac{\frac{2\pi}{3} - 2\theta_R - 4 \cos(\frac{\pi}{6} + \theta_R) \cos \theta_R}{\sqrt{\cos^2 \theta_R + \frac{\sqrt{12}}{3} (\frac{\pi}{3} - \theta_R - 2 \cos(\frac{\pi}{6} + \theta_R) \cos \theta_R) - \cos \theta_R}} \right)^{-1} \quad (4.13)$$

where  $a$  is the triangle side length,  $\theta_R$  is the receding contact angle (rad). As is shown in Figure 4.4 the water phase occupies the corner space in a water-wet situation. When capillary pressure is high, the corner films become small, as a lot of oil is allowed into the pore throat. If capillary pressure falls, the corner films become larger and the water saturation increases.

From the corner half angle ( $\beta$ ) and the contact angle ( $\theta$ ) one can calculate the position of the oil-water interface  $b$  in the corner [Valvatne and Blunt, 2003]:

$$b = r_c \frac{\cos(\beta + \theta)}{\sin \beta} \quad (4.14)$$

where  $b$  is the side length of the corner fill (m) and  $\beta$  is the corner half angle (rad). When this formula is applied to an equilateral triangle ( $\beta = 30^\circ$ ) under the assumption that the contact angle is zero for a fully water-wet situation ( $\theta = 0^\circ$ ), this relation simplifies to:

$$b = r_c \cot(\beta) \quad (4.15)$$

Taking the fully water-wet situation ( $\theta = 0^\circ$ ) also simplifies the expression for the entry radius of curvature:

$$r_{c,entry} = a \left( \frac{\frac{2\pi}{3} - 2\sqrt{3}}{1 + \frac{\sqrt{12}}{3} (\frac{\pi}{3} - \sqrt{3}) - 1} \right)^{-1} \quad (4.16)$$

In our model  $b$  is the side length of the triangle in the corner as shown in Figure 4.4. The corner geometry is simplified to a triangle in order to be able to use the electrokinetic equations designed for triangular channels.

So, if the expression  $r_{c,entry} > r_c$  holds, the pores can be filled with oil and the value of  $b$  for the side length of the triangle can be calculated with Equation 4.15. If the expression does not hold, the pore remains fully water-filled and the side length of the full triangle is still  $a$ .

The water saturation of a pore throat not invaded by oil is of course  $S_w = 1$ . For a pore throat where oil was able to invade, the water saturation can be calculated as follows:

$$S_w = \frac{3 \frac{\sqrt{3}}{4} b^2}{\frac{\sqrt{3}}{4} a^2} = \frac{3b^2}{a^2} \quad (4.17)$$

The three in the numerator exists, because there are three corner films in an equilateral triangle. The maximum reachable water saturation of this capillary tube model is 0.75 ( $S_w = 0.75$ ), because otherwise the corner films start to overlap at higher water saturations.

The oil saturation can of course be calculated as:

$$S_o = 1 - S_w \quad (4.18)$$

The zeta potential is averaged, as there are two sides of the water filled triangle in contact with the rock and one side in contact with the crude oil. The averaging procedure is simple and is done as follows:

$$\zeta_{average} = \frac{2\zeta_r + \zeta_o}{3} \quad (4.19)$$

where  $\zeta_o$  is the zeta potential of oil in water (V) and  $\zeta_r$  is the zeta potential of rock in water (V).

#### OIL-WET CONFIGURATION

The oil-wet configuration is shown in the bottom right image of Figure 4.4. The side length  $a$  of this triangle is given by Equation 4.5. The area of this triangle is given by Equation 4.7 and the perimeter by Equation 4.6.

It is now important to determine how large  $b$  is; this can be done in exactly the same way as in the water-wet case. Now though, the triangles in the corner are filled with oil, as oil is the wetting phase. We assume in the fully oil-wet case that the triangle starts off as being fully oil filled. When capillary pressure increases, water is able to invade the pores and the oil corner films become smaller.

In the water-wet model, water always flows through triangular elements. As you can see in Figure 4.4, this is not the case in the oil-wet model. In the oil-wet model, water flows through a geometry of hexagonal shape.

For simplicity, it is assumed that we are dealing with a hexagonal geometry with equal side lengths. When water saturation varies, the size of the oil in corners varies. This leads to unequal side length of the hexagon, but we average this out in the following way:

$$t = \frac{a - 2b + b}{2} = \frac{a - b}{2} \quad (4.20)$$

where  $t$  is the hexagonal side length (m). The perimeter of the hexagon is then given by:

$$p = 6t \quad (4.21)$$

and the area of the hexagon can be described as follows:

$$A = \frac{3\sqrt{3}}{t^2} \quad (4.22)$$

The zeta potential is also averaged, but in a different manner than in the water-wet case. The zeta potential is averaged in the following manner:

$$\zeta_{average} = \frac{b\zeta_o + (a - 2b)\zeta_r}{b + a - 2b} = \frac{b\zeta_o + (a - 2b)\zeta_r}{a - b} \quad (4.23)$$

The water saturation can be calculated by dividing the area of the water-filled hexagon over the area of the full triangle:

$$S_w = \frac{\frac{3\sqrt{3}}{t^2}}{\frac{\sqrt{3}}{4}a^2} = \frac{12}{t^2 a^2} \quad (4.24)$$

and the oil saturation can then be calculated as:

$$S_o = 1 - S_w \quad (4.25)$$

To make sure that the model does not become completely unphysical there are certain limits to the value of  $b$  and  $t$ . These should be limited to prevent water saturation to become larger than 1, as the geometry of the hexagon differs from the triangle. So if:  $b > 0.5a \rightarrow b = 0.5a$  and if  $t > \frac{1}{3}a \rightarrow t = \frac{1}{3}a$ .

If no water has been able to flow into a pore throat element, then the response in terms of a coupling coefficient over that pore element will be zero.

#### MIXED-WET CONFIGURATION

Although we do not use a mixed-wet model to describe streaming potentials, it is good to realize how such a situation in a triangular geometry may look like. This is because no real (reservoir) situation is completely water-wet, nor oil-wet. The real situation and the model situation are showed in Figure 4.5. The filling procedure of this pore throat element is as follows. First, the element is filled completely with water, making it water-wet. Then oil migrates in, and changes the wettability of the element. It cannot remove all the water however, as the water remains in the corners. You can see that the curvature around the water in the corners is different, when you compare it to the middle left image in Figure 4.4. Then when waterflooding is applied to produce the oil out of the element, one can see that there remains a film of oil in between the the water filled areas. The right image in Figure 4.5 then shows how this would look like in a model situation, with simplified geometries. This model was not used in this thesis, but is shown merely as a context to the fully water-wet and fully oil-wet situations.

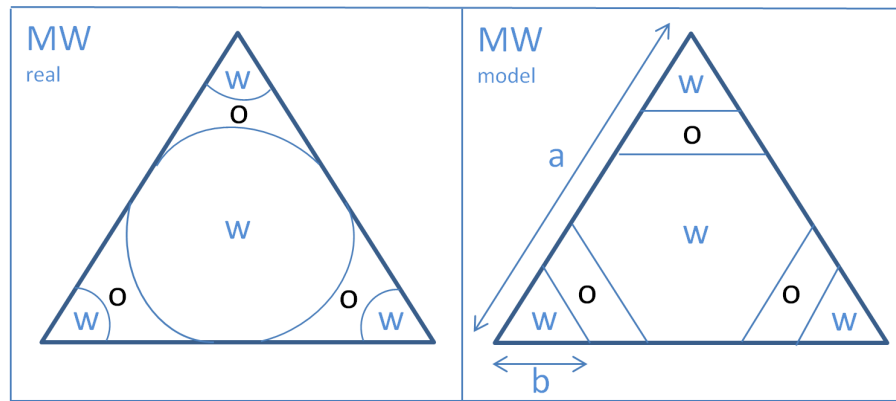


Figure 4.5: Real and model situation for a mixed-wet triangle

#### 4.4.3. FLOW CHART MODELING

Figure 4.6 shows a flow chart for the modeling, in which schematically is shown what types of input go into the capillary tube model, the bundle-of-tubes model and the pore-network model. First inputs are the ionic strength, physical constants (such as  $k_B$ ,  $\epsilon$ ,  $z$ ,  $e$ ,  $D$  (solute diffusion coefficient), molar weights and  $N_A$ ), the percentage of divalents and the temperature. From this, the fluid conductivity ( $\lambda_0$ ; Equation 2.40), the fluid density ( $\rho_w$ ; [McCain, 1991]), the fluid viscosity ( $\eta_w$ ; [McCain, 1991]), the number of ions in the bulk solution ( $n_\infty$ ; Equation 2.12) and inverse Debye length ( $\kappa$ ; Equation 2.5) are calculated.

Then you decide the amount of phases used, and the capillary pressure in the case of two phases. Based on the number of phases, one chooses the geometry as explained in the previous section. For single-phase, one can take both cylindrical or triangular. For two-phase, one can use triangular or hexagonal based on the configuration. For the triangular and hexagonal geometry,  $\alpha$  and the area  $A$  are also input. Also, the interfacial tension between the two liquid phases is an input in the two-phase model. To complete the input for the capillary tube model, one also needs the radius of the pore throat and the zeta potential data from electrophoretic experiments. Again, based on the configuration a certain averaging procedure can be applied.

If all the input is present, the input is presented into Equations 4.1, 4.2 or 4.3 based on the geometry and whether the double layers are thick or thin.

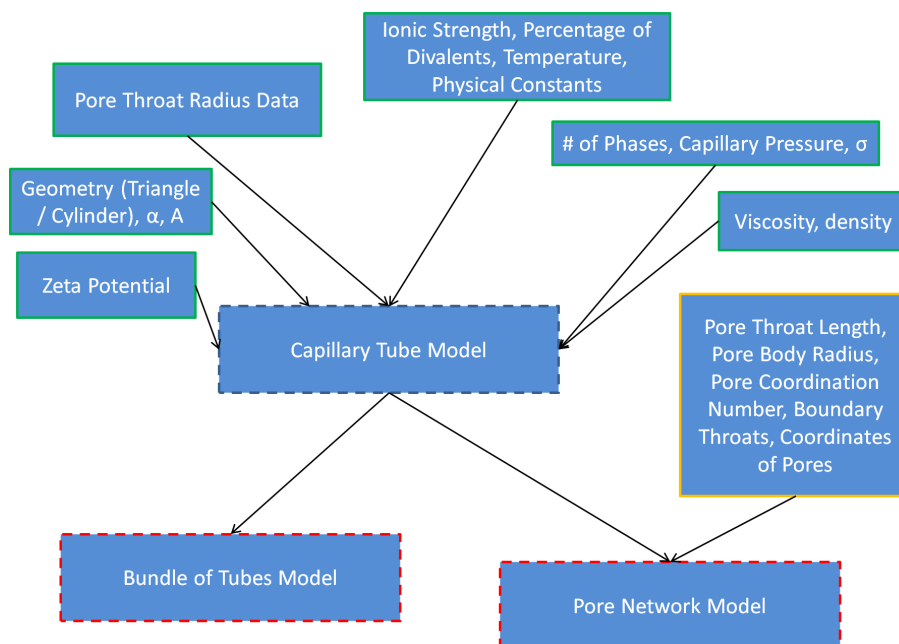


Figure 4.6: Flow chart for the modeling. Inputs for the capillary tube model, bundle-of-tubes model and pore-network model are shown

Then, several capillary tubes with different radii, can be combined into a bundle-of-tubes model (BOT). Or, they can be combined into a pore-network model. For that, several other inputs from the pore-network extraction are needed as indicated in the orange box in Figure 4.6 in order to get the full information on the pore-network.

#### 4.5. BUNDLE OF TUBES MODEL

A bundle-of-tubes model is one of the simplest ways to represent a porous medium. In a bundle-of-tubes model the porous medium is represented by several straight parallel channel with different radii. Over the tubes, there is one value for the pressure drop ( $\Delta P$ ) and one value for the potential drop ( $\Delta V$ ) across the bundle of tubes. A schematic of such a model can be seen in Figure 4.7.

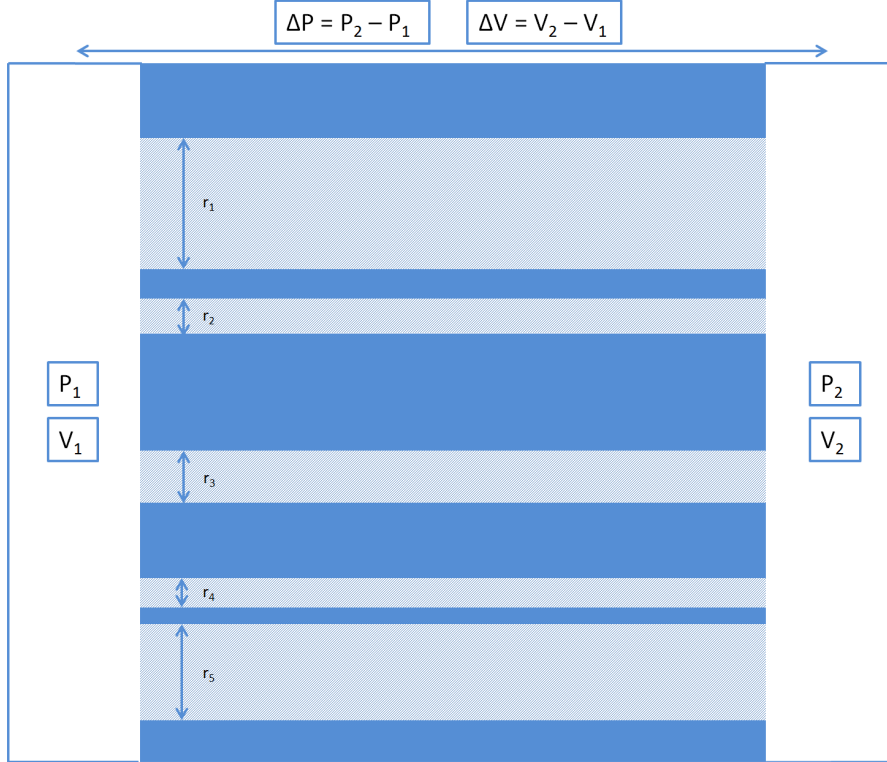


Figure 4.7: Schematic of the bundle-of-tubes model (BOT)

In this Figure, there are five different channels, all with their own assigned radius. The pressure and potential drop over all these tubes are equal, since this is physically obliged. All channels have a flow rate  $Q$  through them, which is determined by the Poiseuille flow equation for a cylindrical channel and by similar equations for different shapes of the channels.

Then, it is possible to calculate the coupling coefficient over the whole system. To do this, all the summated  $L_{21}$  terms are divided by all the summated  $L_{22}$  terms for the  $n$  channels:

$$C_{s,bundle} = - \frac{\sum_{i=1}^n L_{21}^i}{\sum_{i=1}^n L_{22}^i} \quad (4.26)$$

where  $C_{s,bundle}$  is the coupling coefficient (V/Pa) over the whole bundle, and  $L_{21}^i$  and  $L_{22}^i$  are the streaming and conduction current terms respectively for a certain channel  $i$ .

#### 4.6. PORE NETWORK MODEL

A pore-network model is a more realistic way of describing a porous medium. In a pore-network model, the porous medium is represented by pore elements as spheres, and pore throat elements with either a cylindri-

cal, triangular or hexagonal shape. In this section, a schematic of a PNM is described and also the equations for this small example. The example of a PNM is shown in Figure 4.8.

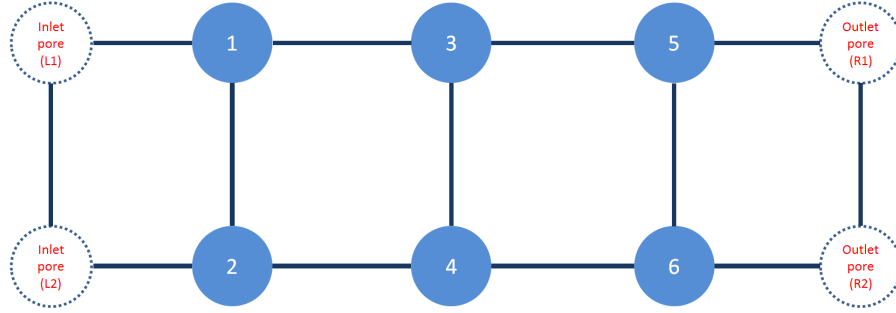


Figure 4.8: Schematic of the pore-network model with 6 pores (PNM)

One can set up a set of two equations for each node, in order to describe the electrokinetic coupled transport around that node. We will now describe this for the six nodes in the example pore-network. The first equation per node will be:  $Q = \sum_{ij} (L_{11}^{ij} \Delta P^{ij} + L_{12}^{ij} \Delta \psi^{ij}) = 0$ . The second equation per node will be  $J = \sum_{ij} (L_{21}^{ij} \Delta P^{ij} + L_{22}^{ij} \Delta \psi^{ij}) = 0$ . The superscript  $ij$  stands for the pore throat connecting pore  $i$  with pore  $j$ . Later on these equations will form a matrix system. First, we show the equations for the six nodes.

For node 1:

$$Q = L_{11}^{1L1} (P_1 - P_{L1}) + L_{11}^{12} (P_1 - P_2) + L_{11}^{13} (P_1 - P_3) + L_{12}^{1L1} (\psi_1 - \psi_{L1}) + L_{12}^{12} (\psi_1 - \psi_2) + L_{12}^{13} (\psi_1 - \psi_3) = 0 \quad (4.27)$$

$$J = L_{21}^{1L1} (P_1 - P_{L1}) + L_{21}^{12} (P_1 - P_2) + L_{21}^{13} (P_1 - P_3) + L_{22}^{1L1} (\psi_1 - \psi_{L1}) + L_{22}^{12} (\psi_1 - \psi_2) + L_{22}^{13} (\psi_1 - \psi_3) = 0 \quad (4.28)$$

For node 2:

$$Q = L_{11}^{2L2} (P_2 - P_{L2}) + L_{11}^{21} (P_2 - P_1) + L_{11}^{24} (P_2 - P_4) + L_{12}^{2L2} (\psi_2 - \psi_{L2}) + L_{12}^{21} (\psi_2 - \psi_1) + L_{12}^{24} (\psi_2 - \psi_4) = 0 \quad (4.29)$$

$$J = L_{21}^{2L2} (P_2 - P_{L2}) + L_{21}^{21} (P_2 - P_1) + L_{21}^{24} (P_2 - P_4) + L_{22}^{2L2} (\psi_2 - \psi_{L2}) + L_{22}^{21} (\psi_2 - \psi_1) + L_{22}^{24} (\psi_2 - \psi_4) = 0 \quad (4.30)$$

For node 3:

$$Q = L_{11}^{31} (P_3 - P_1) + L_{11}^{34} (P_3 - P_4) + L_{11}^{35} (P_3 - P_5) + L_{12}^{31} (\psi_3 - \psi_1) + L_{12}^{34} (\psi_3 - \psi_4) + L_{12}^{35} (\psi_3 - \psi_5) = 0 \quad (4.31)$$

$$J = L_{21}^{31} (P_3 - P_1) + L_{21}^{34} (P_3 - P_4) + L_{21}^{35} (P_3 - P_5) + L_{22}^{31} (\psi_3 - \psi_1) + L_{22}^{34} (\psi_3 - \psi_4) + L_{22}^{35} (\psi_3 - \psi_5) = 0 \quad (4.32)$$

For node 4:

$$Q = L_{11}^{42} (P_4 - P_2) + L_{11}^{43} (P_4 - P_3) + L_{11}^{46} (P_4 - P_6) + L_{12}^{42} (\psi_4 - \psi_2) + L_{12}^{43} (\psi_4 - \psi_3) + L_{12}^{46} (\psi_4 - \psi_6) = 0 \quad (4.33)$$

$$J = L_{21}^{42} (P_4 - P_2) + L_{21}^{43} (P_4 - P_3) + L_{21}^{46} (P_4 - P_6) + L_{22}^{42} (\psi_4 - \psi_2) + L_{22}^{43} (\psi_4 - \psi_3) + L_{22}^{46} (\psi_4 - \psi_6) = 0 \quad (4.34)$$





# 5

## RESULTS AND DISCUSSION

This chapter will describe the results obtained in streaming potential experiments, electrophoretic experiments and modeling. Also, a comparison between streaming potential data and modeling data is made, the differences between the two will be described and explained. Apart from this, the trends in all data will be described and explained according to physical phenomena.

### 5.1. EXPERIMENTS

This section will describe the streaming potential measurements, both single and two-phase. Also, the zeta-sizer results are presented and some links are made between the two.

#### 5.1.1. STREAMING POTENTIAL

##### SINGLE-PHASE

Single-phase streaming potential experiments have been performed on QF20, Bentheimer and Berea 700. The results of these experiments in terms of the coupling coefficient are plotted in Figures 5.1 and 5.2, where the coupling coefficient is plotted against injected fluid molarity and fluid conductivity (average of in- and outflow conductivity) respectively. For QF20 and Bentheimer the measurements are only performed at 20 °C and with only *NaCl*. For Berea 700, the measurements are performed at 20 and 70 °C and with added divalents to prevent clays to deflocculate.

The measurements on the QF20 sample were not possible above a salinity of  $10^{-4}$  mol/l. Above this salinity, the response becomes too small to measure and distinguish from the background noise. This is because the pressure drop over the QF20 is significantly lower than over the Bentheimer or Berea cores. As the streaming potential signal is measured in  $V/Pa$ , a better permeability at the same flow rate, means a lower pressure difference. This means the signal which can be measured is lower. Bear in mind that at a higher salinity the conduction current is higher as the fluid conductivity is higher (more ions in solution). This means it is more difficult for a high streaming potential to exist, which is in effect a balance between streaming current and conduction current at a certain flow rate.

For Bentheimer sandstone, measurements become difficult around a molarity of  $10^{-1}$  mol/l. At this salinity, measurements were difficult to reproduce; at lower salinities measurement were good. The coupling coefficient of Bentheimer sandstones at very low salinity (close to  $10^{-5}$  mol/l) match well with the QF20 data in that region. At  $10^{-4}$  mol/l, the both data sets do not match though. This is due to the uncertain measurement of QF20 at this salinity, where measurements were already very difficult to perform (signal was very small and it was hard to distinguish between noise and signal). Although both lithologies contain almost exclusively silica (which should lead to approximately the same zeta potential), the bigger pore geometry of the QF20 compared to the Bentheimer (reflected in the permeability), would have to lead to higher values of the coupling coefficient at very low salinities, if double layer overlap is important. It could be that Bentheimer and QF20 and both too permeable (too large geometry) for overlapping to occur (Debye length at  $10^{-5}$  M is around 100 nm, also see Figure 5.4) and only Stern layer conduction prevents a higher build up of potential. Models as described later on in the results section, show that a Stern layer conduction of around  $\Sigma_S^{Stern} = 1E-8$  can have significant effect on the coupling coefficient curves, as seen in Figure 5.31.

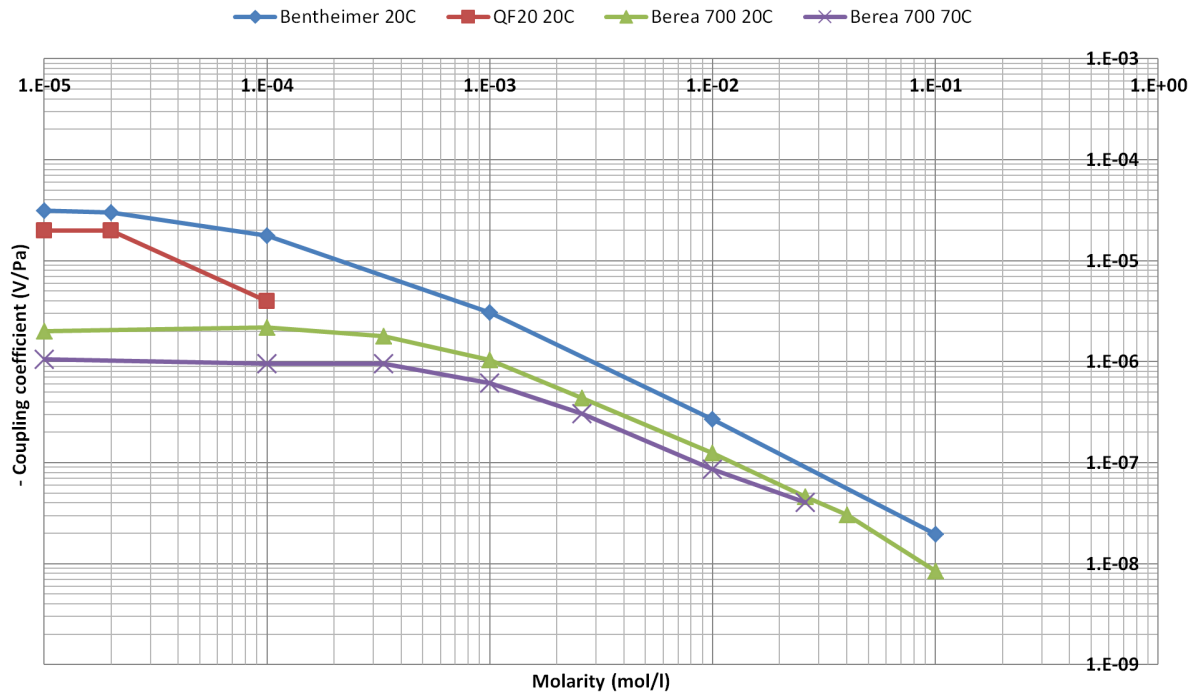


Figure 5.1: Coupling coefficients plotted against molarity for QF20, Bentheimer and Berea 700

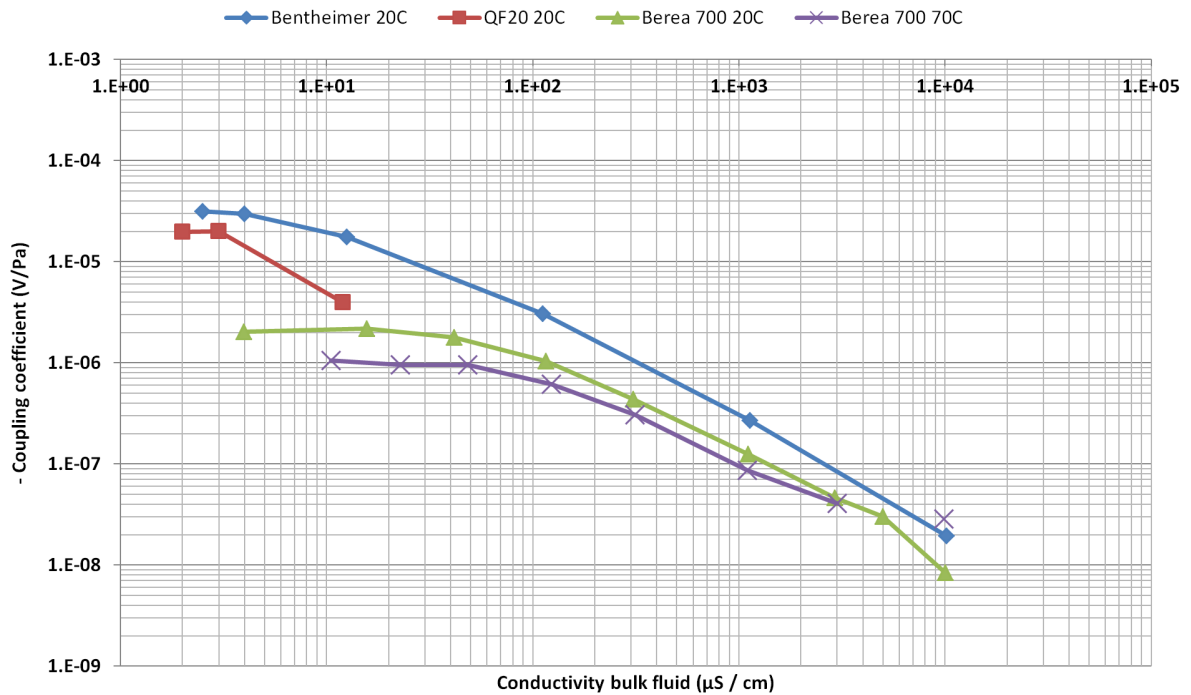


Figure 5.2: Coupling coefficients plotted against fluid conductivity for QF20, Bentheimer and Berea 700

The idea of double layer overlap originates from the basics behind the coupling coefficient plot against molarity, which is illustrated in Figure 5.3. The right side of the curve is geometry independent, this is the case when double layers on the surface are thin (high salinity or small zeta potential) compared to the channel/pore radius. This means a large value for  $\kappa r$ . The left hand side of the curve is geometry dependent, this is the case when double layers on the surface are thick compared to the channel radius and they meet in the middle (overlapping double layers). This is the case when the value for  $\kappa r$  is small. This leads to a curve as

illustrated in Figure 5.3, where the right side is linear in a log-log plot and the left side flattens, as the overlapping of double layers increases. The flattening of the curve on the left side can also be due to Stern layer conduction, which is also considered as an important influence on the bend. Figure 5.4 shows the double layer thicknesses for several molarities. It can be seen the thickness of the double layer becomes more important at lower salinities, the Debye length at an  $NaCl$  concentration of  $10^{-5} M$  is around 100 nm, as can be seen in Figure 5.4.

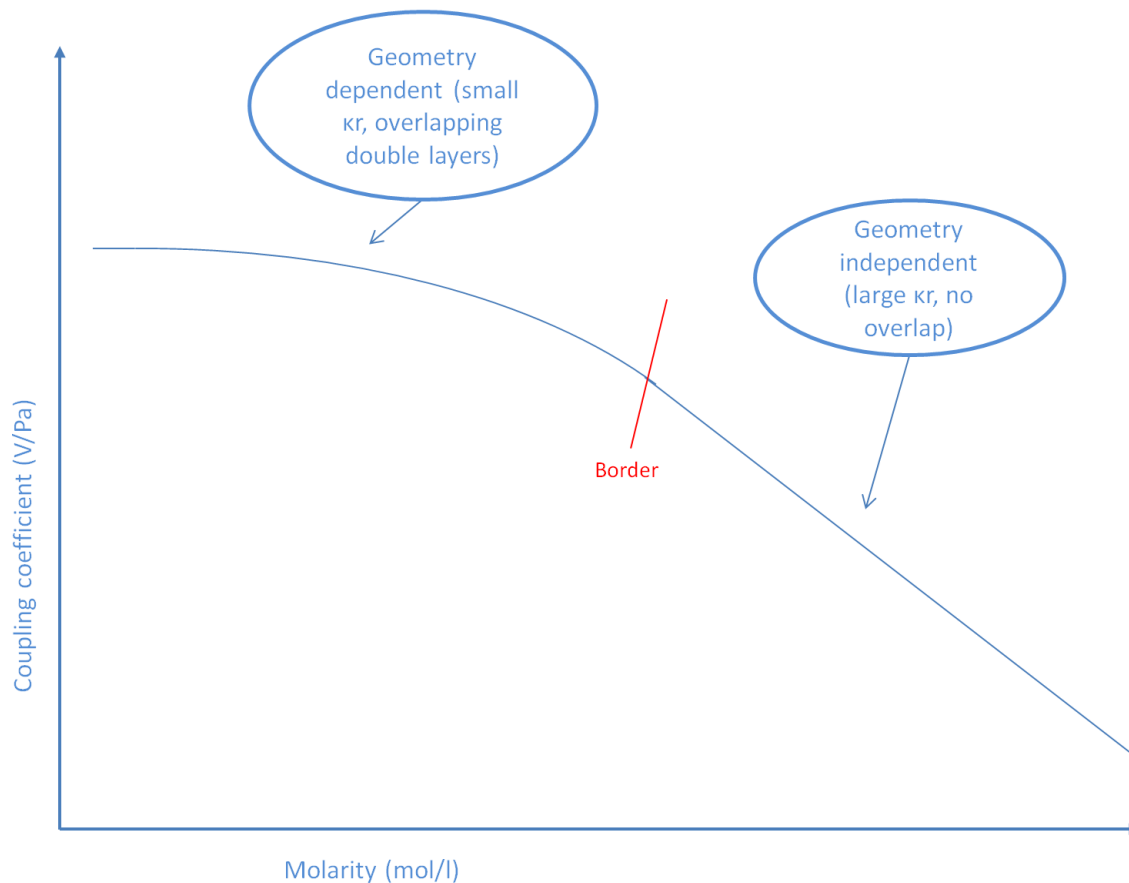


Figure 5.3: Coupling coefficient against fluid molarity: concept of geometry dependence

For Berea 700 sandstone, measurements were possible up until a molarity of  $10^{-1} mol/l$ . They are performed at both 20 and 70 °C. In the curve for Berea 700, the bend due to the overlapping of double layers and Stern layer conduction is observed a lot earlier than in the Bentheimer sandstone. This is due to the smaller inner geometry of the Berea sandstone, which is also reflected in the lower permeability of the Berea 700 sandstone. An influence on this might also be a higher value for Stern layer conduction. This is further quantified in Section 5.3, where the results for Berea 700 are compared to the different models. In the high salinity range, the data does come close to one another, which is expected, as the coupling coefficient is independent of geometry there and Stern layer conduction has a smaller influence. In practice, it was very hard to get the effluent around the same conductivity of the injected brines for low salinities. This is probably due to the fact that the rock releases ions from its surface. This is also the reason that the conductivity at which was measured has not become as low as in the Bentheimer case, which you can observe in Figure 5.2. On a side note, a little bit of fines came out of the sample when first flowing through it for a short period of time. This did not cause a change in permeability.

In between the measurement at 20 °C and 70 °C, a switch from HS to LS was made. This switch resulted in severe formation damage inside the core, as the salinity limit was exceeded due to cation stripping. This resulted in a pressure increase over the core by a factor of two, which indicates a permeability decrease by a factor of two. Also, the effluent showed a great amount of fines, which is shown in Figure 5.5. This is

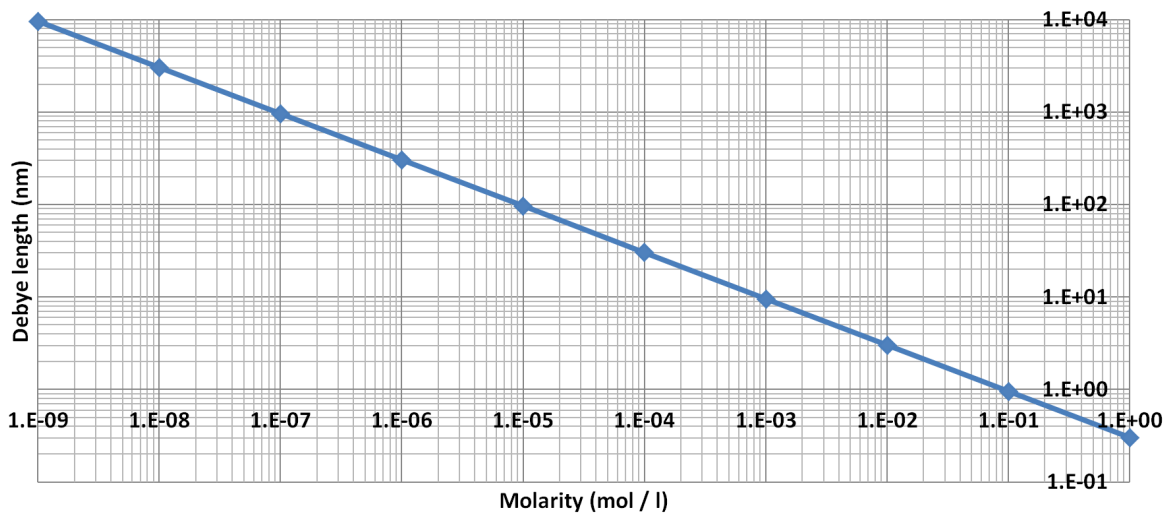


Figure 5.4: Debye length plotted against fluid molarity of an *NaCl* solution

important to take into account in the interpretation of the difference between the coupling coefficients for Berea 700 at both temperatures. At 70 °C, one would expect the coupling coefficient to be slightly higher than at 20 °C (see model in Figure 5.31). The difference at low salinity observed in Figures 5.1 and 5.2 is therefore mainly caused by the formation damage, in which deflocculated clays clog pore throats, making the radius of the effective cross-sectional flow area through the porous medium smaller. These are more favorable conditions for double layers to overlap. At medium salinities, one can see that the results for Berea 700 at both temperatures coincide very well. The measurements at 70 °C and very high salinity ( $> 10^{-1} \text{ mol/l}$ ) remained very high, suggesting a failure of the electrodes. After testing it showed that one of the electrodes did not have the correct half cell potential of around 220 mV. Therefore, these results were discarded.

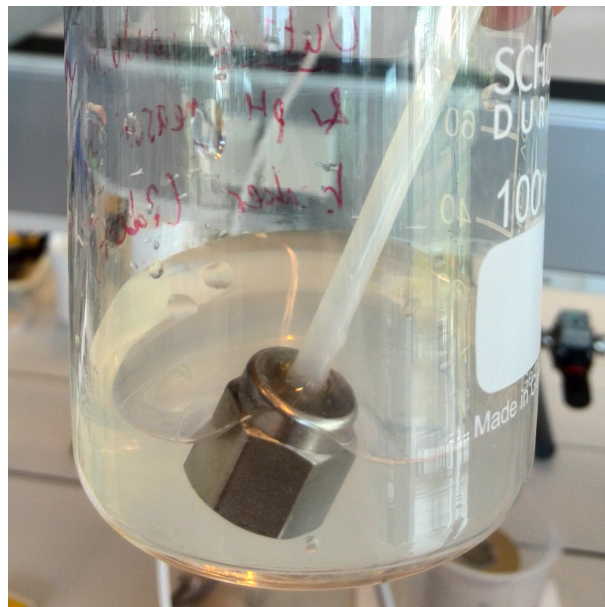


Figure 5.5: Fines released from the Berea 700 sample after a switch from HS to LS (large step salinity change)

To check quality of a measurement, one can make plots of the pressure versus the potential and the pressure versus the flow rate. Both should show a linear relation. Figures 5.6 and 5.7 show an example of this for Berea 700 sandstone at 20 °C and  $10^{-4} \text{ mol/l}$  brine.

It is interesting to note that, when the Berea 700 core was flushed with Dagang brine at 20 °C, the streaming potential response was opposite in sign to the measurements before this. The coupling coefficient at this

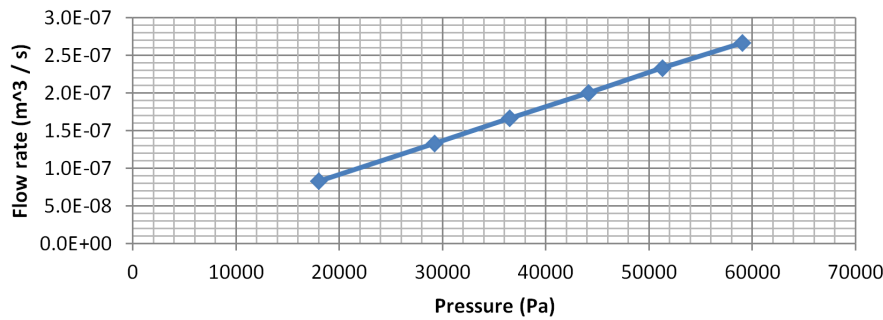


Figure 5.6: Flow rate plotted against pressure of a measurement on Berea 700

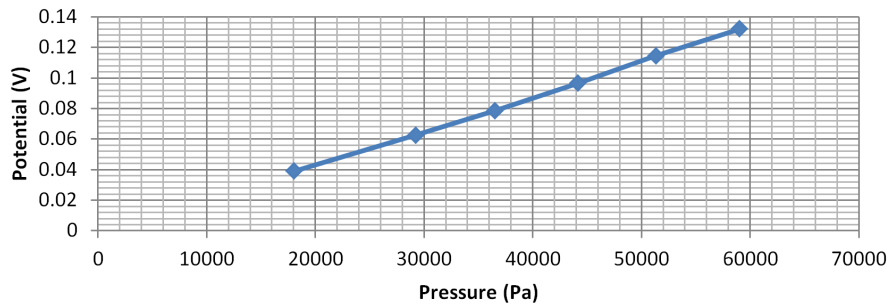


Figure 5.7: Flow rate plotted against pressure of a measurement on Berea 700

brine composition was found to be  $C_s = 5.9E - 9 V/Pa$ . This might be due to the differing composition of the Dagang brine, which is able to screen the surface charge, which may lead to a reversed zeta potential compared to the surface potential (see Figure 2.13 for the concept). Apart from  $NaCl$  and  $CaCl_2$ , Dagang brine also contains  $MgCl_2$  and  $KCl$ . It is important to realize that the processes ongoing inside the core are complex. The measured streaming potential is dependent on ion exchange processes, surface charges of the rock, the fluid conductivity, the amount of divalents in solution, conductivity through the Stern layer, flow rate, clays on the rock surface, clays which deflocculate and clogged pores, the reliability of the electrodes (and influence of cavities in the rock), noise from surrounding activity, the geometry of the internal pore structure, the core preparation process and so on.

#### TWO-PHASE

Two-phase streaming potential experiments have been performed on both Bentheimer and Berea 700 sandstones. In Bentheimer sandstone, the oil phase constitutes of hexadecane. In Berea 700 sandstone, Crude Oil H is used. First, we look at the difference between the single-phase and two-phase experiments for Bentheimer, then the same comparison is made for Berea 700. We will try to compare the two-phase results for Bentheimer and Berea, but since both the oil used and the composition of the rock is different, this comparison is difficult. The experiments are performed at residual oil saturation ( $S_{or}$ ).

Figures 5.8 and 5.9 show the coupling coefficient plotted against molarity and fluid conductivity respectively for Bentheimer sandstone. To obtain the two-phase situation, hexadecane was injected at high rates (25 ml/min), whereafter brine is pumped through the sample at high rates (25 ml/min) to obtain a residual hexadecane saturation. The Figures 5.8 and 5.9 show the data for Bentheimer single-phase (20 °C) and Bentheimer two-phase (one without divalents (only  $NaCl$ ) and one with 10 %  $CaCl_2$ ). One can see that the two-phase data points have lower values in the low salinity region. This can be caused by a combination of two effects.

Firstly, two-phase flow through a porous medium at a certain residual oil saturation leads to a smaller effective cross-sectional flow area (effective pore space) for the water phase. This is also reflected in a higher pressure drop over the core for the same flow rate, in other words a certain relative water permeability ( $k_{rw}$ ), which should be multiplied with the original permeability ( $k$ ) to obtain the water permeability ( $k_w = k_{rw}k$ ). A smaller flow path for the water phase means a smaller effective radius of the porous medium through which the brine flows. This leads to a smaller value of  $\kappa r$ , which means overlapping occurs earlier on (at higher

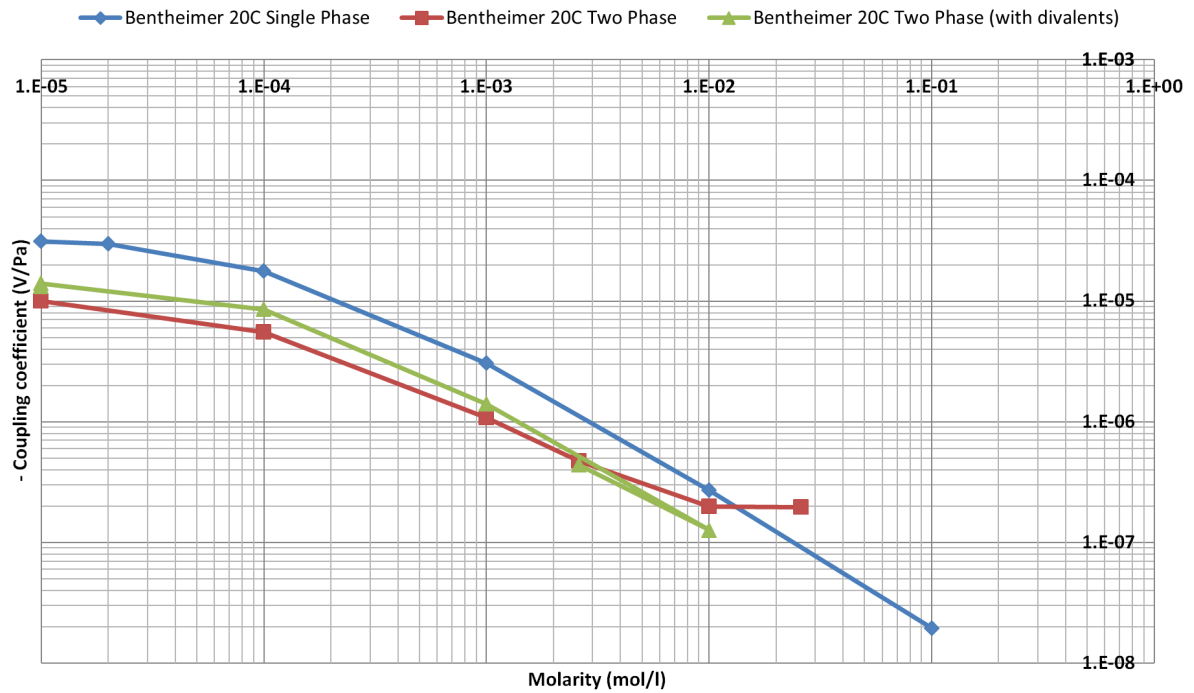


Figure 5.8: Coupling coefficients plotted against molarity for Bentheimer sandstone (single phase and two phase at 20 °C)

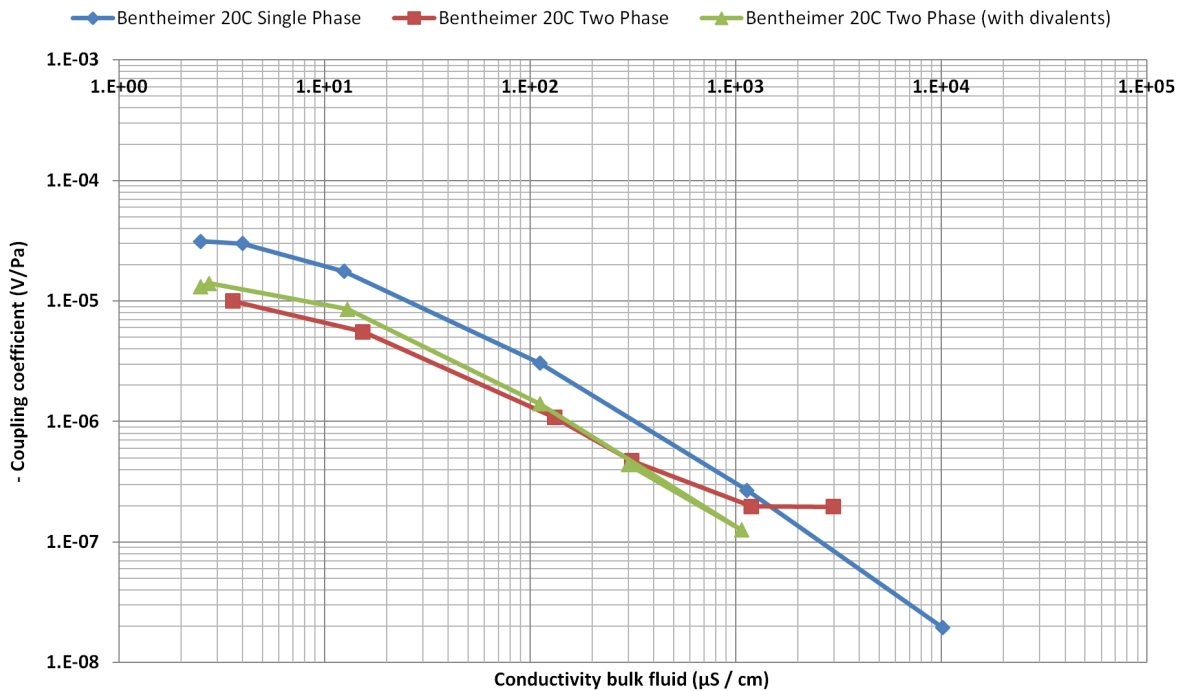


Figure 5.9: Coupling coefficients plotted against fluid conductivity for Bentheimer sandstone (single phase and two phase at 20 °C)

salinity than in single-phase experiments) and the bend in the curve occurs earlier. At a salinity higher than  $10^{-3} \text{ mol/l}$ , one can see that the points merge together again into a straight, geometry independent line. An example of this effect is shown in Figure 5.33. Another aspect that could be causing the lower coupling coefficient curve at these low salinities, is as follows. A relative permeability is usually smaller than the saturation in the case of straight line relative permeabilities. This means flow velocity will be lower for the same pressure drop with decreasing water saturation. If flow velocity becomes lower, it will not be able to transport as much

charge downstream and the coupling coefficient will be lower.

Secondly, the hexadecane is non-polar. This means it does not contribute to the charge screening in the water phase. If the oil phase is polar it can lead to a higher value of the streaming potential and therefore a later bend (in other words at a lower salinity than in the two-phase case with non-polar oil).

The measurement of Bentheimer at 20 °C two-phase (red dots) at a molarity of 0.026 mol/l slightly differs from the linear trend expected in this region. However, this is a questionable measurement as it was very difficult to measure a proper response at this salinity. The measurement consist of only one measurement at a single rate of 15 ml/min, whereas a typical measurement is an average value for a range of rates.

If one looks at the difference between the two two-phase scenarios (one with divalents added and the other without divalents added), one can see that, in the low salinity region, the curve for the scenario in which divalents were added lies slightly higher. When more divalents are added, the double layer thickness on the rock is smaller, or in other words the Debye length is smaller. This might cause double layer overlapping to occur later on. One must bear in mind that the differences between the two curves are small though.

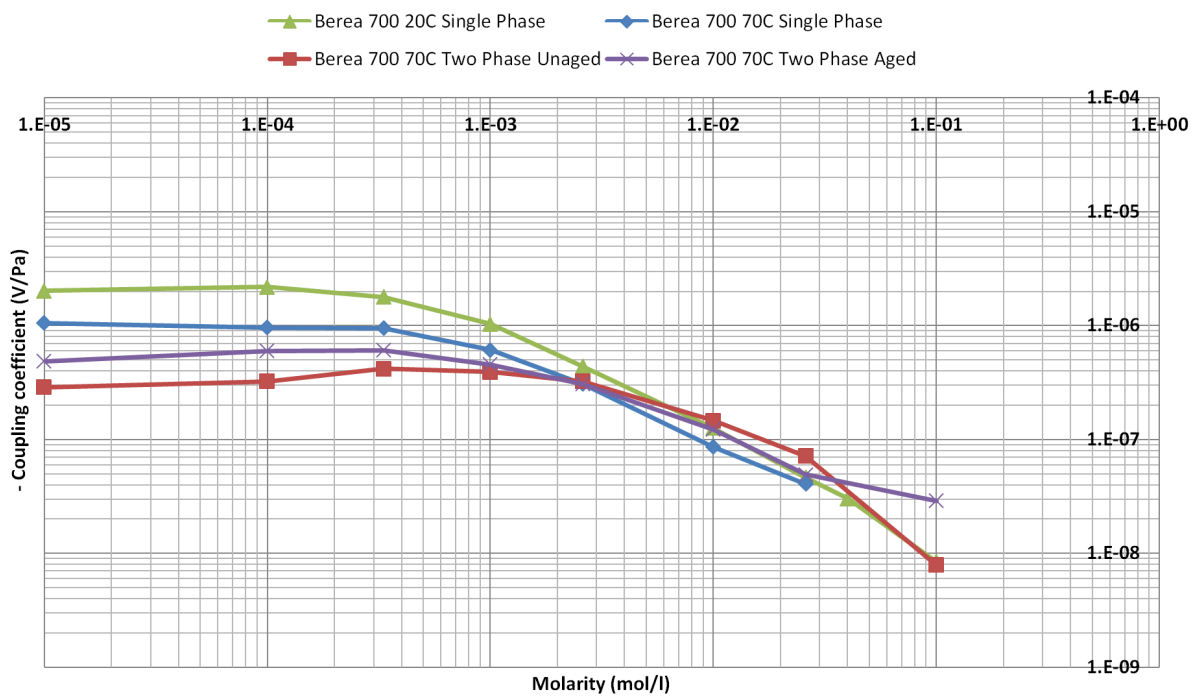


Figure 5.10: Coupling coefficients plotted against molarity for Berea sandstone (single phase at 20 and 70 °C, two phase at 70 °C)

Figures 5.10 and 5.11 show the coupling coefficient plotted against molarity and fluid conductivity respectively for Berea 700 sandstone. In experiments with Berea 700, divalents are always added to the injected brines. Two two-phase experiments have been performed, one with an unaged core and one with an aged core. The unaged core was saturated with crude oil, but the oil saturation that was achieved was not high enough, according to calculations it was only  $S_o = 0.58$ . Knowing the oil saturation was not high enough, we performed two-phase experiments at residual oil saturation to have a comparison to the aged sample later on. After these experiments were performed, the core was flushed with a mixture of PAO40 and decane of various ratios and viscosities in order to lower the residual water saturation as much as possible. The method is explained in Appendix B. When oil was flushed back into the sample, a calculated saturation was achieved of  $S_o = 0.80$ , which should be sufficient to properly age the sample at 70 °C for four weeks. The residual oil saturation for the aged core is calculated at  $S_{or} = 0.19$ .

The comparison between the single-phase data at two different temperatures has already been made in Subsubsection 5.1.1.1. Now, we compare the single-phase measurements with the two-phase measurements at 70 °C. As in the case for the Bentheimer two-phase results, here, for Berea 700, the curve for two-phase measurements is lower in the low salinity region than the curve for the single-phase results at 70 °C. This is again due to the fact that the effective pore radius is smaller due to the presence of the oil phase. This leads to a smaller value of  $\kappa a$  at a certain molarity and an earlier bend in the coupling coefficient curves. Again, the argument that the effective flow (velocity) will be lower for the same pressure drop with decreasing water

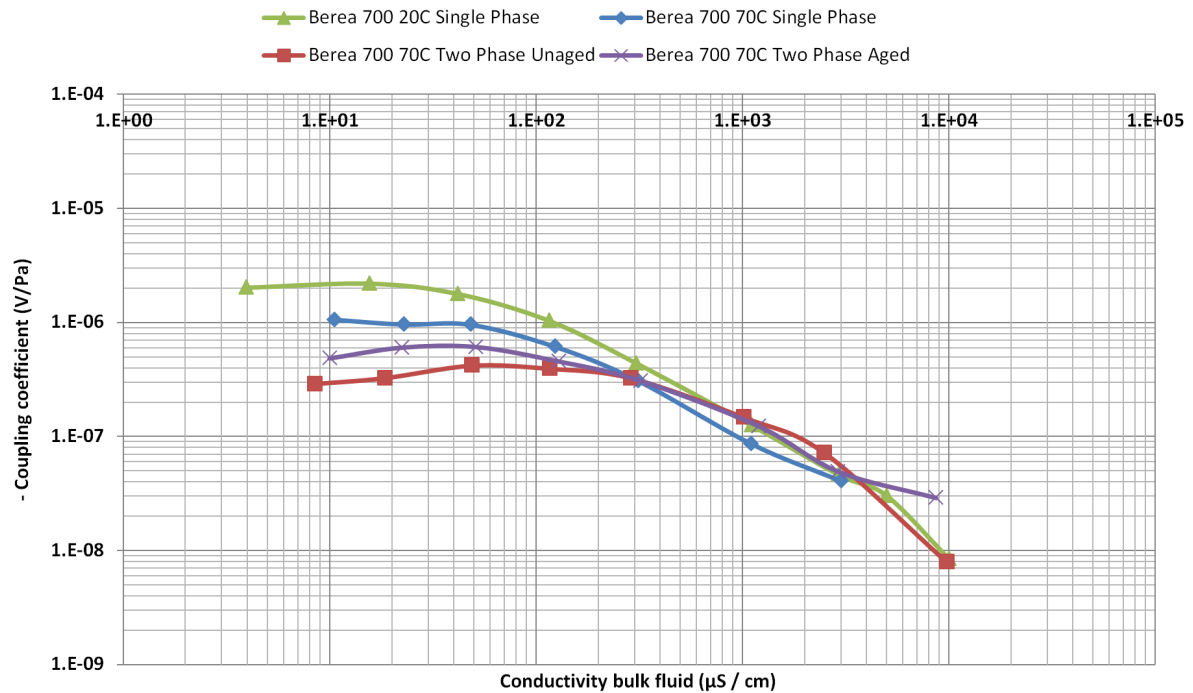


Figure 5.11: Coupling coefficients plotted against fluid conductivity for Berea sandstone (single phase at 20 and 70 °C, two phase at 70 °C)

saturation, could also hold. If flow velocity becomes lower, the liquid will not be able to transport as much charge downstream and the coupling coefficient will be lower. The oil used does have a certain polarity now, without this the curve would probably have been slightly lower. At higher salinities, the two phase curve and single phase curve lie close to each other again.

If one studies Figures 5.10 and 5.11 carefully, another trend is visible in the very low salinity region. There, the coupling coefficient seems to go down again as salinity decreases. This could be caused by Stern layer conduction. Stern layer conduction is a small conduction of current upstream through the Stern layer. Although the effect is small, at lower salinity, the conduction through the bulk fluid decreases and Stern layer conduction has a relatively larger influence on the coupling coefficient. The effect lowers the coupling coefficient slightly, as it provides a path for current to flow back. In Section 5.3, we quantify the contribution of Stern layer conduction. The shape of the curves, as observed up until now, is caused by the combination of Stern layer conduction, the overlapping of double layers and the fact that the flow (in a two-phase situation) transporting ions might be lower.

The data for Berea 700 two-phase unaged and aged cases lie rather close to each other, especially in the high salinity region of the graphs. Only in the low salinity region, one can observe from Figures 5.10 and 5.11 that the values of the coupling coefficient lie slightly higher for the aged case. Calculations show that the oil saturation in the aged core are slightly lower than in the unaged case (also described in the text a couple of paragraphs down), and this may cause the aged case with a lower oil saturation to give a slightly higher response in the low salinity region. A lower oil saturation causes a bigger effective flow area (higher flow rate and less overlapping) for the water phase and a higher curve. It is difficult to correlate this effect to a different wetting tendency of the rock surface, as we expect the wettability change already at a higher salinity. Both surfaces therefore (in the aged and unaged case) should have the same wetting affinity. Regarding the Berea 700 two-phase aged measurement at 0.1 M, this data point was obtained after flushing the sample with Dagang brine and a synthetic brine of 0.4 M. The measurement at 0.4 M was not possible and between the measurement at 0.4 M and the measurement at 0.1 M, the streaming potential signal was reversed, so the measurement is therefore not very reliable and had not yet reached a steady-state. This is related to the observations as described in the next paragraph.

As in the single-phase case with Berea 700, in the two phase response for the unaged sample again some curious results are observed at very high salinity and especially when flooding the core with Dagang brine. As described before, the Berea 700 core is saturated with crude oil and Dagang brine. When experiments

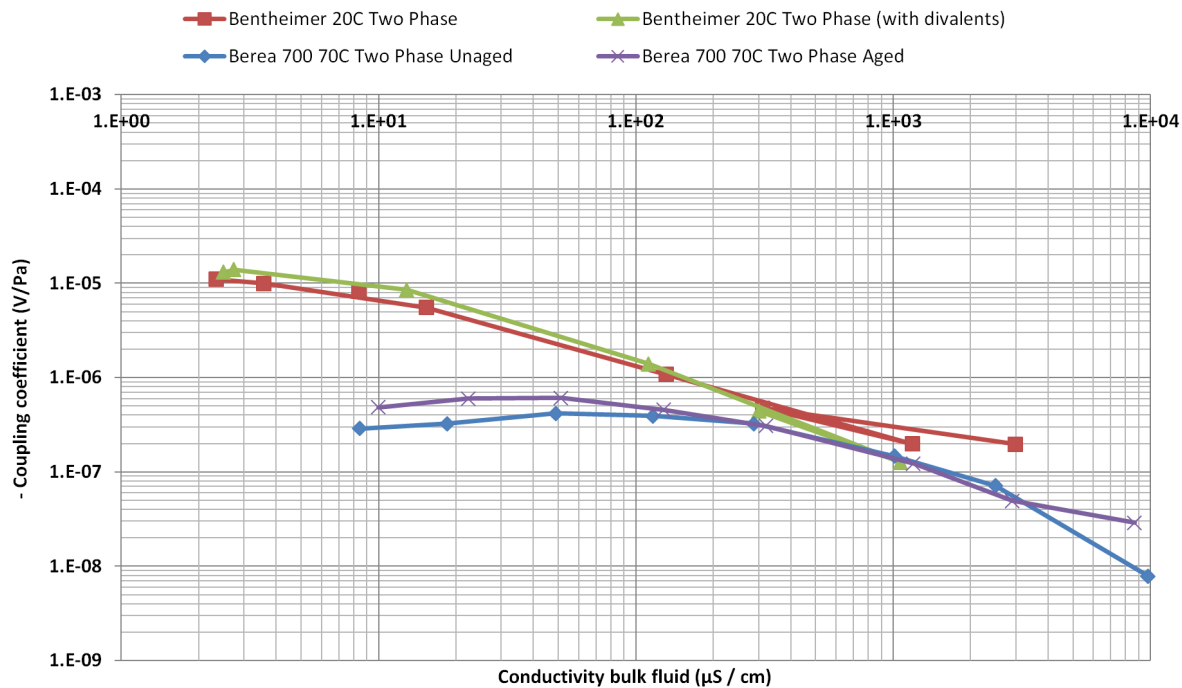


Figure 5.12: Coupling coefficients plotted against fluid conductivity for two phase experiments in Berea 700: Unaged and Aged

start, it is flooded with Dagang brine first. After flooding with Dagang, injection brine was switched to a synthetic brine ( $NaCl$  with 10 % added  $CaCl_2$  (0.4 M)). The measurement at Dagang was not well recorded as one electrode was defect. However, when the electrode was replaced and synthetic brine of 0.4 M was injected, the streaming potential response was reversed, indicating a positive zeta potential, which means that the potential at the shear plane is of opposite sign compared to the surface potential. This is probably caused by the high amount of ions present in the synthetic brine and the remaining ions coming from the Dagang brine. The coupling coefficient is given as:  $C_s = 1.57E - 7$ . After going all the way to the lowest measured salinity, a quality check was performed to see whether the strange result of charge inversion could be reproduced. Now, at the synthetic brine of 0.4 M, no measurement was possible, but after a switch to Dagang brine, a streaming potential measurement was possible. Again the streaming potential response was reversed, indicating a positive zeta potential. The coupling coefficient is given by:  $C_s = 5.21E - 8$ .

For the aged Berea 700 sample, a similar behavior was observed. When Dagang brine was pumped through the sample, the streaming potential response had a different sign than later on at lower salinity. This indicates again a positive zeta potential. The coupling coefficient of this measurement is given by:  $C_s = 8.6E - 8$ . After this, the measurement at 0.4 M synthetic brine was not possible, as the signal started to change signs.

This clearly indicates that a switch from a HS brine to a brine of significant lower salinity, leads to a change in zeta potential or even a reversal in zeta potential. This change in zeta potential on the surface of the rock, indicates a change in affection of the rock from oil towards brine. This is because a surface with a positive zeta potential is more likely to attract the negatively charged components in the crude oil. A more negative zeta potential means that it is more difficult for oil to reside on the rock surface. The lack of positive ions (especially the lack of multivalent ions) in the electrolyte at lower salinity prevents charge screening of the surface charge within a short distance and this prevents the oil components from binding to the surface.

The oil production is also monitored in the experiments. For the unaged sample, all of the production occurred directly at high salinity, in other words no measurable quantities of oil were released from the core when the switch was made to lower salinity. The effluent brine did have an oily look throughout the experiment, indicating that small amounts of oil were still released. The residual oil saturation at which the experiments were performed in the unaged sample was:  $S_{or} = 0.25$ . In the case of the aged sample, all oil production occurred at injection of a HS brine (Dagang) as well. Calculations showed that the residual oil saturation was at  $S_{or} = 0.19$ . In the interpretation of these numbers, one must realize that we are considering very small volumes. The pore volume of the sample is only 11.3 ml.

In our experiments no measurable incremental oil production was seen when the switch from Dagang to synthetic brines was made. Therefore, it is not possible to compare the oil production in our streaming potential measurements to the oil production as observed in imbibition experiments by [Suijkerbuijk et al. \[2012\]](#) (also described in Subsection 2.1.5 and Figure 2.9). Further experiments are necessary to determine increased oil production by LSF in core flooding experiments.

### 5.1.2. ELECTROPHORESIS: ZETASIZER

To characterize the zeta potential ( $\zeta$ ) of the rocks used in the streaming potential measurements, electrophoretic measurements are performed with the zetasizer machine. The zeta potential is measured over a salinity and pH range for three different lithologies (Berea 700, Bentheimer and Berea 18). The data obtained in these measurements is used as an input into the capillary tube, bundle-of-tubes (BOT) and pore-network models (PNM).

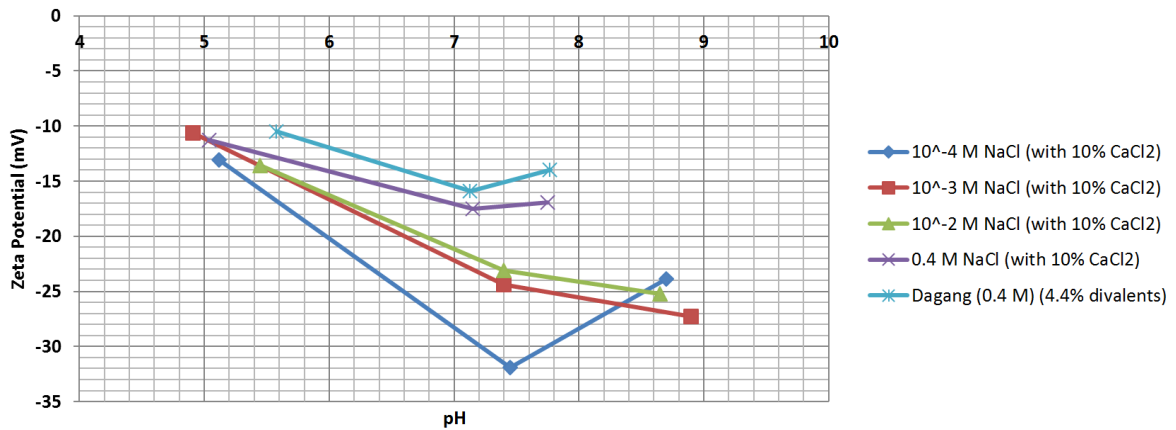


Figure 5.13: Zeta potential plotted against pH for several molarities for Berea 700 at 20 °C

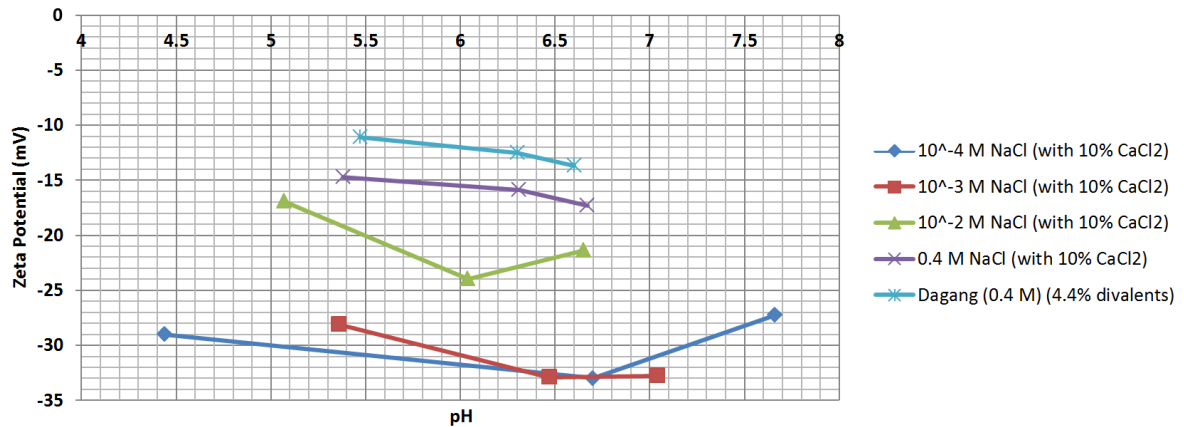


Figure 5.14: Zeta potential plotted against pH for several molarities for Bentheimer at 20 °C

Figures 5.13, 5.14 and 5.15 show zeta potential plotted against pH for Berea 700, Bentheimer and Berea 18 respectively. All figures contain this plot for several molarities, which includes Dagang brine. One can see that the zeta potential decreases with pH for all molarities and rock types. The points that do not show this trend can be considered outliers. As pH decreases, the solutions surrounding the crushed rock particles will contain more positive ions and therefore more charge on the surface can be screened, leading to a decrease of the zeta potential. As fluid molarity increases, one can also see that the zeta potential decreases. This is caused by the fact that an electrolyte with a higher salinity contains more ions and therefore screens the surface charge faster (shorter Debye length), leading to a lower measured zeta potential. As the ionic strengths of the Dagang brine and the synthetic 0.4 M brine are the same, the higher amount of divalents in the Dagang

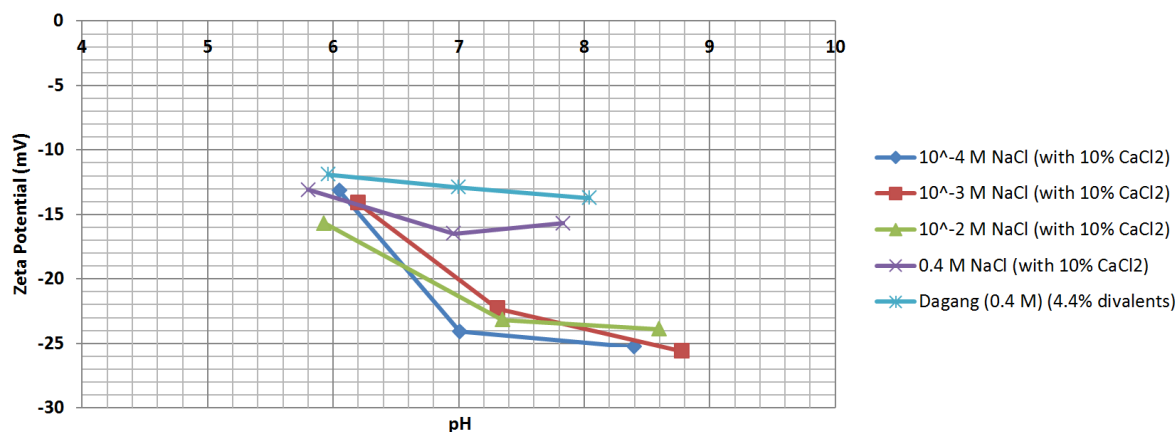


Figure 5.15: Zeta potential plotted against pH for several molarities for Berea 18 at 20 °C

brine, leads to lower values of the zeta potential, compared to the synthetic brine.

The zeta potential curves all head towards a certain PZC, which lies between a pH of 1 – 3 for all the rock types. The equilibrium pH for Berea 700 and Berea 18 lies between 8 and 9. For Bentheimer sandstone, equilibration pH lies between 6.5 and 7.

The trends in Figures 5.15 and 5.13 for the Berea 700 and Berea 18 sandstones show quite similar behaviour. This can be explained by the fact that the composition of both sandstones (quartz and clay contents) is quite similar. The trendline for Bentheimer, as observed in Figure 5.14 is less steep than in the Berea 700 and Berea 18 cases (Figures 5.17 and 5.14). This might be due to the fact that in the Berea 700 and Berea 18 case more acid needs to be added to achieve lower pH values, as the sandstone keeps reacting with the added acids, which increases the pH. In the Bentheimer case, less acid is added, so there are less ions to screen the surface charge and this means there are less ions present to lower the zeta potential. This might also explain why the curves are steeper for lower salinities with Berea 700 and Berea 18. The lower the salinity, the more influence the addition of acids has on the composition of the electrolyte; a lot of ions are added compared to the amount of ions present before the addition of acid. So, the addition of acid changes the effective salinity.

Reflecting back on observations made in the single-phase and two-phase streaming potential experiments with Berea 700 sandstone (as described in the previous section), recall that when Dagang brine was pumped through the core, the measured charge would reverse (single-phase at 20 °C and two-phase at 70 °C). This means that the zeta potential is positive. Looking at the the zeta potential data obtained in zeta-sizer experiments, one would expect this to show in the Berea 700 curve for Dagang at a pH range between 7 – 8 (range as observed in the streaming potential experiments). However, the zeta potential in this range, according to electrophoretic measurements, lies between -20 and -10 mV.

To model the streaming potential phenomena, the data from the zetasizer experiments is used as input. Therefore, the pH of the streaming potential experiments at the different salinities was used to obtain a value of the zeta potential at this certain pH and salinity. For streaming potential experiments in Bentheimer, the pH is continuously around a pH of 5.5 – 6. In Berea 700 and Berea 18 sandstone pH lies around a pH of 7 – 7.5. Provided this information, one obtains Figure 5.16, where the zeta potential ( $\zeta_r$ ) is plotted against fluid molarity for the three different lithologies. This data is used to obtain relations for the molarity versus zeta potential.

The relations obtained for the three different sandstones can be seen in Figures 5.17, 5.18 and 5.19. The results of zetasizer experiments for crude oil H and the different brines are shown in Figure 5.20. This data is used as input for the two-phase models containing crude oil ( $\zeta_o$ ).

Important to note is that the relation was not used far outside the measurement domain. The relations are extrapolated to an ionic strength of  $10^{-5}$  mol/l. When lower ionic strengths are modeled, the zeta potential is kept constant at the value at an ionic strength of  $10^{-5}$  mol/l. The relations are displayed in the top right of Figures 5.17, 5.18, 5.19 and 5.20.

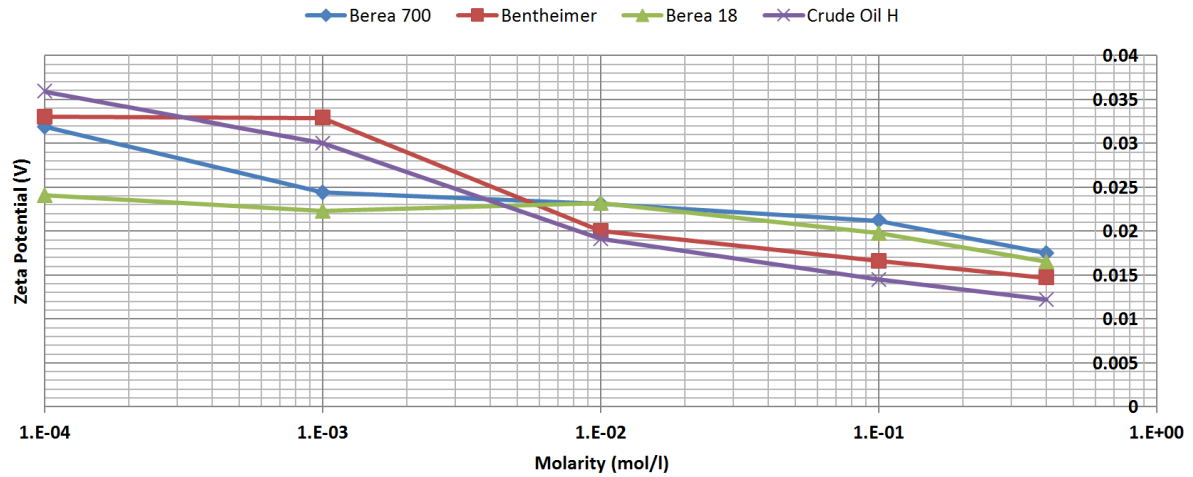


Figure 5.16: Zeta potential plotted for several molarities for Berea 700, Bentheimer, Berea 18 and crude oil H (pH equal to pH in streaming potential experiments)

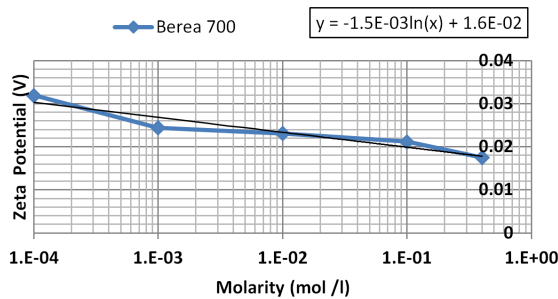


Figure 5.17: Zeta potential plotted against molarity for Berea 700 (pH equal to pH in streaming potential experiments). A trendline is fitted and used as modeling input

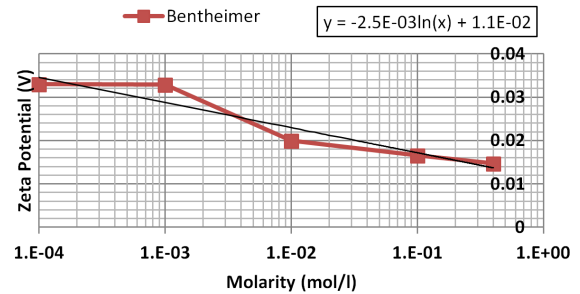


Figure 5.18: Zeta potential plotted against molarity for Bentheimer (pH equal to pH in streaming potential experiments). A trendline is fitted and used as modeling input

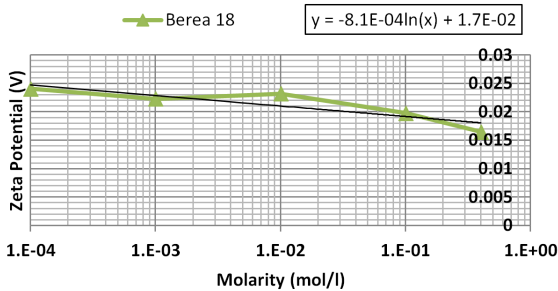


Figure 5.19: Zeta potential plotted against molarity for Berea 18 (pH equal to pH in streaming potential experiments). A trendline is fitted and used as modeling input

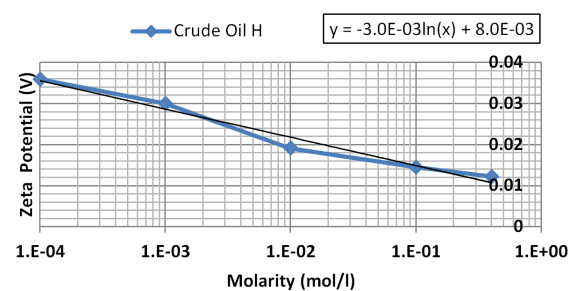


Figure 5.20: Zeta potential plotted against molarity for crude oil H. A trendline is fitted and used as modeling input

## 5.2. MODELING

In the modeling section, we start by presenting the results of the pore network extraction. Secondly, the different sandstones are compared based on pore throat size distributions and porosity. Then, the Gouy-Chapman model is described. After this, the single-phase streaming potential phenomenon is modeled by means of a capillary tube model, a bundle-of-tubes model and a pore-network model. Then, we describe the two-phase modeling, where the capillary tube and bundle-of-tubes modeling approaches are used. In the next section, we will compare the streaming potential experimental results with the streaming potential models that use zetasizer measurements as input. The differences will be explained and some additional

calculations will be done to improve the match, for example the introduction of a Stern layer conduction term as a fitting parameter.

### 5.2.1. NETWORK EXTRACTION

In order to get a certain pore throat size and pore body size distribution, micro CT data is used as input into a pore network extraction code. Table 5.1 shows the size of the input images (in voxels, which is essentially a three dimensional pixel). The voxel size (or side length) is equal to the resolution of the micro CT data, which is  $1.84 \mu\text{m}$ .

Table 5.1: Sizes of the input images for the pore network extraction (number of voxels in each direction), the porosity and average pore throat and body radii

Sandstone	x	y	z	Porosity (-)	$r_{throat,average}$ (m)	$r_{body,average}$ (m)
Berea 700	367	436	324	0.21	2.31E-6	4.54E-6
Bentheimer	310	344	364	0.21	4.61E-6	7.86E-6
Berea 18	362	390	319	0.20	2.55E-6	5.06E-6

The fourth column of Table 5.1 shows the porosity as detected by the pore network extraction code. One cannot conclude anything from these values, as they lie too close to one another. We are looking at a very small scale, where sensitivity to any heterogeneity of the sample is large. The samples, that are taken, lie below the representative elementary volume (REV). To illustrate the size of the image that is inputted into the pore network extraction code, the side length of the image is around 0.7 mm. The sandstone cores used in the experiments are a lot larger: around 10 cm in length and 2 cm in diameter.

The fifth and sixth columns of Table 5.1 show the average pore throat and body radii for the three sandstones. The values for Bentheimer sandstone are clearly a factor two larger than those for Berea 700 and Berea 18. As the permeability of Berea 18 is lower than the permeability of Berea 700, one would expect the average pore throat to be smaller in Berea 18, but this is not the case. The average pore body radius in Berea 18 is also a little bit larger. This might also be due to the sampling of the sandstone.

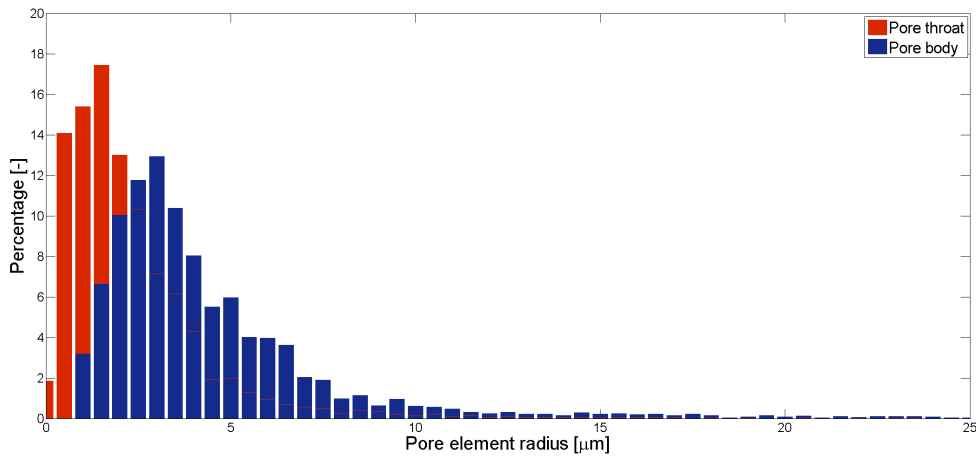


Figure 5.21: Pore throat size and pore body size distribution for Berea 700 sandstone

Figures 5.21, 5.22 and 5.23 show the pore size distributions as obtained from the pore network extraction for Berea 700, Bentheimer and Berea 18 sandstones respectively. Visually, the histograms for Berea 700 and Berea 18 display quite similar behaviour, which is reflected in the similar average values for the pore throats and bodies radii. The pore size distribution of the Bentheimer sandstone does show a clear difference, as is visible in Figure 5.22. There are a lot more pore throats and pore bodies in the larger radius region in the Bentheimer. This explains the better permeability of Bentheimer compared to Berea 700 and Berea 18, as well as the higher values for the average pore throat and pore body radius, as shown in Table 5.1.

The mode of the pore throat size distribution for Berea 700 and Berea 18 lies around  $1.8 \mu\text{m}$ . For the

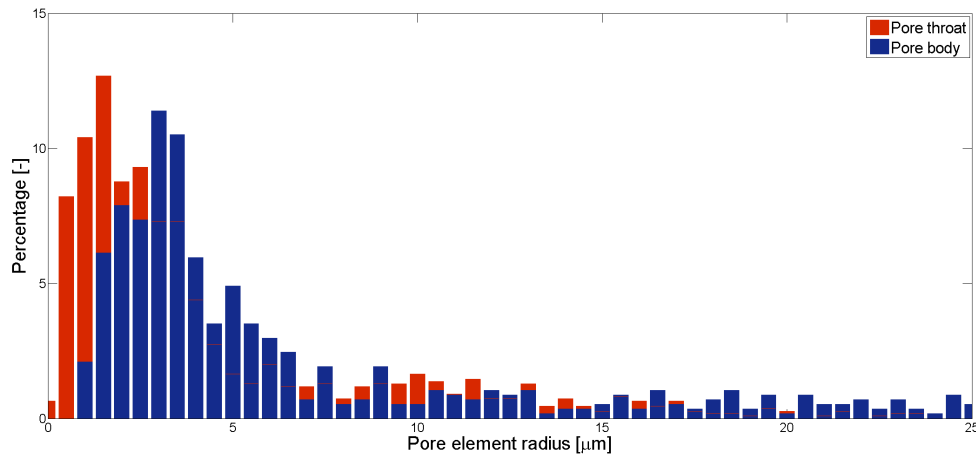


Figure 5.22: Pore throat size and pore body size distribution for Bentheimer sandstone

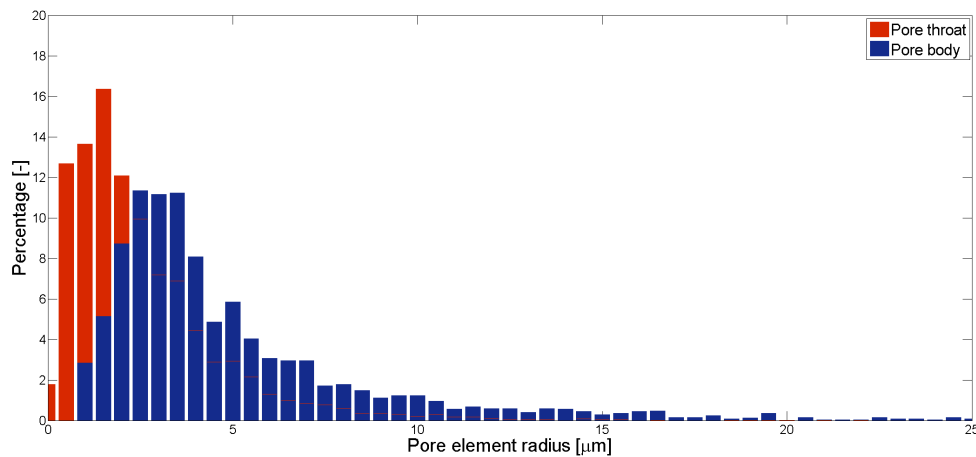


Figure 5.23: Pore throat size and pore body size distribution for Berea 18 sandstone

Bentheimer, this is around  $2 \mu\text{m}$ . The mode of the pore body radius lies around a value of  $3 \mu\text{m}$  for all three cases.

Important to realize is that the pore size distributions obtained with the pore network extraction are based on micro CT data with a resolution of  $1.84 \mu\text{m}$ , so pore throats with a size under resolution will not be taken into account. Also, the smallest point of a pore throat in a real porous medium may be smaller than the pore throat cylinder size from the extraction. Next to that, the boundary between rock and pore space as interpreted in image analysis software is sensitive to visual judgment and only two phases are distinguished in this process (rock and pore space). The distinction between quartz and clay is absent.

Strangely, the data obtained with MICP as shown in Figure 3.2 have a peak in pore throat diameter around  $22 \mu\text{m}$  (radius of  $11 \mu\text{m}$ ). This value is very far off the peak as observed in the pore size distribution as obtained in the pore network extraction, where the peak lies around  $1.8 \mu\text{m}$ .

### 5.2.2. GOUY-CHAPMAN MODEL

As explained in Subsection 2.5.2, the Gouy-Chapman models the potential distribution in the diffuse layer. This is similar to the potential distribution inputted into the streaming potential models. Figure 5.24 shows the Gouy-Chapman model for 1:1 and 2:2 electrolyte solution of  $10^{-4} \text{ mol/l}$ . On the y-axis the potential is displayed, and one can see that when one moves further from the surface (with a potential of  $\psi = -25 \text{ mV}$ ) the potential gradually becomes lower, until it goes to zero asymptotically. In the case with the 2:2 electrolyte, this charge screening takes place more than twice as fast, indicating that the Debye length is at least twice as

small. Figure 5.24 is here to illustrate the influence of divalents on the Debye length.

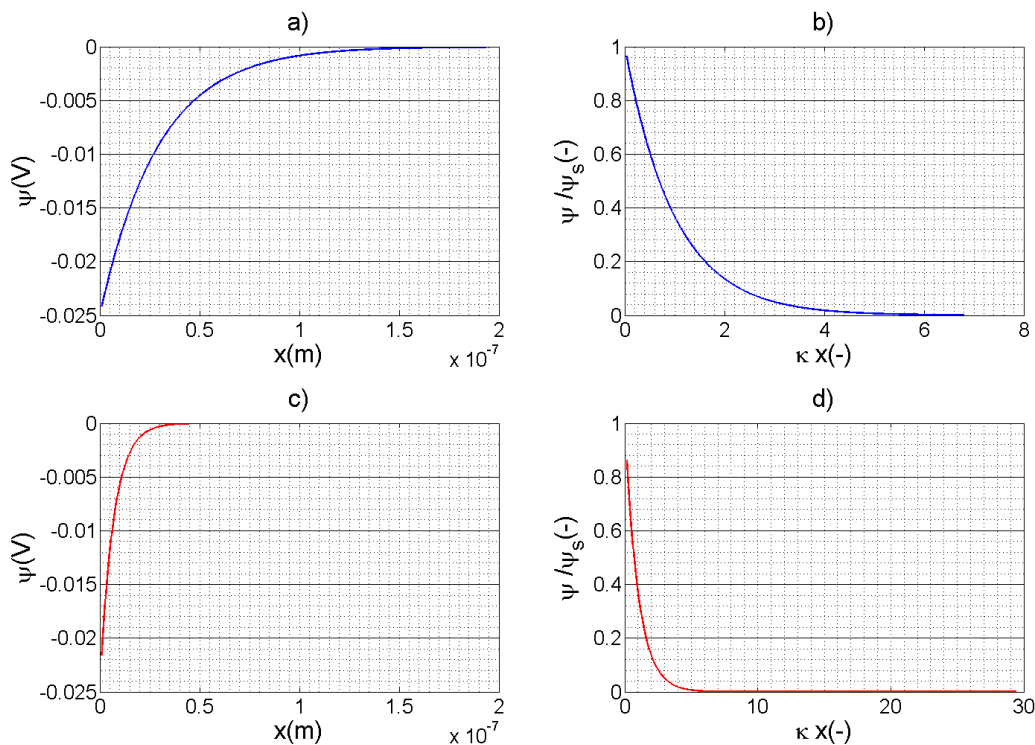


Figure 5.24: Potential variation with distance for a charged surface of  $\psi = 25 \text{ mV}$ : a) and b)  $10^{-4} \text{ mol/l}$  1:1 electrolyte solution, c) and d)  $10^{-4} \text{ mol/l}$  2:2 electrolyte solution.  $\Psi_s$  symbolizes the surface potential

### 5.2.3. SINGLE-PHASE

In this subsection the models for single-phase streaming potential will be discussed, based on a capillary tube model, a bundle-of-tubes model and a pore-network model.

#### CAPILLARY TUBE MODEL

Figure 5.25 shows a 3D plot of the coupling coefficient ( $C_s$ ) against ionic strength ( $I$ ) and capillary radius ( $r$ ) for a cylindrical geometry as described in Equation 4.1. This figure captures the idea of geometry dependence and fluid ionic strength dependence of the streaming potential, in other words it shows the important trends. The coupling coefficient becomes larger when salinity is lower; and at low salinity and/or small capillary radii (small  $\kappa r$ ) the coupling coefficient does not increase any further due to overlapping of the electric double layer (a phenomenon also called surface conduction, not to be mistaken with Stern layer conduction, which is real surface conduction). Figure 5.25 also shows the geometry independence at high salinities. At low salinity, the coupling coefficient is clearly geometry dependent.

Figure 5.26 shows the coupling coefficient plotted against ionic strength for one capillary channel with radius  $r = 1E - 7$ . Here, one can also observe the flattening of the curve, caused by overlapping double layers. The capillary tube model responds to changes in temperature, changes in the amount of divalents and changes in geometry, e.g. triangular or cylindrical geometry. To illustrate this, we will use a Berea 700 sandstone with a capillary channel of  $r = 1E - 7$  as in Figure 5.26. Although the zeta potential input is slightly different in the Bentheimer case, the observed trend will be comparable.

Figure 5.27 shows a comparison of trends. The blue line shows a Base Case, where no divalents are added, the temperature is  $20 \text{ }^\circ\text{C}$  and the geometry is cylindrical. The red line shows Case 1, where 10 % of divalents are added ( $\text{CaCl}_2$ ). The green line shows Case 2, where the temperature is raised to  $70 \text{ }^\circ\text{C}$ . The purple line shows Case 3, where the geometry is changed from cylindrical to triangular.

Case 1 shows that the amount of divalents present in the brine, influences the streaming potential greatly, as the divalents suppress the thickness of the electric double layer (as illustrated in Figure 5.24) and this leads

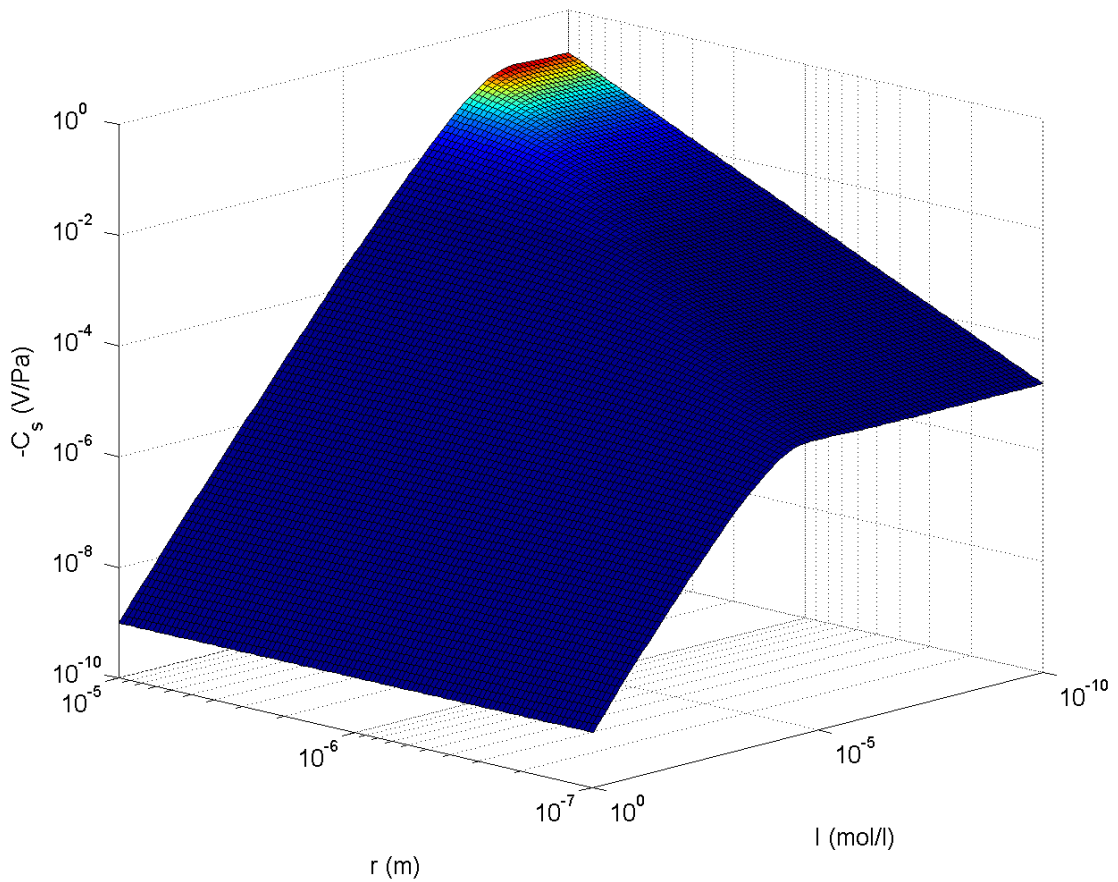


Figure 5.25: Coupling coefficient plotted against capillary radius and fluid molarity (only NaCl) for a cylindrical capillary for Berea 700 at 20 °C

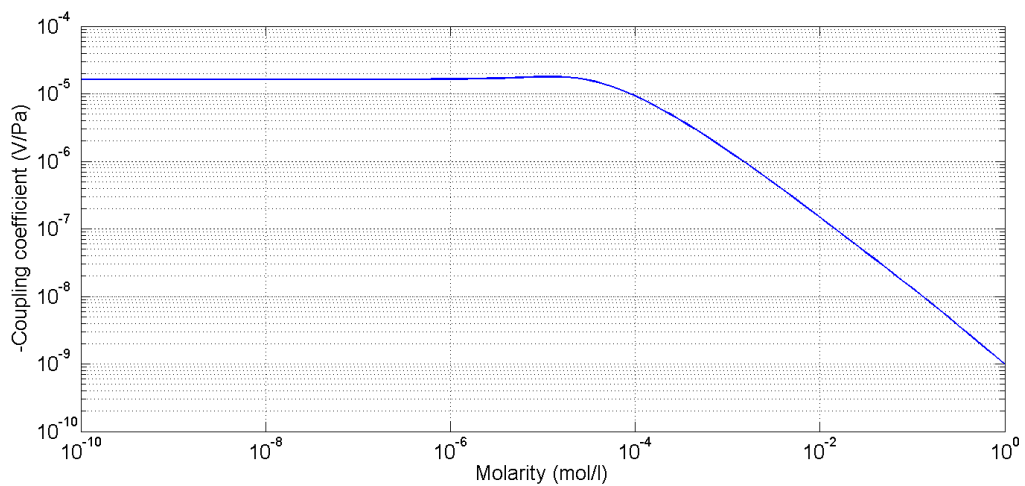


Figure 5.26: Effect of surface conductance in a single circular capillary of  $r = 1E-7$  for different fluid molarities (only NaCl) for a Berea 700 sandstone at 20 °C

to a delayed overlapping of double layers when moving from high salinity to low salinity. This is why the red curve extends out higher than the blue base case curve.

Case 2 shows that an increase in temperature does not change the coupling coefficient by much. The

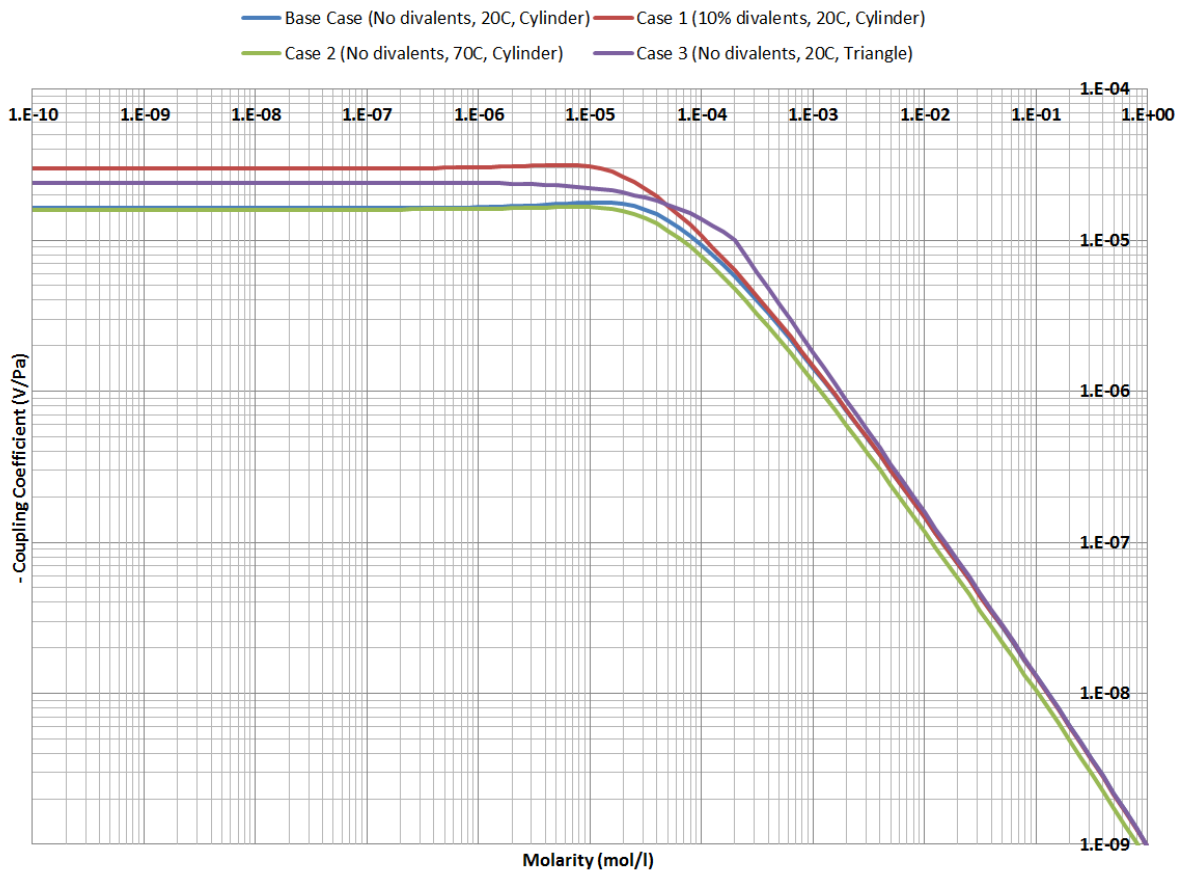


Figure 5.27: Trends in the single phase model for Berea 700 sandstone with a capillary channel of  $r = 1E - 7$  (amount of divalents, temperature, geometry)

temperature increase influences almost every input of the equation ( $\uparrow$  temperature,  $\downarrow$  electric permittivity,  $\uparrow$  conductance,  $\downarrow$  viscosity), but when one looks at the coupling coefficient these factors and changes almost balance out completely. The case for increased temperature does show a slightly lower curve than the base case, but this is a small change.

Case 3 shows that a change in geometry also influences the coupling coefficient curve. The radius of the cylinder is taken as the inscribed radius of the triangle, so the triangular geometry is slightly larger than the cylinder it is compared to. The cross-sectional area is larger and therefore one can see that the overlapping occurs in a later stage. The discontinuity in the curve for case 3 is caused by a switch from the equation for large  $\kappa r$  to small  $\kappa r$ .

Figure 5.28 shows the base case model ( $r = 1E - 7$ , no divalents, 20 °C, cylindrical geometry) for the three different sandstones. The differences in the curves are only caused by the difference in zeta potentials, which are given as an input according to the relations in Figures 5.17, 5.18 and 5.19. The value of the zeta potential influences the thickness of the double layer. In the low-salinity region, the curves converge, as double layers there overlap so much, that the small difference in zeta potential does not cause a different charge transport and thus the coupling coefficients are almost equal. In the region where salinity is higher, the curves are dominated by the value of the zeta potential, which is described by the relations in Figures 5.17, 5.18 and 5.19. For example, the Bentheimer curve starts at a lower value at high salinity and then climbs to a higher value of the coupling coefficient at lower salinity. This is because the input of the zeta potential has a steeper gradient.

Figure 5.29 shows models for Bentheimer and Berea 700 with the assigned average pore throat radius ( $r_{throat,average}$ ) as input of the capillary tube model. For the Bentheimer, a cylindrical capillary tube is modeled, without any added divalents at 20 °C. For the Berea 700 sandstone, a cylindrical capillary tube is modeled, with 10 % divalents and at both 20 and 70 °C. One can see that the Bentheimer model extends further to the top, as the Bentheimer has a larger average pore throat size. Also, the curve for the Berea 700 at an

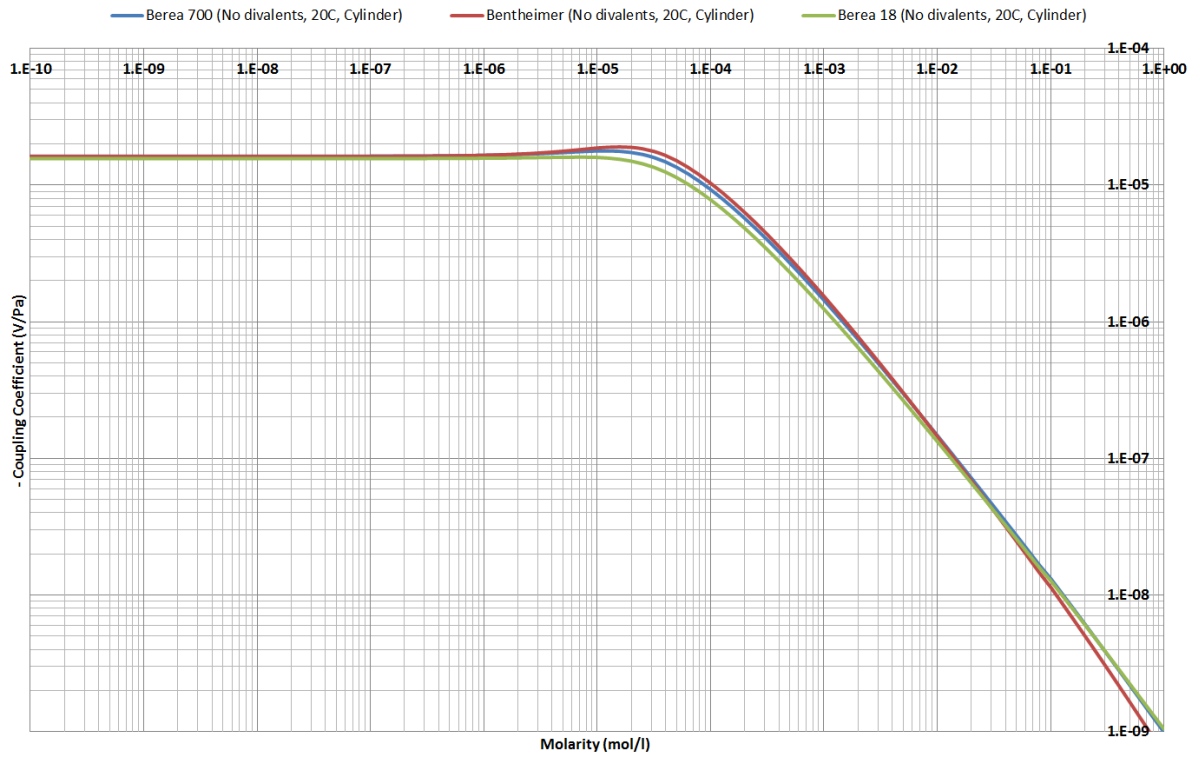


Figure 5.28: Trends in the single phase model for a cylindrical capillary channel of  $r = 1E-7$  without divalents at  $20\text{ }^{\circ}\text{C}$  for different lithologies)

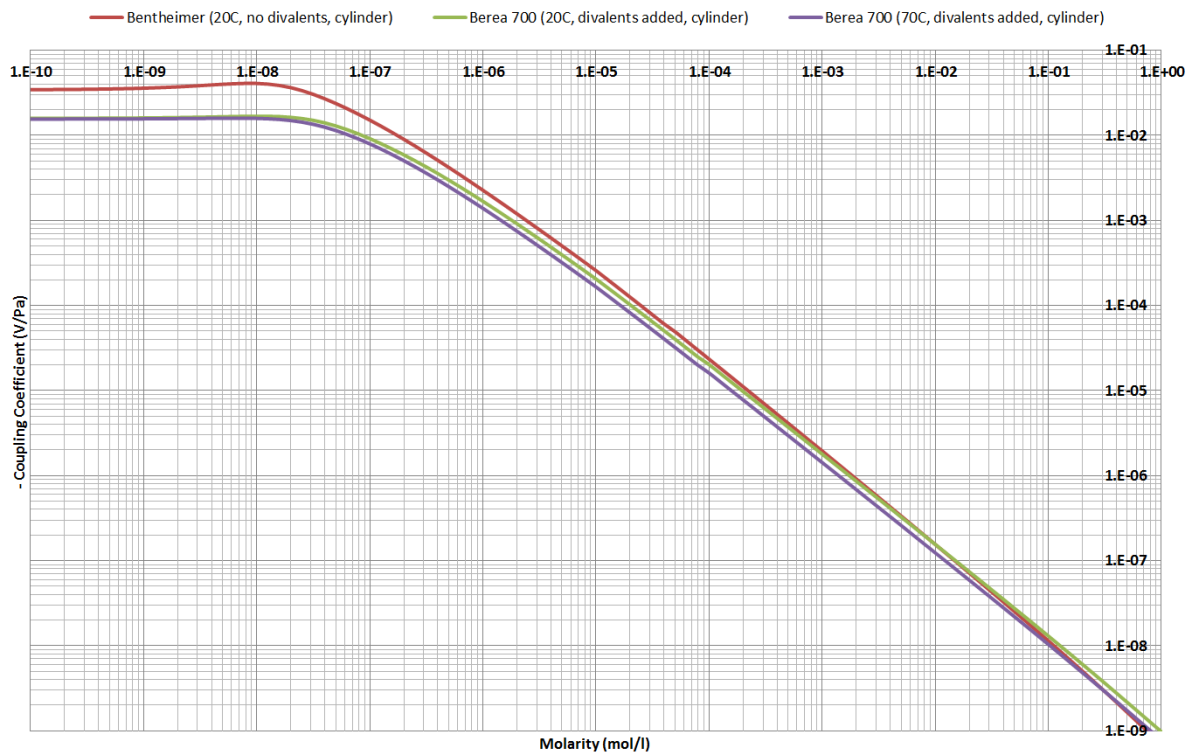


Figure 5.29: Coupling coefficient curves for Bentheimer and Berea 700 sandstone for their assigned average pore throat radius ( $r_{throat,average}$ ) and a cylindrical geometry)

increased temperature of 70 °C lies slightly below the curve for 20 °C.

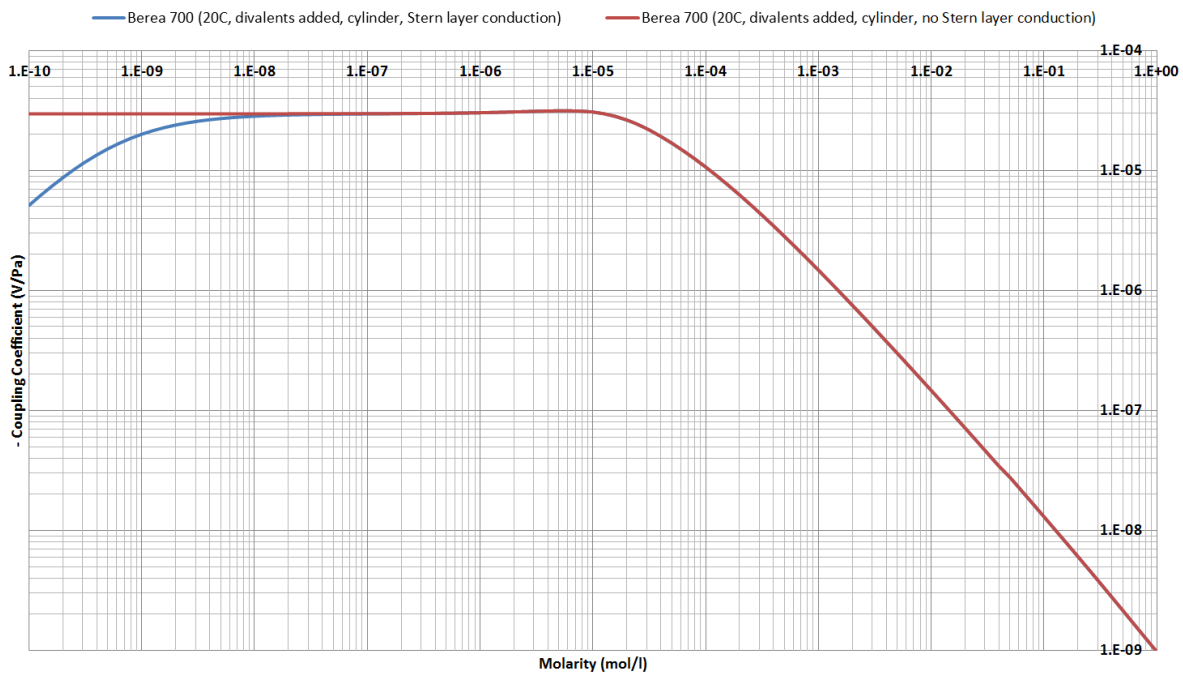


Figure 5.30: Trends in the single phase model for a cylindrical capillary channel of  $r = 1E - 7$  for Berea 700 with divalents at 20 °C for for a case with Stern layer conduction and one without Stern layer conduction

Figure 5.30 shows a comparison of the Berea 700 model (a cylindrical geometry, with added divalents, at 20 °C and a pore throat radius of  $1E-7$  m) with the equivalent model now containing Stern layer conduction. The Stern layer conduction is inserted in the equations as described in Subsection 4.4.1. The value that is used for the Stern layer conduction is:  $\Sigma_S^{Stern} = 1E - 15$  in Siemens. As can be seen in Figure 5.30, the Stern layer conduction becomes more important at a lower salinity. At this low salinity, the conductivity of the fluid is very low, and therefore conduction over the surface of the rock forms a significant contribution to the flow of charge upstream, and therefore a reduction of the streaming potential value.

#### BUNDLE OF TUBES (BOT) MODEL

In this Subsubsection, bundle-of-tubes models for single-phase streaming potential will be discussed. These bundle-of-tubes models are based on the model as explained in Section 4.5. Over this bundle exists one pressure difference and one potential difference. The bundle-of-tubes models use the pore size distributions as obtained from the pore network extraction as an input. These will be the base cases. Also, cases where Stern layer conduction is included will be discussed, as well as cases where the pore size distribution is lowered with two orders of magnitude to get an idea of such an effect.

Figure 5.31 shows bundle-of-tubes models for Bentheimer (no divalents, cylinder, 20 °C and no Stern layer conduction), and Berea 700 at both 20 °C and 70 °C (no divalents, cylinder and no Stern layer conduction), as well as these three models including Stern layer conduction with a value of  $\Sigma_S^{Stern} = 1E - 8$ .

One can see that both in the case of the model with and without surface conduction added in, the curve for the Bentheimer lies above the curves for Berea 700 in the low salinity region. This is because Bentheimer has more pore throats with a larger radius.

For the two Berea cases without Stern layer conduction added in, the curve for 20 °C lies above the curve for 70 °C. In the case of the Berea with Stern layer conduction, the curve for 70 °C lies above the curve of 20 °C.

Clearly visible is that the Stern layer conduction has a large influence on the coupling coefficients at much lower salinity. This is because, at much lower salinity, the conduction of the fluid in between the shear planes becomes very low, whereas the Stern layer conduction in the model remains constant. Therefore, at lower salinity, the relative importance of Stern layer conduction increases. This prohibits the existence of a large potential difference, as shown in the model without Stern layer conduction. On a side note, this very low salinity is out of the scope of LSF, which is concentrated on a salinity region around 1500 – 5000 ppm.

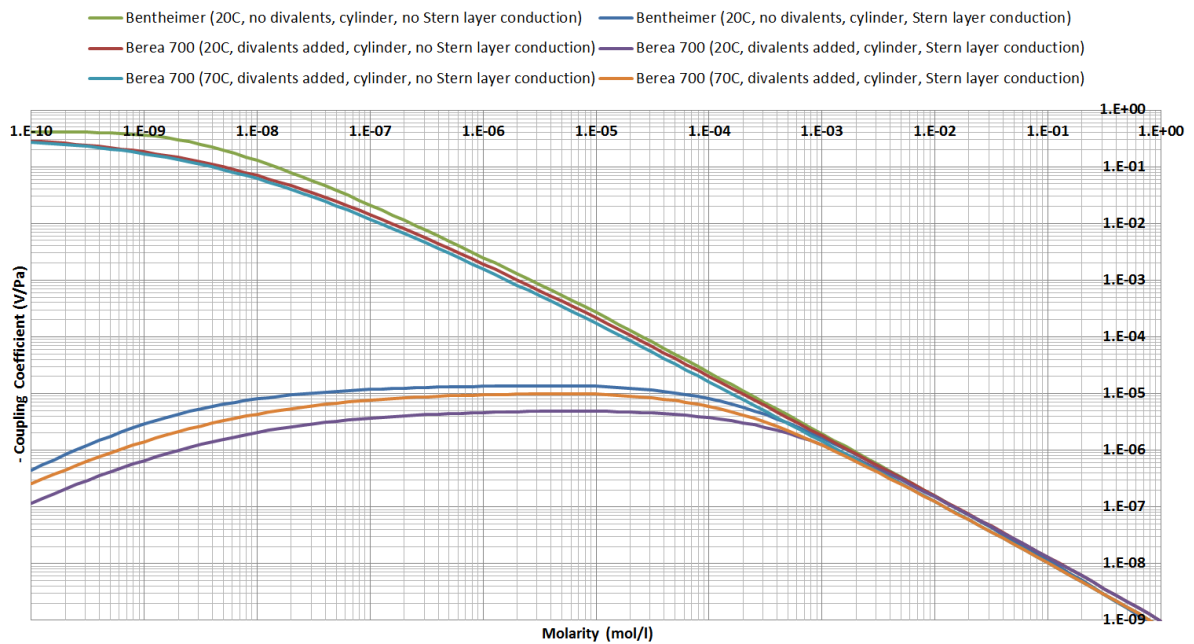


Figure 5.31: Bundle-of-tubes models for single-phase streaming potential in Bentheimer and Berea 700. Input are the pore throat radii from micro CT data. Bentheimer is only considered at 20 °and without divalents (as in the experiments) and Berea 700 is considered at both temperatures and with divalents. Three curves include Stern layer conduction with a value of  $\Sigma_S^{Stern} = 1E-8$  to sketch the influence of the Stern layer conduction

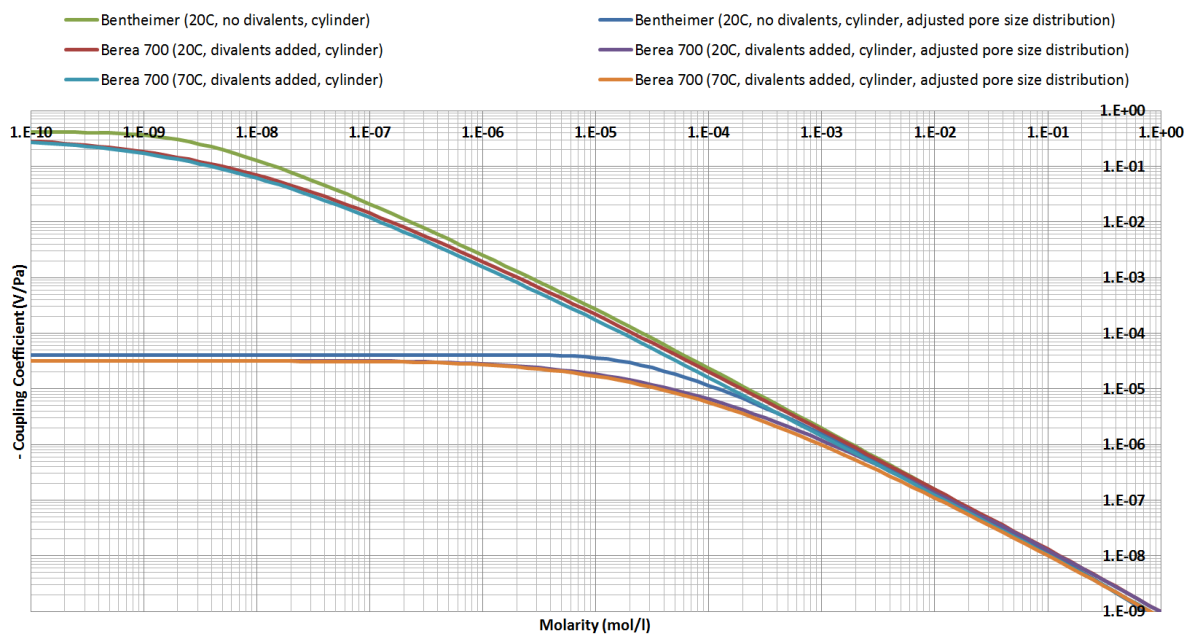


Figure 5.32: Bundle-of-tubes models for single-phase streaming potential in Bentheimer and Berea 700. Input are the pore throat radii from micro CT data. Bentheimer is only considered at 20 °and without divalents (as in the experiments) and Berea 700 is considered at both temperatures and with divalents. Three curves have an adjusted pore size distribution as input; all the pore throat sizes are multiplied by a factor of  $10^{-2}$

Figure 5.32 shows the three curves without Stern layer conduction or adjusted pore throat distribution, as displayed in Figure 5.31 as well. In addition, it shows the results for a bundle-of-tubes model where the pore throat radius distribution is lowered entirely by two orders of magnitude (a factor of  $10^{-2}$ ).

Because of the smaller pore throat radii, the double layers start overlapping at a lower salinity and this is shown in the earlier bend of the coupling coefficient (already at a higher salinity / lower coupling coefficient).

The bend of this model is around the same place as the bend showed in Figure 5.31, which is caused by Stern layer conduction. They differ in appearance as the Stern layer conduction becomes more important at lower salinity (therefore it shows the continued bend downwards at low salinity) and the bend of the curve in the model with adjusted pore throat radii is caused by the earlier overlapping of the double layers, when going from high to low salinity. This does not show increased importance from low salinity to very low salinity, as the charge transport upstream and downstream reaches a certain maximum. This maximum is caused by the fact that a slight increase of overlapping of two already overlapping double layers, does not change the coupling coefficient significantly anymore.

#### PORE-NETWORK MODEL (PNM)

Results of pore-network modeling have unfortunately not been obtained. However, one can argue here that a pore-network model would give a different response to an applied pressure drop over the system than a bundle-of-tubes model would. This is because in a BOT model all tubes of different radii have the same pressure drop over them. Looking at the coupled electrokinetic equations for a BOT model, one can observe that the large tubes will play a large role in determining the potential drop over the system, as can be seen in the BOT models discussed in the previous section. However, a sandstone sample does not have its pores parallel to each other, but instead the pore bodies and pore throats form a network with a certain coordination number  $z$ . The liquid flowing in this medium will try to find the path of least resistance. This path of least resistance will be a series of pores, in which the largest part of the pressure drop will be over the smaller pore throats in this series. This would increase the relative importance of these small pores with regard to the potential drop over the system. Therefore, the coupling coefficients at lower salinities will be lower in the PNM than in a BOT model.

#### 5.2.4. TWO PHASE

In this subsection the models for two-phase streaming potential will be discussed. Two types of bundle-of-tubes models are presented, one with a water-wet configuration and one with an oil-wet configuration.

##### BUNDLE OF TUBES (BOT) MODEL

The geometry of the water-wet and oil-wet models is described in Subsection 4.4.2. Here, the results of these two-phase BOT models are presented for different oil saturations and with adjusted pore sizes, and Stern layer conduction added in.

Figure 5.33 shows seven different curves. One is the base case single-phase BOT for Berea 700 at 20 °C with added divalents and without Stern layer conduction. The first three curves below that show the water-wet two-phase BOT model for different capillary pressures. These different capillary pressures cause different oil saturations in the bundle. Oil saturations range from  $S_o = 0.06$  to  $S_o = 0.38$ . One can see that a higher oil saturation, which means a lower water saturation, causes the curve to be lower at low salinity. They show an earlier bend. This is due to the fact that the effective pore radius for water to flow is smaller for higher saturations of oil. Also, the velocity of the fluid may be lower for a similar pressure drop over the system.

The other three curves in Figure 5.33 show the same water-wet two-phase BOT model, but now for an adjusted pore throat radius distribution, which is lowered entirely by two orders. The lowering of the radii of the tubes with two orders of magnitude, leads to an increase of capillary pressure of two orders of magnitude to obtain the same oil saturations in the model. The other conditions are similar to the other curves. One can see that the curves with the adjusted pore throat distribution show a bend in the curve already around a salinity of  $10^{-4}$  and again, a higher oil saturation leads to a smaller effective radius for the water to flow and thus a lower curve.

Figure 5.34 shows the a water-wet two-phase BOT model with Stern layer conduction added in. The value for the Stern layer conduction is  $\Sigma_S^{Stern} = 1E - 8$ . One curve shows the base case single-phase BOT model for Berea 700 at 20 °C and with added divalents. The other three curves represent the water-wet BOT model with decreasing water saturation moving downward. The characteristics of the curve match with the characteristics (the downward bend in the curve at low salinity due to the increase of relative importance of Stern layer conduction there) that can be observed in Figures 5.30 and 5.31.

Figure 5.35 shows a couple of two-phase oil-wet BOT curves compared against the single-phase Berea 700 base case. One can see that the curves are very close to the single-phase case. This is because in the oil-wet model, the water resides in the middle, and therefore, unlike in the water-wet triangular corners, the water sits in the middle and the area of the effective flow path (effective area of the hexagonal shape in the middle) of the water is rather similar to the single-phase case. Also, due to the same designed geometry, the

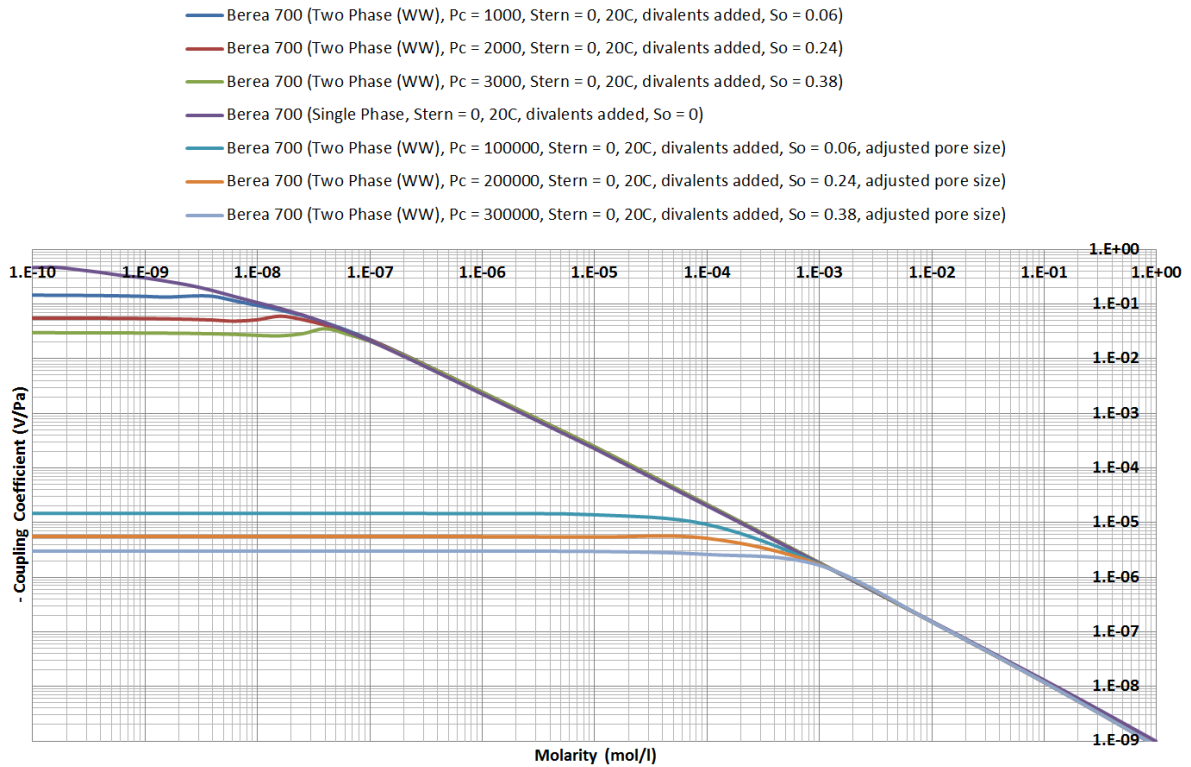


Figure 5.33: Water-wet bundle-of-tubes models for two-phase streaming potential in Berea 700. Three curves have original pore throat radii as input and different capillary pressures (in  $Pa$ ) determine the different saturations. The other three curves have an adjusted pore size distribution as input, and therefore need a higher capillary pressure (in  $Pa$ ) for the same saturations; all the pore throat sizes are multiplied by a factor of  $10^{-2}$

model would become unphysical at an oil saturation under  $S_o = 0.33$ . One can see that with increasing water saturation the curves differ more from the single-phase base case, but due to these two limitations the model does not differ enough to be useful. On the other hand, it sketches the theoretical case for a fully oil-wet model, which does not occur inside a reservoir rock, but might well be a good representation of a real full oil-wet case.

### 5.3. COMPARISON OF EXPERIMENTS AND MODEL

In this section, we will compare the experimental lab data with the different models as discussed before. This includes capillary tube models, bundle-of-tubes models and also BOT models that include Stern layer conduction as well as models that contain an adjusted pore size distribution.

Figure 5.36 shows a comparison of the Bentheimer 20 °C single-phase lab data with several models. The model that shows the best fit is the BOT model with Stern layer conduction added in. Figure 5.37 shows a comparison of the Bentheimer 20 °C two-phase lab data with the different models: a BOT model, a BOT model with added Stern layer conduction and a BOT model with an adjusted pore size distribution. The best fit is again given by the BOT model with added Stern layer conduction. Figure 5.38 shows a comparison of the Bentheimer 20 °C two-phase lab data with added divalents (10 %  $CaCl_2$ ) with models. Here, the BOT model with Stern layer conduction added in gives a good fit as well.

Figure 5.39 shows all Bentheimer lab data (see previously Figure 5.8) with the best-fit models as discussed in Figures 5.36, 5.37 and 5.38. The figure also show a fit to data assembled by Vinogradov et al. [2010] as used by Glover et al. [2012]. This is a fit to a data set containing a lot of experimental streaming potential results.

One can see that the models give a reasonable fit to the lab data. However, the models are better at predicting trends in the data than they are at accurately representing the lab data. One should also keep in mind that the Stern layer conduction is used as a fitting parameter to get a better match of the lab data to the model at low salinity. The BOT model without Stern layer conduction or adjusted pore throat distribution is very far off the laboratory data in the low salinity region. Also, the adjustment of the pore throat radius distribution with two orders of magnitude is a big change, and although the models fits, this is not a realistic model of the

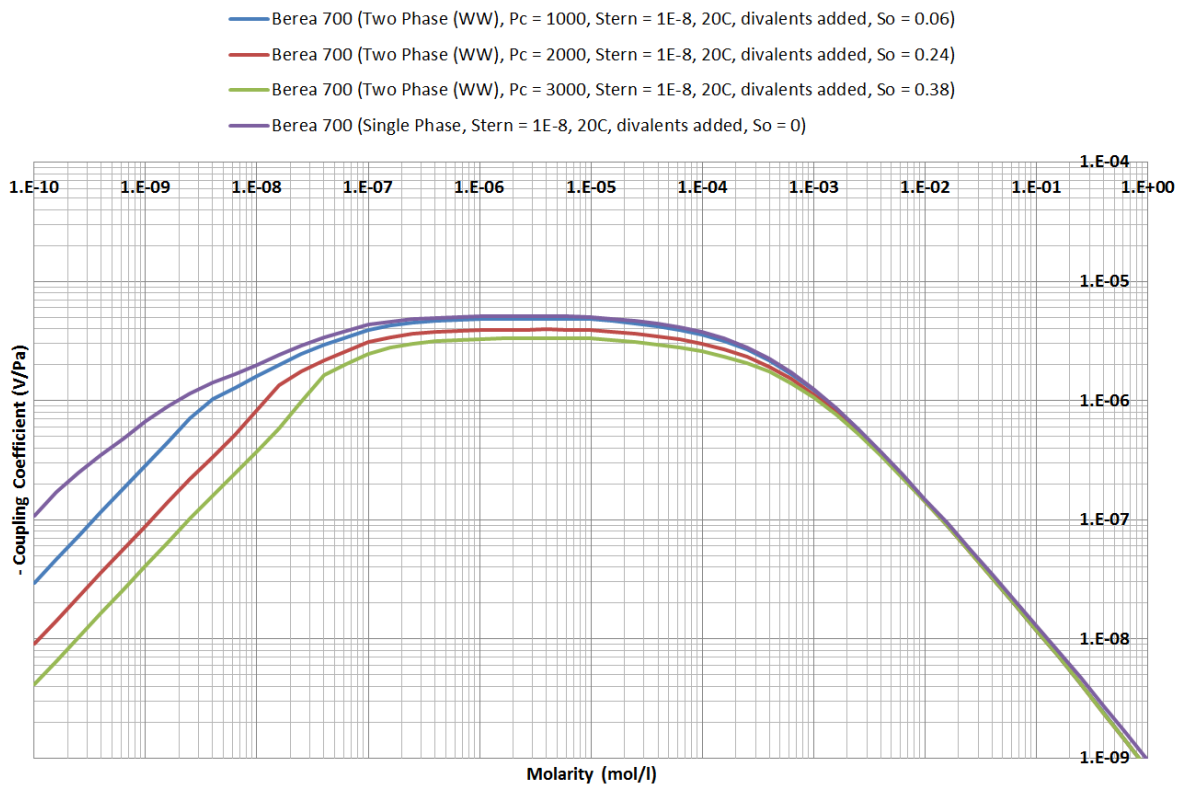


Figure 5.34: Water-wet bundle-of-tubes models for two-phase streaming potential in Berea 700. The four curves have original pore throat radii as input and include Stern layer conduction of  $\Sigma S^{Stern} = 1E-8$  and different capillary pressures determine the different saturations

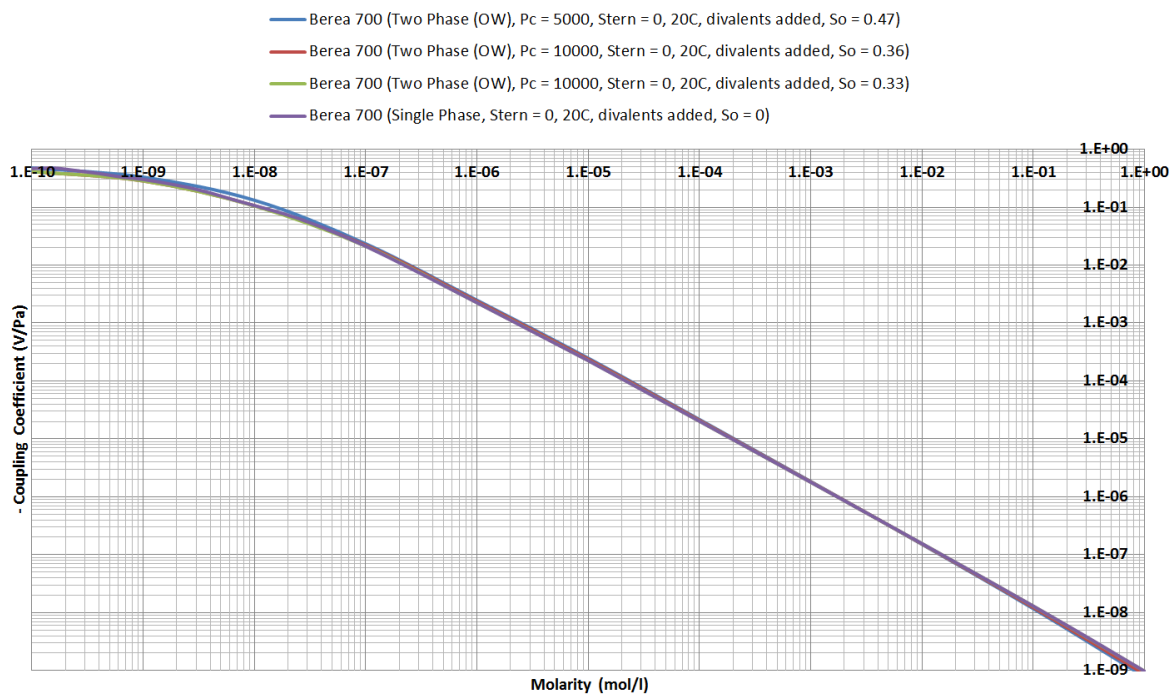


Figure 5.35: Oil-wet bundle-of-tubes models for two-phase streaming potential in Berea 700. The four curves have original pore throat radii as input and different capillary pressures determine the different saturations

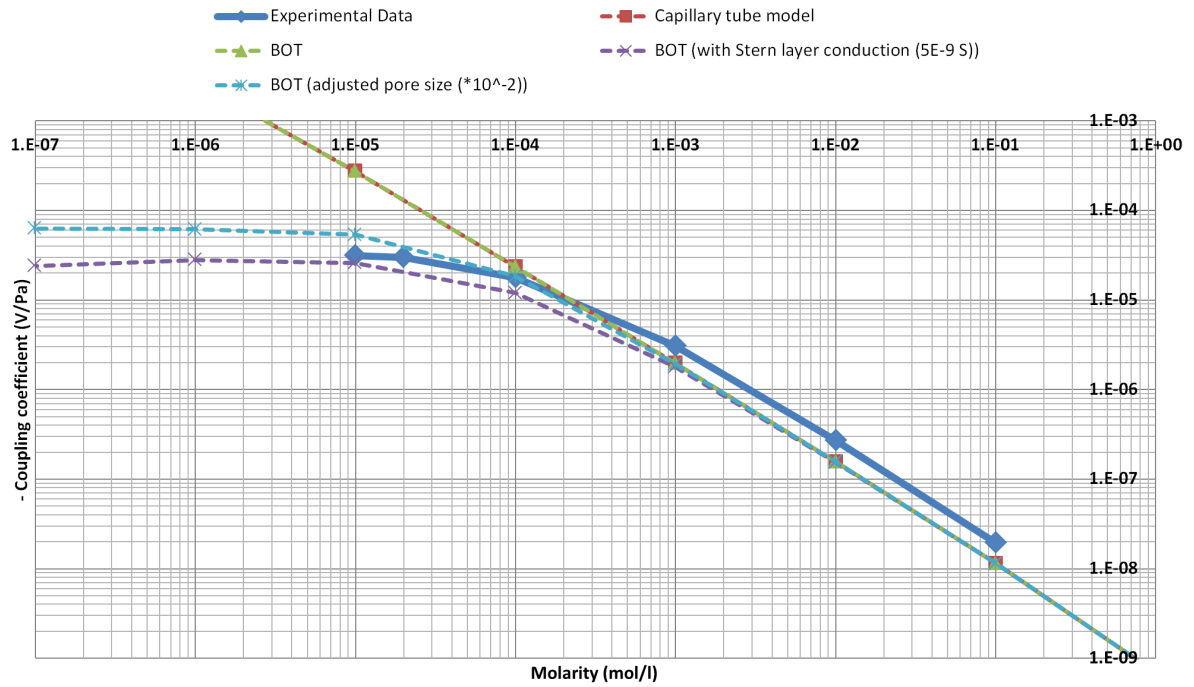


Figure 5.36: A comparison for Bentheimer 20°C single-phase lab data with models: a capillary tube model, a bundle-of-tubes model, a BOT model with Stern layer conduction (5E-9 S) and a BOT model with an adjusted pore size distribution (multiplied with  $10^{-2}$ )

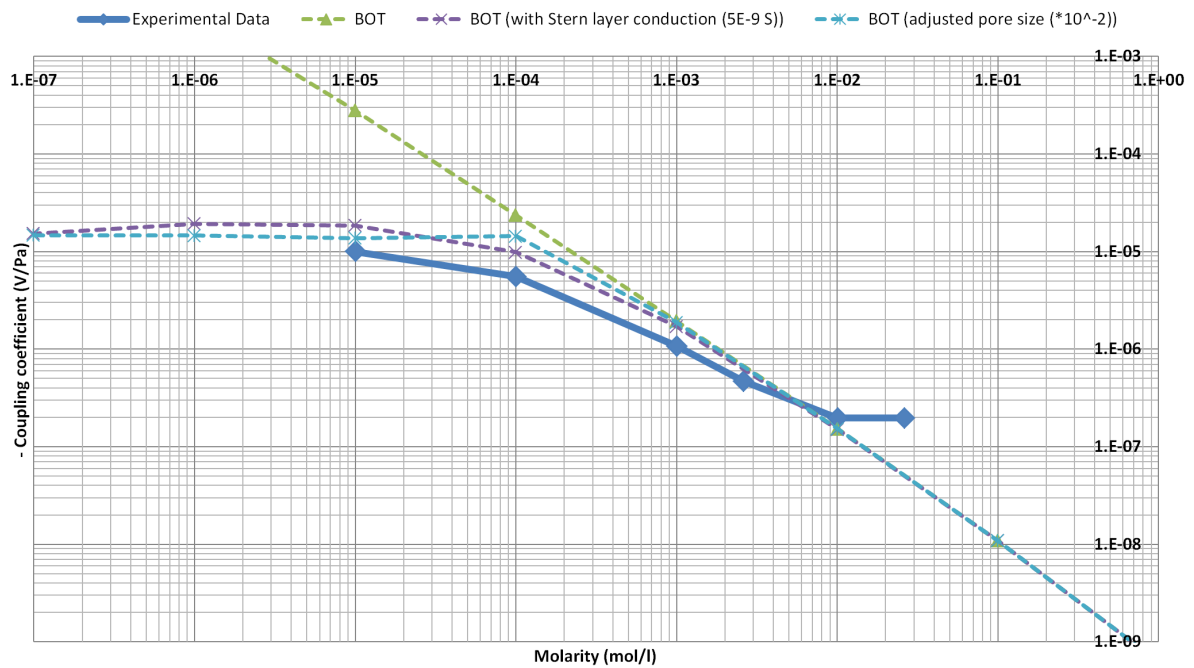


Figure 5.37: A comparison for Bentheimer 20°C two-phase lab data with models: a bundle-of-tubes model, a BOT model with Stern layer conduction (5E-9 S) and a BOT model with an adjusted pore size distribution (multiplied with  $10^{-2}$ ).  $S_o = 0.22$  in all cases

phenomena occurring inside the core.

Figure 5.40 shows a comparison of the Berea 700 20 °C single-phase lab data with several models. The model that shows a good fit is the BOT model with Stern layer conduction added in. The Stern layer conduction has a different value than in the Bentheimer case to obtain the fit. Figure 5.41 shows a comparison of the Berea 700 70 °C single-phase lab data with several models. The value for the Stern layer conduction is again

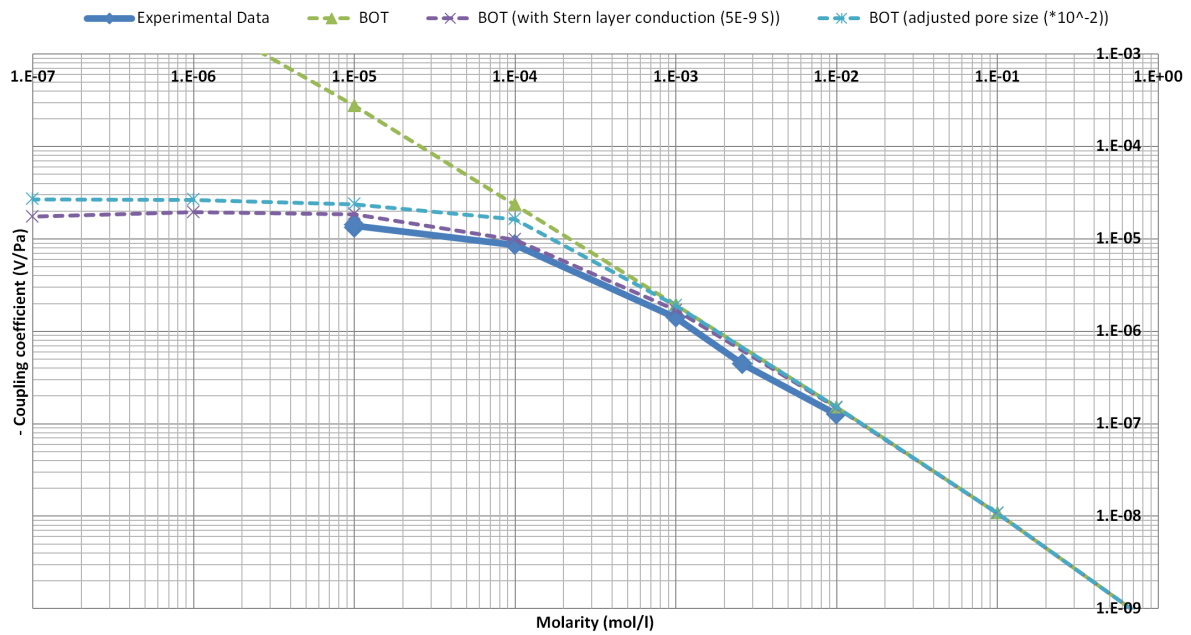


Figure 5.38: A comparison for Bentheimer 20 °C two-phase (with added divalents) lab data with models: a bundle-of-tubes model, a BOT model with Stern layer conduction (5E-9 S) and a BOT model with an adjusted pore size distribution (multiplied with  $10^{-2}$ ).  $S_o = 0.22$  in all cases

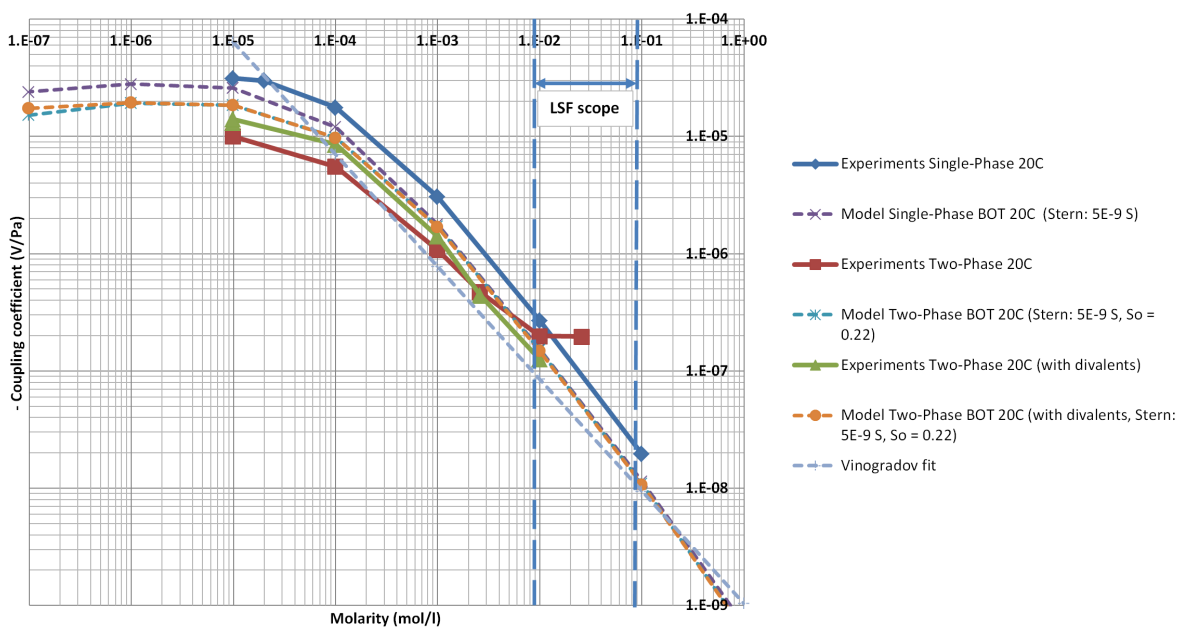


Figure 5.39: All Bentheimer lab data compared to the best-fit models

adjusted for a fit. Also, the factor of the adjusted pore size multiplication is adjusted.

Figure 5.42 shows a comparison of the Berea 700 70 °C unaged two-phase lab data with the different models: a BOT model, a BOT model with added Stern layer conduction and a BOT model with an adjusted pore size distribution. The oil saturation is calculated at  $S_o = 0.24$ . The model with adjusted pore size radii comes closest to a fit, but no model fits really well to the data. Figure 5.43 shows a comparison of the Berea 700 70 °C aged two-phase lab data with the different models. The oil saturation is calculated at  $S_o = 0.2$ . The model with Stern layer conduction added in comes close to a fit.

Figure 5.44 shows an overview of all Berea 700 lab data (see previously Figure 5.10) with the the models that gives the approximate best fit. The figure also show a fit to data assembled by Vinogradov et al. [2010]

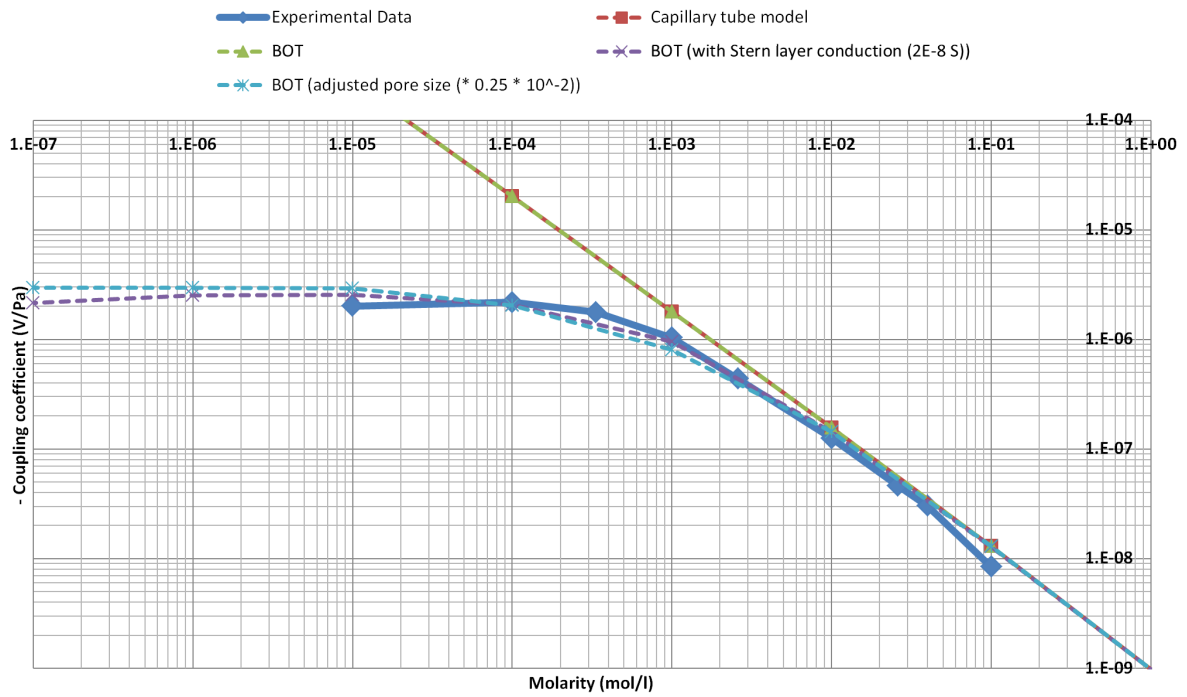


Figure 5.40: A comparison for Berea 700 20 °C single-phase lab data with models: a capillary tube model, a bundle-of-tubes model, a BOT model with Stern layer conduction (2E-8 S) and a BOT model with an adjusted pore size distribution (multiplied with  $0.25 \times 10^{-2}$ )

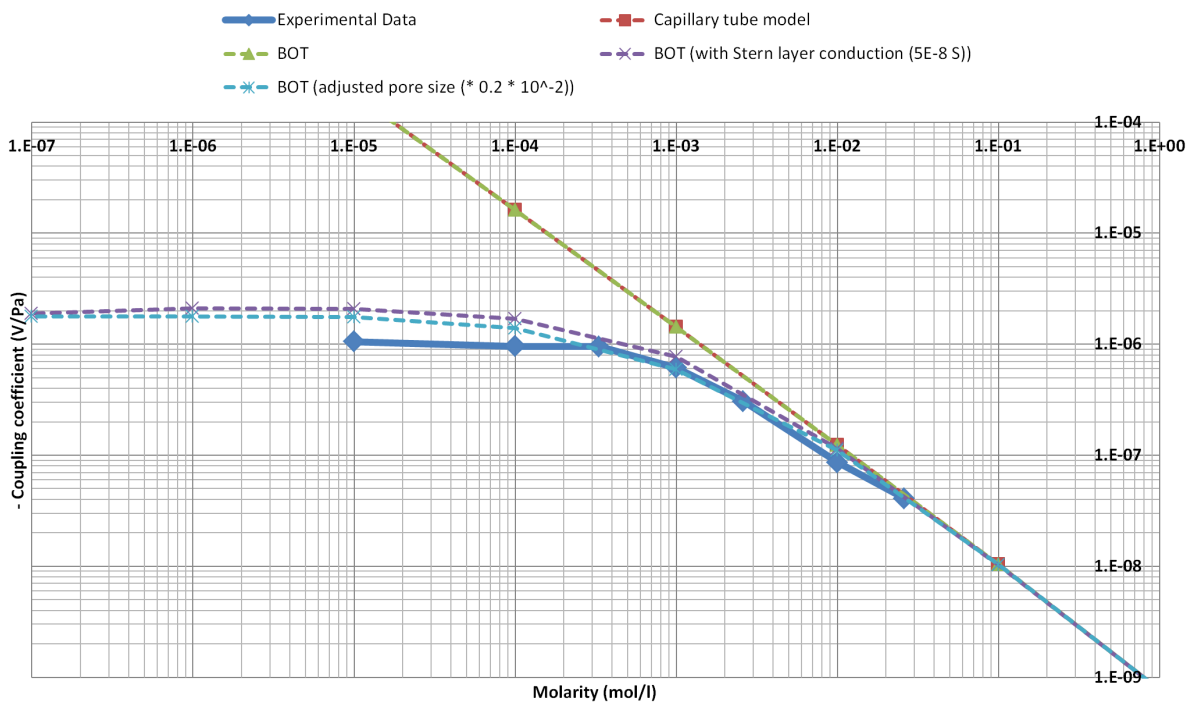


Figure 5.41: A comparison for Berea 700 70 °C single-phase lab data with models: a capillary tube model, a bundle-of-tubes model, a BOT model with Stern layer conduction (5E-8 S) and a BOT model with an adjusted pore size distribution (multiplied with  $0.2 \times 10^{-2}$ )

as used by Glover et al. [2012]. This is a fit to a data set containing a lot of experimental streaming potential results. Again, although the models give reasonable fits, they are especially useful to predict the trends in the data. Unfortunately, the models and experimental data lie very close to each other in the region that is of most interest to LSF.

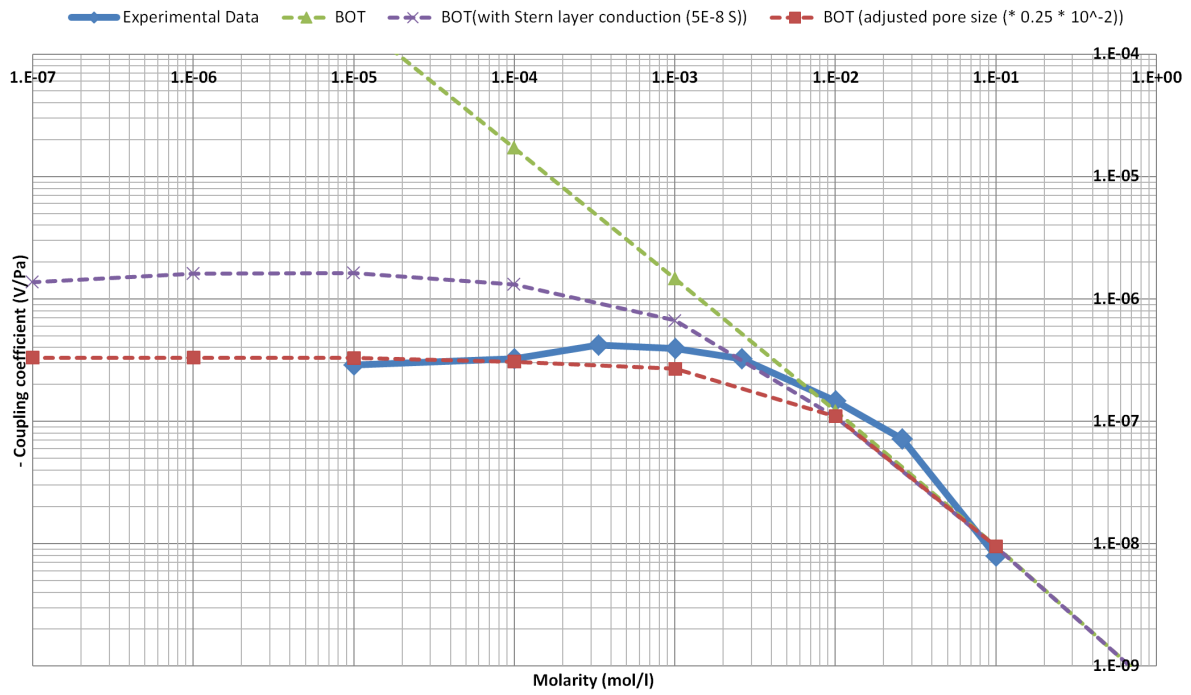


Figure 5.42: A comparison for Berea 700 70 °C two-phase unaged lab data with models: a bundle-of-tubes model, a BOT model with Stern layer conduction (5E-8 S) and a BOT model with an adjusted pore size distribution (multiplied with  $0.25 \times 10^{-2}$ ).  $S_o = 0.24$  in all cases

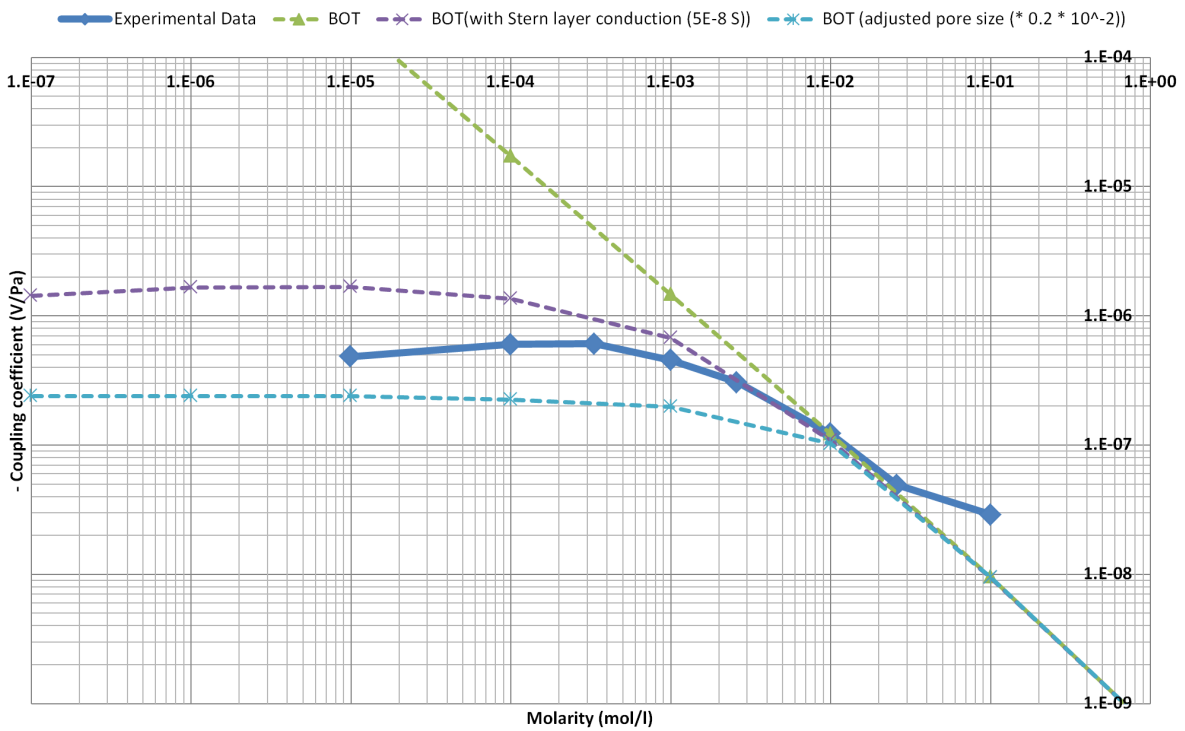


Figure 5.43: A comparison for Berea 700 70 °C two-phase aged lab data with models: a bundle-of-tubes model, a BOT model with Stern layer conduction (5E-8 S) and a BOT model with an adjusted pore size distribution (multiplied with  $0.2 \times 10^{-2}$ ).  $S_o = 0.20$  in all cases

### 5.4. FURTHER DISCUSSION

In this section, the further subjects of discussion are highlighted, first for the experiments and then for the modeling part.

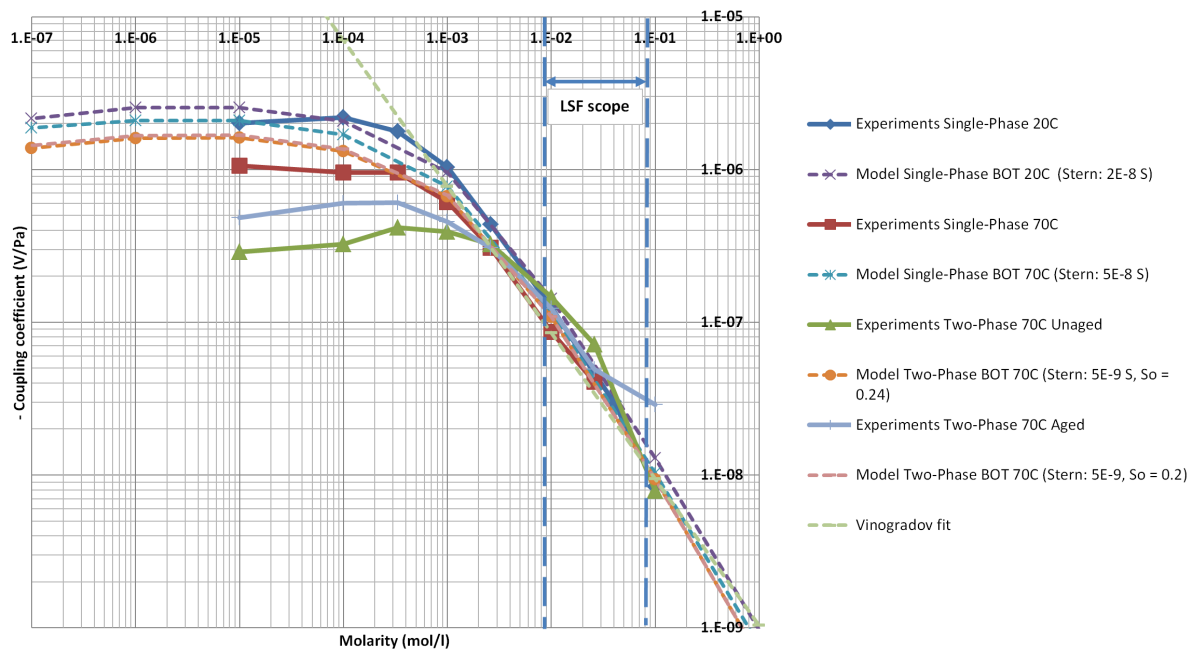


Figure 5.44: All Berea 700 lab data compared to the best-fit models

First of all, in the experiments, a pressure differential meter is used to measure the pressure drop over the core. The flow lines to this pressure differential meter are filled with very low conductive demineralized water. Although the conductivity in these lines is low, it does provide a path for potential to leak, in other words for current to flow back upstream. This effect will become more important at lower salinity. Tests did not show a visible difference in streaming potential, but it might be still influencing the measurements.

Also, measurements at higher salinity can be difficult to obtain, as the conductivity of the electrolyte is very high and a streaming potential does not develop easily. Besides this, there are a lot of processes ongoing in the sandstone core that influence the streaming potential measurements. There are ion exchange processes ongoing in the core, that lead to different outflow salinities compared to the inflow salinities for example. This may lead to nonlinearity of the SP phenomena, as with high flow rates the ion exchange processes might not be as influential as at low rates. Clays on the sandstone surface and irregularities cause different double layers at every place on the rock surface, which all influence the SP response. All these influences can cause the measurement results to differ, when the boundary conditions have not been changed. High flow rates (25 ml/min) that are used to obtain measurements at high salinity could also be tampering with the linear viscous flow profile through the pores.

We assume that the electrodes that measure the streaming potential lie in an equipotential plane and that they do not influence the electric field. However, core cavities are drilled into the rock, that cause a change of the in-situ conditions.

The use of very low salinity electrolytes can lead to formation damage, as we have seen happening in the Berea 700 core. In this case, part of the clays were obviously removed from the core. The charge distribution on the surface of the rock and also the geometry of the pores might have changed.

In the model, first of all, the geometry of the pore throats is simplified to either a cylindrical or a triangular geometry. Besides that, ion exchange is not accounted for in the models, they take the zeta potential at the shear plane as a basis and this zeta potential is constant throughout the whole model. At the basis of all the input equations of the model lie a lot of assumptions as well, which are described in the designated sections. An example of these assumptions is the presence of the surface of shear and the fact that the equations are solved under the Debye-Huckel approximation, which does not allow for asymmetrical electrolytes and high surface potentials.

The amount of oil saturation in the model, is also highly simplified. A certain capillary entry pressure, causes the fully water-wet or oil-wet pores either to be filled with some oil/water or not. The wetting angle is taken for a fully oil- or water-wet situation.

Also, the input of the model generated with the code by [Dong \[2007\]](#) may not lead to an exact represen-

tation of the pore throat radii. Besides that, we also add Stern layer conduction and an adjusted pore size distribution in the model to obtain better fits.

Apart from an indication of wettability alteration when switching from Dagang brine to a synthetic 0.4 M brine (due to charge inversion), no further indication of wettability alteration could be seen at lower salinities. No easy screening criteria based on the zeta potential are possible to be drawn from this work.

## 5.5. RECAP RESULTS AND DISCUSSION

The streaming potential measurements show higher values for the coupling coefficient at very low salinity ( $10^{-5} - 10^{-3} M$ ) if pore geometry is larger. The coupling coefficient is lower in the very low salinity region ( $10^{-5} - 10^{-3} M$ ), when oil saturation in the sample is higher. At a higher salinity ( $10^{-2} - 1 M$ , the LSF region (1500 - 5000 ppm)) it is more difficult to distinguish between the types of sandstone and measurements become difficult as the bulk fluid becomes more conductive. Also, at higher salinity ( $10^{-2} - 1 M$ ) it is more difficult to distinguish between single-phase and two-phase measurements (differences in oil saturation). That region is less geometry dependent and less dependent on Stern layer conduction. The addition of divalents to the brines, leads to smaller double layers (shorter Debye length). This gives higher coupling coefficients at very low salinity ( $10^{-5} - 10^{-3} M$ ). The difference in streaming potential curves between the unaged and aged Berea 700 case is due to a difference in oil saturation. The three effects that have the largest influence on the coupling coefficient are Stern layer conduction, the overlapping of double layers and the effective flow (velocity) through the pores. No measurable incremental oil production was seen in the switch from Dagang brine to synthetic brines; this does not necessarily mean that the LSF effect has not occurred.

Charge inversion was observed in three cases, with single-phase streaming potential experiments at 70 °C and the two-phase unaged and aged streaming potential experiments at 70 °C all with Dagang brine. This indicates that the zeta potential has an opposite sign compared to the surface charge and this might indicate that the positively charged system would like to bind negative oil components to it. This might influence wettability of the rock. The effect is not seen with all other brines, not even a synthetic brine of the same ionic strength (containing less divalents).

The zetasizer experiments show clear trends. When ionic strength is lowered, the zeta potential becomes more negative. When pH is lowered, the zeta potential becomes less negative. This is the case for all brine-rock combinations. The oil-rock experiments have only been performed at one pH and when ionic strength is lowered, the zeta potential becomes more negative. The zeta potentials do not become positive, so there is no charge inversion.

The pore throat size distribution from the network extraction code shows a clear difference between Berea and Bentheimer sandstones. The Bentheimer sandstone has more pore throat radii of larger size.

The capillary tube model is able to show trends in temperature, divalent content and geometry. Also, the concepts of overlapping double layers and Stern layer conduction are visible in the model. Bundle-of-tubes models that use pore throat radii from the pore network extraction also show these trends in temperature, divalent content and geometry, as well as overlapping double layers at low salinities. It is possible to add Stern layer conduction to the BOT models as well. A model that can describe the overlapping of double layers and the Stern layer conduction has not been made before. BOT models with an adjusted pore size distribution are also considered. The two-phase water-wet BOT model is able to represent trends in oil saturation.

The models are compared to the experimental data. This comparison shows that the models that include the overlapping of double layers and Stern layer conduction represent the laboratory data best. The Stern layer conduction can be used as a fitting parameter. The two-phase water-wet models show similar trends compared to the lab data. 0



# 6

## SUMMARY AND CONCLUSIONS

This chapter will present a summary of the content of this thesis. Hereafter, we itemize the conclusions as they can be deduced from the discussions in this thesis.

A streaming potential setup has been established at Delft University. This setup can be used for follow-up experiments. The components of the setup and experimental protocols are described in detail. It is possible to do single-phase and two-phase experiments in the setup. Experiments with crude oil had not been done before. Detailed methods to obtain a low residual water saturation in the core for aging are also described. The fluid-rock combinations that are used in both the streaming potential and zetasizer experiments and the motivations behind these choices are described in detail. Protocols for the zetasizer experiments are also described; zetasizer experiments over a range of pH should not be performed automatically.

The equations used in the modeling part allow for different geometries (cylinder and triangle), temperatures, divalent content, the overlapping of double layers and Stern layer conduction. The combination of overlapping double layers and Stern layer conduction has not been presented before. Input of the models are pore size distributions obtained from micro CT data and zeta potentials as obtained from zetasizer experiments. We introduce the possibility of modeling two-phase electrokinetic flow in a water-wet and oil-wet configuration. The idea for the mixed-wet configuration is presented. These equations can be used as input for a BOT model or a PNM.

The streaming potential measurements show higher values for the coupling coefficient at very low salinity ( $10^{-5} - 10^{-3} M$ ) if pore geometry is larger. The coupling coefficient is lower in the very low salinity region ( $10^{-5} - 10^{-3} M$ ), when oil saturation in the sample is higher. At a higher salinity ( $10^{-2} - 1 M$ , the LSF region (1500 - 5000 ppm)) it is more difficult to distinguish between the types of sandstone and measurements become difficult as the bulk fluid becomes more conductive. Also, at higher salinity ( $10^{-2} - 1 M$ ) it is more difficult to distinguish between single-phase and two-phase measurements (differences in oil saturation). That region is less geometry dependent and less dependent on Stern layer conduction. The addition of divalents to the brines, leads to smaller double layers (shorter Debye length). This gives higher coupling coefficients at very low salinity ( $10^{-5} - 10^{-3} M$ ). The difference in streaming potential curves between the unaged and aged Berea 700 case is due to a difference in oil saturation. The three effects that have the largest influence on the coupling coefficient are Stern layer conduction, the overlapping of double layers and the effective flow (velocity) through the pores. No measurable incremental oil production was seen in the switch from Dagang brine to synthetic brines; this does not necessarily mean that the LSF effect has not occurred.

Charge inversion was observed in three cases, with single-phase streaming potential experiments at 70 °C and the two-phase unaged and aged streaming potential experiments at 70 °C all with Dagang brine. This indicates that the zeta potential has an opposite sign compared to the surface charge and this might indicate that the positively charged system would like to bind negative oil components to it. This might influence wettability of the rock. The effect is not seen with all other brines, not even a synthetic brine of the same ionic strength (containing less divalents). It would be interesting to investigate this in more detail.

The zetasizer experiments show clear trends. When ionic strength is lowered, the zeta potential becomes more negative. When pH is lowered, the zeta potential becomes less negative. This is the case for all brine-rock combinations. The oil-rock experiments have only been performed at one pH and when ionic strength is lowered, the zeta potential becomes more negative. The zeta potentials do not become positive, so there is no charge inversion.

The pore throat size distribution from the network extraction code shows a clear difference between Berea and Bentheimer sandstones. The Bentheimer sandstone has more pore throat radii of larger size.

The capillary tube model is able to show trends in temperature, divalent content and geometry. Also, the concepts of overlapping double layers and Stern layer conduction are visible in the model. Bundle-of-tubes models that use pore throat radii from the pore network extraction also show these trends in temperature, divalent content and geometry, as well as overlapping double layers at low salinities. It is possible to add Stern layer conduction to the BOT models as well. A model that can describe the overlapping of double layers and the Stern layer conduction has not been presented before. BOT models with an adjusted pore size distribution are also considered. The two-phase water-wet BOT model is able to represent trends in oil saturation.

The models are compared to the experimental data. This comparison shows that the models that include the overlapping of double layers and Stern layer conduction represent the laboratory data best. The Stern layer conduction can be used as a fitting parameter. The two-phase water-wet models show similar trends compared to the lab data.

For readability, we will present the conclusions in bullet points:

- Streaming potential capabilities for single- and two-phase measurements have been established at Delft University.
- A model (single- and two-phase (water-wet and oil-wet)) has been established that contains both the overlapping of double layers and Stern layer conduction. The model uses input from micro CT data (pore throat radius) and zetasizer measurements. This has not been done in literature before.
- At a higher salinity ( $10^{-3} - 1 M$ ), which coincides with the LSF region of interest (1500 – 5000 ppm), the coupling coefficients are geometry independent, not influenced by Stern layer conduction and more difficult to obtain, due to a high bulk conductivity of the liquid. It is hard to distinguish between measurements in this region; they all lie on the same line.
- Charge inversion in presence of Dagang brine in Berea 700 at 70 °C, indicates a flipped sign of the zeta potential. This might indicate that the positively charged system would like to bind negative oil components to it. This might influence wettability of the rock.
- A comparison of modeling data to experimental data shows that the models that include the overlapping of double layers and Stern layer conduction represent the laboratory data best. The Stern layer conduction can be used as a fitting parameter. The two-phase water-wet models show similar trends compared to the lab data. The three effects that have the largest influence on the coupling coefficient are Stern layer conduction, the overlapping of double layers and the effective flow (velocity) through the pores.

So if we look back on the goals of this thesis formulated in the first chapter, one can make the following table:

Table 6.1: Reflection on goals set at the start of this thesis

1.	The comparison of single-phase streaming potential measurements to models (BOT and PNM) with electrophoretic measurements as zeta potential input	≈ ✓
2.	The comparison of single-phase streaming potential measurements to two-phase streaming potential measurements	✓
3.	The comparison of two phase streaming potential measurements with water-wet and oil-wet models (BOT)	✓
4.	The use of streaming potential measurements to assess the qualitative response in two-phase core flooding and the relation to wettability change	✓

# 7

## RECOMMENDATIONS

This chapter discusses the recommendations for future research based on this thesis, both on the theoretical and practical side of streaming potential research. For readability, we will present the recommendations in bullet points as well.

First, we start with general recommendations:

- In regular core flooding experiments, only the pressure drop ( $\Delta P$ ) is recorded. It is very useful to add a measurement of the potential drop ( $\Delta V$ ) to this. Although streaming potential experiments are sensitive and difficult to perform, the addition of streaming potential measurements can give extra information on surface processes ongoing inside the core.
- The assessment should be made whether continued streaming potential research is useful for LSF, as the measurements are difficult in the LSF salinity region. However, streaming potential research might be useful for the fundamental understanding of charge reversal and/or the assessment of other EOR methods.
- It would be very useful to see what the results for the coupling coefficient over a PNM would be compared to a BOT streaming potential model. This is essential to check the validity of the BOT models presented in this thesis.
- It would be useful to obtain zetasizer results at increased temperature (70 °C). This allows for better comparison with the streaming potential data. Also, this data would be a more valid input of the SP models.
- The validity of the pore network extraction code should be verified for several sandstones of lower permeability, where resolution of the micro CT data may become an issue regarding visibility of the pore throats and therefore the validity of the extraction.
- It would be useful to include ion exchange processes in the streaming potential models, as the assumption that the surfaces do not react and have a constant zeta potential, is not viable.

Recommendations for the streaming potential setup:

- In follow-up research it would be good to measure the total conductivity of the core at high salinity and at each measurement salinity in order to use the relation by [Briggs \[1928\]](#) to calculate the zeta potential out of the experimental results. This would provide an indication of the Stern layer conduction and would improve the fit of the models to the experimental data. Also, this would show whether the model is giving a useful physical representation of reality.
- The streaming potential setup should be standardized as much as possible in order to lower preparation and measurement time. A perfect example of this is the PEEK core holder. It was used instead of manually fabricated core holders. The electrodes should preferably be placed outside the sandstone core directly in the flow lines close to the core. This would prevent the necessity of drilling holes in the core, would lower preparation time and would make electrode replacement easier.

- Both the pressure drop and potential drop in the streaming potential setup should be digitally recorded. This allows for better data interpretation and filtering in hindsight. Also inline pH and conductivity measurements would improve data interpretation.
- The electrodes used in the experiments should be made strongly water-wet. This may prevent oil to impair the measuring abilities of the electrodes.
- The experiments on Berea 700 should be repeated to examine the validity of the values obtained in the lab.

# A

## ELECTROPHORESIS

In the sections on streaming potential, we described the flow behavior of an electrolyte past a stationary charged surface in presence of an applied pressure gradient, which is the reciprocal of the situation in which there is an external electric field. In electrophoresis, a colloidal particle, which has a surface charge, immersed in an electrolyte solution is subject to an applied external electric field. The particle is susceptible to move in response to the applied electric field and a relative displacement of particle in relation to the bulk electrolyte occurs. Key is to understand the electrophoretic velocity of a charged particle when it is placed in an electric field. This leads to the understanding of dilute particle concentration in an electrolyte, from which one wants to extract the zeta potential. The electrophoretic mobility of a particle can be described for two situations. The first situation is when  $\kappa r \ll 1$  and the particle small or the electrolyte is infinitely dilute, this means that there are very little mobile ions in solution. The second case is when  $\kappa r \gg 1$  and the particle large or the electrolyte solution highly concentrated. There are three coupled physical processes that are essential for a complete analysis of electrophoresis of a charged particle in an electrolyte solution [Masliyah and Bhattacharjee, 2006]:

1. Interaction of the charged particle with the external electric field, which gives rise to an electrical force on the particle
2. Formation of the electric double layer surrounding the particle giving rise to a spatially inhomogeneous charge distribution, which results in an electrical body force driven fluid flow
3. Transport of ions relative to the charged particle under the combined influence of convection, diffusion, and migration.

The full governing equations, describing the three coupled phenomena above can be simplified in order to render them to analytical solution techniques. The simplified models should account for the transport mechanisms present in the system. For a finite-thickness electric double layer around a charged particle, these are:

1. Electrophoretic retardation: The ion cloud around a particle, which has a charged surface, is of opposite charge. The fluid around the particle will move in respect to the imposed electric field in the opposite direction of the particle motion. The opposite movement of the fluid tends to retard the movement of the particle
2. Relaxation: Opposed to the situation with a stationary particle, the charge cloud around a moving particle in the presence of an electric field is not symmetric. In general, a particle has a different dielectric permittivity and conductivity than the surrounding fluid and this will give rise to a polarization charge and an associated field at the particle surface. This induced charge relaxes through diffusion and migration. When  $\kappa r < 0.1$  these effects are not important
3. Surface conductance: The distribution of ions in the mobile region of the electric double layer gives rise to a higher conductivity close to the surface than that in the bulk electrolyte. At small values of  $\zeta$  and  $\kappa r$ , the electrical conductivity inside the double layer is close to the bulk conductivity. When  $\zeta$  and  $\kappa r$  are

not small, the electrophoretic mobility of a particle is influenced by different electrolyte conductivities in the double layer. If surface conductance is important, the calculated values for the zeta potential may be too low.

All approximations start at one similar assumption. That is, the external electric field is much smaller in magnitude than the field produced by the charged particle. Now two simple approaches for the electrophoretic particle mobility are considered, one for small and one for large  $\kappa r$ .

#### FOR SMALL $\kappa r$

Masliyah and Bhattacharjee [2006] have done the derivation for the electrophoretic mobility from the Poisson-Boltzmann equation in the Debye-Hückel limit. The velocity of the center of the charge cloud can be given by:

$$U_R = -\frac{2}{3} \frac{\epsilon \zeta}{\eta} (\kappa r) E_\infty \quad (\text{A.1})$$

where  $E_\infty$  is the external field (V/m). This is also the retardation velocity of the fluid surrounding the particle and it approaches zero as  $\kappa r \rightarrow 0$ . If the particle volume fraction  $\phi_p$  goes to zero (infinitely dilute colloidal suspension), the the Stokes hydrodynamic drag force on the spherical particle with radius  $a$  is given by:

$$F_H = 6\pi\eta r(U - U_R) \quad (\text{A.2})$$

where  $U - U_R$  represents the velocity of the particle relative to the electrolyte solution. If the particle in non-accelerating the electrical and drag forces can be balanced ( $F_E = F_H$ ), leading to:

$$U = -\frac{2}{3} \frac{\epsilon \zeta}{\eta} E_\infty \quad (\text{A.3})$$

This solution is called the Hückel solution for the electrophoretic velocity, which is valid for small  $\kappa r$ . A more common way of writing is:

$$EM = \frac{U}{E_\infty} = \frac{\epsilon \zeta}{\eta} \quad (\text{A.4})$$

where  $EM = U/E_\infty$  is the electrophoretic mobility or velocity per unit field strength ( $m^2 V^{-1} s^{-1}$ ). An increase in electrophoretic mobility can be caused by either an increase in surface potential or a decrease in solution viscosity. The Hückel solution is valid for small  $\kappa r$  and accounts for the retardation effect. As the solution assumes a spherically symmetric double layer it does not account for the relaxation effect.

#### FOR LARGE $\kappa r$

For large values of  $\kappa r \gg 1$ , so when particle radius is large or the Debye length is small, the electric double layer becomes extremely thin and curvature effects of the particle do not play a large role anymore. Now the ions can be considered to move relative to a planar surface. The analysis based on this assumption is generally referred to as the Helmholtz-Smoluchowski solution. The fluid velocity at the particle surface is assumed to be zero, and the fluid velocity farther away is given as  $-U$ . We start with:

$$\eta \frac{d^2 u_x}{dy^2} = -\rho_f E_\infty \quad (\text{A.5})$$

where  $u_x$  is the velocity of the fluid tangential to the plate (m/s) and  $\rho_f$  is the charge density. If one combines this with the Poisson equation:

$$\epsilon \frac{d^2 \psi}{dy^2} = -\rho_f \quad (\text{A.6})$$

one obtains:

$$\eta \frac{d^2 u_x}{dy^2} = -\epsilon E_\infty \frac{d^2 \psi}{dy^2} \quad (\text{A.7})$$

The boundary conditions for this problem are:

1.  $\psi \rightarrow 0$  and  $u_x \rightarrow -U$  as  $y \rightarrow \infty$
2.  $\frac{d\psi}{dy} \rightarrow 0$  and  $\frac{du_x}{dy} \rightarrow 0$  as  $y \rightarrow \infty$
3.  $\psi = \zeta$  and  $u_x = 0$  at  $y = 0$

which leads to the expression of electrophoretic mobility for large  $\kappa r \gg 1$  and small  $ze\zeta/k_B T < 1$ :

$$\boxed{EM = \frac{U}{E_\infty} = \frac{e\zeta}{\eta}} \quad (\text{A.8})$$

Both the Helmholtz-Smoluchowski and Hückel analyses are independent of particle size.

#### FOR INTERMEDIATE $\kappa r$ : A SOLUTION BY HENRY

The analysis of Henry bridges the gap between the Helmholtz-Smoluchowski and Hückel solutions. Henry developed the theory describing the electrophoretic transport problem with a set of fluid mechanical and electrostatic equations. Henry makes two main assumptions, namely that the electric double layers are not disturbed by the flow (total potential within the double layer is a linear combination of the electric double layer potential and the potential due to the externally imposed field) and that the Debye-Hückel approximation for low surface potentials is assumed. It considers an equilibrium shape if the electrical double layer and the effects arising from convective relaxation and surface conductance are not accounted in the analysis. This leads to the following set of equations.

The following relation gives the electric force on the particle in the x-direction:

$$F_E = [-4\pi r^2 \epsilon \frac{d\psi}{dR} |_{R=r}] E_\infty \quad (\text{A.9})$$

The term in brackets is the total surface charge. At a steady state, the sum of the hydrodynamic and electric forces is zero as the particle does not have any acceleration. This means  $F_H = F_E$  and:

$$U = [\frac{2e\zeta E_\infty}{3\eta}] f(\kappa r) \quad (\text{A.10})$$

where

$$\begin{aligned} f(\kappa r) = & 1 + \frac{1}{16}(\kappa r)^2 - \frac{5}{48}(\kappa r)^3 - \frac{1}{96}(\kappa r)^4 + \frac{1}{96}(\kappa r)^5 \\ & + \frac{1}{8}(\kappa r)^4 e^{\kappa r} \left(1 - \frac{(\kappa r)^2}{12}\right) \int_{\kappa r}^{\infty} \left(\frac{e^{-t}}{t}\right) dt \end{aligned} \quad (\text{A.11})$$

This can also be expressed in terms of electrophoretic mobility:

$$\boxed{EM = \frac{U}{E_\infty} = [\frac{2e\zeta}{3\eta}] f(\kappa r)} \quad (\text{A.12})$$



# B

## EXPERIMENTAL PROTOCOL AND SEQUENCE

### B.1. STREAMING POTENTIAL

In Subsubsection 3.2.2.1, the fabrication of the core holders was discussed. Below, we describe the experimental protocol:

Preparation steps:

1. Connect in- and outflow lines to the core holder
2. Install flow lines to the differential pressure gauge
3. Fill flow lines to the pressure differential meter with demineralised water and make sure no air is trapped, then attach to the core holder
4. Check in demineralised water whether the electrodes give a potential of around 220 mV (if not: replace electrode, they are quite sensitive)
5. Screw the electrodes into the core holder
6. Solder the electrodes to the connecting wire
7. Make sure oven and pump are at the desired temperature
8. Prepare the brines

For single-phase experiments, one follows the following steps:

1. Flow  $CO_2$  into the core to displace the air inside
2. Flow HS brine into the core and switch on the back pressure at 5 bar to dissolve the  $CO_2$  into the brine
3. Flow brine until the SP signal stabilizes (at relatively high rates, 10 – 15 ml/min)
4. Check whether brine in- and outflow conductivity match
5. Take streaming potential measurements (note the potential difference ( $\Delta V$ ) and the pressure difference ( $\Delta P$ )) for different flow rates
6. Measure pH and fluid conductivity of the input brine and effluent brine
7. Then switch to a brine of lower salinity and follow the same steps. Be aware of formation damage risks. Formation damage can be avoided by staying above the Scheuermann limits, as described in Subsubsection 2.1.2.3. Furthermore, it is important to go from HS to LS in small steps.

In order to do two-phase experiments, it is important to do the following preparation steps to saturate the core with crude oil and formation brine:

1. Flow  $CO_2$  into the core to displace the air inside
2. Flow desired Formation (FM) brine into the core and switch on the back pressure at 5 bar to dissolve the  $CO_2$  into the brine
3. Check whether brine in- and outflow conductivity match
4. Flow crude oil into the sample, starting at very low rates (0.1 ml/min) and slowly working the way up to high rates (20 ml/min)
5. Measure water and oil production as precisely as possible. Note: dead volumes in the flow lines should be accurately calculated
6. Calculate the residual water saturation and decide whether it is low enough (should at least be:  $S_{wr} < 0.2$ )
7. Set the core aside and let it age for four weeks at 70 °C. Close all the ports and remove the electrodes. Clean the pump and all the flow lines

Measurements step for two-phase streaming potential experiments:

1. Connect the pressure meter and flow FM brine into the sample and measure oil production
2. Screw in the electrodes and start measurement cycle at residual oil saturation from HS → LS
3. Check whether brine in- and outflow conductivity match
4. Take streaming potential measurements (note the potential difference ( $\Delta V$ ) and the pressure difference ( $\Delta P$ )) for different flow rates
5. Measure pH and fluid conductivity of the input brine and effluent brine
6. Then switch to a brine of lower salinity and follow the same steps. Be aware of formation damage risks. Also, measure incremental oil production at each step to a lower salinity

If at step 6, one decides that the residual water saturation is not low enough, one can inject a viscous fluid to lower the water saturation even further. In our work, mixtures of PAO40 (Poly Alpha Olefin) and decane were used. PAO40 is a very viscous fluid. Mixtures of 50, 25, 10 and 1 cp (only decane) at 70 °C were made and injected into the core. Figure B.1 shows the volume percentage of PAO40 plotted against the viscosity of the mixture. After the injection of the PAO40 mixtures, one injects crude oil until only crude oil is produced; the procedure thus continues at step four of the two-phase protocol. This procedure increases the oil saturation inside the core from  $S_o = 0.5$  to  $S_o = 0.8$ .

Further points of attention are:

1. Be aware for FM damage, caused by the deflocculation of clays from the rock surface. If clays come loose they can clog pores and therefore reduce permeability. It is best to work from HS to LS in small steps. Make sure that the right amount of divalents is added to the solutions. A big step from HS to LS can lead to 'cation stripping' and a lower effective molarity in the formation. This could cause clays to deflocculate and clog pores, reducing permeability of the core.
2. If there is no flow, the measured potential difference over the core should be zero/ close to zero. If this is not the case, there might be something wrong with the electrodes

A typical measurement performed in the streaming potential experiment looks like as displayed in Figure B.2. There you can see the streaming potential response at several flow rates. To get a coupling coefficient  $C_s$  (V/Pa) for a certain molarity, one averages the coupling coefficient of the various flow rates. This means you obtain one coupling coefficient per molarity. Attached to this data are the in- and outflow conductivity, the fluid molarity and the in- and outflow pH.

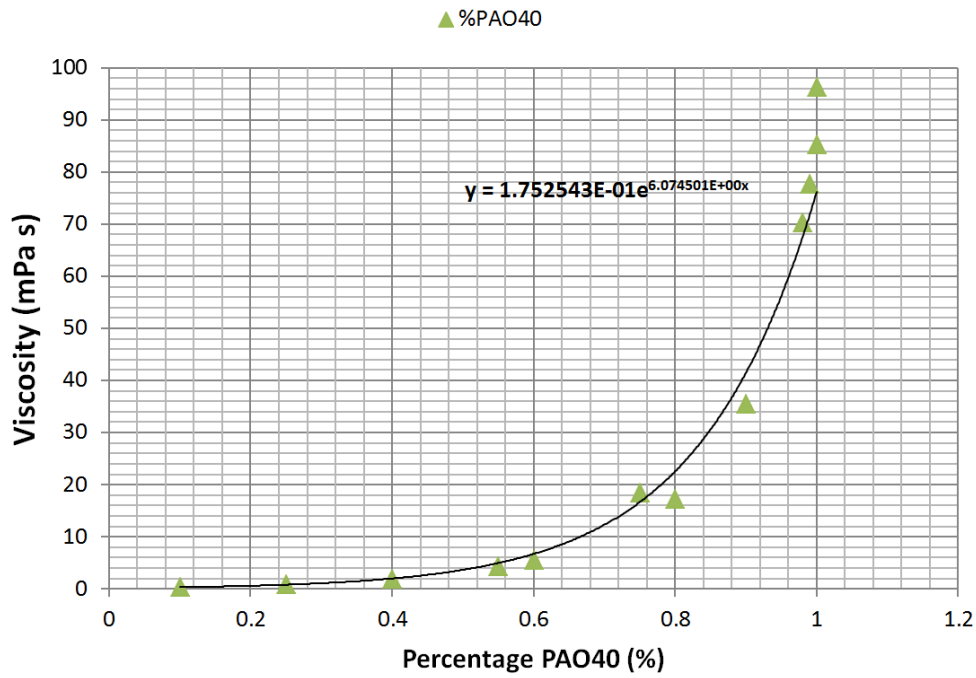


Figure B.1: Viscosity of PAO40/Decane mixtures plotted against the volume percentage of PAO40

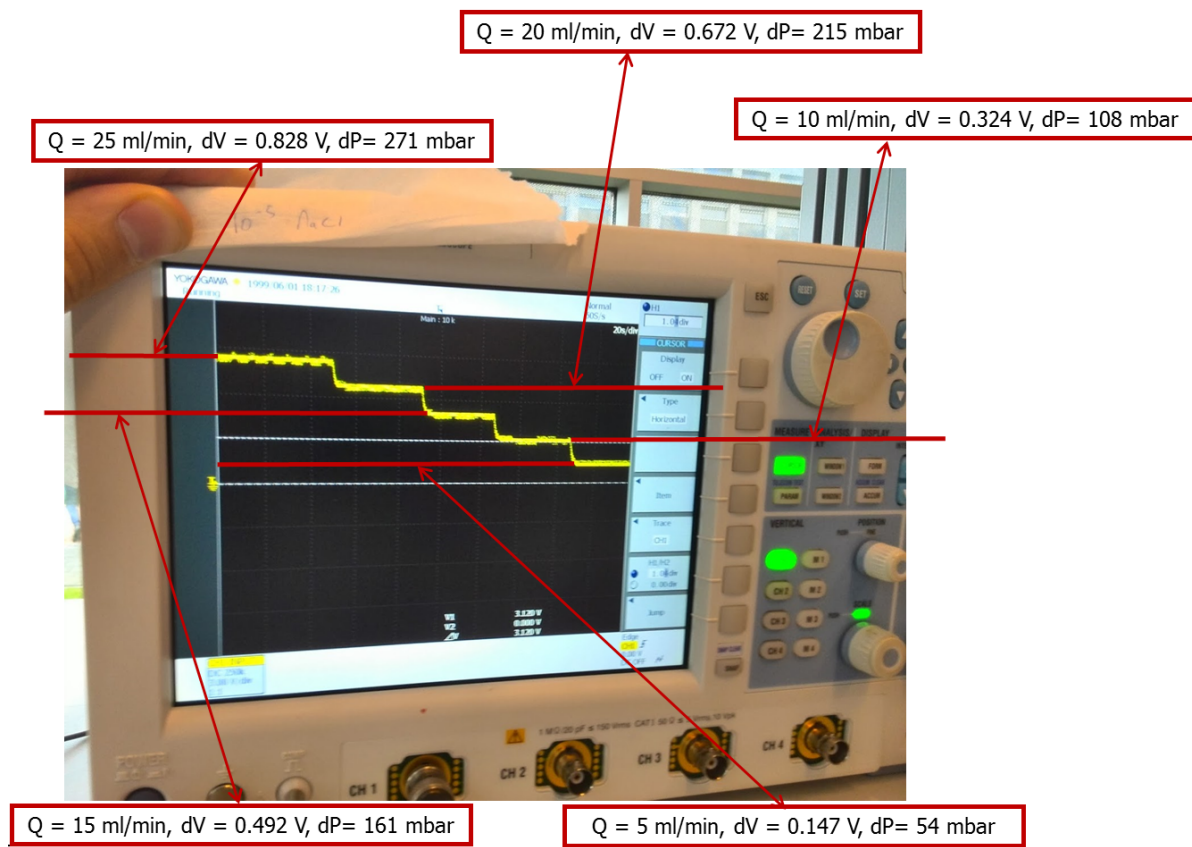


Figure B.2: Example of a streaming potential response on the oscilloscope for Bentheimer SST

## B.2. ZETASIZER

This section will describe the steps that can be followed to obtain good results in the zetasizer device. First, rock in brine is discussed, then oil in brine and then some tips and comments on how to use the autotitrator. The measurements in the Zetasizer are performed at 25 °C and atmospheric pressure (1 bar).

### ROCK IN BRINE

Sample preparation:

1. Crush rock gently to prevent intra-granular fracturing (do this in a mortar)
2. Take 0.5 g of rock and put this into a plastic vial that fits into the zetasizer pH meter / autotitrator
3. Add 10 mL of desired brine to this (rock should be 0.5 wt %)
4. Use a sonicator to deflocculate particles: 5 minutes at intermediate power
5. For manual pH measurements, add the amount of acid for the desired pH
6. Leave the suspension overnight for equilibration

Manual measurements:

1. Clean the cuvet/cell with demiwater → ethanol → demiwater
2. Flush cuvet with same brine as used in the experiment
3. Measure pH of the solution
3. Take a few milliliters of the supernatant part of the suspension and place in the cuvet
4. If the supernatant part of the suspension is too clear, manually shake it, wait for the large particles to settle and take a few milliliters from this part and place in the cuvet
5. Conduct the measurement quickly, as the suspension is not stable
6. For this: Go to the Measure → Manual Tab → Measurement Type → Zeta Potential; Select Material: Silica; Select Dispersant: Water
7. Select 4 measurements with 30 runs, with 0 seconds of equilibration time between the measurements
8. Place the cuvet inside the zetasizer and place two plugs on the ends
9. Make sure that there are no air bubbles trapped inside the cuvet
10. Press OK and Start

### OIL IN BRINE

Sample preparation:

1. Take one part of oil (1 ml) and nine parts of brine (9 ml) and put this into a plastic vial that fits into the zetasizer pH meter / autotitrator (1:10 ratio)
2. Use a sonicator to make a brine-oil emulsion that is as stable as possible
3. Leave the suspension overnight for equilibration
4. Before performing the measurement shake the vial and/or use the sonicator to make a stable emulsion

The measurement procedure for oil in brine is almost the same as the procedure for the rock-brine combination. The only step that should not be taken is the pH measurement, as the oil might damage the pH meter. Also extra care should be taken when looking at the quality of the emulsion as it degrades fast. Check this thoroughly and if the quality is too low, do an extra round of shaking and sonication on the sample.

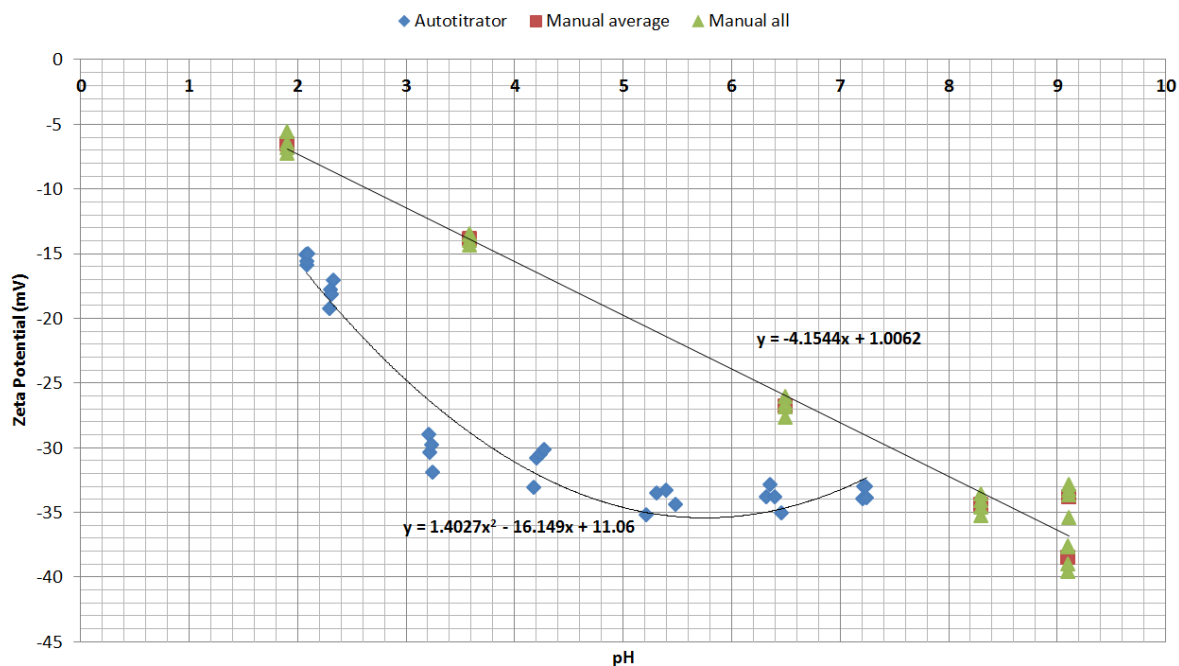


Figure B.3: Comparison of manual titration to autotitration for Berea 18 with a  $3.33 \times 10^{-4} \text{ mol/l}$  (with 10 % of divalents) brine. The blue dots represent the measurements from autotitration, the green dots the manual measurements and the red dots are the average value of the manual measurements per pH

#### AUTOTITRATION

Instead of adding acids or bases manually to the samples, it is also possible to use the autotitration function the zetasizer offers. Using this function saves time, as acids and bases do not need to be added manually. It is important to keep in mind though that the equilibration time the automatic mode offers is not enough to let the samples equilibrate fully, as this may take a full day.

A comparison between autotitration and manual titration was done for Berea 18 with a  $3.33 \times 10^{-4} \text{ mol/l}$  (with 10 % of divalents) brine for a pH range. This comparison shows that the autotitration cannot be used on Berea 18 sandstone, as is shown in Figure B.3.

The procedure for autotitration is as follows:

1. Clean the cuvet/cell with demiwater -- ethanol -- demiwater
2. Flush cuvet with same brine as used in the experiment
3. Go to the Tools Instrument → MPT-2 → Manual Control → Clean Tab
4. Put a vial with demiwater into the titrator → attach the flow lines from the titrator to the cuvet placed in the zetasizer → Press clean
5. Detach the demiwater vial → Press clean again (now only with air)
6. Go to the Prime Tab → Place an empty vial/beaker under the titrator → Press prime
7. Clean the flow lines and pH meter with demiwater
8. Take a new vial in which you put the supernatant part of the suspension from the original beaker (around 9 mL)
9. If the supernatant part of the suspension is too clear, put it back into the original beaker, manually shake it, wait for the large particles to settle and take from this part around 9 mL and place in the vial
10. Go to the Fill Tab → Put the supernatant sample in the titrator and add a magnetic stirrer

11. Place the pH meter above the stirring magnet and pull out stirrer
12. In the fill tab → Select 2 cycles → Press fill
13. Make sure to visually inspect the cuvet after this step. If there are still some air bubbles or even rock particles in the flow line, clean them out
14. Then the preparations are done and the lid of the zetasizer can be closed
15. Go to Measure → Manual → Measurement Type → Titration → pH → Zeta Potential
16. Select Material Silica
17. Select Dispersant Water
18. Measurements: Select 4 measurements with 30 runs, with a desired amount of equilibration time between the measurements (not too much, as suspension is not stable)
19. Fill in the titrant sample strength and whether they are acids or bases; initial volume is around 10 mL
20. In Sequence Tab → Select start at current pH (around 7) and go down with steps of 1 to pH 2. The accuracy of pH can be around 0.3
21. Press OK and press Start

# C

## PORE NETWORK EXTRACTION

To generate input for all the different models, the raw data obtained out of the micro-CT scan is at first loaded into the AVIZO image processing software. First, one needs to filter the micro-CT data. This can be done by using the command: Image Processing → Smoothing and Denoising → Non-Local Means Filter. An example of such a data set can be seen in Figure C.1.

The filtered image can be saved in the .am format familiar to AVIZO. The raw and filtered data have a certain resolution and size. The resolution obtained in the micro-CT scanner in Rijswijk is around  $1.84 \mu\text{m}$ . This is the size of a pixel. A voxel is a three dimensional pixel, with its sides in length equal to the pixel size.

To exclude the black space around the core in the micro-CT data and to make the data easier to handle for the pore-network extraction code, the data needs to be cropped to a smaller size. It is good to take a smaller rectangle inside the cylindrical scanned data. The lengths in the x, y and z direction of this volume are important to note. Figure C.2 shows the cropped data set.

Then, a watershed segmentation is used to determine whether a piece in the micro-CT scan data is pore space or rock matrix. A watershed segmentation uses the gradient in color in the picture to determine where certain boundaries lie. The color gradient at the boundary of pores and rock is usually the largest. These boundaries then indicate the separation between pore spaces and matrix rock. Conceptually, watershed segmentation first consisted of placing a water source in each regional minimum, then the relief is flooded and barriers are build where different sources are meeting. The resulting set of barriers constitutes a watershed by flooding. In AVIZO, one determines the amount of phases to be watershed (two in our case), then the program will calculate the color gradient of the image and visually the boundary can be set in the proper range (boundary of pore and pore space). After this, the range of pore space and matrix rock can both be set. This input makes a good watershed possible. Figure C.3 shows the image after watershed segmentation.

The output of the watershed segmentation can then be transformed to a binary file of the proper format, in which ones (blue) will indicate rock matrix, and zeros pore space (black). This is shown in Figure C.4.

The binary image generated out of the watershed image can be saved in a 3D raw data file, which consists only of 1's and 0's, and has the extension .raw. This extension should then be changed in .dat to function as an input for the pore-network extraction. An oversight of the whole process can be seen in Figure C.5. You can see that the filtered data is first watershed, then made into a binary image and then this binary image is thresholded, in order to have proper 1's and 0's.

This process is repeated for all three rocks, namely Berea Block 18, Berea 700 and Bentheimer sandstones. It is possible to further filter the data by means of an erosion → dilution or a gap filling procedure. This can further enhance the image that is inputted into the pore network extraction. One should always visually inspect the input though.

To extract a pore-network from this data we use a pore-network extraction code fabricated by Dong [2007]. This code uses a maximal ball algorithm to divide the image in pore throats and pore bodies. The maximal ball algorithm starts at a certain voxel. It tries to find the largest inscribed spheres that just touch the grain or the boundary. Those included by other spheres are viewed as inclusions and removed. The remaining balls are called maximal balls and describe the pore space without redundancy. Locally, the largest maximal balls identify pores. The smallest balls between pores are the pore throats [Dong, 2007].

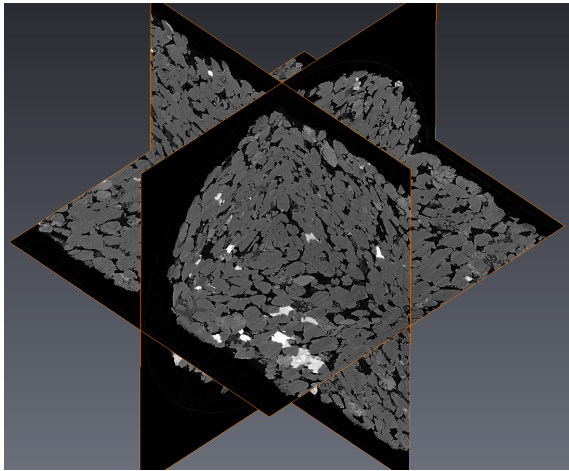


Figure C.1: Filtered micro-CT data in AVIZO

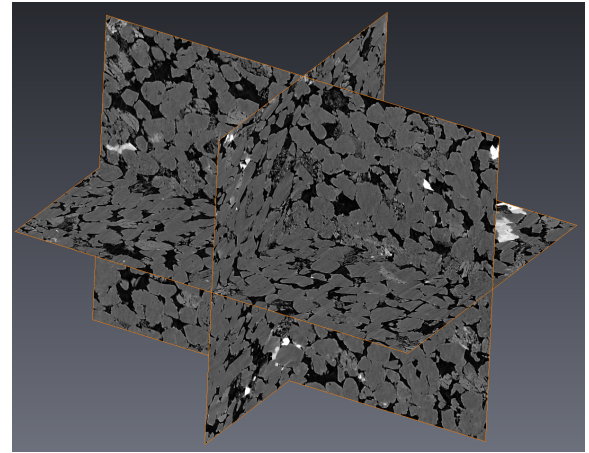


Figure C.2: Filtered and cropped micro-CT data in AVIZO

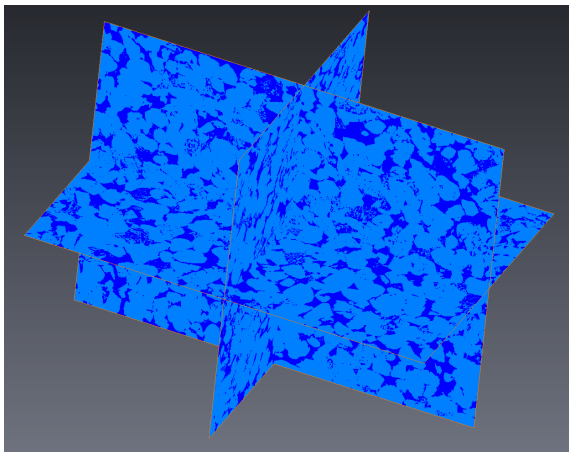


Figure C.3: Filtered and cropped micro-CT data in AVIZO

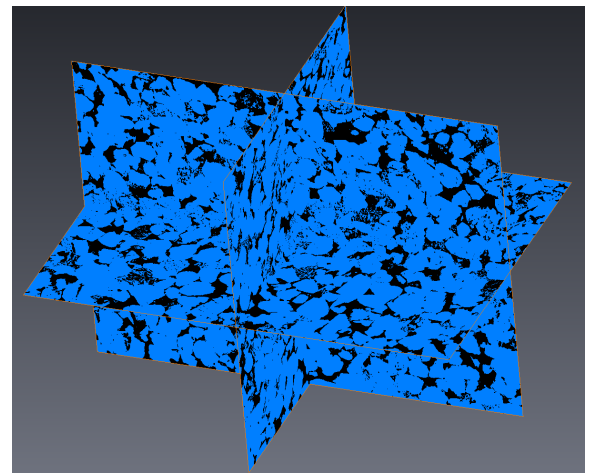


Figure C.4: Binary image of the filtered and cropped micro-CT data in AVIZO

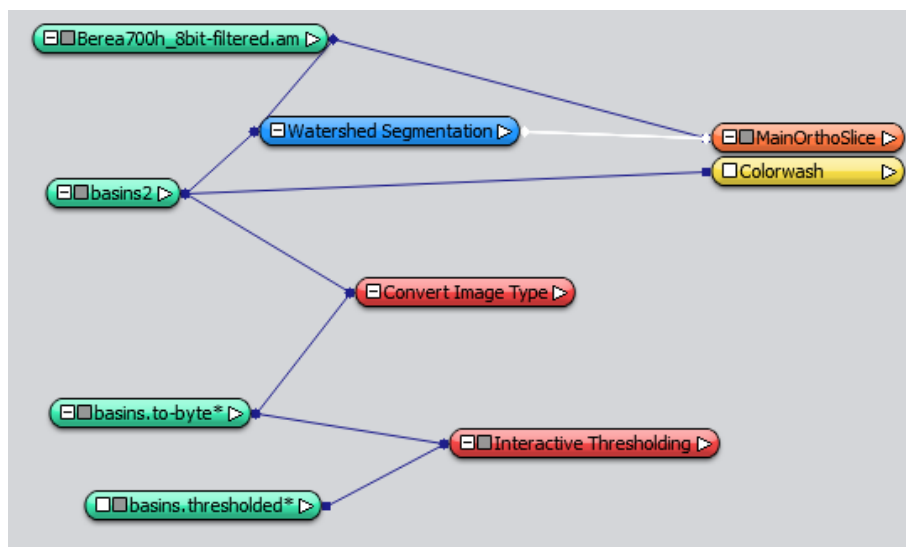


Figure C.5: Flow chart of the steps taken in AVIZO in order to obtain correct input for the pore-network extraction code

These pore throats all have their assigned throat index, index of two connecting pores, throat radius, length (from pore center to pore center) and shape factor, which are outputted in four different files. The pore bodies all have their assigned pore index, x, y and z coordinates, pore radius, pore shape factor, the pore connection number z, data on whether the pore is an inlet or outlet pore and the connecting throat indices [Sochi, 2007]. Input of that model are the .dat file fabricated with AVIZO, whether the data is binary, micro-CT or raw data (in our case binary), the size of the image in x,y and z direction, the resolution of the image and the minimum amount of clustered pores to be used in the extraction. This is given as a number R, which represents the minimum amount of R\*R pores that are taken as input into the pore-network extraction.

The output files can be read out with a MATLAB code by Hogenkamp [2014] and can be used as input for the bundle of tubes model and of streaming potential. An adjusted MATLAB code is made in order to generate the correct input for the pore-network model. Figure C.6 shows the pore throat size and pore radius size distribution for a Berea 18 SST.

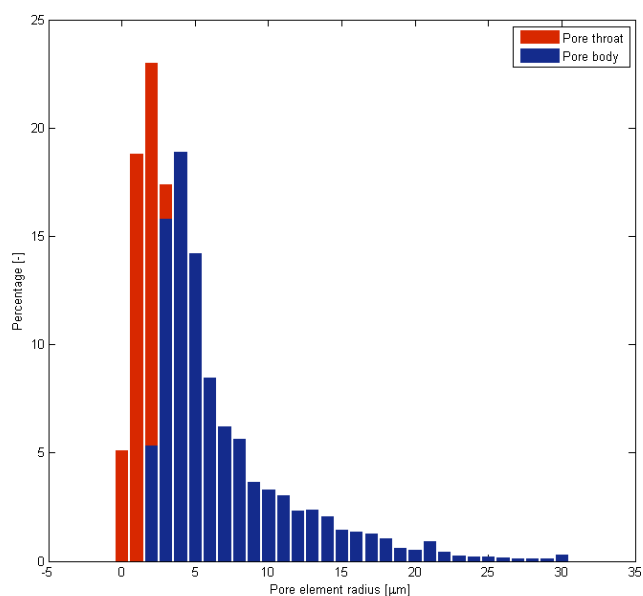


Figure C.6: Pore throat radius and pore body radius distribution for a Berea 18 SST



# D

## EXPERIMENTAL DATA

This chapter shows the raw experimental data of all the streaming potential and zetasizer experiments. The data will be mainly displayed in tables.

### D.1. STREAMING POTENTIAL

This section contain all the raw zetasizer data.

Table D.1: Single-phase data QF20 at 20 °C, no divalents are added to the *NaCl* brines

<i>Molarity</i> <i>mol/l</i>	<i>Conductivity</i> <sub>average</sub> <i>μS/cm</i>	<i>C<sub>s,average</sub></i> <i>V/Pa</i>	<i>Q/ΔP</i> <i>m<sup>3</sup>/(Pas)</i>
1.00E-05	2	-1.98E-05	1.63E-10
2.00E-05	3	-1.99E-05	1.65E-10
1.00E-04	12	-3.99E-06	1.68E-10

Table D.2: Single-phase data Bentheimer at 20 °C, no divalents are added to the *NaCl* brines

<i>Molarity</i> <i>mol/l</i>	<i>Conductivity</i> <sub>average</sub> <i>μS/cm</i>	<i>C<sub>s,average</sub></i> <i>V/Pa</i>	<i>Q/ΔP</i> <i>m<sup>3</sup>/(Pas)</i>
1.00E-05	2.5	-3.13E-05	1.53E-11
2.00E-05	4	-2.99E-05	1.54E-11
1.00E-04	12.5	-1.76E-05	1.55E-11
1.00E-03	112	-3.05E-06	1.56E-11
1.00E-02	1131.5	-2.69E-07	1.58E-11
1.00E-01	10150	-1.95E-08	1.56E-11

Table D.3: Two-phase data Bentheimer at 20 °C, no divalents are added to the *NaCl* brines

<i>Molarity</i> <i>mol/l</i>	<i>Conductivity</i> <sub>average</sub> <i>μS/cm</i>	<i>C<sub>s,average</sub></i> <i>V/Pa</i>	<i>Q/ΔP</i> <i>m<sup>3</sup>/(Pas)</i>
1.00E-05	3.6	-1.00E-05	2.20E-12
1.00E-04	15.4	-5.54E-06	2.26E-12
1.00E-03	132	-1.08E-06	2.59E-12
2.60E-03	313	-4.72E-07	2.49E-12
1.00E-02	1192	-1.98E-07	2.54E-12
2.60E-02	3000	-1.97E-07	2.56E-12

Table D.4: Two-phase data Bentheimer at 20 °C, 10 % divalents ( $CaCl_2$ ) are added to the  $NaCl$  brines

<i>Molarity</i> <i>mol/l</i>	<i>Conductivity</i> <sub>average</sub> $\mu S/cm$	$C_{s,average}$ <i>V/Pa</i>	$Q/\Delta P$ $m^3/(Pas)$
1.00E-05	2.5	-1.31E-05	1.67E-12
1.00E-05	2.75	-1.40E-05	3.21E-12
1.00E-04	12.9	-8.54E-06	3.22E-12
1.00E-03	112.1	-1.40E-06	3.29E-12
2.60E-03	301	-4.40E-07	3.32E-12
1.00E-02	1067.5	-1.26E-07	3.37E-12

Table D.5: Single-phase data Berea 700 at 20 °C, 10 % divalents ( $CaCl_2$ ) are added to the  $NaCl$  brines. The value in bold is the coupling coefficient measured with Dagang brine (reverse sign)

<i>Molarity</i> <i>mol/l</i>	<i>Conductivity</i> <sub>average</sub> $\mu S/cm$	$C_{s,average}$ <i>V/Pa</i>	$Q/\Delta P$ $m^3/(Pas)$
1.00E-05	3.95	-2.02E-06	4.57E-12
1.00E-04	15.65	-2.19E-06	4.54E-12
3.33E-04	41.65	-1.78E-06	4.56E-12
1.00E-03	115.45	-1.04E-06	4.57E-12
2.60E-03	306	-4.38E-07	4.67E-12
1.00E-02	1105	-1.25E-07	4.44E-12
2.60E-02	2915	-4.63E-08	4.48E-12
4.00E-02	4990	-3.03E-08	4.38E-12
1.00E-01	10040	-8.42E-09	4.39E-12
4.00E-01	44050	<b>5.92E-09</b>	4.36E-12

Table D.6: Single-phase data Berea 700 at 70 °C, 10 % divalents ( $CaCl_2$ ) are added to the  $NaCl$  brines

<i>Molarity</i> <i>mol/l</i>	<i>Conductivity</i> <sub>average</sub> $\mu S/cm$	$C_{s,average}$ <i>V/Pa</i>	$Q/\Delta P$ $m^3/(Pas)$
1.00E-05	10.55	-1.05E-06	6.04E-12
1.00E-04	22.85	-9.58E-07	5.88E-12
3.33E-04	48.25	-9.53E-07	4.61E-12
1.00E-03	123.55	-6.12E-07	4.57E-12
2.60E-03	312.5	-3.07E-07	4.23E-12
1.00E-02	1101.5	-8.63E-08	4.19E-12
2.60E-02	3002.5	-4.07E-08	4.02E-12

Table D.7: QC of single-phase data Berea 700 at 70 °C, 10 % divalents ( $CaCl_2$ ) are added to the  $NaCl$  brines. Brine at 0.4 M is Dagang brine

<i>Molarity</i> <i>mol/l</i>	<i>Conductivity</i> <sub>average</sub> $\mu S/cm$	$C_{s,average}$ <i>V/Pa</i>	$Q/\Delta P$ $m^3/(Pas)$
4.00E-01	43550	-2.94E-07	3.71E-12
1.00E-02	1180	-1.63E-07	3.03E-12
2.60E-02	2951.5	-7.04E-08	2.70E-12
1.00E-03	146.4	-7.97E-07	2.71E-12
2.60E-03	326.5	-5.32E-07	2.73E-12
1.00E-01	9830	-6.68E-08	2.73E-12

## D.2. ZETASIZER

This section contains the raw zetasizer data.

Table D.8: Two-phase unaged data Berea 700 at 70 °C, 10 % divalents ( $CaCl_2$ ) are added to the  $NaCl$  brines. The top value in bold is the coupling coefficient measured with 0.4 M synthetic brine, the bottom one with Dagang brine (reverse sign)

<i>Molarity</i> <i>mol/l</i>	<i>Conductivity</i> <i>average</i> $\mu S/cm$	$C_{s,average}$ <i>V/Pa</i>	$Q/\Delta P$ $m^3/(Pas)$
1.00E-05	8.5	-2.89E-07	8.46E-13
1.00E-04	18.5	-3.25E-07	8.95E-13
3.33E-04	49	-4.17E-07	9.38E-13
1.00E-03	116.5	-3.92E-07	9.84E-13
2.60E-03	287.5	-3.24E-07	1.02E-12
1.00E-02	1017.5	-1.47E-07	1.03E-12
2.60E-02	2500	-7.15E-08	1.05E-12
1.00E-01	9785	-7.90E-09	9.95E-13
4.00E-01	35050	<b>1.57E-07</b>	1.01E-12
4.00E-01	42400	<b>2.45E-07</b>	9.51E-13

Table D.9: Two-phase aged data Berea 700 at 70 °C, 10 % divalents ( $CaCl_2$ ) are added to the  $NaCl$  brines. The value in bold is the coupling coefficient measured with Dagang brine (reverse sign)

<i>Molarity</i> <i>mol/l</i>	<i>Conductivity</i> <i>average</i> $\mu S/cm$	$C_{s,average}$ <i>V/Pa</i>	$Q/\Delta P$ $m^3/(Pas)$
1.00E-05	10	-4.84E-07	1.16E-12
1.00E-04	22.4	-6.01E-07	1.18E-12
3.33E-04	51.3	-6.09E-07	1.18E-12
1.00E-03	129	-4.55E-07	1.20E-12
2.60E-03	321.5	-3.07E-07	1.23E-12
1.00E-02	1201.5	-1.23E-07	1.23E-12
2.60E-02	2910	-4.92E-08	1.23E-12
1.00E-01	8670	-2.89E-08	1.20E-12
4.00E-01	42100	<b>8.55E-08</b>	1.09E-12

Table D.10: Zeta potential data for rock-brine combinations. The top matrix indicates the measurement pH, the middle matrix the measured zeta potential in mV and the bottom matrix indicates the standard deviation of the measurements in mV

<b>pH</b>	<b>Berea 700</b>			<b>Bentheimer</b>			<b>Berea 18</b>		
10 <sup>-4</sup> M	8.7	7.45	5.12	7.66	6.7	4.44	8.4	7.01	6.05
10 <sup>-3</sup> M	8.9	7.4	4.91	7.04	6.47	5.36	8.78	7.31	6.2
10 <sup>-2</sup> M	8.65	7.4	5.45	6.65	6.04	5.07	8.6	7.35	5.93
10 <sup>-1</sup> M	8.15	6.9	5.76	6.95	6.23	5.3	8.3	7.14	5.85
0.4 M	7.75	7.15	5.04	6.67	6.31	5.38	7.83	6.96	5.8
Dagang (0.4 M)	7.77	7.13	5.58	6.6	6.3	5.47	8.04	7	5.96
<b>ZP (mV)</b>	<b>Berea 700</b>			<b>Bentheimer</b>			<b>Berea 18</b>		
10 <sup>-4</sup> M	-23.9	-31.9	-13.1	-27.3	-33	-29	-25.3	-24.1	-13.2
10 <sup>-3</sup> M	-27.3	-24.4	-10.6	-32.8	-32.9	-28.1	-25.6	-22.3	-14.1
10 <sup>-2</sup> M	-25.2	-23.1	-13.6	-21.4	-24	-16.9	-23.9	-23.2	-15.7
10 <sup>-1</sup> M	-22.1	-21.2	-14.3	-18.5	-16.1	-16.6	-21.1	-19.8	-16.4
0.4 M	-16.9	-17.5	-11.3	-17.3	-15.9	-14.7	-15.7	-16.5	-13.1
Dagang (0.4 M)	-14	-15.9	-10.5	-13.7	-12.5	-11.1	-13.75	-12.9	-11.9
<b>SD (mV)</b>	<b>Berea 700</b>			<b>Bentheimer</b>			<b>Berea 18</b>		
10 <sup>-4</sup> M	1.16	0.822	0.548	2.17	1.33	2.69	0.238	1.72	0.9
10 <sup>-3</sup> M	1.95	1.24	0.443	2.03	3.03	0.898	1.71	0.597	1.81
10 <sup>-2</sup> M	0.606	0.793	0.802	2.13	1.9	1.42	0.457	0.952	0.294
10 <sup>-1</sup> M	0.956	0.525	0.748	2.51	1.53	1.41	0.591	0.634	0.898
0.4 M	1.85	2.31	0.819	0.987	2.18	1.08	1.16	1.16	2.55
Dagang (0.4 M)	1.75	0.64	1.12	2.24	2.02	1.52	1.18	1.91	1.02

Table D.11: Zeta potential data for oil-brine combinations. Ratio of 1:10 oil:brine. Top vector indicates the zeta potential in mV, bottom vector the standard deviation in mV

<b>ZP (mV)</b>	<b>Crude Oil H</b>
$10^{-4}$ M	-35.9
$10^{-3}$ M	-30
$10^{-2}$ M	-19.1
$10^{-1}$ M	-14.5
0.4 M	-12.2
Dagang (0.4 M)	-13
<b>SD (mV)</b>	<b>Crude Oil H</b>
$10^{-4}$ M	7.46
$10^{-3}$ M	4.19
$10^{-2}$ M	4.09
$10^{-1}$ M	2.68
0.4 M	1.06
Dagang (0.4 M)	2.25

## BIBLIOGRAPHY

- Abdallah, W., Buckley, J., Carnegie, A., Herold, J., Graue, A., Habashy, T., Seleznev, N., Signer, C., Hussain, H., Montaron, B., and Ziauddin, M. (2007). Fundamentals of wettability. *Oilfield Review*, 19.
- Alotaibi, M. B., Nasralla, R. A., and Nasr-El-Din, H. A. (2011). Wettability Studies Using Low-Salinity Water in Sandstone Reservoirs. *SPE Reservoir Evaluation and Engineering*, (December 2011).
- Austad, T., Rezaeidoust, A., and Puntervold, T. (2010). Chemical Mechanism of Low Salinity Water Flooding in Sandstone Reservoirs. In *Proceedings of SPE Improved Oil Recovery Symposium, Tulsa, Oklahoma*. Society of Petroleum Engineers.
- Bernard, G. (1967). Effect of Floodwater Salinity on Recovery of Oil from Cores Containing Clays. *SPE California Regional Meeting, Los Angeles, California, 26-27 October*.
- Blunt, M. J., Jackson, M. D., Piri, M., and Valvatne, P. H. (2002). Detailed physics, predictive capabilities and macroscopic consequences for pore-network models of multiphase flow. *Advances in Water Resources*, 25(8-12):1069–1089.
- Briggs, D. (1928). Streaming Potential. *Journal of Physical Chemistry*, 32:641.
- Brunet, E. and Ajdari, A. (2004). Generalized Onsager relations for electrokinetic effects in anisotropic and heterogeneous geometries. *Physical Review E*, 69(1):016306.
- Clementz, D. M. (1977). Clay Stabilization in Sandstones Through Adsorption of Petroleum Heavy Ends. *Journal of Petroleum Technology, September 1977*.
- Craig, R. (2004). *Craig's Soil Mechanics*. Spon Press, London, 7th editio edition.
- Crain, E. (2014). *Crain's Petrophysical Handbook*.
- Dong, H. (2007). *Micro-CT Imaging and Pore Network Extraction*. Phd thesis, Imperial College.
- Dubey, S. T. and Doe, P. H. (1993). Base Number and Wetting Properties of Crude Oils. *SPE Reservoir Engineering*, (August):195–200.
- Flury, M. and Gimmi, T. (2002). Solute Diffusion. *Methods of Soil Analysis*, 4:1323 – 1351.
- Glover, P. W. J. (2013). Slide set: Electrokinetic Properties of Rocks.
- Glover, P. W. J., Walker, E., and Jackson, M. D. (2012). Streaming-potential coefficient of reservoir rock: A theoretical model. *Geophysics*, 77(2):D17–D43.
- Guichet, X. (2003). Streaming potential of a sand column in partial saturation conditions. *Journal of Geophysical Research*, 108(B3):2141.
- Hirasaki, G. J. (1991). Wettability : Fundamentals and Surface Forces. *SPE Formation Evaluation*, (June).
- Hogenkamp, P. (2014). *The Effect of the Contact Angle on the Macroscopic Transport Properties*. Msc thesis, Delft University of Technology.
- Hughes, D., Larsen, S., and Wright, R. (2010). Review of Low Salinity Water Flooding. Technical report.
- Hughes, D., Law, S., Pitt, G., Wright, R., Marinou, E., and Sutcliffe, P. (2012). Low Salinity EOR " State of Play " Review. Technical report.
- Hunter, R. J. (1981). *Electrokinetic Phenomena*. Academic Press, New York.
- Israelachvili, J. N. (2011). *Intermolecular and Surface Forces*. Elsevier, Amsterdam, third edit edition.

- Jackson, M. D. (2008). Characterization of multiphase electrokinetic coupling using a bundle of capillary tubes model. *Journal of Geophysical Research*, 113(B4):B04201.
- Jackson, M. D., Gulamali, M. Y., Leinov, E., Saunders, J. H., and Vinogradov, J. (2012). Spontaneous Potentials in Hydrocarbon Reservoirs During Waterflooding : Application to Water-Front Monitoring. *SPE Journal*, (March):53–69.
- Joekar-Niasar, V. (2010). *The Immiscibles: Capillarity Effects in Porous Media*. PhD Thesis, Utrecht University.
- Joekar-Niasar, V., Dijke, M. I. J., and Hassanizadeh, S. M. (2012). Pore-Scale Modeling of Multiphase Flow and Transport: Achievements and Perspectives. *Transport in Porous Media*, 94(2):461–464.
- Lager, A., Webb, K. J., Black, C. J. J., Singleton, M., and Sorbie, K. S. (2006). Low Salinity Oil Recovery - An Experimental Investigation. In *Proceedings of the International Symposium or the Society of Core Analysts, Trondheim, Norway*, pages 1–12.
- Ligthelm, D., Gronsveld, J., Hofman, J., Brussee, N., Marcelis, F., and Van Der Linde, H. (2009). Novel Waterflooding Strategy by Manipulation of Injection Brine Composition ( SPE-119835 ). In *Proceedings of the SPE EUROPEC/EAGE ATCE, Amsterdam, The Netherlands*, number June 2009.
- Linde, N., Jougnot, D., Revil, A., Matthäi, S. K., Arora, T., Renard, D., and Doussan, C. (2007). Streaming current generation in two-phase flow conditions. *Geophysical Research Letters*, 34(3):L03306.
- Mahani, H. (2013). Slide set Low Salinity (LS) Water Flooding.
- Mahani, H., Berg, S., Ilic, D., Bartels, W.-B., and Joekar-Niasar, V. (2014). Kinetics of Low-Salinity-Flooding Effect. *SPE Reservoir Evaluation and Engineering*, Preprint(Preprint).
- Mahani, H., Sorop, T. G., Ligthelm, D., Brooks, A. D., Vledder, P., Mozahem, F., and Ali, Y. (2011). Analysis of Field Responses to Low-salinity Waterflooding in Secondary and Tertiary Mode in Syria. In *Proceedings of the SPE EUROPEC/EAGE ATCE, Vienna, Austria*.
- Malmberg, C. and Maryott, A. (1956). Dielectric Constant of Water from 0 to 100 C. *Journal of Research of the National Bureau of Standards*, 56(I):1–8.
- Marcelis, A. (2012a). Personal communication: Scanning Electron Microscopy analysis Berea 18.
- Marcelis, F (2006). Personal communication: XRD analysis on Berea and Bentheimer sandstone samples.
- Marcelis, F (2012b). Personal communication: X-ray diffraction semi-quantitative mineralogical analysis of 1 sample of Berea Sandstone Block 18.
- Masliyah, J. H. and Bhattacharjee, S. (2006). *Electrokinetic and Colloid Transport Phenomena*. John Wiley & Sons, New Jersey, first edit edition.
- McCain, W. (1991). Reservoir-Fluid Property Correlations - State of the Art. *SPE Reservoir Engineering*, (May):266 – 272.
- Mcguire, P. L., Chatham, J. R., Paskvan, E. K., Sommer, D. M., and Carini, F. H. (2005). Low Salinity Oil Recovery: An Exciting New EOR Opportunity for Alaska's North Slope. In *Proceedings of the SPE Western Regional Meeting, Irvine, California*, pages 1–15.
- Meunier, A. (2005). *Clays*. Springer Science & Business Media, Berlin, isbn 3-540 edition.
- Mortensen, N. A., Olesen, L. H., and Bruus, H. (2006). Transport coefficients for electrolytes in arbitrarily shaped nano and micro-fluidic channels. *New Journal of Physics*, 8(37).
- Mungan, N. (1967). Permeability Reduction Through Changes in pH and Salinity. *Journal of Petroleum Technology*, December:1449 – 1453.
- Nasralla, R. A., Bataweel, M. A., and Nasr-El-Din, H. A. (2011). Investigation of Wettability Alteration by Low Salinity Water in Sandstone Rock. In *Proceedings of SPE Offshore Europe Oil and Gas Conference and Exhibition, Aberdeen, United Kingdom*.

- Nasralla, R. A. and Nasr-el din, H. A. (2012). Double-Layer Expansion : Is It A Primary Mechanism of Improved Oil Recovery by Low-Salinity Waterflooding? In *Proceedings of SPE Improved Oil Recovery Symposium, Tulsa, Oklahoma*, number 2008.
- Pride, S. R. and Morgan, F. D. (1991). Electrokinetic dissipation induced by seismic waves. *Geophysics*, 56(7):914–925.
- Revil, A. and Glover, P. W. J. (1998). Nature of surface electrical conductivity in natural sands, sandstones and clays. *Geophysical Research Letters*, 25(5):691–694.
- Revil, A., Linde, N., Cerepi, A., Jougnot, D., Matthäi, S., and Finsterle, S. (2007). Electrokinetic coupling in unsaturated porous media. *Journal of colloid and interface science*, 313(1):315–27.
- Revil, A., Pezard, P. A., and Glover, P. W. J. (1999a). Streaming potential in porous media: 1. Theory of the zeta potential. *Journal of Geophysical Research*, 104(B9):20,021–20,031.
- Revil, A., Schwaegel, H., Cathles, L. M., and Manhardt, P. D. (1999b). Streaming potential in porous media: 2. Theory and application to geothermal systems. *Journal of Geophysical Research*, 104(No. B9):20,033–20,048.
- Ruhl, C. (2014). BP Energy Outlook 2035. Technical Report January, British Petroleum, London.
- Scheuerman, R. F. and Bergersen, B. M. (1989). Supplement to SPE18461, Injection-Water Salinity, Formation Pretreatment, and Well Operations Fluid-Selection Guidelines.
- Scheuerman, R. F. and Bergersen, B. M. (1990). Injection-Water Salinity, Formation Pretreatment, and Well-Operations Fluid-Selection Guidelines. *Journal of Petroleum Technology*, (July):836–845.
- Schoemaker, F. C., Grobbe, N., Schakel, M. D., de Ridder, S. a. L., Slob, E. C., and Smeulders, D. M. J. (2012). Experimental Validation of the Electrokinetic Theory and Development of Seismoelectric Interferometry by Cross-Correlation. *International Journal of Geophysics*, 2012:1–23.
- Secombe, J., Lager, A., Jerauld, G., Jhaveri, B., Buikema, T., Bassler, S., Denis, J., Webb, K., Cockin, A., Fuego, E., and Paskvan, F. (2010). Demonstration of Low-Salinity EOR at Interwell Scale, Endicott Field, Alaska. In *Proceedings of SPE Improved Oil Recovery Symposium, Tulsa, Oklahoma*, volume 2008.
- Shaw, D. (1980). *Introduction to Colloid and Surface Chemistry*. Butterworths, London, 3rd edition.
- Skrettingland, K., Holt, T., Tweheyo, M. T., and Skjevraak, I. (2011). Snorre Low-Salinity-Water Injection — Core-flooding Experiments and Single-Well Field Pilot. *SPE Reservoir Evaluation and Engineering*, (April):182 – 192.
- Sochi, T. (2007). *Pore-Scale Modeling of Non-Newtonian Flow in Porous Media*. Phd thesis, Imperial College.
- Sorbie, K. S. and Collins, I. R. (2010). A Proposed Pore-Scale Mechanism for How Low Salinity Waterflooding Works. *Proceedings of SPE Improved Oil Recovery Symposium, Tulsa, Oklahoma, 24-28 April 2010*.
- Speight, J. (1980). *The chemistry and technology of petroleum*. Marcel Dekker, New York.
- Sprunt, E. S., Mercer, T. B., and Djabbarah, N. F. (1994). Streaming potential from multiphase flow. *Geophysics*, 59(5):707–711.
- Stein, D., Kruihof, M., and Dekker, C. (2004). Surface-Charge-Governed Ion Transport in Nanofluidic Channels. *Physical Review Letters*, (July):1–4.
- Suijkerbuijk, B. M. J. M., Hofman, J., Ligthelm, D. J., Romanuka, J., Brussee, N., van der Linde, H., and Marcelis, A. (2012). Fundamental investigations into wettability and low salinity flooding by parameter isolation. In *Proceedings of SPE Improved Oil Recovery Symposium, Tulsa, Oklahoma*, number February.
- Suijkerbuijk, B. M. J. M., Kuipers, H. P. C. E., Kruijsdijk, C. P. J. W. V., Berg, S., Winden, J. F. V., Ligthelm, D. J., Mahani, H., Pingo Almada, M., Van den Pol, E., Joekar-Niasar, V., Romanuka, J., Vermolen, E. C. M., and Al-Qarshubi, I. S. M. (2013). The Development of a Workflow to Improve Predictive Capability of Low Salinity Response. In *Proceedings of the IPTC, Beijing, China, 26-28 March 2013*.

- Tang, G.-Q. and Morrow, N. R. (1999). Influence of brine composition and fines migration on crude oil/brine/rock interactions and oil recovery. *Journal of Petroleum Science and Engineering*, 24(2-4):99–111.
- Valvatne, P. H. and Blunt, M. J. (2003). Predictive Pore-Scale Network Modeling. In *Proceedings of SPE ATCE, Denver, Colorado*.
- Vinogradov, J., Jaafar, M. Z., and Jackson, M. D. (2010). Measurement of streaming potential coupling coefficient in sandstones saturated with natural and artificial brines at high salinity. *Journal of Geophysical Research*, 115(B12):B12204.
- Vledder, P., Fonseca, J. C., Wells, T., Gonzalez, I., and Ligthelm, D. (2010). Low Salinity Water Flooding : Proof Of Wettability Alteration On A Field Wide Scale. In *Proceedings of SPE Improved Oil Recovery Symposium, Tulsa, Oklahoma, 24-28 April 2010*, number Lil.